Dynamic Modelling and Thermo-Economic Optimization of a Small-Scale Hybrid Solar/Biomass Organic Rankine Cycle Power System

Khaled Hossin

PhD

2017

Dynamic Modelling and Thermo-Economic Optimization of a Small-Scale Hybrid Solar/Biomass Organic Rankine Cycle Power System

Khaled Hossin

A thesis submitted in partial fulfilment
of the requirements of the
University of Northumbria at Newcastle
for the degree of
Doctor of Philosophy

Research undertaken in the
Faculty of Engineering and Environment

March 2017

Abstract

The use of solar thermal energy to drive both large and small scale power generation units is one of the prospective solutions to meet the dramatic increase in the global energy demand and tackle the environmental problems caused by fossil fuels. New energy conversion technologies need to be developed or improved in order to enhance their performance in conversion of renewable energy. The Organic Rankine Cycle (ORC) is considered as one of the most promising technologies in the field of small and medium scale combined heat and power (CHP) systems due to its ability to efficiently recover low-grade heat sources such as solar energy. This technology is especially in demand in isolated areas where connection to the grid is not a viable option.

The present research provides thermodynamic performance evaluation and economic assessment for a small-scale (10 kW) hybrid solar/biomass ORC power system to operate in the UK climate conditions. This system consists of two circuits, namely organic fluid circuit and solar heating circuit in which thermal energy is provided by an array of solar evacuated tube collectors (ETCs) with heat pipes. A biomass boiler is also integrated to compensate for solar energy intermittence. A dynamic model for the hybrid ORC power system has been developed to simulate and predict the system behaviour over a day-long period for different annual seasons.

In the thermodynamic investigation, an overall thermodynamic mathematical model of the proposed power system has been developed. The calculation model of the ORC plant consists of a number of control volumes and in each volume the mass and energy conservation equations are used to describe energy transfer processes. The set of equations were solved numerically using a toolbox called Thermolib which works in the MATLAB/Simulink® environment. The numerical results obtained on the performance of the ORC plant were validated against the theoretical and experimental data available in the

open literature. The predicted results were in very good agreement with the data published in the literature. The comparison demonstrated that the developed simulation model of the ORC plant accurately predicts its performance with a maximum deviation of less than 7%. The developed mathematical model then has been used to carry out the parametric analysis to investigate the effect of different operating conditions on the system performance.

The economic analysis has been performed with the use of equipment costing technique to estimate the system's total capital investment cost. This approach is based on the individual costing correlation of each component in the system, considering all the direct and indirect costs of the proposed components. The system cost calculations have been conducted for a range of operating parameters and different working fluids for a fixed value of net power output.

At the final stage of the research, a thermo-economic optimization procedure has been developed using Genetic Algorithm (GA) approach for selection of the rational set of design parameters and operating conditions for optimum system performance.

List of Contents

List of Figures

List of Tables

Acknowledgments

First and foremost, I thank Almighty Allah for giving me the courage, determination and guidance in conducting this research work successfully.

I would like to express my heartily thanks and gratitude to my supervisor, Professor Khamid Mahkamov, for his professional guidance, leadership, continuous support and invaluable help during this work. Also, I would like to thank Dr Basim Belgasim for his support and help.

I wish to express my deepest gratitude and appreciation to my parent for their encouragement and prayer during the period of my study. My special thanks and appreciations must go to my wife for her support, prayer and patience since the beginning of this work. Words cannot express the thanks I owe to my beloved children, Mohamed, Ruba and Tameem for accepting my excuses during my busy times. Also, my sincere thanks go to my siblings for their support and encouragement.

I would like to thank the Libyan Ministry of Higher Education and Scientific Research and the Cultural Affairs Department of the Libyan Embassy in London for providing the financial and managerial support during my PhD study.

Last but not least, many thanks should go to the colleagues, academic and technical staff at Northumbria University for their support, cheerfulness and encouragement.

Khaled Hossin

December 2016, Newcastle upon Tyne, UK

Declaration

I declare that the work contained in this thesis has not been submitted for any other award and that it is all my own work. I also confirm that this work fully acknowledges opinions, ideas and contributions from the work of others.

Name: Khaled Hossin

Signature:

Date: March 2017

Nomenclature

Symbols

A	area, m^2
a_0, a_1	coefficients depend on sky visibility and location altitude, -
Bo	boiling number, -
BWR	back work ratio, -
b	corrugation depth, m
C_{BM}	bare module equipment cost, $
C_{OM}	operating and maintenance cost, $
C_p	specific heat at constant pressure, J/kgK
C_P^0	purchased equipment cost at base conditions, $
C_{tot}	total capital cost, $
$CEPCI$	chemical Engineering plant cost index, -
CRF	capital recovery factor, -
c_0, c_1, c_2	constants for the solar collector efficiency
D_h	hydraulic diameter, m
F_{BM}	bare module factor, -
F_M	material factor, -
F_P	pressure factor, -
G	mass velocity, kg/m^2s
G_t	total solar irradiance, W/m^2
h	specific enthalpy, J/kg
h_{fg}	latent heat of vaporization, J/kg
k	coefficient depend on sky visibility and location altitude, -
k_p	plate thermal conductivity, W/mK
L_e	effective length, m
LEC	levelized energy cost, $/kWh
LHV	lower heating value, J/kg

$LMTD$	logarithmic mean temperature difference, K
M	molecular weight, g/mol
$\dot{m}$	mass flow rate, kg/s
Nu	Nusselt number, -
n	day of the year, -
P	pressure, bar
P_{co}	corrugation pitch, m
Pr	Prandtl number, -
$\dot{Q}$	heat transfer rate, W
R_b	geometric factor, -
Re	Reynolds number, -
T	temperature, K
t_{op}	annual operation time, h
t_p	plate thickness, m
U	overall heat transfer coefficient, W/m^{2}K
$\dot{V}$	volume flow rate, m^3/s
VFR	volume flow ratio, -
v	specific volume, m^3/kg
$\dot{W}$	power, W
W_e	effective width, m
x	vapour quality, -

Greek symbols

α	convective heat transfer coefficient, W/m^{2}K
β	chevron angle or solar collector inclination angle, degree
ΔT_{pp}	pinch point temperature difference, K
η	efficiency, -
θ	beam angle of incidence, degree
θ_z	zenith angle, degree
μ	viscosity, kg/ms

ρ	density, kg/m^3
τ_b	atmospheric transmittance for beam radiation, -
τ_d	atmospheric transmittance for diffused radiation, -
$\emptyset$	enlargement factor, -

Subscripts

amb	ambient
b	boiler or biomass
bf	biomass fuel
c	condenser
col	solar collector
con	condenser's zone
cs	cold side
cw	cooling water
dsh	desuperheater's zone
e	evaporator
ec	economizer's zone
ev	evaporator's zone
g	generator
hs	hot side
htf	heat transfer fluid
hx	heat exchanger
in	inlet
l	liquid
m	mean or motor
out	outlet
p	pump
s	solar
sh	superheater's zone
sp	single phase

sys	system
t	expander
tp	two phase
u	useful
v	vapour
wf	working fluid
$1-8$	cycle locations

Abbreviations

CCHP	combined cooling, heating and power
CHP	combined heat and power
ETC	evacuated tube solar collector
GHG	greenhouse gas
GWP	global warming potential (relative to CO_2)
HTF	heat transfer fluid
IHE	internal heat exchanger
ODP	ozone depletion potential (relative to R11)
ORC	organic Rankine cycle
PHE	plate heat exchanger
RO	reverse osmosis
WHR	waste heat recovery

Chapter 1 Introduction

1.1 Background

Over the last two decades, the global energy demand has increased dramatically on an unprecedented scale in all sectors due to the technological and industrial developments, the tremendous population growth and rapid urbanization. Fig. 1.1 presents an increase in the total primary energy consumption by region during the period from 1980 to 2012. A drastic increase in the total world energy consumption can be seen from 7140 Mtoe in 1980 to approximately 13216 Mtoe in 2012, raising by about 85%. In 2012, Asia and Oceania had the largest energy consumption share with about 38.6% followed by North America and Europe with 22.2% and 15.5%, respectively [1]. More than 80% of the current global energy consumption is estimated to be satisfied with conventional fossil fuels. The overall world primary energy consumption by fuel in 2014 is shown in Fig. 1.2. The figure shows that oil is still the dominant fuel providing 32.7% of the world energy consumption followed by coal and natural gas with 30% and 23.7% of supply, respectively. However, the contribution of the renewable energy resources to the total energy consumption is still as small as around 9.2%. About 6.8% comes from hydro-power resources whilst only 2.4% is delivered by all other renewables [2].

Fossil fuels have finite sources and its consumption rate is much higher than the discovery rate for new reserves. As a result, there has been a growing concern about the fossil fuels being not enough to meet the future energy needs or becoming more expensive due to the increasing demand. Furthermore, the excessive consumption of fossil fuels has also caused many environmental problems such as ozone depletion, global warming, and air pollution [3], as a result of the associated large quantities of greenhouse gas (GHG) emissions. These environmental problems together with the growing awareness about the fossil fuels depletion have been the driving force behind searches for alternative clean sources of energy to replace fossil fuels.

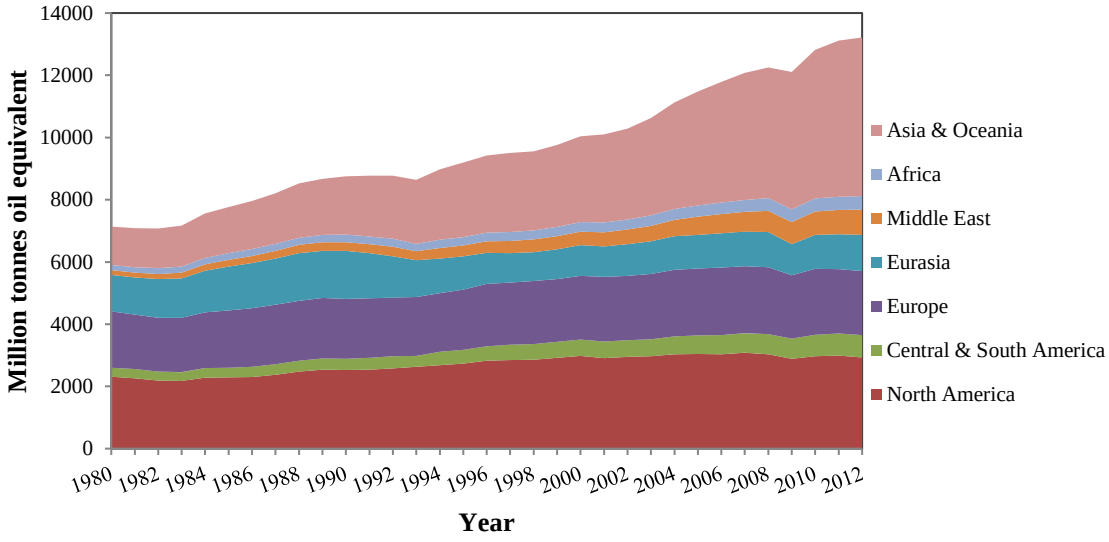

Figure 1.1 Total primary energy consumption by region [1]

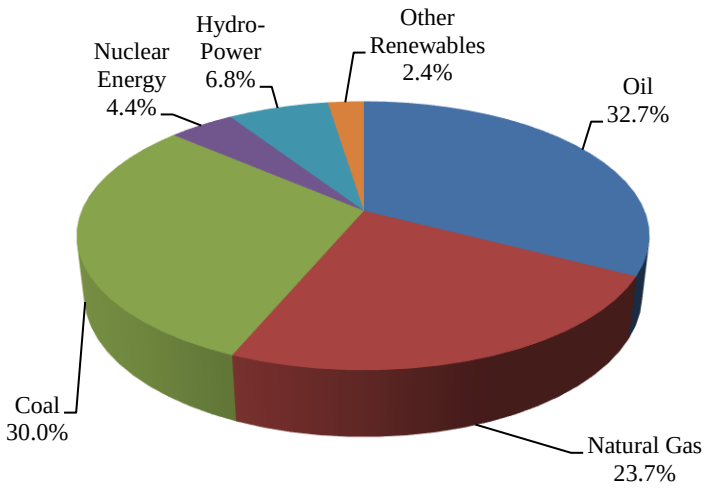

Figure 1.2 Total primary energy consumption by fuel [2]

The use of renewable energy sources such as solar, geothermal, biomass and waste heat from industrial processes to drive Combined Heat and Power (CHP) systems is one of the prospective means to alleviate the energy shortage and solve environmental pollution problems [4, 5]. In the recent years, there has been a gradual shift from the overdependence on fossil fuels toward the use of renewable and cleaner energy sources. Fig. 1.3 shows the total renewable energy consumption throughout the world in the period between 2005 and 2014. In a nine-year span, the use of renewable energy sources increased by approximately four times, from 83.2 Mtoe in 2005 to about 316.6 Mtoe in 2014 [2].

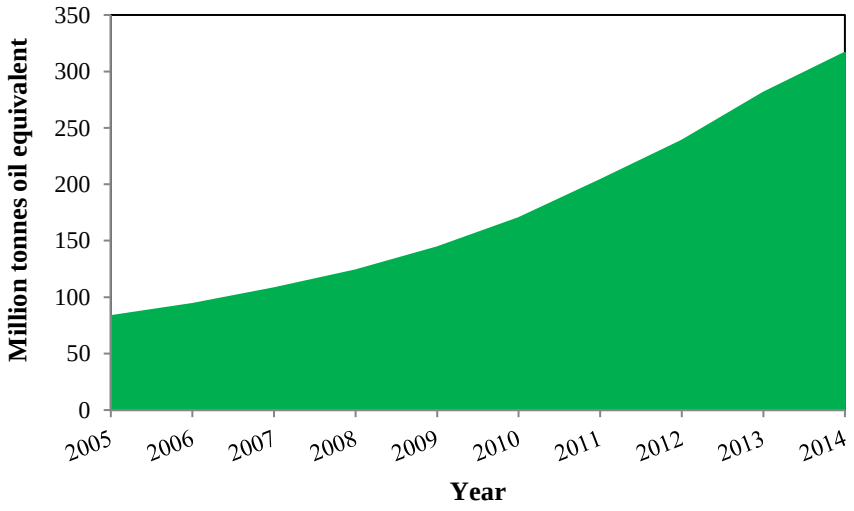

Figure 1.3 Total world renewable energy consumption [2]

Solar radiation is by far the most world's abundant, clean and permanent source of energy. The Sun's total energy is enormous which is radiated outwards in all directions. Only a tiny fraction, namely 1.7×10^{17} W, of the total radiation emitted is intercepted by the Earth's surface [6]. It was highlighted that the total amount of energy received by our planet over a one-year period is approximately ten times that available in all Earth's reserves of fossil fuels and uranium [7]. In addition, the annual amount of solar energy reaching the Earth's surface is estimated to be more than 5200 times of the global energy consumption in 2006 [8].

However, very often solar energy is characterized by low to moderate grade temperatures, especially; in locations where the solar intensity becomes relatively low such as in Europe. In recent years, solar thermal low-temperature applications have become wide-spread across Europe and throughout the world [9]. Using conventional steam Rankine cycles to convert these low-grade energy sources into electricity is a challenging task [10]. Such systems are rather more suitable for high temperature applications. The thermal efficiency of the conventional Rankine cycle is considerably low when the heat source temperature drops below 370 ^{o}C. Also, the steam Rankine cycle is not suitable for small-scale power generation systems (below 1 MW) due to its inherent low thermal efficiency and high capital costs [11]. Due to their large-scale production and high-temperature applicability, conventional steam plants operate mostly on fossil fuels and thus hinder the evolution and the integration of renewable energy resources which are mostly suitable for small-scale systems.

Therefore, developing or improving new energy conversion technologies for harnessing low-grade heat sources becomes viable. Among many well-proven technologies, the Organic Rankine Cycle (ORC) is considered as one of the most promising methods to generate electricity from such energy sources. In ORCs, organic fluids with low boiling temperatures are used as a working substance instead of water, which makes it possible to utilize low-grade heat sources more efficiently in relatively small power systems (from few kW to several MW) [12]. Various low-grade heat sources have been reported in the literature to be applicable with ORCs including solar energy, geothermal energy, biomass and waste heat from industrial processes etc. Further benefits of this technology comprise simple construction, low maintenance, favourable operating pressures, autonomous operation and high flexibility and safety [13-15]. Small-scale ORC systems in the range of 1–10 kWe tend to be the most effective means to satisfy electricity needs of residential units or small commercial buildings, especially in rural areas, as well as reducing greenhouse gas emissions, which would have been produced if fossil fuels were used [16].

However, the intermittent nature of solar radiation which leads to restriction in the generation of electricity by the solar ORC systems represents the main drawback of such

units. Therefore, a thermal energy storage system or another heat source needs to be integrated together with the solar energy source in order to overcome this shortcoming.

Biomass is considered as a significant potential energy source to compensate any shortage in the solar energy supply during cloudy weather or at night. Biomass is the world's fourth largest energy source after coal and crude oil (petroleum and natural gas), satisfying nearly 10% of the world's primary energy demand [17]. It can be used to meet a variety of energy needs including electricity generation, vehicle fuelling, cooling and heating production. Among all the renewable energy sources, biomass is unique as it is the only renewable source of carbon that can be converted into convenient solid, liquid and gaseous fuels through different conversion processes [18]. When a power system is driven by two different sources of energy, such as solar and biomass, then such a system is known as a hybrid energy system.

One of the main challenges in this subject is the lack of research, especially of a whole renewable-energy-based system to produce electricity. The overall system performance is of key importance of any thermal power system; however, the economic considerations should not be ignored. The thermal efficiency of medium-low temperature ORCs is usually low; therefore, a great challenge is the reduction of the capital cost. An economically-feasible ORC system is determined by the selection of a working fluid, the design and the operating features of the system. Different working fluids and operating parameters could lead to different equipment sizes to achieve the desired energy transfer processes, resulting in changes in the cost of the final system products. The economic analysis of such systems in the open literature is, however, still not well covered. Therefore, extensive R & D activities are required to be conducted to develop such technologies in order to improve the energy conversion efficiency as well as reduce the system costs.

The present research outcome is the development of a simulation tool for designing and techno-economic optimisation of a small-scale hybrid solar/biomass ORC power system, consisting of two circuits, namely organic fluid circuit and solar heating circuit in which thermal energy is provided by an array of solar evacuated tube collectors (ETCs) with heat pipes and a biomass boiler, integrated to compensate for solar energy

intermittence. The developed tool is also capable to select the most appropriate working fluid for the plant and dynamically model the hybrid ORC power system to predict the system's behaviour over a day-long period for different annual seasons. This data then can be used to finalise the controlling strategy of plant's operation.

For demonstrational purposes, a 10-kW hybrid ORC plant was used with a location in Newcastle upon Tyne. However, the simulation tool can be used for a wide range of net power outputs and any geographical locations.

1.2 Aims and objectives

This work was originally motivated by plans for a project at Northumbria University to erect a small ORC plant with output power of 10 kW. Unfortunately, unforeseen circumstances led the University to cancel the project; however, the research phase of this project has been continued in order to use it for designing purposes of another ORC plant in the framework of Horizon 2020 project led by Northumbria University.

The overall aim of this research is to develop a simulation tool for designing and techno-economic optimization of a small scale hybrid solar/biomass ORC power system.

The main objectives of the study can be summarised as follows:

- To carry out a comprehensive literature review related to the ORC technology, emphasizing its heat source applications, system design configurations and working fluids used in this technology.
- To develop a simulation model of a solar/biomass ORC power system which was intended to be erected at Northumbria University.
- To compare the numerical results obtained on the performance of the ORC plant to theoretical and real data available in the open literature to validate the developed model
- To select the optimum working fluid based on thermodynamic and economic criteria.

- To conduct an economic feasibility analysis to estimate the system's total capital cost based on the individual costing correlation of each component in the system.
- To carry out a parametric analysis in order to examine the impact of different design and operating parameters on the thermodynamic and economic performance of the system.
- To perform an optimization study using the Genetic Algorithm (GA) to obtain the rational set of design parameters and operating conditions for optimum system performance.
- To use the optimized parameters in the developed quasi-steady model to simulate and predict the system behaviour over a day-long period for different annual seasons for plant's operation control strategy.

1.3 Original contribution to knowledge

Analysis of existing literature indicates that, although ORCs have been investigated in detail, the small-scale ORC technology in the range of 1-10 kW, especially in solar applications, is still not well developed and it is currently at the laboratory prototypes creation phase. It has also been revealed that, in solar ORC systems, most of the studies have concentrated on steady state or fixed solar radiation simulations without considering its variation during the day/year. Finally, the integration of two renewable energy sources to drive ORC systems has not been well investigated.

This research is a contribution to the growing field of science studying the application of renewable energy in the power generation technology.

In this work an accurate comprehensive simulation model was developed in which both the thermal performance and economic feasibility of the hybrid ORC system can be evaluated over a wide range of operating conditions. A quasi-steady model of the innovative hybrid system was also developed to evaluate the system performance over a day-long period for different annual seasons. An optimization procedure was developed using the GA approach to obtain the optimal set of operating parameters based on a thermo-economic criterion.

All the above developments were realised as a single programming tool for selection of most appropriate working fluid for a hybrid ORC plant, its designing and optimisation of its design and operational parameters.

In this way, this study will assist in analysing, designing and optimization with a high degree of accuracy similar systems to achieve higher efficiencies and affordable costs with deployment of renewable energy sources.

The practical application of this developed tool is currently in application for calculations of an ORC plant in the framework of Horizon 2020 Project, led by Northumbria University.

1.4 Thesis structure

This research has been split into several different stages and, therefore, the thesis structure has been organised to reflect the logical sequence of the study to achieve research aims and objectives. The thesis has been divided into eight Chapters as follows:

- **Chapter 1 Introduction.** This Chapter presents a summary of the aims of the research work conducted and describes the structure of this thesis. The contribution to the original knowledge is also highlighted in this Chapter.
- **Chapter 2 The ORC Technology.** A comprehensive review on the current state of the art in the ORC technology, both within industry and academia, is presented in this Chapter. The review focuses on the working fluids selection, applications, design configurations and advantages and disadvantages through the recent research which have been conducted on this technology.
- **Chapter 3 Thermodynamic Modelling of the Hybrid ORC System.** In this Chapter, the physical model of the hybrid ORC system is described along with its design and operational principle. The overall thermodynamic mathematical model of the system is presented which consists of a number of sub-models describing the mass and energy transfer processes in the different system components. The simulation model for solving the governing equations using Thermolib toolbox is

also presented. Finally, the results obtained from the simulation model are validated against theoretical and real data available in the open literature.

- **Chapter 4 Thermodynamic Performance Results.** This Chapter presents the system overall thermodynamic performance as well as some other technical parameters to provide more insight into the technical feasibility and sizing of each individual system component. The procedure to select the optimal working fluid is demonstrated. A parametric analysis of the hybrid ORC system is also discussed.
- **Chapter 5 Economic Analysis of the Hybrid ORC System.** This Chapter presents the economic analysis of the system to estimate its total capital cost based on the individual costing correlation of each component in the system. A parametric study of the proposed system is also discussed in this Chapter. The simulation model using a MATLAB/Simulink environment is presented.
- **Chapter 6 Optimization of the Hybrid ORC System.** This Chapter discusses the optimization procedure of the design parameters using the Genetic Algorithm method. The results obtained from the optimization technique are presented and discussed.
- **Chapter 7 Dynamic Modelling Results.** In this Chapter, the overall performance results for the hybrid ORC system over a day-long period considering the solar intensity variations are presented and analysed for different annual seasons.
- **Chapter 8 Conclusions and Future Recommendations.** In this Chapter, the main conclusions drawn from this research project and the recommendations for future work are presented.

Chapter 2 The ORC Technology

2.1 Introduction

This Chapter presents a comprehensive review on the state of the art in the ORC technology, both within industry and academia. The review focuses on the working fluids selection, applications based on the energy source, design configurations, advantages and disadvantages and the recent theoretical and experimental research which have been conducted on this technology. Finally, the contribution of this study and the main research questions are discussed.

2.2 The organic Rankine cycle (ORC)

The conventional steam Rankine cycle is one of well-known means to convert heat into mechanical power on the large-scale basis. The steam Rankine cycle typically consists of four main components, namely evaporator (steam generator), turbine, condenser and pump, in addition to the use of water as the working fluid. The Rankine cycle using water does not have the ability to efficiently recover low temperature heat sources because the nature of thermo-physical properties of water. It is rather more suitable for high temperature applications in which water needs to be heated to around 450 ^{o}C as a good compromise between the high performance and technical limits of the technology [19]. On the other hand, the water-based Rankine cycle is not feasible for small-scale power generation systems due to its inherent heat losses and high capital cost [20].

With the growing interest in using alternative clean energy sources, the interest in using alternative working fluids has also grown. This has led to the rise of interest to so called Organic Rankine Cycle (ORC). The ORC basically consists of the same four main components of the steam Rankine cycle. In ORCs, however, organic fluids with low boiling temperatures are used as a working substance instead of water. The use of organic

fluids permits lower temperature heat sources, typically between 80 ºC and 350 ºC, to be efficiently recovered and hence converted into mechanical power, offering an attractive performance over the conventional Rankine cycle in small-scale systems (from few kW to several MW) [12]. Therefore, various potential heat sources can be considered to drive ORCs including solar energy [21], geothermal energy [22], biomass energy [23], industrial waste heat [24], internal combustion engine exhaust [25-27], gas turbine exhaust [28, 29], etc. In addition, ORCs can be used in several applications such as in combined heat and power (CHP) systems [30], combined cooling, heating and power (CCHP) systems [31] and water desalination processes [32].

2.2.1 The ORC history

The concept of using different working fluids other than water was originally introduced in 1826 by T. Howard. Later in 1898, the patent of F. Ofeldt was considered as the basis of several ORC engines by adopting naphtha instead of steam [33]. Although the idea of using other working fluids than water is rather old, organic Rankine cycles have never been become popular until the recent years. The modern developed ORC technology can be attributed to the work conducted in the 1970s and 1980s in Italy by Angelino et al. [34], which ultimately led to the successful establishment of the leading European company (TURBODEN) [35] in development and production of ORCs. Currently, TURBODEN has over 300 ORC plants in operation throughout the world in the range of 200 kW and above, producing a total output exceeds 490 MWe.

In the last decade with increasing concern over the climate change and the uncertain future supplies of fossil fuel, there has been a massive surge of interest in ORC technology, particularly at the smaller-scale. However, more development is still required to achieve successful commercialisation of such sizes which are currently at the laboratory prototype stage [36].

2.2.2 Thermodynamics of the ORC

The operation principle of the ORC is basically the same as that of the conventional steam Rankine cycle. The schematic diagram of a basic subcritical ORC is shown in Fig. 2.1, and the processes are plotted on a T-s diagram of Fig. 2.2. The liquid organic fluid is first pressurized in a pump, increasing the fluid pressure (1 to 2). The high pressure fluid then passes through an evaporator where it absorbs the heat from a heat source in a constant pressure process. During this process, the temperature of the working fluid is increased to its saturation temperature where it is fully evaporated and then, if required, superheated (2 to 3). The vapour with high temperature and pressure then flows across an expander producing mechanical work which can be converted into electricity via a generator. The expanded working fluid then passes through a condenser where heat is rejected to a heat sink in a constant pressure process. In this process, the working fluid is cooled down to a saturated vapour and then fully condensed (4 to 1). The liquid working fluid is then pumped again to repeat the cycle.

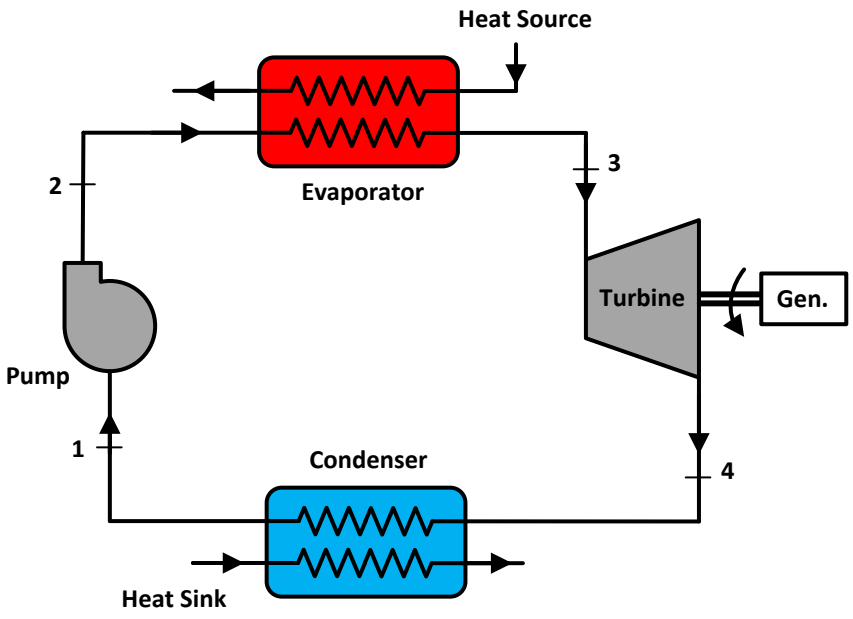

Figure 2.1 Schematic diagram of a basic ORC

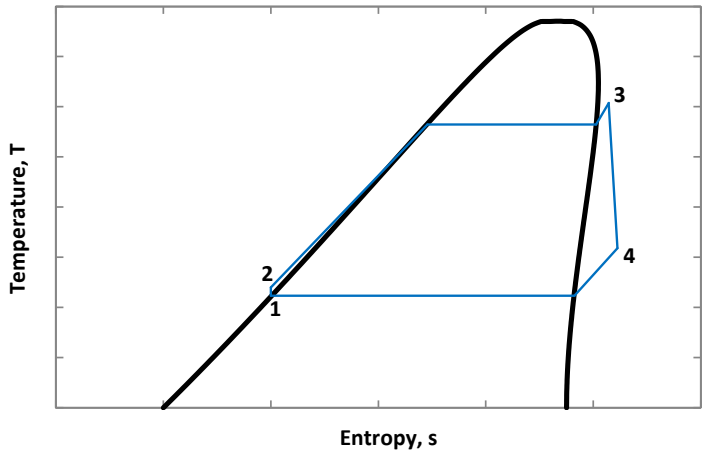

Figure 2.2 T-s diagram of the ORC

The thermodynamic performance of a Rankine cycle is mainly a function of the evaporation and condensation temperatures, the performances of the cycle components and the thermo-physical properties of the working fluid [37]. The evaporation and condensation temperatures are limited to the available heat and sink sources, respectively. An important indicator of the thermodynamic performance of an ORC system is the cycle thermal efficiency. It is a measure of how much net work is produced relative to the amount of heat input to the system (Eq. 2.1). $\dot{W}_t$, $\dot{W}_p$ and $\dot{Q}_{in}$ are the rates of the expander work, pump work and heat absorbed, respectively. To achieve a higher system efficiency, the evaporation temperature should be maximized and/or the condensation temperature should be minimized [38].

$$\eta_{th} = \frac{\dot{W}_t - \dot{W}_p}{\dot{Q}_{in}} \tag{2.1}$$

This can be explained for the ideal cycle with the aid of the Carnot efficiency concept (Eq. 2.2). The hot and cold temperatures, T_H and T_L, correspond to the average temperature at which heat is added (process 2-3) and the average temperature at which heat is rejected (process 4-1), respectively. Increasing the evaporation temperature increases T_H, whilst decreasing the condensation temperature leads to the decrease of T_L.

$$\eta_{Carnot} = 1 - \frac{T_L}{T_H} \tag{2.2}$$

A crucial role in the performance of an ORC is played by the selection of the working fluid. The working fluid not only needs to possess the desired thermo-physical properties that match the application, it also has to be environmentally safe as well as chemically stable at the system operating temperature. Also, for a given working fluid, the condensation temperature determines the condensation pressure, whilst the evaporation temperature determines the evaporation pressure which is supplied via the fluid pump. A high difference between the evaporation and condensation pressures results in the high pump power consumption, leading to a smaller net output power and lower thermal efficiency. In addition, the more efficient system components are, the higher system efficiency can be achieved. These aspects along with other cycle improvements are discussed in more details in the next sections of this Chapter.

2.3 Comparison between ORCs and steam Rankine cycles

In this section, comparisons between the ORC and conventional steam Rankine cycle are presented in terms of working medium, operating conditions, size and complexity of system components, costs and overall performance. One of the main and unique advantages of ORC power systems is the ability to exploit low-grade heat sources with temperatures as low as in the range of 80-150 ^{o}C [36]. The technology is also applicable to any external thermal energy source, with a temperature difference between the heat source and sink ranging from about 30 to 500 ^{o}C [39]. ORC systems are therefore technically suitable for the conversion of renewable energy sources such as solar, geothermal, biomass and industrial waste heat. As a consequence, the ORC technology helps in climate change mitigation caused by GHG emissions from burning of fossil fuels.

In addition to the benefits mentioned above, several advantages of ORCs over conventional Rankine cycles have been reported in a number of recent studies [40-42]. These advantages can be summarized in the following points:

- ORCs are more economical in small-scale systems (up to a few MW) compared to steam Rankine cycles which become profitable only in larger units (above 1 MW).
- The main purpose of the superheating process is to avoid wet droplets formation at the end of the expansion process that could cause turbine blades erosion. This requires of using a superheater with a relatively large heat transfer surface area due to the low heat transfer characteristics of the gaseous/vapour medium, adding extra costs to the power system. Most of the organic fluids remain in the dry region after the expansion process and hence superheating is not required.
- ORCs generally operate at much lower evaporation temperatures and pressures than steam Rankine cycles. This significantly minimizes the thermal stresses and safety precautions of the system components and therefore reduces equipment complexity and cost.
- The condensation pressure of the steam Rankine cycles is below the atmospheric pressure, typically less than 0.1 bar, which increases the possibility of air leakage into the condenser. This results in technical issues, increasing the pressure and hence decreasing the system performance. However, organic fluids with low critical temperatures enable the ORC to operate at condenser pressures higher than the ambient pressure.
- In the steam Rankine cycles, the pressure ratio across the turbine is very high and thus multi-stage turbines are commonly used. This ratio is much lower in ORCs and simple single-stage turbines can be employed.
- The use of organic fluids results in lower enthalpy drops across the turbine with higher mass flow rates and higher isentropic efficiencies. In addition, a lower enthalpy drop leads to a lower turbine rotating speed, allowing direct driving of the electric generator without the use of a gearbox.
- In contrast to steam cycles, a special water treatment is not needed in the ORCs. Also, the use of a deaerator to avoid corrosion of the system metallic equipment caused by the dissolved oxygen in the boiler feed-water is not required.
- Further advantages of the ORC technology include simple construction, low maintenance, autonomous operation and high flexibility and safety.

However, there is also a number of advantages of conventional Rankine cycles over ORCs [40, 41]. These can be listed in the following points:

- The efficiency of the steam Rankine cycles is higher, typically higher than 30%, compared with that of ORCs. The efficiency of current high temperature ORCs does not exceed 24%.
- Steam cycles require less pump power consumption relative to the turbine output power.
- Water has several advantages as a working fluid. It is abundantly available, cheap, chemically stable, non-flammable, non-toxic and environmentally friendly. Water also has low viscosity, resulting in lower friction losses and pressure drops in the heat exchangers and system piping.

To sum up, the ORCs are more preferable compared to conventional steam Rankine cycles when a low temperature heat source is used and/or small to medium-scale power systems are required.

2.4 Organic fluids

Water is the working medium used in the conventional Rankine cycle. Water is not a suitable working fluid for power generation using low-temperature heat sources due to its relatively high boiling point temperature. The organic working fluids for ORC generally refer to organic compounds with low-temperature boiling points and high molecular weights. The low boiling temperature of organic fluid enables the ORC to efficiently harness low-grade heat sources, making it a superior technology for renewable energy utilization. The advantages of using organic fluids over water become obvious for low-grade heat sources when appropriate working fluids and operating conditions are selected [3]. On the other hand, the higher molecular weight enables higher mass flow rate, compact system design and higher expander isentropic efficiency (80-85%) [43].

The range of working fluids that could be used in ORCs is broad and covers a variety of chemical groups including hydrocarbons (HCs), chlorofluorocarbons (CFCs),

hydrochlorofluorocarbons (HCFCs), hydrofluorocarbons (HFCs), perfluorocarbons (PFCs), hydofluoroethers (HFEs), hydrofluoroolefins (HFOs) and fluid mixtures [41].

Due to environmental issues, a number of potential working fluids have already been banned, with others set to be phased out in the near future by international legislations. CFCs, such as R11 and R12, contain chlorine which is the main cause of the ozone layer depletion. According to Montreal Protocol [44], CFCs have already been phased out for production or use due to their high ozone depletion potential (ODP). Besides participating in the destruction of ozone layer, the release of CFCs may also cause a global climate change due their very high global warming potential (GWP) [45]. HCFCs, such as R22 and R123, were developed as replacements of CFCs due to their similar good physiochemical characteristics [46, 47]. However, it should be noted that HCFCs also contain chlorine but with much lower ODP compared to CFCs. Under the same legalisation, Montreal Protocol, HCFCs are also requested to be phased out by 2020 for developed countries and 2030 for developing countries. On the other hand, PFCs have been used as acceptable alternatives to HCFCs due to their zero ODP and high thermal stability such as PF5050 [48]. However, because their high GWP, PFCs were included into the set of the six major GHGs and were scheduled to be voluntarily reduced within the 2008-2012 timeframe according to Kyoto Protocol [49]. The values of ODP and GWP for common working fluids are shown in Fig. 2.3

As described above, it is the urgent task to develop new alternatives having similar working properties to CFCs, HCFCs and PFCs. Since the early of 1990s, HFCs have been used as friendly replacements in many applications such as R134a and R245fa. These working fluids contain no chlorine and thus have zero ODP. However, some HFCs have relatively significant GWP [50].

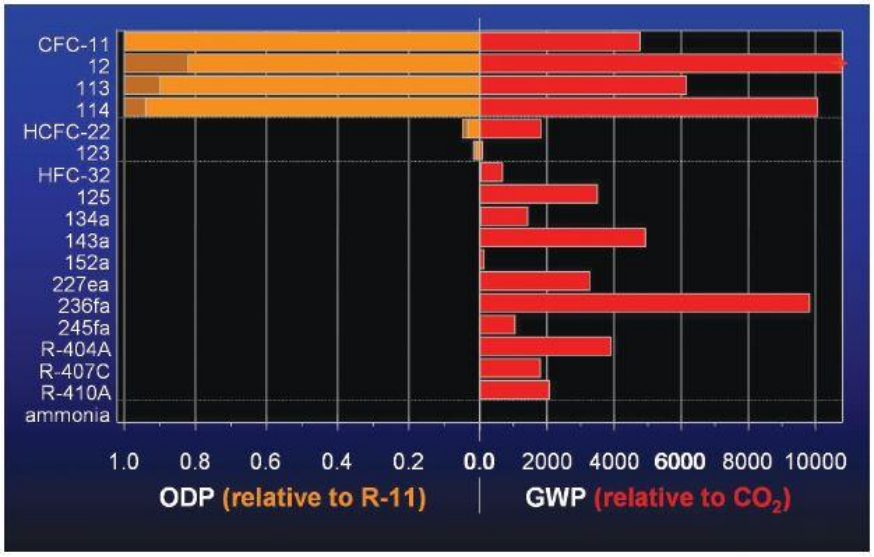

Figure 2.3 ODP and GWP for key working fluids [51]

HFEs are currently considered as replacements to CFCs, HCFCs and PFCs because of their zero ODP and relatively low GWP such as HFE7000 and HFE7100 [52]. HCs, such as butane and pentane, are environmentally friendly working fluids with zero ODP and very low GWP. However, the high flammability is the main negative characteristic that could limit their use [53]. Also, HFOs have zero ODP and very low GWP values, making them as good potential candidates. Examples of such fluids are R1234yf and R1234ze. Fig. 2.4 depicts a general replacement guide for phased out working fluid published by DuPont®.

The result of the above policies is a shift of interest towards the use of zero ODP and low GWP fluids. However, the use of the working fluid still depends on the desired application such as cooling, heating, power generation, etc.

Despite the wide variety of the possible working fluids for ORCs, only few fluids are currently used in practice for commercial ORC power plants. These working fluids together with their main properties are listed in Table 2.1, as given by Colonna et al. [33]. Some of these fluids are adopted in higher temperature applications such as toluene and MDM, while others are suitable for low-temperature applications such as R134a and R245fa.

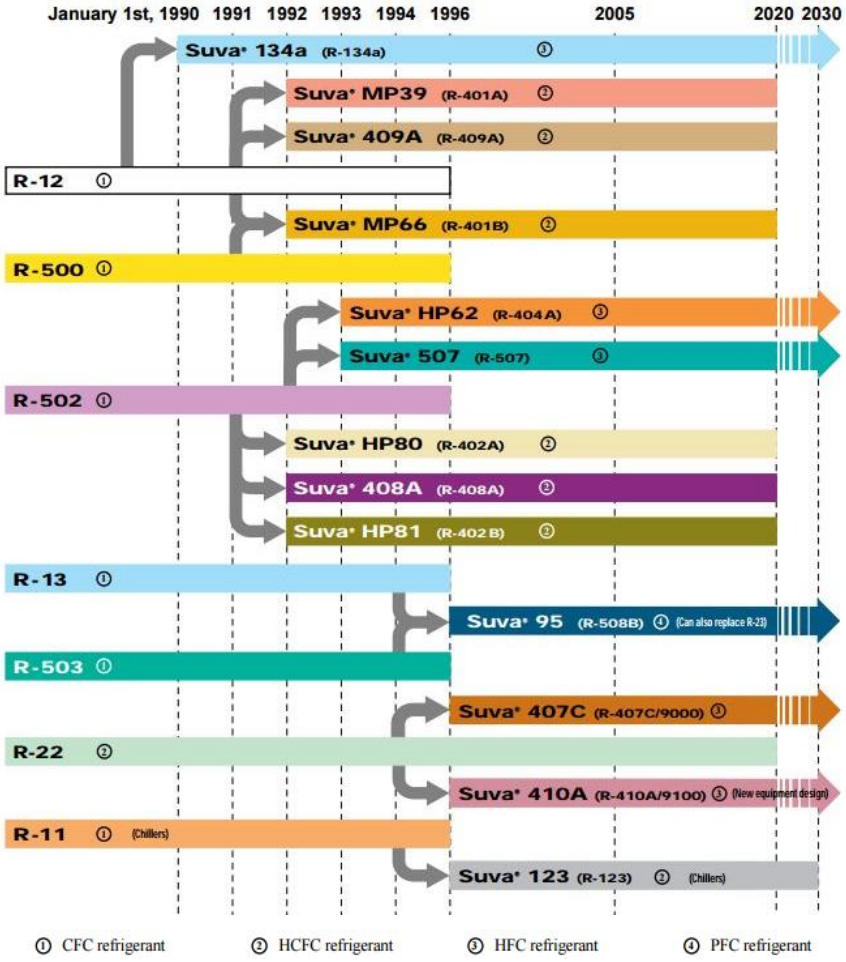

Figure 2.4 Phase out chart and general replacement guide of some common working fluids: Suva® Refrigerants [54]

Table 2.1 The most common working fluids currently in use in ORC power plants

Fluid	Chemical formula	M [g/mol]	T_c [°C]	P_c [bar]
Toluene	C_7H_8	92.1	318.6	41.26
Cyclo-pentane	C_5H_{10}	70.1	238.5	45.15
Iso-pentane	C_5H_{12}	72.1	187.2	33.78
Iso-butane	C_4H_{10}	58.1	134.7	36.29
MDM	$C_8H_{24}Si_3O_2$	236.5	290.9	14.15
MM	$C_6H_{18}OSi_2$	162.4	245.5	19.39
PP1	C_6F_{14}	338.0	182.1	19.23
R245fa	$C_3H_3F_5$	134.0	154.0	36.51
R134a	$C_2H_2F_4$	102.0	101.1	40.59
Solkatherm (SES36)	Mixture	184.9	176.1	28.49

M: molecular weight, T_c: critical temperature, P_c: critical pressure

2.4.1 Working fluids categories

According to the slope of saturated vapour line (*dT/ds*) in the T-s diagram, organic working fluids can be classified into three categories as dry, wet and isentropic [55]. Isentropic fluids have an infinitely large (nearly vertical) slope such as R11 and R12, as shown in Fig. 2.5. The value of the slope is positive (*dT/ds>0*) for dry fluids such as pentane and R123, while it is negative (*dT/ds<0*) for wet fluids such as R22. This feature affects the fluid applicability, cycle efficiency, and arrangement of associated equipment in a power generation system [11]. Wet fluids may form liquid droplets during the expansion process in the turbine, leading to erosion of turbine blades and reduction in its isentropic efficiency [56]. Therefore, wet fluids need to be superheated before entering the turbine using additional heat exchangers with relatively large surface areas to avoid these negative effects [57].

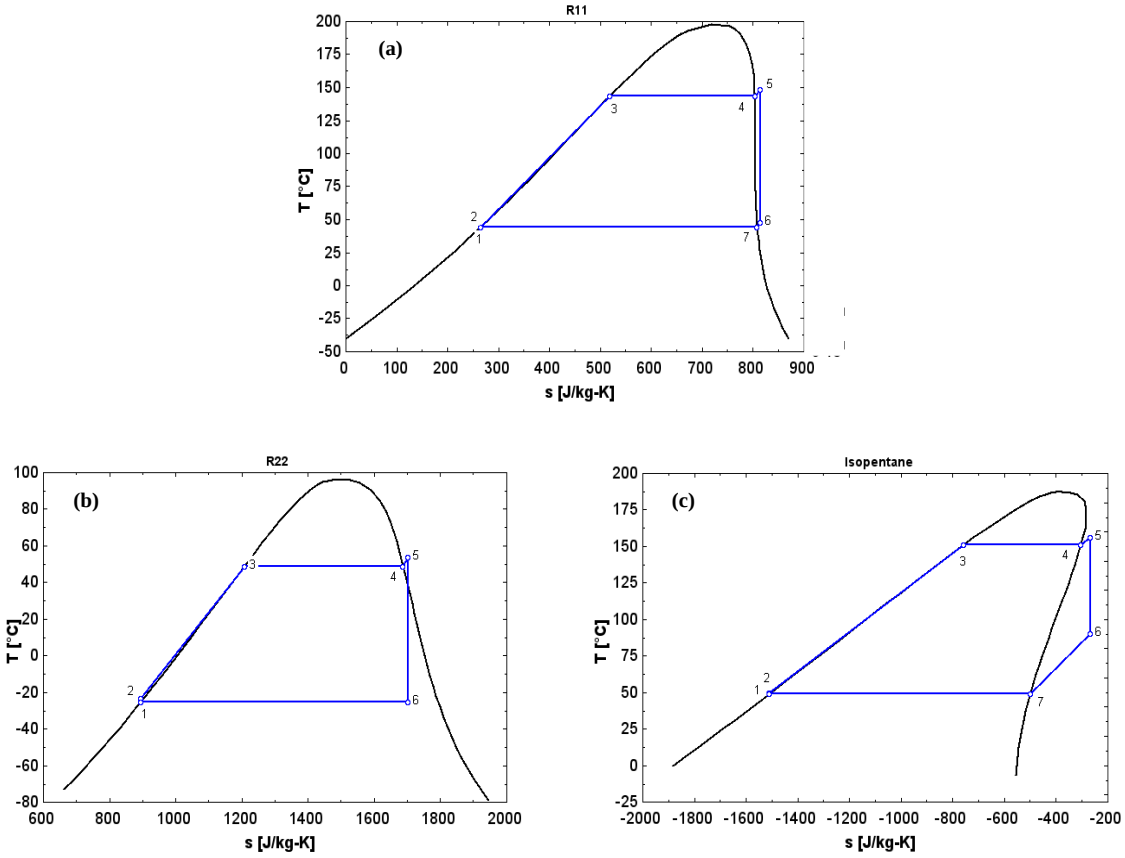

Figure 2.5 Types of working fluids: (a) isentropic, (b) wet and (c) dry [58]

In contrast, dry and isentropic fluids are more appropriate for ORCs. For these types of fluids, the expansion process ends in the superheated vapour (dry) region. The characteristics of dry and isentropic fluids, therefore, eliminate the possibility of the turbine damage as well as the use of superheating apparatus [59, 60]. Additionally, an internal heat exchanger (recuperator) can be utilized to extract the heat still contained within the superheated fluid at the turbine outlet and use it to preheat the liquid leaving the pump before it passes through the evaporator. In this way, the heat input to the system is reduced, increasing the cycle thermal efficiency and simultaneously reducing the condenser load [61]. The larger the temperature difference between the turbine outlet and pump exit, the greater the benefit from the recuperator is achieved. On the other hand, an additional cost is also accompanied with installing a recuperator [60].

2.4.2 Working fluids selection criteria

The working fluid selection plays a crucial role in determination of the entire ORC performance. It has a significant impact on the cycle efficiency, operating conditions, environment, economics and design of the key components of ORC systems [4]. This justifies the abundant number of research papers on the fluid selection in the literature. In general, a suitable working fluid for an ORC system should have some desirable chemical, thermo-physical, economic, environmental and safety characteristics. These include the following [40, 41, 62]:

- Thermodynamic performance: The working fluid should show good heat conversion performance, leading to higher power output and thermal efficiency.
- Saturated vapour line slope: Dry or isentropic fluids (Positive or vertical slope) are more appropriate to avoid the possibility of the turbine damage and the use of superheating apparatus.
- Molecular weight: A high molecular weight leads to a high fluid mass flow rate and a low enthalpy drop during the expansion. This results in a higher turbine isentropic efficiency with a lower rotational speed and smaller number of stages.

- Density: A high fluid density results in low volume flow rates, permitting compact and low cost system components to be used.
- Thermal conductivity: A high thermal conductivity ensures high heat transfer coefficients. This increases the heat transfer rates and reduces the size and cost of the heat exchangers.
- Viscosity: Low viscosity in liquid and vapour phases reduces friction losses. This decreases the pressure drop in the heat exchangers and along the pipes.
- Operating pressures: The fluid should have acceptable operating pressures. High evaporating pressures usually increase the system equipment cost and complexity. Also, the condensation pressure should be above the atmospheric pressure to avoid air leakage into the condenser.
- Stability: Unlike water, organic fluids might deteriorate and decompose at high temperatures. The fluid should be chemically stable within the operating temperature range considered.
- Material compatibility: The working fluid should be non-corrosive and compatible with the construction material of the system components.
- Safety: The fluid should be non-toxic and non-flammable.
- Environmental impact: The ODP, GWP and ALT (Atmospheric Lifetime) are among the environmental impact indicators of the working fluids. The values of these parameters should be as low as possible, considering only fluids not being banned by any international legislation.
- Availability and cost: the fluid should have low cost and be easily available.

There is a wide range of potential organic fluids that could be used in ORC applications. However, in order to achieve higher thermal efficiencies as well as optimal utilization of the available heat source, a careful selection of the working fluid is required. In addition, appropriate criteria other than thermal efficiency should also be considered in the working fluid selection. Although several studies have investigated the selection of the most appropriate working fluid, no single fluid has been identified as ultimately optimal for all ORCs [63]. This is due to the nature and characteristics of the various heat sources considered [10]. On another hand, the problem can also be attributed to the different cycle

operating conditions assumed, as well as to the different criteria used for evaluating the system performance [64, 65].

Various criteria have been proposed for the selection of working fluids for ORCs in the literature. Chen et al. [66] discussed the selection criteria for ORCs supporting his study by screening thirty-five working fluids. It was pointed out that the physical properties, stability, environmental impacts, safety, compatibility, availability and cost are among the important considerations. Qiu [67] developed a non-computational methodology for the selection of organic fluids. Eight mostly-applied working fluids were compared and optimized by means of spinal point method based on thermodynamic, economic and environmental criteria. Stijepovic et al. [68] investigated analytically the relationships between the fluid physical properties and ORC thermodynamic and economic performance.

Several studies have been conducted on the working fluid selection in the literature. However, in this review, a special attention will be paid to those fluids which are particularly suitable for low-temperature heat sources. In this regard, it is helpful to make distinction between low temperature (< 150 ^{o}C) and medium-to-high temperature applications (> 150 ^{o}C)

The thermodynamic performance of ORCs was frequently used in numerous studies as an evaluation criterion for selection of the best working fluid among various candidates. Thermal efficiency, exergy efficiency, net power output, mass flow rate and expander outlet vapour quality are among the performance evaluating parameters used in the literature. Some of the available studies dealt with the thermodynamic cycle alone without directly linking the fluid selection to the heat source temperature. Wang et al. [69] investigated the effect of molecular structures and entropies on the ORC thermal efficiencies. The ORC considered was a subcritical pressure cycle with an evaporation temperature of 90 ^{o}C and a condensation temperature of 35 ^{o}C. The authors noted that the working fluids with low molecular entropies could generate high thermal efficiencies. Rayegan and Tao [64] developed a procedure to identify the most suitable fluids for a solar ORC based on their molecular components and the temperature-entropy diagram.

Thermal and exergy efficiencies, net power generated and vapour expansion ratio were also considered to evaluate 117 working fluids on the basis of two evaporation temperature levels of 85 ºC and 130 ºC. It was found that higher critical temperatures of organic fluids allowed higher evaporation temperature to reach higher thermal efficiencies. Mikielewicz [70] proposed a thermodynamic criterion for fluid selection for subcritical pressure ORC and for supercritical pressure ORCs. Theoretical performances of few fluids have been comparatively assessed for use in low-temperature domestic organic Rankine cycle micro systems. Of the 20 fluids investigated, ethanol, R123 and R141b appeared as the most suitable for small scale domestic CHP applications. Kuo et al. [71] examined the performance of a 50 kW ORC system using 18 different working fluids. A dimensionless group, which called Figure of Merit (FOM), combining Jacob number, evaporation temperature and condensation temperature was proposed for quantitative screening the working fluids as far as the thermal efficiency was concerned. The results indicated that the thermal efficiency increases with the decrease of the FOM. It was also highlighted that the proposed FOM is not only applicable to the investigated eighteen working fluids but also consistent with some existing studies. Deethayat et al. [72] modified the technique proposed by Kuo et al. [71] to develop an empirical correlation between the cycle efficiency of a small-scale ORC and FOM for zeotropic working fluids. For evaporating temperatures of 80-130 ºC and condensing temperatures of 25-40 ºC, the model results were in good agreement with both the experimental and theoretical data from the literature. Saleh et al. [73] screened 31 pure working fluids to be used in a low-temperature ORC. Both the subcritical and supercritical pressure cycles were investigated for an ORC operating between 100 °C and 30 °C. The potential of using an internal heat exchanger was also discussed. The results showed that with the increase of critical pressure of the working fluid, the thermal efficiency increases varying between 0.36% and 13% depending on the working fluid. Also, superheating the working fluid was not always efficient.

It is, however, established that the working fluid selection strongly depends on the temperature level of the available heat source to be used [10]. Accordingly, a number of studies linked the fluid selection to the heat source when considering the thermodynamic cycle. A temperature difference between the heat source and the working fluid at the start of the evaporation process, pinch point, is usually specified. A study on the selection of

working fluids was presented by Badr et al. [63] for an ORC operating between temperature limits of 120 ^{o}C and 40 ^{o}C. The authors discussed the properties that a working fluid should ideally exhibit. It was found that there is no unique working fluid in which all the desired criteria are satisfied. However, it was also indicated that R113 is the most suitable candidate for the application considered. Mago et al. [74] performed the first and second law analyses for the use of an ORC to generate power from a low-grade waste energy heat source ranging from 375 K to 450 K. A pinch point was introduced to determine the evaporation temperature of the working fluid. The effect of the fluid boiling point temperature on the performance of ORC was investigated. It was concluded that the ORC achieves higher thermal efficiency with fluids having higher boiling points. Somayaji et al. [75] presented a performance analysis of the ORC using R113 and R134a in which power is generated using a low-temperature waste heat source. The results for the two working fluids were compared with those of water and ammonia under similar operating conditions. The results showed that the organic fluids provide better performance than water in low temperature applications, with ORC efficiency being typically below 20% depending on the temperature and the matched working fluid. It was also highlighted that organic fluids must be operated at saturated conditions to reduce the total irreversibility of the system.

Aljundi [61] analyzed the effect of using dry hydrocarbon fluids on the performance of a 10 kW ORC driven by a low-temperature (<150 ^{o}C) geothermal or waste heat source. The working fluid temperature at the evaporator outlet was assumed 5 K less than that of the heat source. It was found that the thermal efficiency increases with the critical temperature of the organic fluids monotonously. It was also concluded that, thermodynamically, hydrocarbons such as iso-pentane, n-butane and n-hexane are superior to some refrigerants and could be the next generation working fluids for geothermal or waste heat recovery systems. Papadopoulos et al. [76] applied computer aided molecular design (CAMD) and optimization approaches to select the optimal fluids for ORCs. The heat source used was saturation steam with a temperature of 90 ^{o}C while the maximum temperature of the organic fluid was set as 80 ^{o}C. The optimum designs were searched to identify organic fluids that exhibit optimum ORC performance based on economic, operating, safety and environmental indicators. Wang et al. [77] performed a comparative

analysis of different working fluids to generate a fixed 10 kW power output from exhaust gas of a vehicle engine with 600 K. They reached a conclusion that R11, R141b, R113 and R123 have slightly higher cycle efficiency than other refrigerants; however, R245fa and R245ca are the most suitable working fluids if to take safety and environmental impacts into consideration. Tchanche et al. [78] theoretically assessed the thermodynamic performance and environmental properties of 20 different fluids for low-temperature solar ORC systems (below 90 ^{o}C). Efficiencies, volume and mass flow rates, pressure ratio, flammability, toxicity, ODP and GWP were used in the comparison. The findings showed that R134a is the most appropriate fluid for small-scale applications. Moreover, R152a, R600a, R600 and R290 also showed good performances but some measures for satisfying the safety regulations are required. Xu and Yu [79] proposed a method based on the critical temperature criterion for selection of the working fluids using a heat source with temperatures between 100 and 300 ^{o}C. The results from screening of 57 different fluids demonstrated that some fluids, such as R245fa, can be successfully used over a wide range of the heat source temperatures.

In the recent years, a number of studies have considered the working fluid selection based on the ORC economic feasibility and environmental impact. A thermo-economic-based model of an ORC was developed by Quoilin et al. [80] in order to compare both the thermodynamic and economic performance of several working fluids for low to medium temperature waste heat recovery applications. The thermal efficiency and specific investment cost were both used as evaluation parameters of the ORC system. The results indicated that, for the same fluid, different evaluation criteria led to different optimal operating conditions. The economical optimum was obtained for n-butane with a specific cost of 2136 €/kW and an overall efficiency of 4.47%, producing a net output power of 4.2 kW. Guo et al. [81] investigated a low temperature (90 ^{o}C) geothermally-powered ORC integrated with a heat pump using 27 working fluids. The selection criteria of working fluids included the net power output per unit mass flow rate of the geothermal water (P_{net}), the ratio of total heat transfer area to net power output (A/W_{net}) and the electricity production cost (epc). Results showed that there exist optimum evaporating temperatures varying with different screening criteria and fluids. E170, R600 and R141b showed the lowest A/W_{net} and epc values; however, R236ea provided higher P_{net} values.

A thermo-economic study to select the optimal working fluid for waste heat recovery ORC was conducted by Heberle et al. [82]. The study was performed for a saturated ORC using a heat source temperature of 150 ^{o}C for all the working fluids investigated. In general, a cost-effective ORC system was obtained at lower values of pinch point temperature difference in the evaporator and higher values in the condenser. The results indicated that the use of iso-butane as a working fluid led to the minimum cost per unit exergy with 52 €/GJ. Shengjun et al. [83] carried out thermo-economic performance comparisons and parametric optimization of different fluids for low-temperature (80^{o}C - 100^{o}C) geothermal power generation. The results indicated that the choice of working fluid changes with the performance indicator being optimized. Working fluids with higher values of thermal efficiency and exergy efficiency were R123, R245ca, R245fa and R600. Based on the total heat exchanger area per unit power output and levelized energy cost, it was found that R152a, R134a, R600 and R600a provided the lowest values.

Imran et al. [16] performed an economic assessment of greenhouse gas (GHG) reduction for a waste heat recovery ORC. The GHG emissions for equivalent power and hot water from three types of fossil fuel, namely coal, natural gas and diesel oil were estimated. The total cost of the ORC system was used to analyse the GHG reduction cost for each of the considered fossil fuels. The GHG reduction potential of ORC with R245fa was found to be higher than that with pentane. Throughout the 20-year life cycle of the ORC plant, the GHG reduction cost for R245fa was 0.02 $/kg to 0.04 $/kg and that for pentane was 0.04 $/kg to 0.05 $/kg. It was also concluded that the working fluid, evaporation pressure, and pinch point temperature difference considerably affect the GHG emission. Liu et al. [84] applied the life cycle assessment (LCA) to evaluate the environment impact (EI) for waste heat driven ORCs with a heat source temperature of 150 ^{o}C. Several EI indicators were considered using 7 working fluids including R114, R245fa, R123, R601a, Pentane, R141b and R113. The candidate working fluids showed different effects on the environmental parameters investigated. It was found that the GWP is the most serious EI parameter followed by the human toxicity potential (HTP). Wang et al. [85] assessed different working fluids based on economic and environmental criteria. The heat source of the ORC was waste heat from a cement production line with a temperature of 220 ^{o}C. The net present value (NPV) and payback period (PBP) were used to evaluate

the economic performance while the life cycle assessment (LCA) was used to evaluate the environmental impacts. The ORC with R601 (n-pentane) showed the best economic performance and most significant gas emission reductions. The economic performance of ORCs applied in the cement industry could be further improved when the application scale is increased. Walsh and Thornley [86] evaluated the environment impact and economic feasibility of introducing ORC to recover low-grade waste heat from a metallurgical coke production process. It was found that integrating an ORC with the coke generation process could reduce CO_2 emissions by 1-3% based on output power of 2.31 MW, which was equivalent to a decrease of over 10,000 tons of CO_2 emissions annually. The economic analysis indicated that the payback period was only between 3 to 6 years.

The growing awareness of the climate change as a more significant and more challenging environmental issue has recently resulted in a surge of interest in using working fluids with better environmental characteristic (i.e. ODP and GWP). HFOs are among the fluids that have zero ODP and very low GWP values such as R1234yf and R1234ze(E). Le et al. [87] presented performance optimizations of ORCs powered by a 150 ^{o}C pressurized hot water utilizing different low-GWP working fluids. By using the ranking method and considering a low-GWP criterion, the best working fluids for the system efficiency optimization of basic and regenerative cycles were R32 and R152a, respectively. However, the best working fluid for the net electrical power optimization of the basic cycle was R1234ze(E). Liu et al. [88] evaluated the thermodynamic performance and potential application of eight different HFOs in low-temperature (120 ^{o}C - 150 ^{o}C) geothermal power generation. The results demonstrated that such fluids can achieve a superior system performance to that obtained with R245fa or R134a. McLinden et al. [89] also discussed the potential of using HFOs, and highlighted that R1234yf and R1234ze(E) were promising candidates with better cycle efficiency and safety requirements among others. However, the authors also reported that HFOs were generally more difficult to produce than most HFCs, and would inevitably be more expensive to purchase. Molés et al in [90] and [91] evaluated the performance of HCFO-1233zd(E) and HFO-1336mzz(Z) as alternatives to R245fa in low-temperature ORC systems. The results showed slightly higher net cycle efficiency values are obtained using the proposed fluids as a result of the

lower consumed pump power. However, larger turbine sizes were required when using these fluids.

Fluid mixtures are also considered as real potential working fluids within ORCs for the conversion of low-grade heat into electrical power. The use of fluid mixtures extends the spectrum of candidate working fluids that could be utilized in ORC systems. As a consequence, mixtures could offer environmentally superior alternatives and potential cycle performance improvements. Azeotropic mixtures, which are already being used in the actual installations (e.g. Solkatherm) [92], have an isothermal phase change at constant pressure. On the other hand, zeotropic mixtures are characterized by a temperature glide during the phase change process, Fig. 2.6. This characteristic enables a better fluid match with the thermal profiles of the heat and sink sources in the heat exchangers which results in reducing the irreversibilities associated with the heat transfer processes and improving the cycle performance [37]. In addition, the composition of the mixtures has a significant impact on the ORC performance [93]. Therefore, it is essential for the ORC system design to select a proper mixture composition. Only a few studies have been published on the use of mixtures as ORC working fluids.

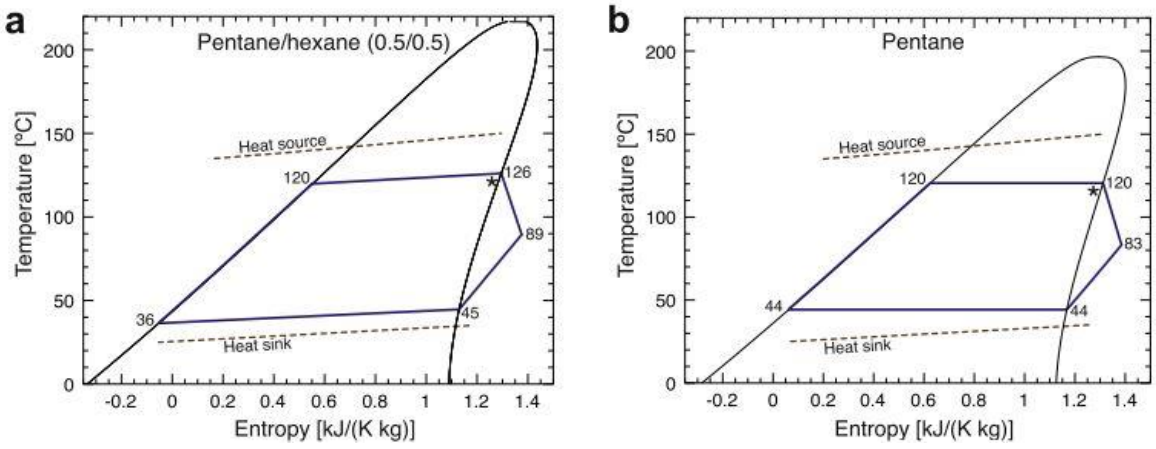

Figure 2.6 T-s diagrams of the ORC processes (a) mixture of pentane/hexane (0.5/0.5) and (b) pure pentane [37]

A number of these studies reported some improvements in the ORC performance using the fluid mixtures. Heberle et al. [94] investigated the performance of isobutane/isopentane and R227ea/R245fa in an ORC system for low-enthalpy geothermal applications. The results showed that the use of zeotropic mixtures could produce higher second law efficiency than pure fluids due to a better thermal match in the evaporator and condenser. Chen et al. [95] introduced a zeotropic mixture of R134a/R32 (0.7/0.3) as a working fluid for a supercritical ORC. The comparative results showed that the supercritical mixture-based ORC gives higher thermal and exergy efficiencies than the subcritical R134a-based ORC over a high cycle temperature range of 120 ^{o}C -200 ^{o}C. A comparative experimental study on the pure fluid (R245fa) and the zeotropic mixtures (R245fa/R152a) in solar ORC was also conducted by Wang et al. [96]. Under a constant fluid volume flow rate, both the thermal efficiency and collector efficiency of zeotropic mixtures were higher than those of the pure fluid.

In contrast, some other studies on the fluid mixtures suggest that the choice of pure working fluids leads to a better system performance. Li et al. [97] compared the performance of the ORC using pure fluid R141b and that with a zeotropic mixture of R141b/RC318 as the working fluid. It was found that the mixture-fluid ORC has lower thermal and exergy efficiencies than the pure-fluid ORC. Wang and Zhao [98] presented an analysis of a solar ORC operating between 85 ^{o}C and 25 ^{o}C and employing three typical mass fractions of R245fa/R152a. The results revealed that zeotropic mixtures provide lower cycle efficiency than pure working fluids in the proposed temperature condition.

In the meantime, the ORC using mixtures as the working fluid generally produces a poor economic performance. Wu et al. [99] conducted thermal and economic analyses of an ORC driven by a 120 ^{o}C air heat source using R227ea/R245fa, Butane/R245fa and RC318/R245fa as working fluids. The results indicated that better thermal performance can be achieved using the zeotropic mixtures. However, the pure-based ORC showed better economic performance than the mixture-based ORC. Heberle et al. [100] presented a thermo-economic analysis of a geothermal ORC system using zeotropic mixtures. It was reported that mixtures lead to higher specific investment costs than pure working fluids due to the additional costs of the increased heat exchangers area. For a heat source of 160 ^{o}C, a decrease in the electricity generation cost was however observed using zeotropic

mixtures as a result of the increased power output and annual amount of electricity generated. The use of zeotropic mixtures and pure fluids in waste heat recovery ORCs was further investigated by Heberle et al. [82]. The results showed that pure working fluids lead to more cost-effective systems than mixtures. The same finding was also demonstrated in [101] as a result of the lower heat transfer coefficients of the mixtures as well as the associated increased design complexity of the heat exchangers.

In spite of many research studies and activities regarding the working fluid selection, there is still absolutely no single fluid has been identified as the most recommended candidate for all ORC applications. This is mainly due to the interdependence between the cycle design, operating conditions, heat source level and selection of the optimal fluid. In addition, the use of different evaluation criteria leads to a different selection of the working fluids. Therefore, the working fluid should be carefully selected in each individual case in order to achieve the best cycle performance, minimum cost and ensure efficient utilization of the available heat source.

2.5 ORC applications based on the energy source

The ORC is characterised by its ability to efficiently convert lower temperature heat into useful work more economically, compared to the conventional steam Rankine cycle. Also, the broad variety of possible working fluids makes the ORC suitable for a wide range of heat sources. The ORC technology is therefore technically suitable for heat to power conversion of renewable energy sources such as solar, geothermal, biomass and industrial waste heat. In addition, ORCs can use the residual thermal energy from other power technologies such as gas turbines and internal combustion engines (ICEs) by acting as a bottoming cycle.

Fig. 2.7 shows how the ORC systems can be coupled with these sources, depending on their heat source potential. The energy source for the gas turbines and ICEs as well as industrial processes often comes from fossil fuels and their waste heat can then be recovered using ORCs. Heat from geothermal and solar sources is usually exploited by ORC systems through heat transfer processes. For biomass, heat energy can be used

directly through combustion or indirectly as waste heat from different power cycles that use other biomass products.

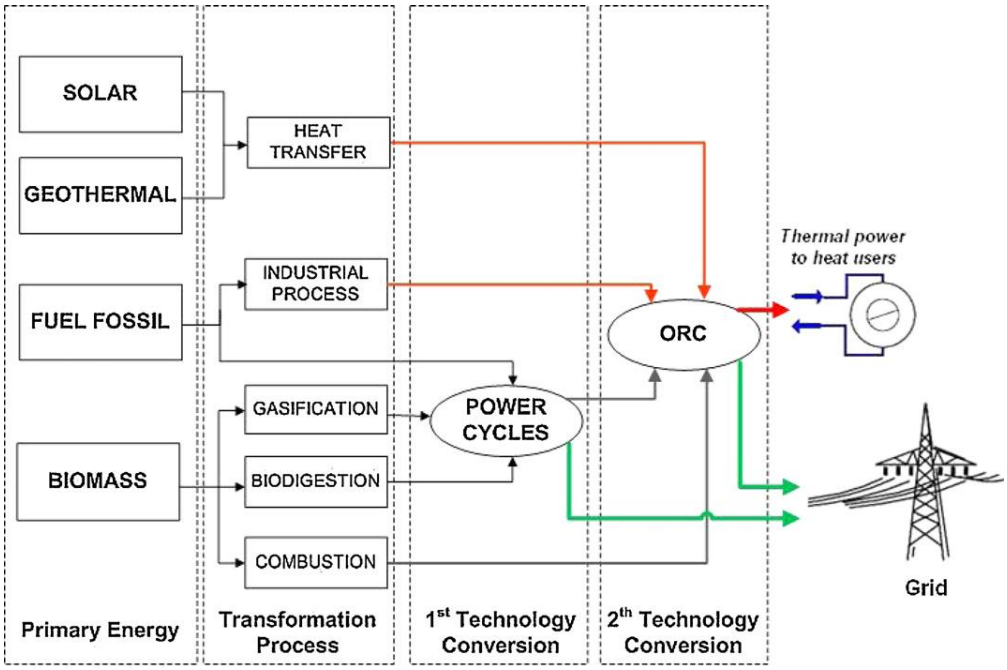

Figure 2.7 An ORC integrated with various heat sources [102]

2.5.1 Solar energy

Solar energy is considered to be the world's largest technically feasible, non-polluting and non-depleting source of energy. Other renewable sources such as wind, ocean thermal, hydropower and biomass are originally derived forms of solar energy [103]. The Potential energy from Sun is enormous compared to actual energy demand and other renewable energy sources. The fraction of the solar radiation reaching the Earth's surface is 1.7×10^{17} W. With this rate, it is estimated that 30 min of solar radiation falling on Earth is equal to the global energy demand for one whole year [104]. However, the intensity of the solar radiation that reaches the Earth's surface varies depending on the atmospheric conditions, location and time.

Solar energy can be harnessed using two primary technologies, e.g., photovoltaic (PV) and solar thermal systems. In PV systems, the sunlight is directly converted into electricity using PV panels. However, in the solar thermal technology, the heat from Sun is

captured at different temperature levels using different types of solar thermal collectors. This heat can be used to produce mechanical work, through a thermodynamic cycle, which can be then converted into electricity via an electric generator. The advantage of solar thermal systems over PV ones is the capability to benefit from the hot water production in cogeneration applications, increasing the overall system efficiency. In addition to the power generation, there are several potential fields of application for solar thermal energy including space heating, domestic hot water, refrigeration and air conditioning, seawater desalination, solar drying or any other industrial process [105]. It should be mentioned that the efficiency of the solar collector significantly influences the overall thermal system performance [106].

There are basically two types of solar collectors: non-concentrating and concentrating collectors. The non-concentrating collectors have the same area for intercepting and for absorbing solar radiation, whereas concentrating collectors usually have concave reflecting surfaces to intercept and focus the sun's beam radiation to a smaller receiving area, thereby increasing the radiation flux. Collectors can also be classified according to their motion into stationary and sun-tracking collectors. The stationary collectors are permanently fixed in position and do not track the sun's movement. The sun-tracking collectors require either a single axis or a two-axes tracking system [104]. Various solar thermal collectors are available, ranging from flat plate collectors operating at few dozen degrees to heliostat field collectors operating at above 1000 °C. Table 2.2 presents a comprehensive list of solar thermal collector technologies with their typical operating temperature and concentration ratio ranges [41, 104, 107].

Table 2.2 Types of solar thermal collectors [41, 104, 107]

Motion	Collector type	Concentration ratio	Temperature range [ºC]
Stationary	Flat plate collector (FPC)	1	30-80 (Advanced FPC: 60-120)
	Evacuated tube collector (ETC)	1	50-200
	Compound parabolic collector (CPC)	1-5	60-240
Single-axis tracking	Linear Fresnel reflector (LFR)	10-40	100-400
	Parabolic trough collector (PTC)	10-50	150-400
Two-axes tracking	Parabolic dish collector (PDC)	200-500	250-700
	Heliostat field collector (HFC)	500 to >3000	500 to >1000

The solar thermal system for a particular application depends on the type of the solar collector along with its operating temperature. Concentrating Solar Power (CSP) systems are implemented with several concentrated solar collectors such as PTCs, PDCs, HFCs or LFRs. However, most of the currently installed CSP plants use a conventional steam Rankine cycle as the power engine. This technology requires a minimum power of several MWe in order to be competitive and involves high collector temperatures [12]. For small-scale power systems, the most appropriate power cycles for CSP technology is Stirling engine integrated with dish type collectors [40, 102]. Low and medium temperature solar collectors, 80 – 300 °C, coupled with ORC modules could efficiently operate in cogeneration applications producing clean electricity and hot water. Also, such systems have the potential to operate well in regions with low solar radiation intensities [41, 103]. ORCs are a promising technology to reduce the investment cost at small scale, in which the total installed power can be scaled down to the kW levels. The working principle of solar ORC systems is schematically presented in Fig. 2.8. Lower temperature solar collectors, less than 80 °C, are usually used to produce hot water for domestic use and space heating [103].

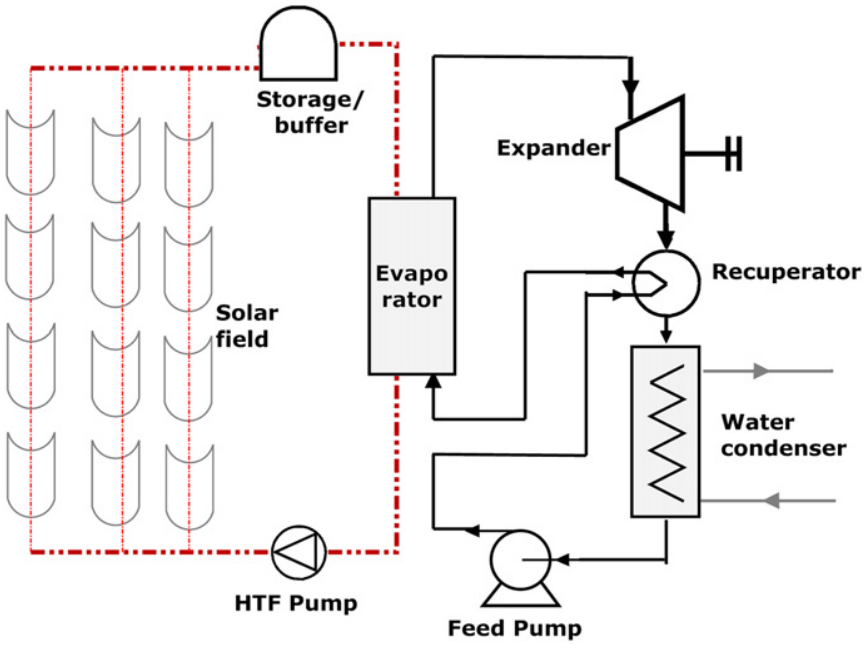

Figure 2.8 Schematic diagram of a solar ORC system [40]

Due to the intermittent nature of solar energy, thermal energy storage systems are usually employed between the solar collector and the power cycle to maintain the stability of power output during lower solar insolation or at night [108].

Currently, there are only few commercial ORC power plants driven by solar energy in operation. A 1 MWe solar ORC power plant, located in Arizona, USA, is in operation since 2006 utilizing a PTC technology. The ORC module, supplied by ORMAT, uses n-pentane as the working fluid. The overall solar to electricity efficiency is 12.1% at the design point [109]. Another prototype of a 5 kWe scale was constructed in 2009 within the frame of POWERSOL project in Almeria, Spain. The fluid used is SES36 and the theoretical overall efficiency is 7% [110].

In recent years, some researchers have paid more attention to employing ORCs in solar energy applications for this to be abundant and sustainable. Solar ORC systems have been studied both theoretically and experimentally. Nafey et al. [111] developed a new visual library working under MATLAB/Simulink environment for design and simulation of different solar desalination systems. A combined solar ORC/RO desalination plant was considered as a case study. Results showed that a total PTC area equal to 1887 m^2 could achieve output power and overall exergy efficiency of 394 kWe and 11.61%, respectively. Energy, exergy, and cost analyses were further carried out by Nafey and Sharaf [112] for a MW-scale combined solar ORC/RO desalination unit with three different solar collectors. Different working fluids were investigated under different operating conditions (saturation and superheat) and compared with water. It was shown that the minimum total collector area, specific total cost, and exergy destruction rate are achieved with toluene and water. Wang et al. [113] carried out an off-design performance analysis for a solar ORC consisting of CPCs, thermal storage tank and R245fa. The system's off-design behaviour was also analysed over a whole day and in different months. The results indicated that the decrease in environment temperature, or the increase in thermal oil mass flow rates of the vapour generator and CPC results in increasing both the net power output and average exergy efficiency. Also, the system achieved the maximum average exergy efficiency in December and the maximum net power output in June and September. Li et al. [114] investigated the performance of a 200 kW transcritical ORC cogeneration system producing electricity and fresh water driven by PTCs. It was highlighted that the solar

ORC could achieve system efficiency close to 21% using hexamethyldisiloxane (MM) as the working fluid.

Over the last decade, small-scale solar ORCs have become a mature technology and, at the same time, remain the subject for intense research. Such systems can be applied for residential or small business units. Quoilin et al. [12] described the design of a small-scale ORC system (3 kWe) driven by PTCs. Four different organic fluids and two different expander configurations were investigated for a temperature range of 100-200 ^{o}C. It was indicated that an overall efficiency in the range of 7 - 8% can be reached. It was observed that Solkatherm is the most efficient fluid. However, it required also the largest expander swept volume, which increases the system cost. Also, R245fa showed a good efficiency and required much smaller equipment. Wang and Zhao [98] analytically studied a low-temperature solar ORCs using a pure fluid (R245fa) and different mass fractions of zeotropic mixtures (R245fa/R152a) within a cycle operating between 25 and 85 ^{o}C. Investigations showed that, in contrast to the pure fluids, the isentropic mixture had the lowest ORC efficiency. It was also concluded that a significant gain in the system efficiency could be obtained when superheating was used in combination with internal heat exchanger (IHE). One year later, Wang et al. [96] extended their work to experimentally investigate a micro solar ORC system using FPCs and the same working fluids. The results showed that, by increasing of R152a mass fraction, the system pressure level and output power increased accordingly. The collector and thermal efficiencies using zeotropic mixtures were comparatively higher than those of pure fluid. A 1.7 kW solar ORC unit utilizing R245fa and a rolling-piston expander was also experimentally examined by Wang et al. [115] using two different types of solar collectors. The system showed overall efficiency values of 4.2% and 3.2% using ETCs and FPCs, respectively.

Saitoh et al. [116] developed experimentally a micro-scale solar ORC system (< 1 kW) working with R113 and operating between 100 and 200 ^{o}C. A 5.75 m^2 CPC and a displacement-type scroll expander were adopted. The results showed that an overall efficiency of 7% was obtained. When the cooling water was used for the system cogeneration, the total efficiency of 42% was attained. Twomey et al. [117] performed a dynamic performance evaluation of a micro-scale solar ORC cogeneration system driven by 50 m^2 ETCs. The ORC thermal efficiency obtained was 3.47%, with a maximum

expander isentropic efficiency of 59%. The maximum instantaneous generated power was 676W while the hot water produced was 2540 L/day. Marion et al. [118] studied the effects of wind, ambient temperature and solar radiation on a micro solar CHP ORC system using a small FPC in a DVG configuration and R365mfc as the working fluid. At a solar radiation of 425 W/m^2, experiments indicated that a significant reduction in the area related to the turbine power, namely from 12 to 8 W/m^2, was observed when the wind speed increased from 0 to 4.5 m/s. The simulated results concluded that the optimum evaporation temperature to produce the maximum power highly depended on the solar radiation and wind speed with a value varying from 70 to 105 °C. The corresponding mechanical and thermal efficiencies were from 3.1 to 6.9% and from 34 to 48%, respectively. Gang et al. [119] presented design and construction of a 3.75 kW ORC facility using R123 as the working fluid. The experimental results showed that, for 1 kW turbine power, a turbine isentropic efficiency of 65% and an ORC system efficiency of 6.8% could be obtained. The hot and cold sources were hot oil and water, respectively, with the temperature difference of 70 °C.

There are only few studies have been carried out on cascade type (two-stage) ORCs. The basic operation principle of such cycles is that the heat extracted from the refrigerant condensation of the high temperature stage (e.g. upper stage) is used to evaporate the refrigerant of the low temperature stage (e.g. lower stage), thus increasing significantly the overall efficiency [120]. Kosmadakis et al. [121] presented a comparative study to select the best working fluid for the high-temperature stage of a two-stage solar ORC for RO desalination. The low-stage operating temperature was 77 ^{o}C with R134a, while the high-stage maximum operating temperature was 137 ^{o}C. The results showed that among 33 working fluids, R245fa was the most appropriate one. In addition, the economic feasibility of a two-stage solar ORC to drive a 2 m^3/h RO desalination unit was further investigated by Kosmadakis et al. [122] using 60 ETCs with a total gross area of 240 m^2. The specific fresh water cost of the developed two-stage solar ORC/RO system was estimated to be 6.85 €/m^3, being much lower than the values of the single-stage system. The same authors, in [123], conducted a parametric study of the proposed two-stage solar ORC/RO system and observed an increase of 1.38% in the annual fresh water production by adjusting the ETC slope to 35^o. Although the total cost was increased by increasing the collectors' gross

area, a minimum fresh water specific cost was reached at the maximum area of 480 m^2. Similarly, Bao et al. [124] proposed an auto-cascade solar ORC system consisting of a zeotropic mixture of Isopentane/R245fa, two solar collectors and two expanders in which heat from the expanders' exhaust is recovered twice, using an IHE and a regenerator. It was shown that, with regeneration, the proposed system efficiency with 0.32 R245fa on mass basis mixture was significantly higher than that of the single-stage system. Pei et al. [125] proposed a low-temperature solar ORC with two-stage collectors and heat storage units to improve the heat collection efficiency. FPCs were used to preheat R123 prior to entering a higher temperature heat exchanger connected with CPCs. The results indicated that the increase in the collector efficiency of the two-stage system is appreciable.

2.5.2 Biomass energy

Biomass is the fourth largest source of energy in the world after coal, petroleum and natural gas, providing about 10% of the world's primary energy consumption [106]. Biomass, as a renewable energy source, is a biological material which comprises all the living matter present on Earth. It is derived from growing plants including trees and agricultural crops or from animal manure [126]. Currently, biomass resources are mainly used for heating, cooling and electricity generation [127].

As an energy source, biomass can either be used directly via combustion, or converted into other energy products such as biofuels [128]. In direct combustion, the solid biomass is burned in a boiler to obtain heat energy which is in turn converted into electricity through a thermodynamic cycle (e.g. steam cycle, ORC, Stirling engine). Alternatively, other thermochemical conversion technologies such as gasification and pyrolysis are used to transform the solid fuel into gas or liquid which can then be burned in an ICE or a gas turbine. The latter technique is characterized by higher potential energy conversion efficiencies compared to direct combustion. However, these technologies are not always economically viable as well as require high gas purification treatments [128, 129].

Direct combustion of solid biomass is the most common method of energy conversion using ORCs. Also, different variety of fuel types with good burning characteristics can be used including logs, sawdust, woodchips, pellets and compacted agricultural residue [103]. In typical biomass ORC systems, an intermediate oil loop is integrated between the boiler and the ORC. The oil loop ensures low boiler pressures, load change buffering and simpler control and operation [41]. The thermal oil, as a heat transfer fluid, operates usually at a temperature varying from 150 to 320 °C [40].

Biomass ORCs are often operated as CHP systems in order to increase their overall efficiency, in which a local heating demand is required. The higher the biomass heat source temperature is available; the CHP application becomes technically more feasible. In such systems, the ORC condensing temperature is typically as high as around 90 - 100 °C. At this temperature level, hot water can be then produced in the condenser to satisfy the requirements of heating purposes [23]. Therefore, low critical temperature working fluids are not suitable for such applications due to their relatively high pressures at higher condensing temperatures. The schematic diagram of a typical biomass CHP system using the ORC technology is shown in Fig. 2.9. Heat from the combustion gases is transferred to the heat transfer fluid (thermal oil). The heat transfer fluid is then directed to the ORC evaporator to transfer its heat to the working fluid. The evaporated working fluid is then expanded to generate electricity before it passes through the condenser to reject its heat. The condensation heat is used for hot water generation. Fig. 2.10 shows the energy flow diagram of an ORC CHP system. Although the electrical efficiency of the system is limited to 18%, the overall efficiency (electrical and thermal) of the system is 88%.

The number of installed biomass ORC plants is rapidly increasing as the technology is becoming mature and cost effective. Biomass ORC CHP plants at the medium scale range (200 – 2000 kW) are now commercially available with more than 140 installed units throughout the world [102]. However, smaller size units at several kW scale range are still under development. A 1000 kWe facility located in Lienz, Austria is an example of biomass ORC CHP plants. The plant supplies the town of Lienz with district heat (60,000 MWh/year) and feeds the electricity produced (7200 MWh/year) into the public grid [130].

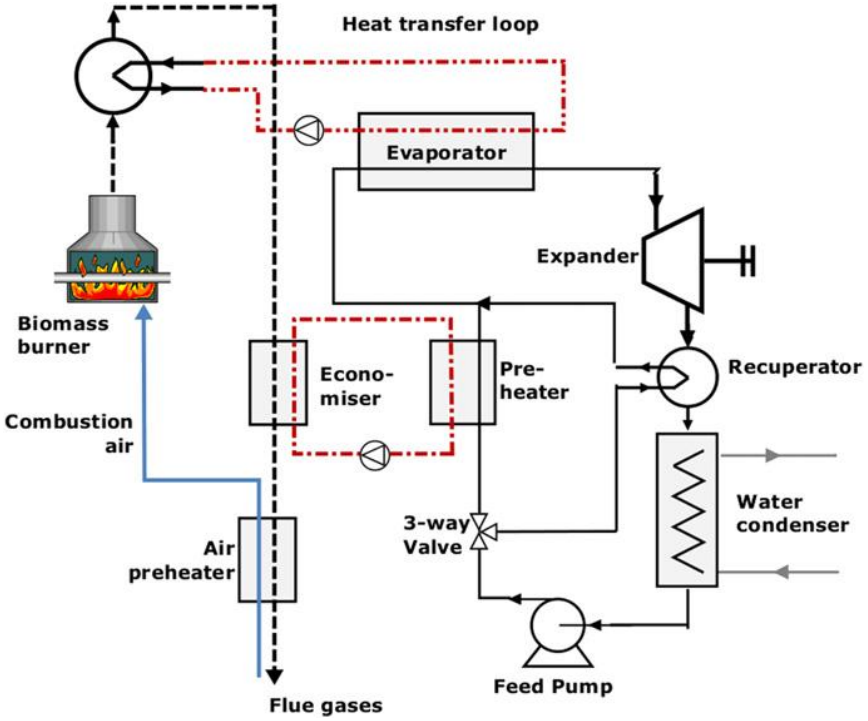

Figure 2.9 Schematic diagram of a biomass CHP ORC system [40]

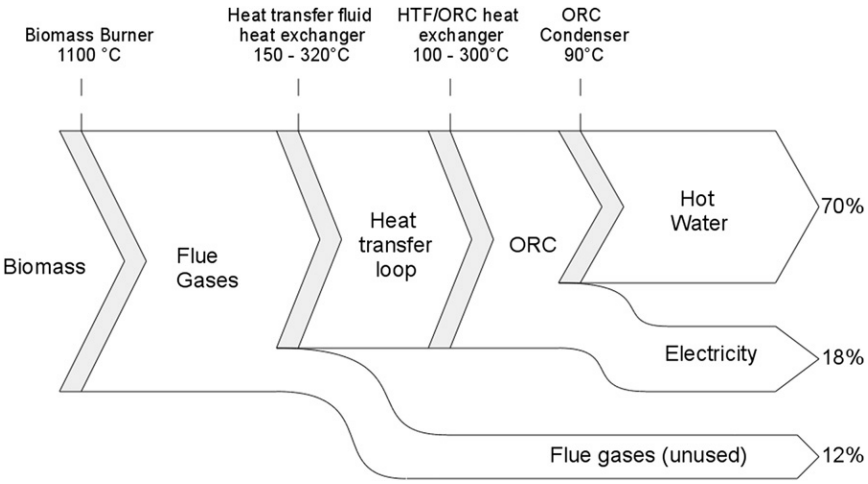

Figure 2.10 Energy flow diagram of a biomass CHP ORC system [40]

Biomass-based ORC systems have been studied over recent years by numerous researchers. In most of these studies, such systems are used for cogeneration, trigeneration or multigeneration applications in which multiple useful forms of power are produced. Al-Sulaiman et al. [131] presented energy and exergy analyses of a biomass trigeneration ORC system, providing electricity, cooling and heating. They concluded that there is a significant improvement in the system performance when trigeneration is used as compared to only electrical power generation. The study demonstrated that the system efficiency increases, in average, from 12% for electrical power to 88% for trigeneration. Moreover, the maximum exergy efficiency of the ORC was 13% whereas for trigeneration it increased to 28%. For the same trigeneration ORC system, Al-Sulaiman et al. [132] also conducted greenhouse gas emission and exergy assessments. It was found that the main two sources of exergy destruction are the biomass combustor and ORC evaporator and their values decreased as the pinch point temperature increased. The results also showed that the CO_2 emissions drop to around one seventh per MWh produced when trigeneration was used as compared to only electrical power production case. Also, Huang et al. [133] carried out a techno-economic assessment of a 200 kWe biomass-fuelled trigeneration ORC system using three different biomass fuel types. The results showed that the maximum efficiency and the best breakeven electricity selling price were 11.1% and 221 £/MWh for power only, 85% and 87 £/MWh for combined heat and power and 71.7% and 103 £/kWh for trigeneration, respectively.

Ahmadi et al. [134] performed exergy analysis and environmental impact assessment of a biomass-based multigeneration ORC system, producing electricity, heating, cooling, hydrogen and hot water. The exergy results showed that the combustor and ORC evaporator were the two main sources of irreversibility. The system performance was considerably affected by the pinch point temperature, the ORC turbine inlet pressure and the ORC pump inlet temperature. Also, the multigeneration system exhibited lower CO_2 emissions than conventional power generation and CHP systems. The multigeneration ORC system, with fresh water production, was further investigated by Ahmadi et al. [135] by conducting thermoeconomic modelling and multi-objective optimization studies. The optimization results showed that ORC turbine inlet pressure and temperature, ORC turbine

and pump isentropic efficiencies and evaporator pinch point temperature difference had important effects on the trade-off between exergy efficiency and total cost rate.

Although biomass-fired CHP systems with ORC have been investigated over the recent years, very little literature is available on the performance and evaluation of small and micro-scale biomass ORC systems. Liu et al. [20] studied a 2 kWe biomass-fired micro-scale CHP system based on an ORC using three organic working fluids. The hot water temperature of the biomass boiler, the condenser cooling water temperature and the working fluid used showed the presence of considerable effects on the performance of the proposed system. The highest predicted ORC and electric efficiencies were 16.6% and 13.5%, respectively, using n-pentane. The overall CHP efficiency of the system was in the order of 80% for all three ORC fluids. A thermodynamic model to optimize the performance of a small-scale combined cooling, heating and power (CCHP) plant based on biomass combustion was developed by Maraver et al. [136] using different working fluids. Toluene in a recuperative ORC showed a slightly better thermodynamic performance, although it was limited to the use of a turbine type expander. For a volumetric type expander, the optimal CCHP system was found with the use of n-pentane in a recuperative ORC.

2.5.3 Geothermal energy

Geothermal energy is a renewable heat resource that comes from water underneath the Earth's surface with temperatures varying from a few tens of degrees up to 300 ºC, depending on the drilling depth and geological characteristics [137]. The geothermal source can either exist in the form of dry-steam, a steam-water mixture or just liquid water. The fluid nature and temperature of the geothermal field determine the type of technologies that can be applied to extract and use its available heat [138, 139].

For higher temperature geothermal reservoirs, typically above 200 °C, and producing dry steam, the best and more economic method is to pass steam directly through turbines in an open cycle to generate electricity. When the geothermal wells produce a mixture of steam and liquid, the flash-steam plant is a relatively simple way to convert the geothermal

energy into electricity. First, the mixture is separated into distinct steam and liquid phases. A proportion of the hot water is then flashed to steam, either at one or two pressure stages, which is finally used to drive a turbine. If hot water with a temperature of 150 °C or less is produced from the geothermal well, it becomes inefficient and economically unfeasible to implement a flash-steam plant. Alternatively, binary cycle power plants such as ORCs are the most common technology for utilizing such resources for electricity generation, as shown in Fig. 2.11. The geothermal fluid from the production well is used to transfer its heat to the organic working fluid in the evaporator before it is disposed of in the injection well. The working fluid vapour then passes throughout the ORC components to generate electricity in such a way that has already been discussed previously.

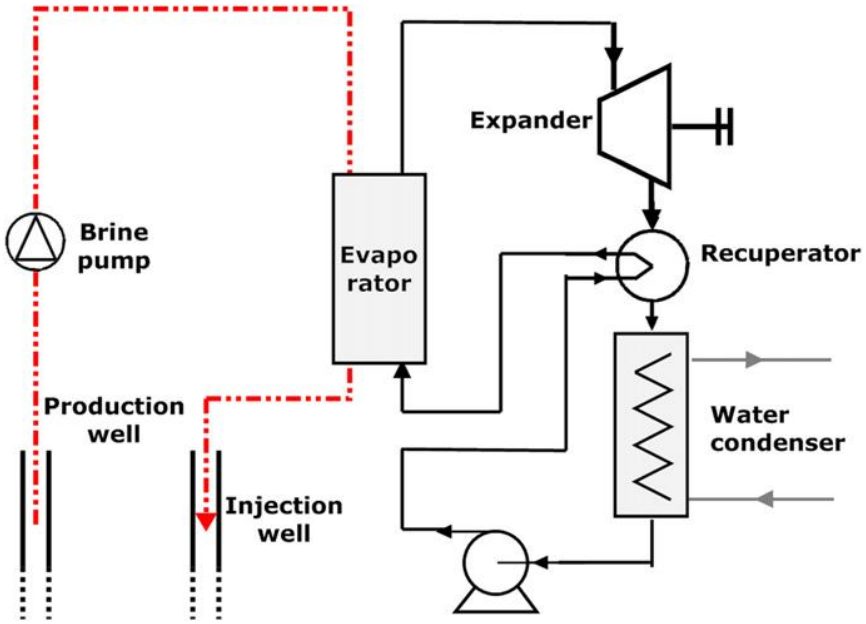

Figure 2.11 Schematic diagram of a geothermal ORC system [40]

Geothermal water vapour usually contains different chemical compositions with proportions vary with the geothermal reservoir. The return stream temperature must be higher than the salt saturation temperature to prevent salt from precipitating out of the geothermal vapour or water [106].

In low-temperature geothermal ORC systems, the pumps consume around 30 - 50% of the gross output power. The greatest share is mainly consumed by the geothermal pump which needs to circulate a considerably high flow rate of geothermal water [40]. Also, the environmental conditions have a more significant impact on the performance of low-temperature systems. In hot regions, a high condensation (sink) temperature leads to a very low efficiency [106]. It should also be mentioned that the geothermal ORC systems require a high initial capital investment. The drilling cost of the geothermal wells could reach up to 70% of the total plant investment cost, depending on the geological formation and well depth [40].

In 2007, the number of geothermal ORCs in operation throughout the world reached 162 units with a total capacity of 373 MW. These units represent 32% of all installed geothermal plants but generate only 4% of the total power using this type of energy source [137]. An example of geothermal plants using the ORC technology is located in Neustadt–Glewe, Germany. This was the first geothermal power plant in Germany which operates with a heat source of 98 °C to generate a rated capacity of 210 kWe [140].

The geothermal ORC has been studied by many researchers for a range of geothermal water temperatures and plant capacities. Hettiarachchi et al. [141] presented a cost-effective optimum design criterion for a 10 kWe ORCs utilizing a low-temperature geothermal source (70 - 90 ^{o}C). Ammonia was recommended as the best fluid based on the total heat transfer area to net power produced although it did not have the maximum cycle efficiency. The authors also stated that the presence of wet vapour at the end of the expansion and very high evaporation pressure limited the use of ammonia in low-temperature geothermal applications. Shengjun et al. [83] conducted performance comparison and parametric optimization of subcritical and transcritical ORCs for low-temperature (80 - 100 ^{o}C) geothermal power generation. R123 in subcritical ORCs yields the highest thermal and exergy efficiency values of 11.1% and 54.1%, respectively. R125 in the transcritical cycle showed excellent economic and environmental performance, although its thermal and exergy efficiencies were lower than those of R123 in the subcritical cycle. Heberle and Brüggemann [142] studied the performance of a CHP ORC system (above 1 MWe) for geothermal resources at a temperature level below 450 K based on the second law analysis. The results showed that for a CHP generation, the second law

efficiency of a geothermal power plant can be significantly increased in comparison to a power generation mode.

El-Emam and Dincer [143] presented thermodynamic and economic analyses of a 5 MWe geothermal recuperated ORC based on both energy and exergy concepts. The study was carried out for a range of geothermal water temperatures of 160 - 175 ^{o}C using isobutene. The energy and exergy efficiency values were found to be 16.37% and 48.8%, respectively, for optimum operating conditions. Astolfi et al. [144, 145] carried out thermodynamic and techno-economic optimizations of binary ORC power plants for the exploitation of low-medium temperature geothermal sources in the range of 120 - 180 °C. It was found that configurations based on supercritical cycles, employing fluids with a critical temperature slightly lower than the temperature of the geothermal source, led to the highest efficiencies and lowest electricity cost for most of the investigated cases. Guo et al. [146] investigated a geothermally-driven cogeneration system comprising an ORC and a heat pump using different working fluids. A geothermal water temperature in the range of 80-100 ^{o}C was used. Results indicated that fluids having higher normal boiling point values showed higher values of the ratio of power produced to power consumed but lower values of the ratio of heat supplied to the user and heat produced by the geothermal source. Moreover, Guo et al. [81] further investigated the system by conducting a techno-economic study using 27 working fluids. E170, R600 and R141b showed the lowest values of electricity production cost and total heat transfer area per net power output; however, R236ea provided higher net power output per unit mass flow rate of the geothermal water. Yang and Yeh, 2016 [147] investigated the economic optimization for an ORC system utilizing a geothermal energy source with a temperature of 100 ^{o}C and a capacity above 300 kWe. The results showed that R600 performs the most satisfactorily followed by R600a, R1233zd, under economic performance optimization, and these fluids would have reductions in the proportion of equipment purchased cost.

2.5.4 Waste heat recovery

The residual heat from a combustion process or any other chemical or thermal process is known as waste heat as it is usually discharged directly to the environment without being practically used. Industrial processes, thermal engines and mechanical equipment are considered as the major sources of waste heat [148, 149]. The amount of heat wasted produced through these processes is massive. In the industrial sector alone, it is estimated that about 20 - 50% of the total energy input is ultimately rejected as waste heat. In the transport sector, typical internal combustion engines (ICEs) only converts around 30 - 35% of the fuel energy into mechanical power. This indicates that at least 65% of the total input fuel energy is wasted to the surroundings in the form of exhaust gases (400 - 900 ^{o}C) and the engine cooling system (80 - 100 ^{o}C) [106, 150].

Although the waste heat from different processes are inevitable, the potential for recovering this heat has been particularly promising in which the total energy recovery efficiency can be significantly improved. In some cases, the recovery of waste heat can increase the energy efficiency of the system by up to 50% [43]. Waste heat recovery (WHR) technologies not only improve the efficiency of the system but also considerably reduce their fossil fuel consumption, as well as reduce associated operating costs and mitigate pollutant emissions [16, 41]. In addition, the capacity requirements for facilities' thermal conversion devices can be reduced, leading to reductions in the capital costs.

The key parameters that evaluate the feasibility of a waste heat source include mass flow rate, temperature, pressure, chemical composition and minimum allowable temperature of the heat source. The heat source temperature plays a vital role in determining the WHR technology that can be used. It also influences the energy conversion efficiency and significantly impacts the heat exchanger area requirements. Waste heat sources can be grouped based on the temperature level in three main categories [43], namely low (< 230 ^{o}C), medium (230 - 650 ^{o}C) and high (> 650 ^{o}C) temperature sources. Statistical studies point out that low-grade waste heat accounts for more than 50% of the total heat generated in the industry [11]. Typical temperatures of common waste heat sources along with the corresponding suitable recovery methods are listed in Table 2.3 [43].

A wide range of energy recovery technologies has been developed to exploit the abundant amounts of heat wasted. These include various types of heat exchangers for reusing the waste heat in industrial processes, heat pumps for cooling and heating facilities, and heat to mechanical/electrical power converters. Power generation from waste heat can be achieved using thermodynamic power cycles such as steam Rankine cycle, ORC, Kalina cycle, Goswami cycle, etc [66, 151]. Steam Rankine cycles are successfully implemented to recover medium to high temperature waste heat sources. However, such systems cannot be cost-effective neither at smaller scale nor for low temperature sources [152]. Power production from low to medium temperature heat source has technical and feasibility constraints, and limited choices are available for low temperature heat engines. ORCs and Kalina cycles have demonstrated their ability to efficiently harness such sources with an advantage going to the former due to their much less complexity and less maintenance needed [66]. A schematic diagram of a WHR ORC system is shown in Fig. 2.12. In such systems, waste heat can either be directly used to evaporate the working fluid in a heat exchanger or to firstly heat a thermal fluid in an intermediate heat transfer loop. The heat transfer fluid is then used as a heat source for the ORC. [153]. A potential of 3000 MWe is estimated for power generation from industrial waste heat in the US, Europe (EU-12) and Germany using the ORC technology, with 750 MWe for the U.S. and 500 MWe for Germany [154].

Over the recent years, there have been increasing numbers of WHR ORC installations built in different locations. A 3 MWe ORC is installed in Mirom Roeselare, Belgium by TURBODEN in 2008. The heat source is hot water wasted from an incinerator plant with a temperature of 180 ºC. Also, a small scale ORC with a capacity of 150 kWe is in operation since 2009 in Nieuweroord, Netherlands. The ORC, supplied by Tri-o-gen, is powered by a waste heat source from two Jenbacher biogas engines (2×835 kW) with a temperature of about 500 ºC [41].

Table 2.3 Waste heat sources and heat recovery methods [43]

Category	Heat source	Temperature [ºC]	Heat recovery method
High-temperature (> 650 ºC)	Nickel refining furnace	1370-1650	Combustion air preheat
	Steel electric arc furnace	1370-1650	Steam generation (heating)
	Basic oxygen furnace	1200	Steam Rankine cycle
	Copper refining furnace	760-820	Furnace load preheating
	Steel heating furnace	930-1040	Transfer to med/low-temp. processes
	Hydrogen plants	650-980	
	Fume incinerators	650-1430	
	Glass melting furnace	1300-1540	
	Coke oven	650-1000	
	Iron cupola	820-980	
Med-temperature (230 - 650 ºC)	Steam boiler exhaust	230-480	Combustion air preheat
	Gas turbine exhaust	370-540	Steam Rankine cycle
	Reciprocating engine exhaust	320-590	Organic Rankine cycle
	Heat treating furnace	430-650	Furnace load preheating
	Drying & baking ovens	230-590	Feed-water preheating
	Cement kiln	450-620	To low-temp. processes
Low-temperature (< 230 ºC)	Exhaust gases exiting recovery devices in gas-fired boilers, ethylene furnaces, etc.	70-230	Space heating Domestic water heating Heat pump
	Process steam condensate	50-90	Organic Rankine cycle
	Cooling water from:		Kalina cycle
	Furnace doors	30-50	
	Annealing furnaces	70-230	
	Air compressors	30-50	
	Internal combustion engines	70-120	
	Air conditioning and refrigeration condensers	30-40	
	Drying, baking, and curing ovens	90-230	
	Hot processed liquids/solids	30-230	

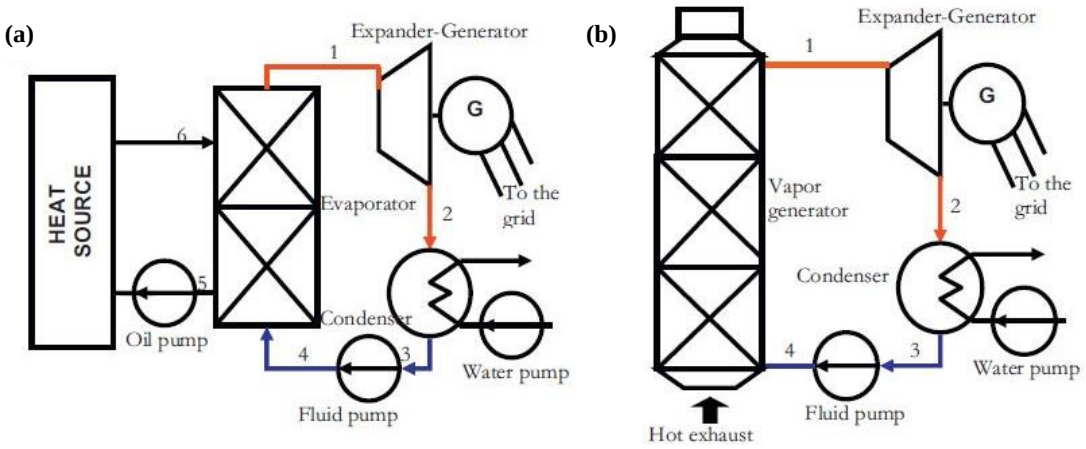

Figure 2.12 Schematic diagram of a WHR ORC system, (a) with and (b) without an intermediate thermal loop [41]

The use of waste heat from different sectors to drive ORCs has been investigated in numerous studies. Yu et al. [155] investigated the performance of a bottoming ORC for a diesel engine using R245fa. Results indicated that approximately 75% and 9.5% of waste heat from engine exhaust gases and jacket water, respectively, can be recovered. ORC expansion power and recovery efficiency of 14.5 kW and 9.2%, respectively, were obtained. Also, the thermal efficiency of the diesel engine can be improved by up to 6.1%. Parametric optimization and performance analysis of an ORC-based WHR system using R12, R123 and R134a were performed by Roy et al. [156]. Real time data of flue gases from a coal-fired steam power plant (4×210 MW) with a temperature of 140 ^{o}C were utilized as a heat source. The results showed that R123 provided the maximum power output, first and second-law efficiencies among all the selected fluids with values of 19.09 MW, 25.3% and 64.4%, respectively. Similarly, Srinivasan et al. [157] examined the exhaust WHR potential from actual data of a dual fuel low temperature combustion engine using a small-scale ORC. The available exhaust gas temperature was 551.5 K and the working fluid used in the ORC was R113. It was found that the fuel conversion efficiency improved by an average of 7% whilst NOx and CO_2 specific emissions decreased by an average of 18%.

On the other hand, low-grade waste heat power generation has been experimentally tested in many studies. Zhou et al. [158] experimentally studied a micro ORC for WHR from low-temperature flue gases in the range of 90 - 220 ^{o}C and using R123. The results showed that the cycle efficiency, net output power and exergy efficiency increased whilst the heat recovery efficiency decreased with the increment of the evaporating pressure. The maximum cycle efficiency and net output power were 8.5% and 645 W, respectively. Superheating of the working fluid produced negative effects on system performance. Muhammad et al. [159] presented experimental investigations of a 1 kWe ORC system using R245fa as a working fluid for low-grade WHR from steam with the temperature in the range of 100 - 140 ^{o}C. The maximum system thermal efficiency was 5.75% and maximum expander isentropic efficiency obtained was 77.74% during the experiment. It was also observed that an increase in the degree of superheating by 1 ^{o}C reduced the thermal efficiency of system by 0.021%. Desideri et al. [160] experimentally evaluated the performance of an 11 kWe ORC system for low-temperature (up to 125 ^{o}C) WHR

applications using two different working fluids. A maximum expander isentropic efficiency of 60% was reached using SES36, and a value of 52% was reached with R245fa. However, for a given pressure ratio, the expander output power was higher with R245fa than with SES36.

2.5.5 Multiple heat sources

Multiple-heat-source systems involve the use of more than one energy source to drive a thermal power cycle system. If two heat sources are integrated, the system is then known as a hybrid power system. In hybrid thermal power systems, one of the heat sources is usually solar energy in which the other source can be used during insufficient availability of solar energy or at night. Therefore, such systems could run continuously without the use of bulky thermal storage systems. In general, the lower temperature heat source is used to preheat the working fluid, while the higher temperature heat source is used for evaporation and superheating [161].

A hybrid solar/gas driven micro-CHP system (1.5 kWe) was experimentally tested for a small-scale application by Yagoub et al. [162]. The heat input to the system was provided by ETCs, supplemented by a condensing gas boiler at 90 ^{o}C. HFE-301 and n-pentane were evaluated as working fluids for the system. The results showed that HFE-301 performed better than n-pentane achieving electrical and overall efficiencies of 7.6% and 17%, respectively. Kane et al. [163] experimentally tested a small hybrid ORC power system (10 to 25 kWe) based on laboratory and on-site conditions. Two superposed ORCs were integrated with linear Fresnel concentrators (100 m^2) and waste heat from both the exhaust gases and block cooling water of a Diesel engine. The results showed a system efficiency of 7.74% for the solar mode only. In the hybrid mode, an efficiency of 41.1% was achieved based on the fuel input only (total electrical power/LHV_{fuel}).

A very few studies have been conducted to analyse the possibility of integrating two renewable energy sources to drive an ORC system. Most of these studies focused on the solar and geothermal energy as the hybrid heat source. Tempesti et al. [164, 165] conducted thermodynamic analysis and economic assessment of a 50 kWe CHP ORC

system powered by a combination of geothermal and solar sources. Single and double stage system arrangements were proposed. A geothermal energy source at a low temperature (80 - 100 ^{o}C) was used to preheat the working fluid. Only ETCs were used in the single-stage arrangement, while both ETCs and PTCs were used in the double-stage configuration. Astolfi et al. [166] analysed a combined solar/geothermal hybrid ORC plant, including an intermediate enthalpy geothermal source (150 ^{o}C) and a solar PTC field (60,000 m^2). Competitive levelized costs of electricity at 145-280 €/MWh were obtained compared to large stand-alone concentrating solar power plants. Dynamic simulation and parametric analysis of a solar/geothermal hybrid cogeneration plant based on a 1 MW ORC powered by a medium-enthalpy geothermal source (150 ^{o}C) and a PTC solar field (10,000 m^2) were performed by Calise et al. [167]. The results indicated that the combination of solar and geothermal sources increases both the electrical and thermal power production. However, the hybrid system showed less profitability than conventional geothermal ORC systems.

2.6 ORC configurations

Although the basic ORC has been successfully adopted by industry, performance improvements and cost reduction are still needed. Therefore, different architectures of the ORC systems have been developed. This can be achieved by adding extra components and processes to the original basic cycle, aiming to enhance the overall system performance. In general, these modifications mainly maximize the mean temperature difference between the heat addition and heat rejection, leading to an increase in the system thermal efficiency [168]. However, some complexities and extra costs are also added to the system. Along with the basic ORCs, the most common cycle configurations include recuperated ORCs, regenerative ORCs and ORCs with reheat [103]. In this section, these cycle configurations are presented and compared with the basic ORC.

2.6.1 The basic ORC

The basic ORC, which is the baseline ORC, is shown in Fig. 2.13. It consists of four major components including the evaporator, turbine, condenser and pump. The liquid working fluid absorbs heat in the evaporator at the high pressure where phase change from liquid to vapour state takes place. The high enthalpy saturated or superheated vapour then expands in the turbine to produce mechanical power which can be transformed to electricity via a generator. The exhausted low pressure working fluid from the expander is cooled down to the saturated liquid in the condenser. The liquid working fluid is pressurised in the pump and finally directed to the evaporator to repeat the cycle.

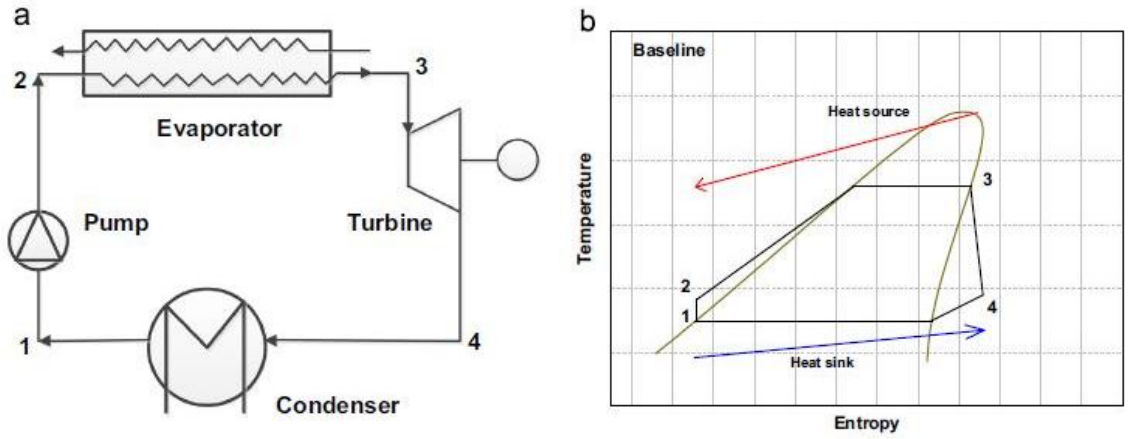

Figure 2.13 Basic ORC system, (a) schematic of the cycle and (b) T-s diagram [169]

2.6.2 The recuperated ORC

For ORCs using dry working fluids, the state of working fluid leaving the expander is always superheated with a temperature being higher than the condensation temperature [59, 61, 62]. As a result, the load on the condenser also increases [66]. The heat still contained within the fluid at the expander outlet can be recovered by implementing an internal heat exchanger (IHE), also known as a recuperator, between the expander and the condenser, as shown in Fig. 2.14. This heat (process 4-4a) is used to preheat the liquid leaving the pump before it enters the evaporator (process 2-2a). The advantage of the

recuperated ORC system is that the same power output can be produced with a smaller amount of input heat, thereby increasing the cycle efficiency [73]. Simultaneously, the condenser load is decreased [98, 170], leading to a smaller heat transfer area. However, the use of a recuperator would only be beneficial if the expander exit temperature is markedly higher than the condenser temperature [171]. The main disadvantage of such a system is the additional cost and weight of installing the recuperator [60].

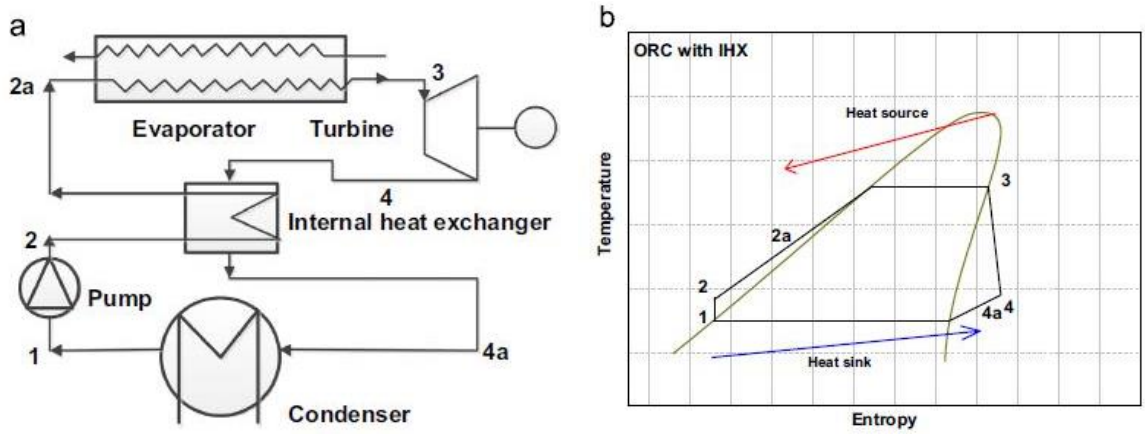

Figure 2.14 Recuperated ORC system, (a) schematic of the cycle and (b) T-s diagram [169]

2.6.3 The regenerative ORC

The schematic of the cycle and the corresponding T-s diagram of a regenerative ORC are shown in Fig. 2.15. The basic concept of the regenerative ORC is closely similar to that of the recuperated ORC system. In both systems, the working fluid is preheated before entering the evaporator. In the regenerative ORC system, a fraction of the working fluid is extracted after the first stage expansion to an intermediate pressure (state 3a), while the main stream proceeds to the second-stage turbine. The extracted vapour is used in a direct contact feed heater to preheat the working fluid leaving the pump 1 (state 1a). This ends up with saturated liquid at a higher temperature (state 2a). In this way, the heat input in the evaporator to produce the same amount of work is reduced, increasing the cycle efficiency [169]. The mass fraction and pressure of the turbine bleeding play a key role in the performance of regenerative ORC system [172].

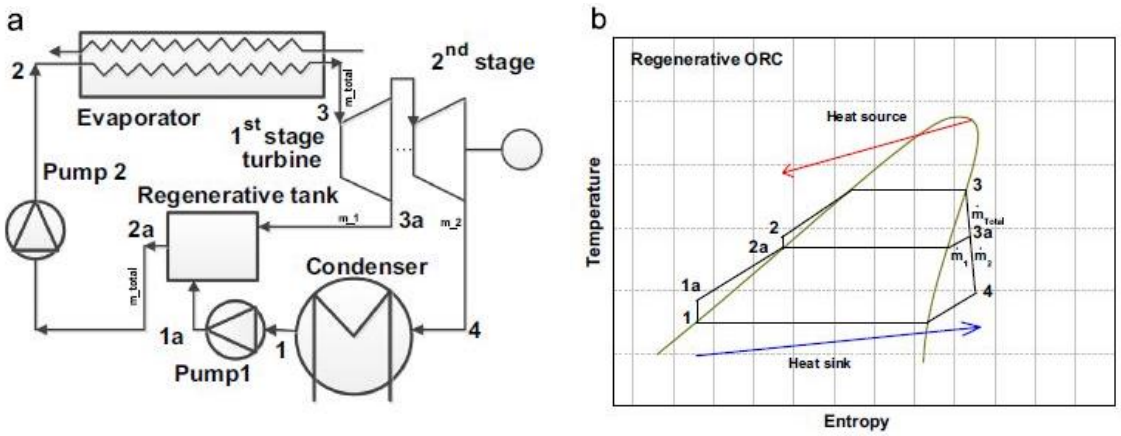

Figure 2.15 Regenerative ORC system, (a) schematic of the cycle and (b) T-s diagram [169]

2.6.4 The ORC with reheat

The main purpose of the reheating cycle is to avoid the moisture content at the final stages of the expansion process [169]. Such a cycle configuration is typically used when the system operates with a wet working fluid, having the advantage of eliminating turbine blades damage. Therefore, the reheat cycle is considered as a practical solution in modern conventional steam Rankine cycles [103]. A schematic of the reheat ORC and its T-s diagram are shown in Fig. 2.16. In this cycle configuration, two stages of the expanders (high and low pressure) are used in series. After the high pressure vapour from the evaporator expands in the first-stage turbine (3-3a), it is redirected to the evaporator where it is reheated before passing through a second-stage turbine at lower pressure (3b-4). The reheat temperature (state 3) is usually equal to the inlet temperature of the first-stage turbine (state 3b) [169].

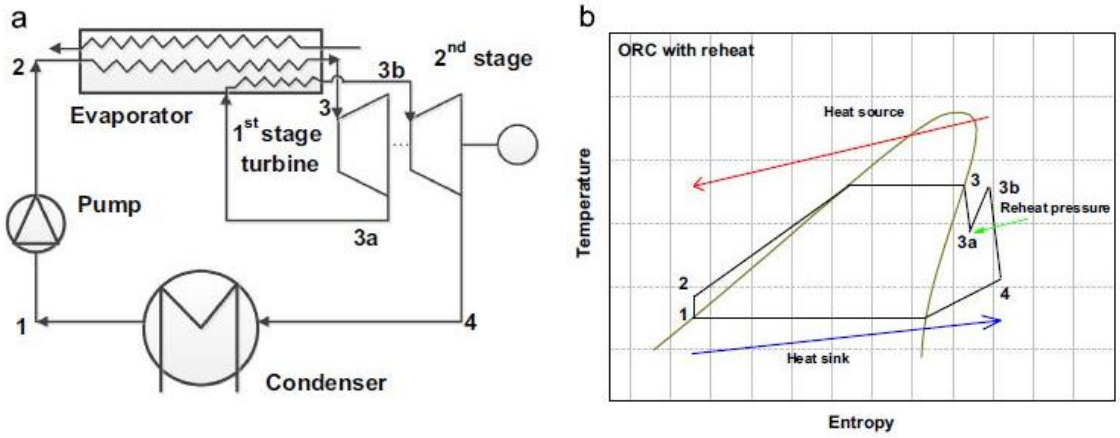

Figure 2.16 Reheat ORC system, (a) schematic of the cycle and (b) T-s diagram [169]

Integrating the ORC with a recuperator is suggested by several researchers [66, 73] in order to reuse the heat after the expansion process for preheating the working fluid. A typical example of this type of work is that developed by Aljundi [61] to investigate the effect of different dry working fluids on the performance of a geothermal ORC system. It was concluded that incorporation of an IHE when using dry fluids lowers the required input energy in the evaporator and improves the thermal efficiency of the cycle. Similarly, Li et al. [97] analysed the effects of the evaporation temperature and the use of an IHE on the performance of a WHR ORC system. Although the power output of the system slightly decreased using the IHE, both the thermal and exergy efficiencies were considerably improved. Dai et al. [171] optimized the performance of ORC based on low grade WHR utilizing different working fluids. They concluded that the cycle with R236ea had the highest exergy efficiency, and adding an IHE into the ORC system could not improve the performance under the given waste heat condition. Guo et al. [173] carried out a thermodynamic analysis of 12 working fluids for a transcritical ORC system with a recuperator and driven by a low-temperature geothermal heat source varying between 80 and 120 ^{o}C.

The recuperated ORC system with the use of zeotropic mixtures has been also reported in a number of studies [37, 94, 98, 170]. However, these studies primarily focused on the investigation of zeotropic working fluids potential for ORC applications.

Regenerative ORC systems have been also investigated in a number of studies in the literature. Pei et al. [125] analysed a solar thermal ORC with regeneration for electricity production. The overall efficiency with regenerative ORC was about 8.6% which was higher than that without regeneration by 4.9%. Mago et al. [174] presented an analysis of a regenerative ORC using four different dry fluids. The results showed that the regenerative ORC has a higher thermal efficiency and a lower irreversibility compared with the basic ORC. Furthermore, the authors demonstrated that the increase in the thermal efficiency due to regeneration depends on the working fluid used.

Meinel et al. [175] compared the performance of the basic, recuperated and regenerative ORCs utilizing a waste heat source of 490 ^{o}C and different working fluids. For isentropic fluids, the thermal efficiency of the regenerative ORC was higher than those of the basic and recuperated ORCs. However, for dry fluids, the thermal efficiency of the recuperated ORC was higher than both the basic and regenerative ORCs. The three cycle configurations were comparatively assessed by Imran et al. [172] for low-temperature geothermal applications. Results indicated that the thermal and exergy efficiencies for recuperated and regenerative ORCs are higher than that of basic ORC but with an additional specific investment cost of 2-3% and 6-9% for recuperated and regenerative cycles, respectively. R245fa provided the highest system efficiency and minimum specific cost for all cycles. Also, Yari and Mahmoudi [176] analysed the thermodynamic performance of the three configurations for a WHR application. The amount of thermal energy recovered in the evaporator was higher for the basic ORC followed by the recuperated and regenerative ORCs, respectively. As a result, the basic ORC proved to be the best configuration for having the highest efficiency. Also, the basic and recuperated ORCs showed higher economic performance compared to the other cycles. For the same three configurations, Tchanche et al. [177] performed exergy analysis of a micro solar ORC for driving a small scale RO desalination unit. It was concluded that integration of recuperation or regeneration is not significantly rewarded in terms of energy and exergy efficiency gain and cannot be considered as economically profitable for a heat source temperature below 100 ^{o}C.

A cycle integrating both the recuperation and regeneration was analysed by Desai et al. [178]. As an average, an improvement in the thermal efficiency of the new cycle configuration of 16.5% was obtained compared to the basic ORC.

In the open literature, the reheat ORC configuration has not been widely investigated [103, 169]. An ORC with reheat for solar applications was considered in the work of Price and Hassani [179]. They determined that the thermal efficiency of the cycle with reheat is only slightly higher than the case without reheat. The same conclusion was also reached by Mago et al. [174], highlighting that the performance of this type of cycles is very similar to that of basic ORC. Furthermore, the total cost of the reheat cycle is considered higher because a two-stage (low and high) pressure expander and an extra heat exchanger are needed. Therefore, the reheat cycle is not considered as a viable alternative.

2.7 ORC manufacturers and market evolution

The ORC was introduced to the market at the beginning of 1980s by a limited number of manufacturers. However, with the recent development of this technology, the market has witnessed a significant growth in the commercial ORC units. Currently, several manufacturers are available which provide ORC systems with a wide range of power output and applicable heat source. Table 2.4 shows a list of the most known ORC manufacturers with the corresponding plant capacity, applicable heat source and working fluid [180]. For convenience, ORCs can be classified according to their size as very small (< 10 kW), small (10-100 kW), medium (100-400 kW) and large (400 kW up to several MW) [103]. As shown in Table 2.4, most of the commercial ORC plants available in the market are in either medium or large scale sizes. This indicates that this technology is well developed for larger scale power production. Although a number of companies have entered the ORC market with micro and small units in the recent years, very few ORC plants are available in the kW power range. In terms of the number of installed ORC units and total installed power, there are three leading companies, namely TURBODEN, ORMAT and Maxxtec. These three companies have installed more than 90% of the total installed units worldwide with also more than 90% of the total installed power [40].

Table 2.4 ORC manufacturers and their system configurations [180]

Manufacturer	Power range [kW]	Heat source temperature [ºC]	Working fluid
Atlas Copco	<25,000	200-300	Hydrocarbons
Adoratec GmbH/Maxxtec AG	300-2400	320	OMTS
Bosch KWK GmbH	75-375	>140	R245fa
Calnetix Technologies LLC	125	>95	R245fa
Conpower	13-75	>85	SES36
Cryostar SAS (Linde Group)	500-15,000	N/A	R245fa, R-134a
Cryotec Anlagenbau GmbH	100	120	OMTS, Hydrocarbons
Dürr Cyplan	40-1000	90-300	Hydrocarbons
ElectraTherm Inc.	<110	77-116	R245fa
Eneftech Innovation SA	5-30	125-200	R245fa
E-Rational	55-132, 250-500	80-150	R245fa, SES36
Exergy (Maccaferri Industrial Group)	1000-50,000	90-300	Pentane, Isopentane, Cyclopentane, others
Freepower	10-130	N/A	Hydrofluoroether, Hydrocarbons
GE Clean Cycle	50-140	>155	R245fa
GMK (Germany)	500-15,000	<300	GL160 (patented)
Infinity Turbine LLC	10-3000	80-140	R245fa, R-134a
LTi Reenergy	3	>160	N/A
Opcon	100-1600	55-250, >250	Ammonia
Orcan Energy GmbH	N/A	N/A	N/A
Ormat Technologies Inc.	200-70,000	150-300	n-pentane
PureCycle	280	91-149	R245fa
TAS Energy	500-5000	97-260	R134a, R234fa, R245fa
Tri-o-gen	60-165	>350	Toluene
Turboden	200-15,000	100-300	OMTS, SES36

The ORC market is currently growing rapidly. Fig. 2.17 (left) shows the total number of the ORC plants in operation and the total installed power worldwide in the period of 1984-2012. As it can be seen, the market has experienced an exponential growth during the last ten years of that period. Fig. 2.17 (right) also depicts the share of each heat source application in terms of the total number of units. It is obvious that the ORC is now a mature technology for waste heat recovery, geothermal and biomass applications. However, it is still being developed for solar energy applications.

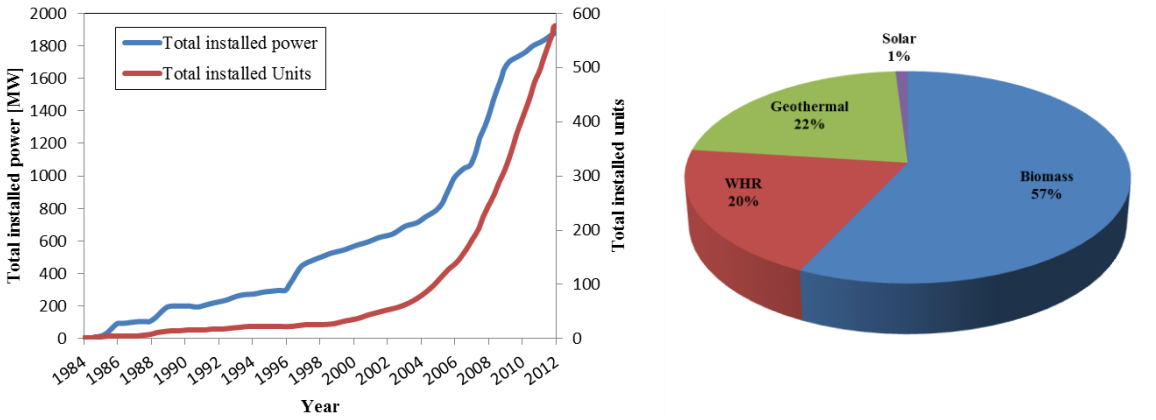

Figure 2.17 ORC market evolution (left) and share of each application based on number of units (right) [40]

2.8 Conclusion based on literature review

It is obvious from the literature review that the use of renewable energy sources in power generation is a promising way to alleviate the continuous increase in energy demand and mitigate the negative environmental impacts. From this review of the current commercial and research status of ORC technology, it is clear that there is a significant interest in the development of small-scale systems (less than 100 kW) for the conversion of solar energy, geothermal, biomass and waste heat into useful power. Although the large-scale ORC systems are successfully commercialized, small-scale ORCs, especially in solar applications, are still under development and at the laboratory demonstration level.

The literate review shows that the small-scale ORC is technologically feasible; however, it is difficult to compete with larger scale units due to its relatively high costs. Most of the work published in the literature deal with thermodynamic assessments, aiming to maximizing the plant efficiency or its power output. However, the traditional thermodynamic analysis alone cannot provide complete set of indications for the power system's overall assessment. Economic analysis of such systems, in the open literature, is still not sufficiently addressed. The combination of carrying out the thermodynamic performance analysis and cost estimation provides a powerful tool for designing such systems. This also requires including individual component sizing models.

There is a wide range of potential organic fluids that could be used in ORCs. Also, there are a number of selection criteria need to be satisfied. Although several studies have investigated the selection of the most appropriate working fluid, no single fluid has been identified as ultimately optimal for all ORCs. Therefore, working fluid selection remains one of the key aspects of any research project.

The literature review also reveals that the previous work in the small scale solar ORCs have mostly focused on the steady state simulation without considering the variation of the solar intensity. The effect of this variation during the day on the system performance is very important and needs further investigations.

The use of two renewable energy sources to drive an ORC system has also been scarcely investigated. Most of these few studies used solar and geothermal energy as the hybrid heat source. Integrating solar and biomass to power a small ORC unit is considered as innovative layout.

It is important to couple the simulation model with an optimisation strategy to arrive at optimal system design parameters. However, a major difficulty resides in the definition of a suitable objective function. Most of the studies on the optimization of ORCs were performed based on the thermodynamic performance (efficiency and power output) which is used as an objective function. There are a number of studies aimed to minimize the heat exchanger area per unit of power output in the optimization process. However, minimizing such the objective function does not lead to an accurate cost estimation. Therefore, the system should be optimized based on a criterion in which the trade-off between system performance and costs is considered.

The aims and objectives of this study are formulated as a result of the conducted literature review. In this research project, the task is to develop an accurate comprehensive mathematical simulation model in which both the thermal performance and economic feasibility of a 10 kW hybrid solar/biomass ORC system are evaluated over a wide range of operating conditions. A quasi-steady model of the innovative hybrid system is to be developed to evaluate the system performance over a day-long period for different annual seasons of the UK climatic conditions. The ORC model will be coupled with the GA

optimization method to obtain the optimal design parameters to provide better system performance at minimum costs.

Chapter 3 Thermodynamic Modelling of the Hybrid ORC System

In this Chapter, the design and operation principle of the hybrid solar/biomass ORC power system are described. The overall thermodynamic mathematical model of the proposed system is presented based on the mass and energy balance equations written for the main system components. Other models for heat exchangers sizing and global solar irradiance estimation are also described. Then, the solution procedures of the governing equations using the Thermolib toolbox in a MATLAB/Simulink® environment are presented. Finally, the validation of the simulation model results against theoretical and real data available in the open literature is discussed.

3.1 System description

Figure 3.1 illustrates the schematic diagram of the proposed ORC driven by a hybrid solar/biomass renewable energy heating source. The hybrid ORC system consists mainly of two circuits: solar/biomass heating circuit and organic fluid circuit. The key components of the system include solar collectors, biomass boiler, evaporator, expander, condenser and working fluid pump. Water is used as a heat transfer fluid (HTF) and is heated up to the desired temperature in the heating circuit using an array of evacuated tube solar collectors (ETCs). If the outlet temperature of the solar collector drops below the reference set-point temperature due to insufficient solar radiation during cloudy weathers or at night, the biomass boiler is used in order to maintain a constant hot water temperature supply.

The liquid organic fluid (state 1) is first pumped to a high pressure (state 2) in the working fluid pump. The high pressure fluid then passes through the evaporator where it absorbs heat from the hot water. During this process, the temperature of the working fluid is increased to its saturation temperature where it is fully converted to vapor (state 3). The vapour with high temperature and pressure then flows across the expander to produce

mechanical work which can be converted into electricity via a generator. The expanded working fluid (state 4) then passes through a condenser where heat is rejected to the cooling water. In this process, the working fluid is cooled down to a saturated vapour and then fully condensed (state 1). The liquid working fluid is then pumped again to repeat the cycle. The corresponding T-s diagram of the above described processes is shown in Fig. 3.2.

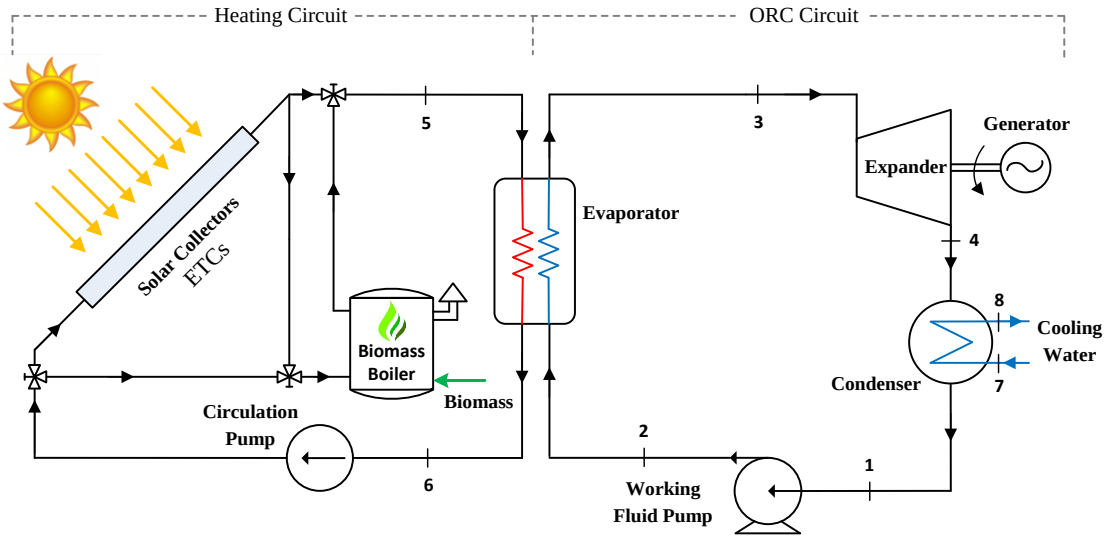

Figure 3.1 Schematic diagram of the hybrid ORC system

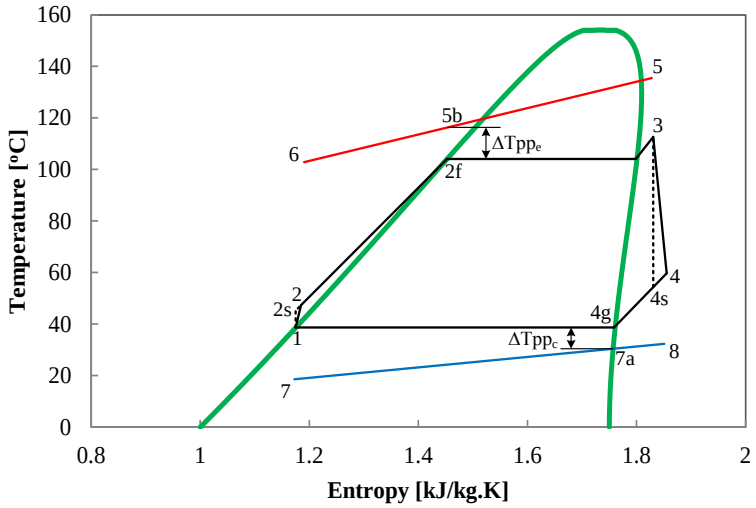

Figure 3.2 T-s diagram of the hybrid ORC system

3.2 Thermodynamic modelling

In order to derive the thermodynamic mathematical model for the whole system, each component in the system is considered as a control volume. The principles of mass and energy conservation are then applied to each control volume separately. The overall thermodynamic mathematical model of the proposed system is developed by interconnecting the sub-models for system components, in which the output of any component is considered as an input to the next one.

The following general assumptions are considered in the analysis of the overall system and its subsystems:

- All the components and processes are considered to be at steady state;
- The changes in kinetic and potential energy are not considered;
- The expander and pump are adiabatic with fixed isentropic efficiencies;
- The heat losses and pressure drop in all system components and piping are neglected.

Assumptions made about heat losses and pressure drop in all components of the system are necessary to reduce the complexity of its mathematical model.

The mass balance equation can be expressed as

$$\sum \dot{m}_{in} - \sum \dot{m}_{out} = 0 \tag{3.1}$$

The general energy balance equation, based on the first law of thermodynamics, can be written as follows:

$$\dot{Q}_{cv} - \dot{W}_{cv} + \sum \dot{m}_{in}\, h_{in} - \sum \dot{m}_{out}\, h_{out} = 0 \tag{3.2}$$

where $\dot{Q}_{cv}$ and $\dot{W}_{cv}$ represent the heat transfer into the control volume and work done by the control volume, respectively; and $\dot{m}$ and h represent the mass flow rate and the specific enthalpy of the streams crossing the control volume boundaries, respectively.

3.2.1 The pump model

The mechanical power required for the working fluid pump is calculated as

$$\dot{W}_{p,s} = \frac{\dot{m}_{wf} v_1 (P_2 - P_1)}{\eta_p} = \dot{m}_{wf}(h_2 - h_1) \tag{3.3}$$

where $\dot{m}_{wf}$ is the working fluid mass flow rate, v_1 is the working fluid specific volume at the pump inlet, η_p is the pump efficiency and P_1 and P_2 are the pressures of the working fluid at the pump inlet and outlet, respectively.

The pump electric consumed power can be calculated in terms of the electric motor efficiency, η_m, as

$$\dot{W}_p = \frac{\dot{W}_{p,s}}{\eta_m} \tag{3.4}$$

3.2.2 The evaporator model

The total heat transfer rate from the HTF to the working fluid in the evaporator is given by

$$\dot{Q}_e = \dot{m}_{wf}(h_3 - h_2) = \dot{m}_{htf} C_{p,htf} (T_5 - T_6) \tag{3.5}$$

where $\dot{m}_{htf}$ and $C_{p,htf}$ are the mass flow rate and specific heat of the hot water in the heating circuit and T_5 and T_6 are the temperatures of hot water streams at the inlet and outlet of the evaporator, respectively.

In the thermodynamic analysis and design, it is useful to introduce the pinch point temperature difference in the heat exchangers. The pinch point temperature difference in the evaporator is defined as the minimum temperature difference between the heat source and working fluid streams as shown in Fig. 3.2. It can be expressed as

$$\Delta T_{ppe} = T_{5b} - T_{2f} \tag{3.6}$$

3.2.3 The expander model

The working fluid vapour passes through the expander to generate mechanical power. The expander shaft output power is given by

$$\dot{W}_{t,s} = \dot{m}_{wf}(h_3 - h_{4s})\eta_t = \dot{m}_{wf}(h_3 - h_4) \quad (3.7)$$

where η_t is the expander isentropic efficiency. The subscripts 4s and 4 in the specific enthalpy denote to the ideal and actual conditions at the expander outlet, respectively.
The output electric power generated by the expander is expressed as

$$\dot{W}_t = \dot{W}_{t,s}.\eta_g \quad (3.8)$$

where η_g is the electric generator efficiency.

3.2.4 The condenser model

The exhaust vapour at the expander exit is directed to the condenser where it is converted to the liquid state by rejecting its heat to the cooling water.

The condenser heat transfer rate can be expressed as

$$\dot{Q}_c = \dot{m}_{wf}(h_4 - h_1) = \dot{m}_{cw}C_{p,cw}(T_8 - T_7) \quad (3.9)$$

where $\dot{m}_{cw}$ and $C_{p,cw}$ are the mass flow rate and specific heat of the cooling water, and T_7 and T_8 are the cooling water temperatures at the inlet and outlet of the condenser, respectively.

The pinch point temperature difference in the condenser, which is the minimum temperature difference between the cooling water and working fluid streams, can be given by

$$\Delta T_{ppc} = T_{4g} - T_{7a} \quad (3.10)$$

3.2.5 The solar collector model

Evacuated tube solar collectors (ETCs) are employed to collect the solar radiation due to their high performance and relatively low cost since complicated tracking systems are not required. This type of collectors can also achieve higher solar collecting temperatures and higher efficiency compared to flat plat collectors (FPCs) [104].

The total amount of solar energy available at the solar collector is expressed as

$$\dot{Q}_s = G_t \cdot A_{col} \tag{3.11}$$

G_t is the total solar irradiance hits the solar collector surface and A_{col} is the collector aperture area.

The useful heat absorbed by the HTF in the solar collector can be given by

$$\dot{Q}_{su} = G_t \cdot A_{col} \cdot \eta_{col} = \dot{m}_{htf} C_{p,htf} \left(T_{col,o} - T_{col,i}\right) \tag{3.12}$$

where η_{col} is the solar collector efficiency which can be expressed in terms of the solar irradiance, mean collector temperature, $T_{col,m}$, and ambient temperature, T_{amb}, as [104]

$$\eta_{col} = c_0 - c_1 \frac{\left(T_{col,m} - T_{amb}\right)}{G_t} - c_2 \frac{\left(T_{col,m} - T_{amb}\right)^2}{G_t} \tag{3.13}$$

Here c_0, $c_1$and c_2 are the efficiency equation constants for the solar collector. Table 3.1 presents the efficiency equation constants of the ETC from three different manufacturers for which calculations of the system performance have been carried out.

Table 3.1 The efficiency equation constants for different ETCs

Model/Manufacturer	$\boldsymbol{c_0}$ [-]	$\boldsymbol{c_1}$ [W/m^2 K]	$\boldsymbol{c_2}$ [W/m^2 K^2]	Ref.
LaZer2 / Solar UK	0.753	1.54	0.0099	[181]
VM 2-20 / Thermo technologies	0.81	1.23	0.0122	[181]
VR12 / ESTEC GmbH	0.825	0.91	0.6×10^{-3}	[164]

3.2.6 The biomass boiler model

The total heat of combustion provided by the biomass boiler is given in terms of the biomass fuel consumption and its lower heating value as

$$\dot{Q}_b = \dot{m}_{bf}.LHV_{bf} \tag{3.14}$$

where $\dot{m}_{bf}$ is the biomass fuel consumption and LHV_{bf} is the lower heating value of the biomass fuel.

The useful heat absorbed by the HTF in the biomass boiler is given by

$$\dot{Q}_{bu} = \dot{m}_{bf} \cdot LHV_{bf} \cdot \eta_b = \dot{m}_{htf} C_{p,htf} \left(T_{b,o} - T_{b,i}\right) \tag{3.15}$$

where η_b is the biomass boiler efficiency.

Then, the total useful heat absorbed by the HTF in the solar collector and biomass boiler can be given by

$$\dot{Q}_u = \dot{m}_{htf} C_{p,htf} (T_5 - T_6) \tag{3.16}$$

3.2.7 The system overall model

The global system model presents interconnection of all plant components in the calculation scheme. Several parameters are used in the evaluation of the system performance including the net power output, ORC efficiency and overall system efficiency. The net output power generated by the hybrid ORC system is calculated as

$$\dot{W}_{net} = \dot{W}_t - \dot{W}_p \tag{3.17}$$

The thermal efficiency of the ORC is the ratio of the net power output to the heat input in the evaporator. It can be expressed as

$$\eta_{ORC} = \frac{\dot{W}_{net}}{\dot{Q}_e} \tag{3.18}$$

The overall efficiency of the hybrid ORC system can be defined as follows

$$\eta_{sys} = \frac{\dot{W}_{net}}{\dot{Q}_s + \dot{Q}_b} \tag{3.19}$$

In addition to the system efficiency, which is used to evaluate the system from a thermodynamic point of view, other parameters are needed to be defined to provide more insight into the technical feasibility and economic competitiveness of the hybrid ORC system. The maximum operating pressure, required solar collector area, the total heat transfer surface area of the heat exchangers, the back work ratio (BWR) and the volume flow ratio (VFR) between the outlet and inlet of the expander are among the key parameters used in this study.

The back work ratio (BWR) is defined as the ratio between the pump consumed power and the expander output power as

$$BWR = \frac{\dot{W}_p}{\dot{W}_t} \tag{3.20}$$

The volume flow ratio (VFR) is defined as the ratio between the volume flow rates at the outlet and inlet of the expander. Increased VFR values are associated with large expander size [182]. Furthermore, lower VFR values ensure the higher isentropic expander efficiency. VFR should be less than 50 in order to achieve turbine isentropic efficiency higher than 80% [183].

$$VFR = \frac{\dot{V}_4}{\dot{V}_3} \tag{3.21}$$

3.2.8 Calculation of the heat exchangers' surface area

Plate heat exchangers (PHEs) with chevron plates provide a high degree of turbulence which results in high heat transfer coefficients and low fouling characteristics, permitting a very compact and lightweight design. PHEs can be easily disassembled for maintenance, cleaning or for modifying the heat transfer area by adding/removing thermal plates, making them an ideal choice for the evaporators and condensers of small scale power systems [184]. The geometrical configuration and specifications of the chevron type PHE are presented in Fig. 3.3 and Table 3.2.

Based on the variation of heat transfer coefficient caused by different phase states, the evaporator is divided into three zones, namely, economizer, evaporator and superheater, while the condenser is divided into two zones, namely, de-superheater and condenser. The logarithmic mean temperature difference (LMTD) approach is used in the analysis of the heat exchangers and for the calculation of the heat transfer area [185]. The heat transfer rate, $\dot{Q}$, in each zone of the heat exchanger is described as

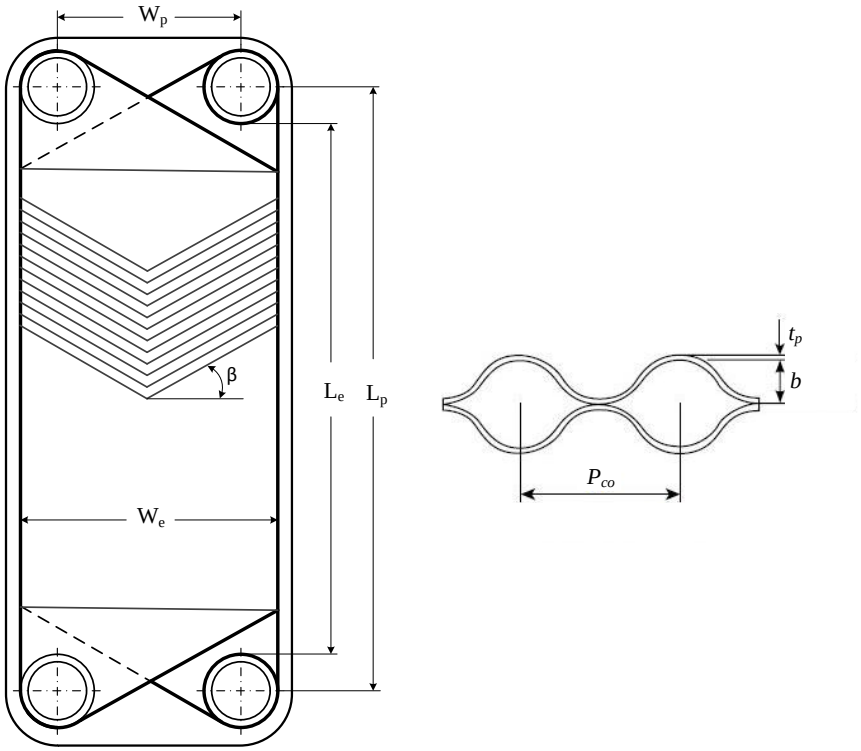

Figure 3.3 Basic geometry of a chevron plate

Table 3.2 Specifications of the plate heat exchanger

Parameter	Value
Effective length, L_e	0.350m
Effective width, W_e	0.110m
Corrugation pitch, P_{co}	0.007m
Corrugation depth, b	0.0025m
Plate thickness, t_p	0.0005m
Chevron angle, β	45^o
Enlargement factor, $\emptyset$	1.17
Plate material	Stainless steel

$$\dot{Q} = U.A.LMTD \tag{3.22}$$

where U and A are the overall heat transfer coefficient and the heat transfer area of each zone, respectively. The overall heat transfer coefficient is calculated as

$$\frac{1}{U} = \frac{1}{\alpha_{hs}} + \frac{t_p}{k_p} + \frac{1}{\alpha_{cs}} \tag{3.23}$$

where α_{hs} and α_{cs} are the convective heat transfer coefficients for the hot and cold sides in the heat exchanger, respectively. t_p and k_p are the thickness and thermal conductivity of the plate material, respectively. The log mean temperature difference, $LMTD$, is defined as follows

$$LMTD = \frac{\Delta T_{max} - \Delta T_{min}}{\ln \frac{\Delta T_{max}}{\Delta T_{min}}} \tag{3.24}$$

where ΔT_{max} and ΔT_{min} are the maximal and minimal temperature differences at each zone terminals of the heat exchangers, respectively.

3.2.8.1 Evaporator

The evaporator is divided into three zones, economizer (ec), evaporator (ev) and superheater (sh); and accordingly the working fluid is in single phase liquid, two phase liquid and vapour, and single phase vapour, respectively. Fig. 3.4 shows the temperature profiles of the heat source and working fluid with the three different zones. To estimate the heat transfer area of each zone in the evaporator, the overall heat transfer coefficients need to be determined along with the associated heat transfers rate and LMTDs for the different zones. The value of the overall heat transfer coefficient depends on the characteristics of the hot and cold streams and the heat exchanger geometry. The convective heat transfer coefficients for the hot and cold sides are calculated using empirical correlations based on the phase of the fluid in each zone.

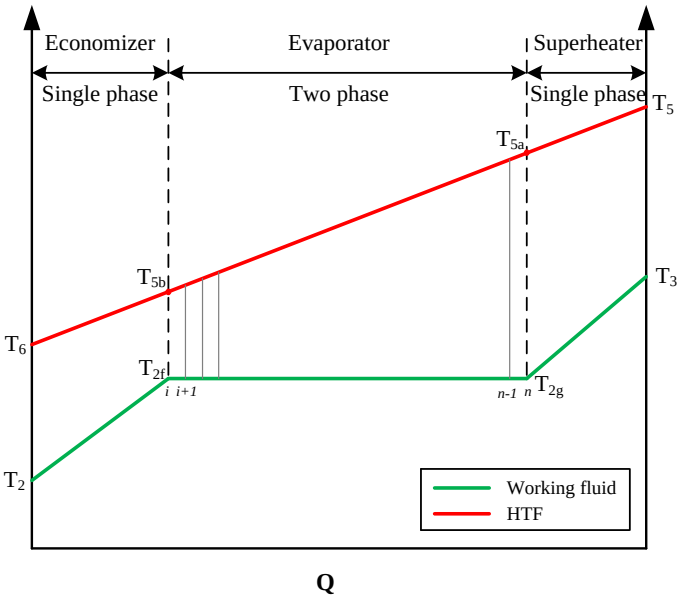

Figure 3.4 Temperature profiles in the evaporator

Single phase region

The working fluid is in a single phase state in both the economizer and superheater. The heat transfer rates in these two zones are calculated as

$$\dot{Q}_{ec} = \dot{m}_{wf}\left(h_{2f} - h_2\right) = \dot{m}_{htf} C_{p,htf} (T_{5b} - T_6) \tag{3.25}$$

$$\dot{Q}_{sh} = \dot{m}_{wf}\left(h_3 - h_{2g}\right) = \dot{m}_{htf} C_{p,htf} (T_5 - T_{5a}) \tag{3.26}$$

The log mean temperature difference for the economizer and superheater are given by

$$LMTD_{ec} = \frac{\left(T_{5b} - T_{2f}\right) - (T_6 - T_2)}{\ln \dfrac{\left(T_{5b} - T_{2f}\right)}{(T_6 - T_2)}} \tag{3.27}$$

$$LMTD_{sh} = \frac{(T_5 - T_3) - \left(T_{5a} - T_{2g}\right)}{\ln \dfrac{(T_5 - T_3)}{\left(T_{5a} - T_{2g}\right)}} \tag{3.28}$$

The overall heat transfer coefficient for the single phase region is calculated as

$$\frac{1}{U_{sp}} = \frac{1}{\alpha_{htf}} + \frac{t_p}{k_p} + \frac{1}{\alpha_{wf}} \tag{3.29}$$

The heat transfer coefficient for the hot water in a plate heat exchanger can be calculated using the correlation developed by Kim as [186, 187]

$$\alpha_{htf} = 0.295 \left(\frac{k}{D_h}\right) Re^{0.64} Pr^{0.32} \left(\frac{\pi}{2} - \beta\right) \tag{3.30}$$

where Re and Pr are Reynolds and Prandtl numbers, respectively. The Reynolds number is defined as

$$Re = \frac{G\, D_h}{\mu_l} \tag{3.31}$$

where G and D_h are the mass velocity and the hydraulic diameter of the flow channel, being expressed as

$$G = \frac{\dot{m}}{N_{ch} b\, W_e} \tag{3.32}$$

$$D_h = \frac{4 \times channel\ flow\ area}{wetted\ perimeter} = \frac{4b\, W_e}{2(b + W_e)\emptyset} = \frac{2b}{\emptyset}\ ;\ b \ll W_e \tag{3.33}$$

The single phase heat transfer coefficient for the working fluid in the plate heat exchanger is as given in [188]

$$\alpha_{wf,sp} = 0.2092 \left(\frac{k}{D_h}\right) Re^{0.78} Pr^{0.33} \left(\frac{\mu_m}{\mu_{wall}}\right)^{0.14} \tag{3.34}$$

where μ is the dynamic viscosity. The Subscripts *m* and *wall* correspond to bulk and wall conditions, respectively.

The required heat transfer surface area for the economizer, A_{ec}, and superheater, A_{sh}, can be obtained using Eq. 3.22.

Two phase region

In the two phase region (evaporation process), the working fluid properties varies dramatically with the dryness fraction variation. Therefore, the two phase region is discretized and divided into a number of sections (n) with relatively small areas in which the thermodynamic properties in each section are assumed to be constant and the variation in the temperature difference is linear. The discretized profile of the two phase region is illustrated in Fig. 3.4. The total area of the two phase zone is then the sum of all n sections. The heat balance of each section in the two phase zone is accordingly given by

$$\dot{Q}_{ev,i} = \dot{m}_{wf}(h_{i+1} - h_i) = \dot{m}_{htf} C_{p,htf,i}(T_{i+1} - T_i) \tag{3.35}$$

The log mean temperature difference for each section is calculated as

$$LMTD_{ev,i} = \frac{\left(T_{htf,i+1} - T_{wf,i+1}\right) - \left(T_{htf,i} - T_{wf,i}\right)}{\ln \frac{\left(T_{htf,i+1} - T_{wf,i+1}\right)}{\left(T_{htf,i} - T_{wf,i}\right)}} \tag{3.36}$$

The two phase overall heat transfer coefficient for a single discretized section is given by

$$\frac{1}{U_{tp,i}} = \frac{1}{\alpha_{htf,i}} + \frac{t_p}{k_p} + \frac{1}{\alpha_{wf,i}} \tag{3.37}$$

The heat transfer coefficient for the working fluid in each section of the two phase region can be determined using the following relation [189]

$$Nu_{tp,i} = \frac{\alpha_{tp,i}\, D_h}{k_l} = Ge_1 Re_{eq,i}^{Ge_2} Bo_{eq,i}^{0.3} Pr_l^{0.4} \tag{3.38}$$

where Ge_1 and Ge_2 are coefficients depend on the heat exchanger geometrical parameters. These coefficients are defined as

$$Ge_1 = 2.81 \left(\frac{p_{co}}{D_h}\right)^{-0.041} \left(\frac{\pi}{2} - \beta\right)^{-2.83} \tag{3.39}$$

$$Ge_2 = 0.746 \left(\frac{p_{co}}{D_h}\right)^{-0.082} \left(\frac{\pi}{2} - \beta\right)^{0.61} \tag{3.40}$$

$Re_{eq,i}$ and $Bo_{eq,i}$ are the equivalent Reynolds and Boiling numbers which are given by

$$Re_{eq,i} = \frac{G_{eq,i} D_h}{\mu_l} \tag{3.41}$$

$$Bo_{eq,i} = \frac{q''}{G_{eq,i} h_{fg}} \tag{3.42}$$

where q'' and h_{fg} are the heat flux and latent heat of vaporization, respectively. $G_{eq,i}$ is the equivalent mass flux which is given by

$$G_{eq,i} = G \left[1 - x_i + x_i \left(\frac{\rho_l}{\rho_v}\right)^{0.5}\right] \tag{3.43}$$

Here x_i is the vapour quality while ρ_l and ρ_v are the liquid and vapour densities. The heat transfer coefficient for the hot water side is estimated using Eq. 3.30

The heat transfer area for the two phase region is then calculated as

$$A_{ev} = \sum_{i=1}^{n} \frac{Q_{ev,i}}{U_{tp,i} LMTD_{ev,i}} \tag{3.44}$$

The total area of the evaporator can be obtained as

$$A_e = A_{ec} + A_{ev} + A_{sh} \tag{3.45}$$

3.2.8.2 Condenser

The condenser is treated exactly in the same way as the evaporator. It is divided into two zones, namely desuperheater (dsh) and condenser (con) as shown in Fig. 3.5. The working fluid in the desuperheator is in single phase vapour whilst in the condenser is in two phase vapour and liquid. The heat transfer correlations for the working fluid in the single phase region are exactly the same as in the evaporator model. However, different correlations are employed for the two phase region.

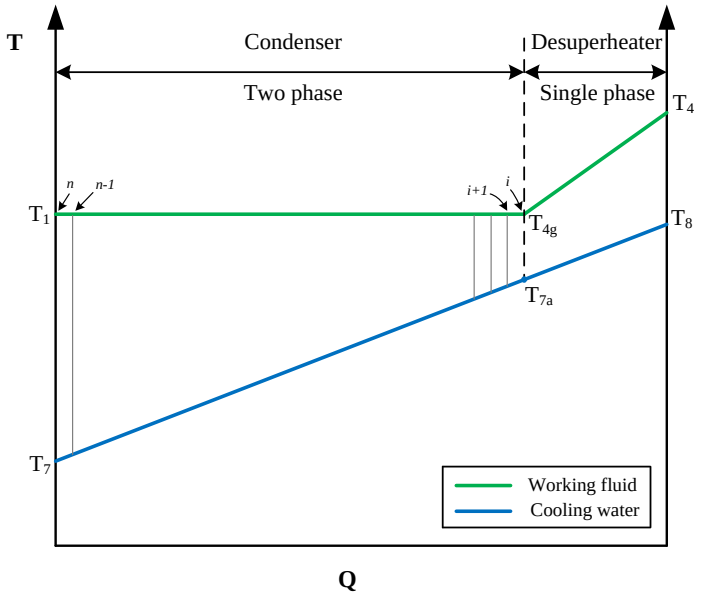

Figure 3.5 Temperature profiles in the condenser

The heat transfer rate in the single phase region (desuperheater) is given by

$$\dot{Q}_{dsh} = \dot{m}_{wf}\left(h_4 - h_{4g}\right) = \dot{m}_{cw}C_{p,cw}(T_8 - T_{7a}) \tag{3.46}$$

The log mean temperature difference for the desuperheater is given by

$$LMTD_{dsh} = \frac{(T_4 - T_8) - \left(T_{4g} - T_{7a}\right)}{\ln\dfrac{(T_4 - T_8)}{\left(T_{4g} - T_{7a}\right)}} \tag{3.47}$$

The heat transfer area of the desuperheater, A_{dsh}, is calculated using Eq. 3.22.

For the two phase region (condensation), the heat transfer coefficient for the working fluid in each section is expressed as [190]

$$Nu_{tp,i} = Ge_3 Re_{eq,i}^{Ge_4} Pr_l^{1/3} \tag{3.48}$$

where $Re_{eq,i}$ is defined as before; and Ge_3 and Ge_4 are expressed as follows

$$Ge_3 = 11.22\left(\frac{p_{co}}{D_h}\right)^{-2.83}\left(\frac{\pi}{2} - \beta\right)^{-4.5} \tag{3.49}$$

$$Ge_4 = 2.81\left(\frac{p_{co}}{D_h}\right)^{0.23}\left(\frac{\pi}{2}-\beta\right)^{1.48} \tag{3.50}$$

The heat transfer coefficient for the cooling water side in the condenser is estimated using Eq. 3.30.

The total heat transfer area of the condenser can be obtained as follows

$$A_c = A_{dsh} + A_{con} \tag{3.51}$$

3.2.9 The global solar radiation model

In this section, a global solar model is implemented in Simulink environment and this predicts the value of solar irradiance for different times in the year for the studied location. The total solar irradiance incident on an arbitrary tilted surface depends on a number of factors including location, time of the day and time of the year. In this work, the solar irradiance is estimated using the clear sky model described in [191]. The total solar irradiance, available on a tilted surface and in a particular location, is estimated as the sum of three components consisting of beam, diffused and reflected radiation as

$$G_t = G_b + G_d + G_r \tag{3.52}$$

where G_b, G_d and G_r are the beam, diffused and reflected radiations on a tilted surface. The total beam radiation on a tilted surface can be calculated as follows

$$G_b = G_o \cdot \tau_b \cdot R_b \tag{3.53}$$

where G_o is the solar radiation incident on a horizontal plane outside of the atmosphere, τ_b is the atmospheric transmittance for beam radiation and R_b a geometric factor defined as the ratio of the beam radiation on a tilted surface to that on a horizontal surface.

$$G_o = G_{sc}\left(1 + 0.033\cos\frac{360n}{365}\right)\cos\theta_z \tag{3.54}$$

Here G_{sc} is the solar constant (1367 W/m^2), n is the day of the year ($1 \leq n \leq 365$) and θ_z is the zenith angle. The atmospheric transmittance for beam radiation is given by

$$\tau_b = a_0 + a_1 exp(-k/\cos\theta_z) \tag{3.55}$$

where a_0, a_1 and k are coefficients depending on the sky visibility and location altitude. The values of these coefficients for the standard atmosphere with 25 km visibility and altitudes of up to 2.5 km can be obtained from the following relations

$$a_0 = r_0[0.4237 - 0.00821(6 - Z)^2] \tag{3.56}$$

$$a_1 = r_1[0.5055 - 0.00595(6.5 - Z)^2] \tag{3.57}$$

$$k = r_k[0.2711 - 0.01858(2.5 - Z)^2] \tag{3.58}$$

where Z is the altitude of the observer in kilometres and r_0, r_1 and r_k are correction factors depending on the type of climate. Values of factors r_0, r_1 and r_k are defined for a midlatitude summer climate as 0.97, 0.99 and 1.02, respectively, [191]. The geometric factor is defined as

$$R_b = \frac{\cos\theta}{\cos\theta_z} \tag{3.59}$$

Here θ is the beam angle of incidence. The total diffused radiation on a tilted surface can be given by

$$G_d = G_o \tau_d \left(\frac{1 + \cos\beta}{2}\right) \tag{3.60}$$

where τ_d is the atmospheric transmittance for diffused radiation and β is the inclination angle of the solar collector. The atmospheric transmittance for the diffused radiation is estimated as

$$\tau_d = 0.271 - 0.294\tau_b \tag{3.61}$$

The total reflected radiation on a tilted surface is calculated as

$$G_r = G_o(\tau_b + \tau_d)\rho_g \left(\frac{1 - \cos\beta}{2}\right) \tag{3.62}$$

where ρ_g is the ground reflectance. The value of ρ_g is approximately 0.2 for grass or concrete grounds and about 0.7 for snow-covered ground [192].

3.3 Simulation procedure

3.3.1 The simulation tool

The simulation software used to model the performance of the current small-scale hybrid ORC power system is called Thermolib 5.2 toolbox which works in a MATLAB/Simulink® environment [193]. This toolbox is developed by EUtech Scientific Engineering GmbH, Germany [194] to design, optimize and dynamically simulate the behaviour of complex thermodynamic systems with a friendly user-interface package. It is dedicated to model various thermodynamic applications such as HVAC systems, power generation, heat pump and refrigeration systems, chemical reaction and fuel cell systems and many more.

The toolbox provides a Simulink blockset for system simulations and a set of MATLAB command line functions for thermodynamic calculations and balancing of the simulated models. The blockset includes Simulink blocks for numerous components, stored as icons in a comprehensive visual Simulink library, for building an entire thermodynamic model made of pipes, pumps, compressors, turbines, valves, heat exchangers, tanks, chemical reactors, burners, fuel cell stacks, etc. This visual library enables the user to simply construct different configurations by just drag-and-drop the required icon (component). By double clicking on each block, a dialog box is opened and all the required data and parameters for the component can be easily entered. In addition, the package enables designers to perform different modifications of the existing components or to develop a conceptual design for new ones with the aid of Simulink. This advantage enables the user to perform further calculations which cannot be directly modelled using the existing Thermolib blocks such as the component detailed geometrical design and sizing.

Thermolib also provides an extendable thermo-physical properties database. This database contains many pure substances and mixtures used in the thermodynamic systems. The thermo-physical database is derived from the JANAF tables in the NASA polynomial representation and can be easily extended by the user. Thereby Thermolib is not limited by ideal gas assumptions and can also handle mixtures of reactive multi-species multi-phase mixtures. The real gas behaviour can be calculated using the Peng-Robinson Equation of State. This allows the Thermolib model to provide a good accuracy near the critical point and near condensation, particularly for calculations of the compressibility factor and liquid density. It can also handle general flash calculations such as the temperature glide of mixtures. For precise calculations involving water and steam, particularly in power plant models, the add-on IAPWS-IF97 formulation of thermodynamic properties is used.

3.3.2 The simulation model developed

The set of the governing equations described in section 3.2 for the hybrid ORC power system were solved using the Thermolib 5.2 toolbox in a MATLAB/Simulink® environment. In order to simulate and predict the overall performance of the hybrid ORC power system, the Thermolib model has been built as a closed loop to represent the real ORC system as shown in Fig. 3.6. In this model, Thermolib blocks that represent the models of the different system components are connected to each other in an appropriate order via signals. These signals contain the required parameters and fluid properties that pre-calculated from a particular block to perform the next block calculations in the system. The working fluid properties were evaluated using the built-in thermo-physical properties database of Thermolib based on the real gas behaviour of Peng-Robinson Equation of State. The detailed Thermolib models for the solar/biomass driven ORC system are further illustrated in Figures 3.7, 3.8 and 3.9.

The heat source model is presented in Fig. 3.7 which used to calculate the total heat energy from both the solar collector and biomass boiler. The solar irradiance is firstly calculated using the global solar radiation model (the first block in Fig. 3.7) which is presented in Section 3.2.9. This model can also predict the solar radiation during a day-long period from sunrise to sunset. The calculated value of the solar radiation is then used as an input to the next block, which includes the ETC and biomass boiler models. This

block is generally used to calculate the total useful heat provided by both the ETC and biomass boiler that is transferred to the working fluid in the ORC. Other parameters such as $\dot{m}_{htf}$, $\dot{m}_{bf}$, A_{col}, η_{col}, $T_{col,o}$ and $T_{b,o}$ are also calculated in this block. The ETC and biomass Simulink models used to carry out the above calculations are presented in Fig. 3.8. The first block to the left in this Figure is used in case of the solar mode operation whilst the two blocks to the right are used in case of the hybrid solar/biomass operation.

The heat exchangers sizing calculations have been modelled using Simulink. Fig. 3.9 shows the evaporator and condenser sizing Simulink models. In these two models, the variations of the heat transfer coefficients, heat transfer rates and log mean temperature differences in the different zones of the evaporator and condenser are evaluated. The total required heat transfer area for both the evaporator and condenser are then calculated. A flow chart, describing the overall calculation procedure in the Thermolib model, is presented in Fig. 3.10.

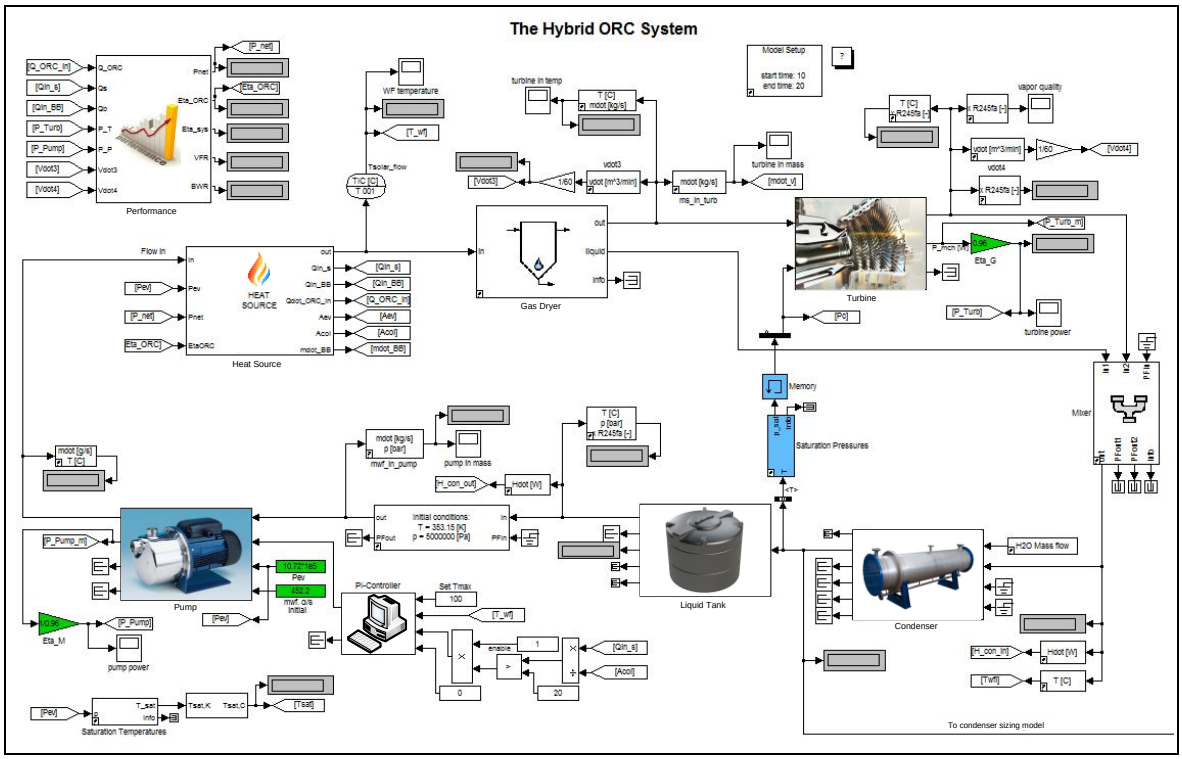

Figure 3.6 The developed Thermolib model of the hybrid ORC system

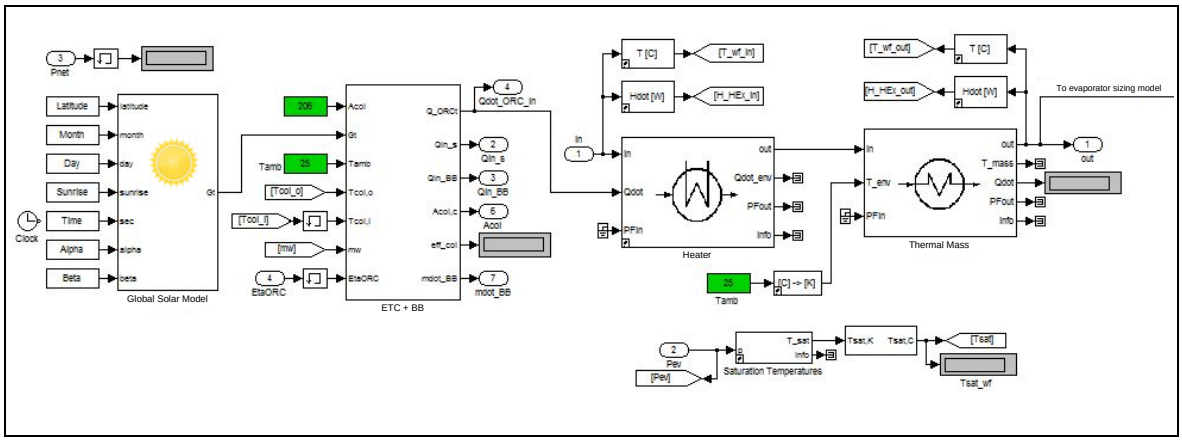

Figure 3.7 The heat source model of the hybrid ORC system

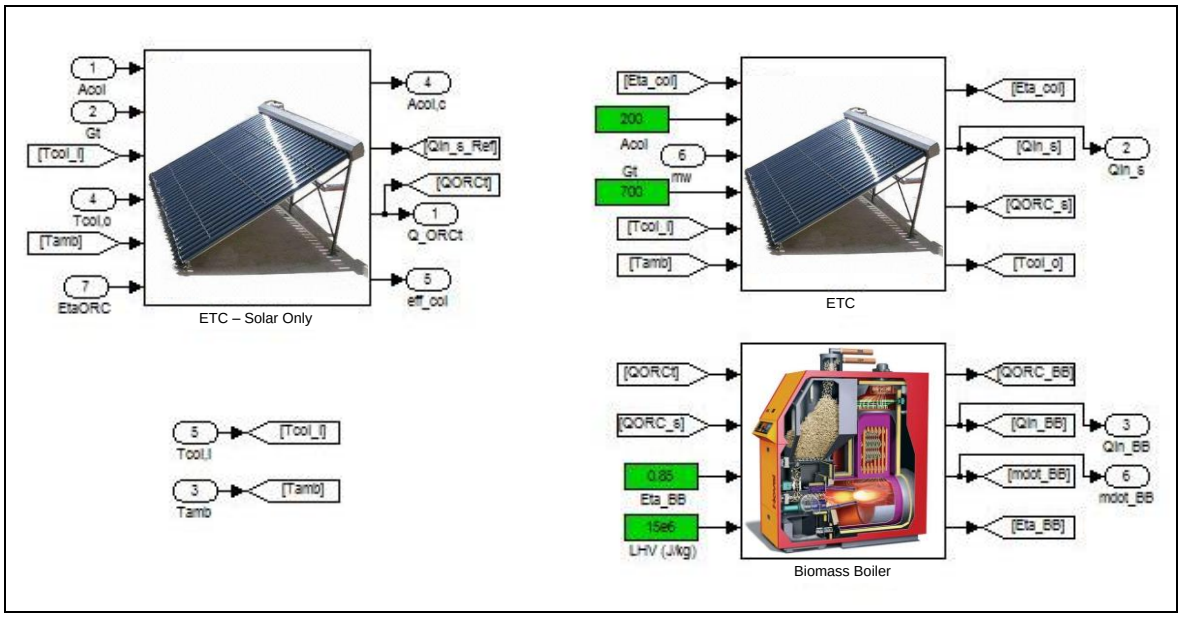

Figure 3.8 The ETC and biomass boiler model

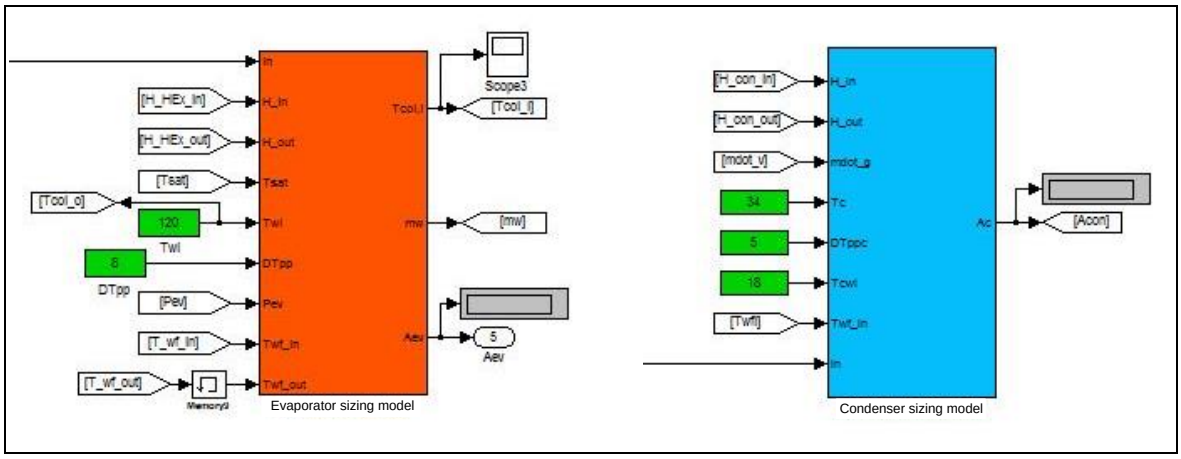

Figure 3.9 The evaporator and condenser sizing models

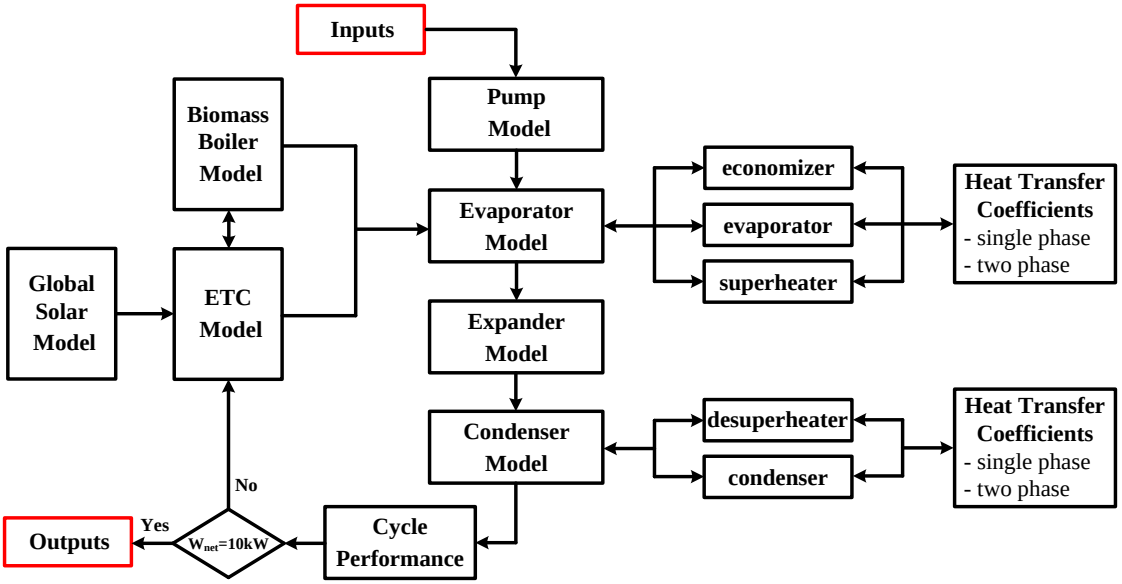

Figure 3.10 Flow chart of the overall calculation procedure in the Thermolib model

3.4 Validation of the simulation model

The most important concern in numerical modelling is the accuracy of the model in predicting the physical behaviour of the real system. This section validates the developed Thermolib simulation model against data available in the open literature. The comparison between the current model results and published theoretical and experimental data was carried out in terms of different operating parameters and performance indicators of the ORC system. This includes operating cycle temperatures, mass flow rates, heat transfer rate, pump power, turbine power, net output power and system efficiency.

3.4.1 Validation against the theoretical case study

This section concerns with validation of the simulation model against a theoretical study conducted by Fu et al. [195, 196]. In this study, the effects of off-design heat source temperature and mass flow rate on the heat transfer characteristics and system performance of a 250 kW ORC system was theoretically investigated. In addition, the evaporation temperature and pinch point temperature difference were examined at off-design conditions for the proposed ORC system.

3.4.1.1 System description and analysis

The ORC system is schematically presented in Fig. 3.11. The system consists of a pump, preheater, evaporator, turbine-generator and condenser. Shell-and-tube type heat exchangers were used for the preheater, evaporator and condenser. Hot water as a heat source was supplied by a boiler with a maximum thermal capacity of 3788 kW whereas cold water was provided from a cooling tower with a maximum capacity of 3860 kW. For the ORC, R245fa was used as a working fluid. The working fluid leaving the evaporator and entering the turbine (state 4) is at saturated vapour condition. Fig. 3.12 illustrates the T-s diagram of the ORC system.

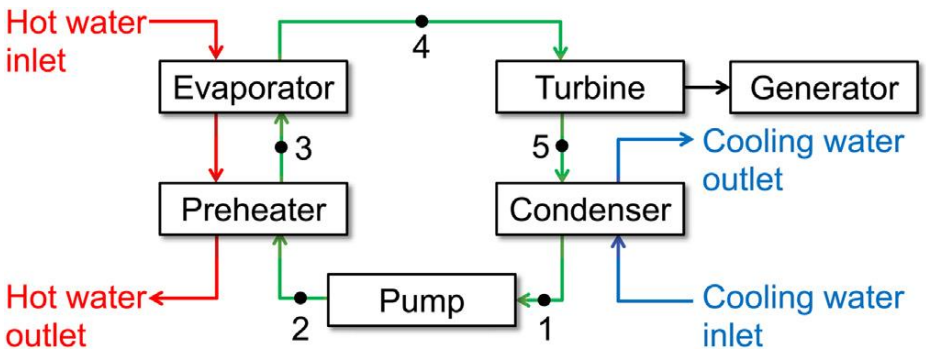

Figure 3.11 Schematic representation of the ORC system [196]

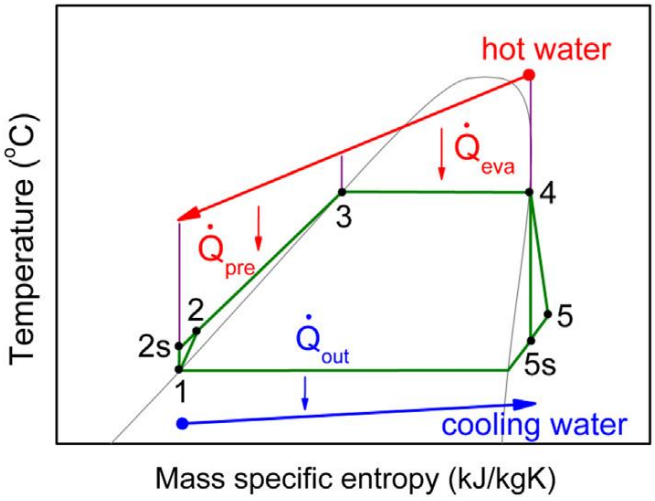

Figure 3.12 T-s diagram of the ORC system [196]

The following assumptions were made during the analysis of the ORC system [195]:

- Each component in the system is at steady state condition;
- The pressure drop in the heat exchangers is neglected;
- The heat losses in all system components and pipes are not considered;
- The pump, turbine and generator have constant efficiencies of 90%, 80% and 90%, respectively.

Based on the abovementioned assumptions, the mathematical models for the system components as well as for the overall system are briefly presented below. The pump consumed power and turbine electrical output power can be, respectively, given by

$$\dot{W}_p = \dot{m}_{wf}(h_{2s} - h_1)/\eta_p \tag{3.63}$$

$$\dot{W}_t = \dot{m}_{wf}(h_4 - h_{5s})\eta_t\eta_g \tag{3.64}$$

where $\dot{m}_{wf}$ is the mass flow rate of R245fa, h is the specific enthalpy and η_p, η_t and η_g are the pump, turbine and generator efficiencies, respectively. The net output power is expressed as

$$\dot{W}_{net} = \dot{W}_t - \dot{W}_p \tag{3.65}$$

The total heat transfer rate in the preheater and evaporator is given by

$$\dot{Q}_{tot} = \dot{Q}_{pre} + \dot{Q}_{ev} = \dot{m}_{wf}(h_3 - h_2) + \dot{m}_{wf}(h_4 - h_3) \tag{3.66}$$

The system thermal efficiency can be obtained from the following equations

$$\eta_{sys} = \frac{\dot{W}_{net}}{\dot{Q}_{tot}} \tag{3.67}$$

3.4.1.2 Model validation

A simulation model was developed for the ORC system described above using Thermolib 5.2 toolbox. The comparisons between the present model results and those obtained from Fu et al. [195] were performed by setting the same operating conditions and using the same working fluid, i.e., R245fa. The mass flow rate of R245fa was kept at a fixed value of 11.85 kg/s. The study was conducted at constant heat source and condensation temperatures of 133.9 ^{o}C and 39 ^{o}C, respectively. The comparisons were carried out for a range of the heat source mass flow rates of 10.0 - 27.4 kg/s. Saturated liquid and saturated vapour conditions were assumed for the working fluid at the outlet of the preheater (state 3) and evaporator (state 4), respectively. Therefore, different evaporation pressures had to be set for each value of the off-design heat source mass flow rate to meet these conditions. Fig. 3.13 shows the evaporation pressure and corresponding evaporation temperature for the studied range of the heat source mass flow rates.

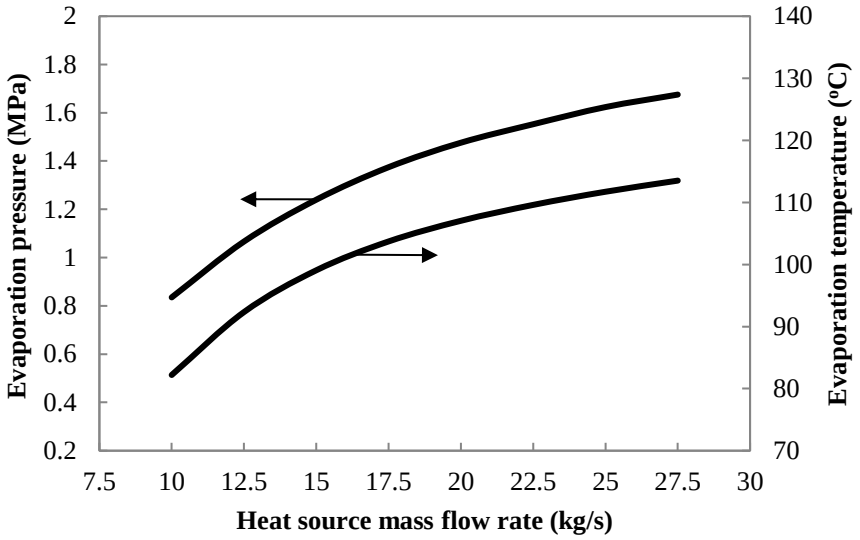

Figure 3.13 Evaporation pressure and temperature at different heat source mass flow rates

The present model results and those obtained from [195] for the variations of the pump consumed power, turbine output power, net output power and system efficiency, respectively, with the heat source mass flow rate are shown in Figs. 3.14 to 3.17. It can be seen that the predicted results from the present model and those published in [195] are in very good agreement in terms of trend and magnitude. The maximum relative deviations between the two curves are 6.53%, 2.58%, 2.89% and 2.33%, respectively, for the pump consumed power, turbine output power, net output power and system efficiency. This demonstrates that the developed model can accurately predict the performance of the proposed hybrid ORC system. The relative deviation is calculated using the following formula

$$DEV = \left| \frac{X_{pm} - X_{ref}}{X_{ref}} \right| \times 100 \tag{3.68}$$

Here X_{pm} denotes to any particular parameter obtained from the present model and X_{ref} is the reference value of the same parameter obtained from the literature.

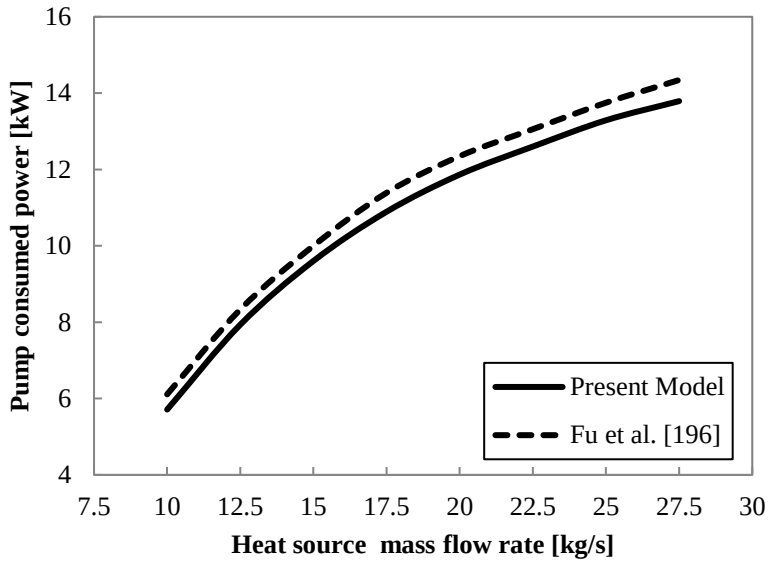

Figure 3.14 Variation of pump consumed power with heat source mass flow rate

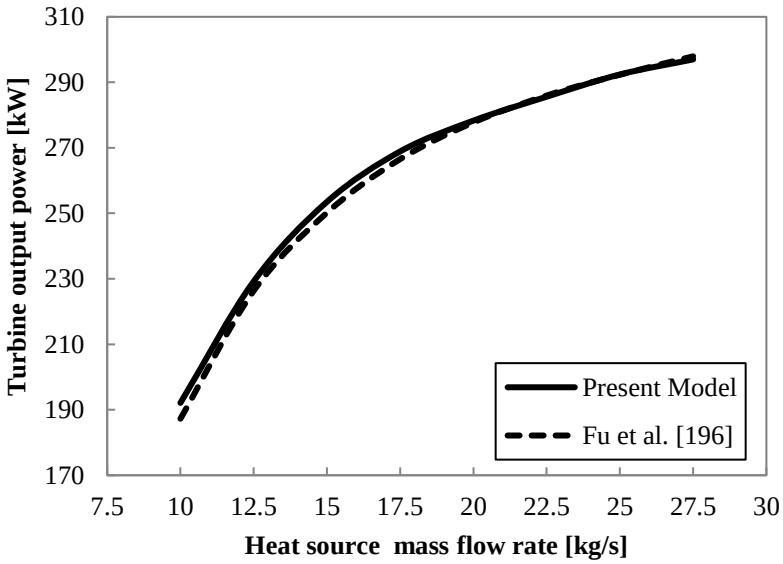

Figure 3.15 Variation of turbine output power with heat source mass flow rate

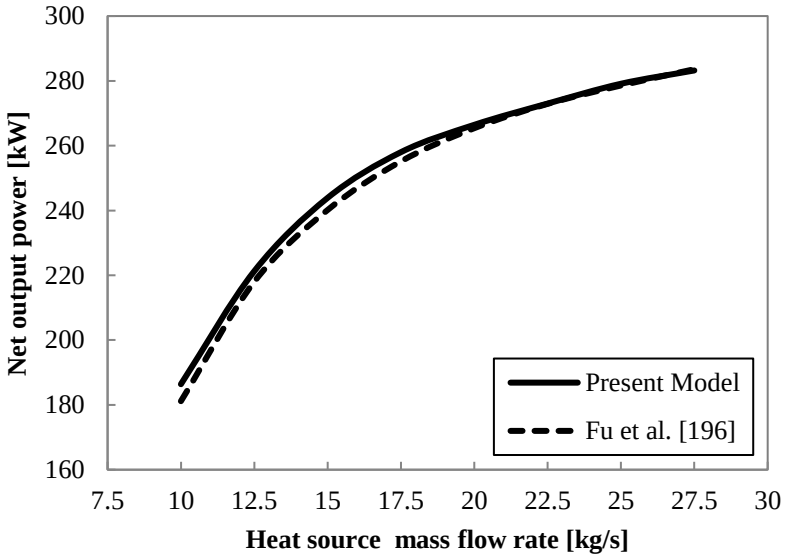

Figure 3.16 Variation of net output power with heat source mass flow rate

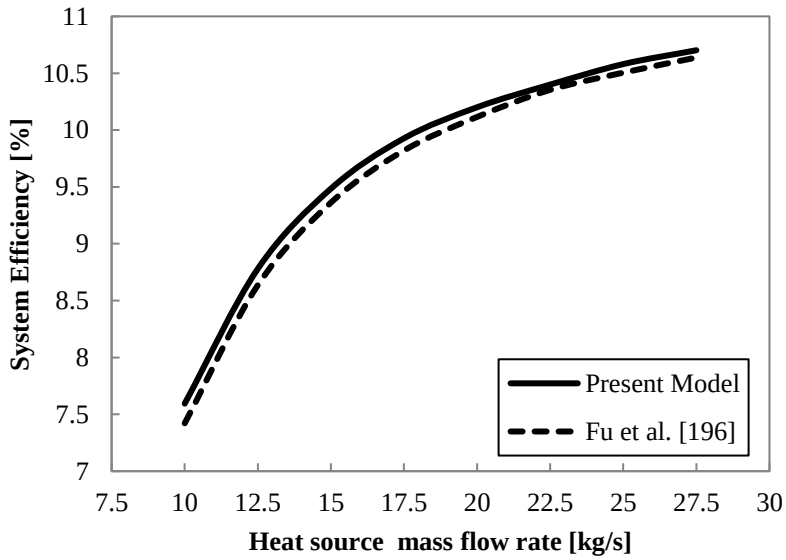

Figure 3.17 Variation of system efficiency with heat source mass flow rate

3.4.2 Validation against experimental data of Chena geothermal power plant

This section focuses on validation of the simulation model against real data of an existing ORC power generation plant. Chena is a small rural town in Alaska, USA. It has hot springs located approximately 96 km east-northeast of Fairbanks, Alaska, at an elevation of about 367 m [197]. It has been used as a recreational facility since its discovery in 1905. According to a report prepared for Alaska Energy Authority in 2007 [197], the cost of electricity in rural Alaska was among the highest in the USA with electricity was mainly supplied by Diesel generators. It was also reported that $365,000 was spent on fuel alone in 2005 for electricity generation at Chena. In 2006, the cost of electricity generation from the Diesel generators was at a rate of 30¢ per kWh [198]. This high cost of power generation was the main motivation for Chena to search for alternative sources of power supply, resulting in the adoption of a plan to utilize the geothermal resources available in the area to drive an ORC power plant.

Among several suppliers, United Technologies Corporation (UTC) was selected to provide the ORC system. Two similar 200 kW ORC units have been installed at Chena hot springs in July 2006 and December 2006, respectively. The Chena plant is the first geothermal power plant installed in the State of Alaska. The successful implementation of this project had resulted in a dramatic reduction in the electricity cost at Chena from 30¢ per kWh to 5¢ per kWh [197].

3.4.2.1 Power plant description

Fig. 3.18 shows the two ORC units installed at Chena hot springs. Each unit of Chena ORC power plant was designed to produce a net electrical output power of 200 kW from a low temperature geothermal heat source. The ORC consists of four main components, namely pump, preheater/evaporator, turbine and condenser. The plant uses R134a as the working fluid. The T-s diagram describing the cycle processes is shown in Fig. 3.19. At the preheater/evaporator, 33.39 kg/s of hot water at 73.33 ^{o}C (point A) enters the unit to preheat and then evaporate the working fluid (process 4-1) before it leaves at 54.44 ^{o}C (point B). The high pressure working fluid is expanded in the turbine to produce mechanical work (process 1-2) before it is de-superheated and condensed using cooling

water at 4.44 ^{o}C (point C) in the condenser (process 2-3). The liquid working fluid is pumped again to the preheater/evaporator (process 3-4) to repeat the cycle.

Figure 3.18 Chena geothermal ORC power plant [198]

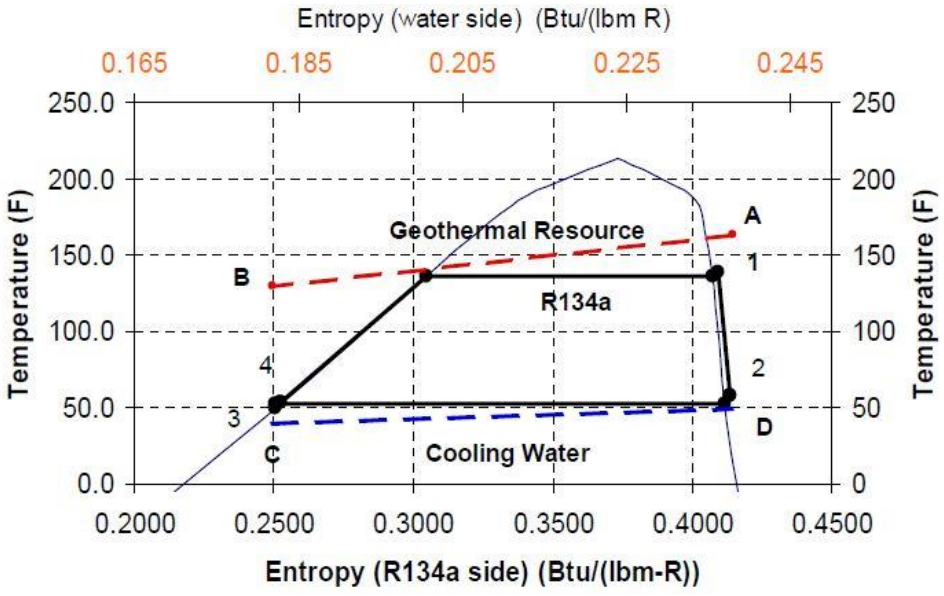

Figure 3.19 T-s diagram of Chena ORC power plant [197]

3.4.1.2 Model validation

In this section, the developed Thermolib model results are validated against the real data of Chena geothermal power plant. The validation was carried out by comparing the developed model results with the real plant data at the nominal design point as shown in Tables 3.3 and 3.4 [197, 199]. From Table 3.4, it can be seen that the results obtained from the developed model are in very good agreement with the real plant data. The maximum deviation between the developed model results and real plant data is less than 1%. This demonstrates that the developed model accurately describes the processes taking place in the real ORC plant as well as its overall system performance.

Table 3.3 Chena power plant operating conditions used in the simulation model

Parameter	Value
Working fluid	R134a
Geothermal water source temperature , ^{o}C	73.33
Geothermal water mass flow rate, kg/s	33.39
Heat added in the evaporator, kW	2580
Cooling water source temperature, ^{o}C	4.44
Turbine inlet pressure, bar	16
Turbine outlet pressure, bar	4.39
Evaporator outlet temperature, ^{o}C	57.78
Condensation temperature, ^{o}C	11.67
Pump power, kW	40
Turbine efficiency, %	80

Table 3.4 Comparison of the simulation model results with real data of Chena power plant

Parameter	Real plant data	Model results	DEV, %
Geothermal water outlet temperature, ^{o}C	54.44	54.8	0.81
Cooling water outlet temperature , ^{o}C	10	9.96	0.40
Cooling water mass flow rate, kg/s	101.68	101.30	0.37
Working fluid mass flow rate, kg/s	12.17	12.24	0.58
Pump outlet temperature, ^{o}C	12.22	12.21	0.08
Heat rejected in the condenser, kW	2360	2337	0.97
Turbine gross electric power, kW	250	251.5	0.60
Net output power, kW	210	211.5	0.71
Thermal efficiency, %	8.14	8.20	0.74

3.5 Summary

The design and operation principle of the hybrid solar/biomass ORC power system were described in this Chapter. The overall thermodynamic mathematical model of the proposed system as well as other models for the heat exchangers sizing and global solar irradiance estimation were presented. The simulation model of the proposed hybrid ORC system was developed using Thermolib 5.2 toolbox in a MATLAB/Simulink® environment. In general, comparisons of the model results with theoretical and experimental data presented in the open literature demonstrate that the accuracy of the developed simulation model is sufficiently high to be used with confidence for further investigations of the proposed system in order to improve its overall performance.

Chapter 4 Thermodynamic Performance Results of the Hybrid ORC System

This Chapter presents the overall thermodynamic performance results of the hybrid ORC system. First, the selection procedure of the optimal working fluid for the proposed hybrid system is presented. The hybrid ORC is sized based on the selected working fluids for fixed net power output. A detailed parametric analysis is then conducted to assess the ORC performance under different operating conditions. The effects of the evaporation pressure, condensation temperature, pinch point temperature difference in the evaporator and condenser, expander isentropic efficiency and pump isentropic efficiency are discussed.

4.1 Description of the adopted location

The city of Newcastle upon Tyne is located in the north east of the UK (54^{o} 59' N latitude, 1^{o} 37' W longitude) and it is 14 km from the east coast of the UK. The climate in this location is relatively cold with an ambient temperature ranging between -5 ^{o}C and 30 ^{o}C [200]. This city was selected as a location to evaluate the thermo-economic performance of the hybrid ORC system.

Measurements of the global irradiance at Newcastle upon Tyne have been carried out by Craggs et al. [201] on vertical and horizontal surfaces for two summers (1994, 1995) and two winters (1993, 1994). It has been reported that the maximum observed global irradiance values for the two summers are in the range of 636-703 W/m^2 and 913-978 W/m^2 for vertical and horizontal surfaces, respectively. In the winter, these values are 768-787 W/m^2 and 207-267 W/m^2 for vertical and horizontal surfaces, respectively.

4.2 Working fluid selection

The overall ORC system performance and economics are significantly influenced by the thermo-physical properties of the working fluid used. In order to select the optimal working fluid, appropriate criteria should however be considered. In this work, the selection procedure is conducted based on various evaluation criteria including the system thermodynamic performance, cost, technical, safety and environmental considerations. As mentioned earlier in Chapter two, fluids can generally be classified based on their critical temperature into low-temperature (< 150 ^{o}C) and medium-to-high temperature applications (> 150 ^{o}C). Fluids with critical temperatures of about 150 ^{o}C and less fall in the low-temperature category [78].

Based on the literature review conducted in Chapter two, the most common fluids that have previously been considered in the screening studies for low-temperature applications or fluids that are used in the commercial ORC power plants are listed in Table 4.1. However, this list can be reduced by firstly eliminating all the fluids with non-zero ODP or with GWP values higher than 1500. Then, fluids having a critical temperature below 80 ^{o}C are discarded due to their very limited evaporation temperature in the subcritical cycles. Also, to avoid the possibility of expander blades damage caused by wet fluids, dry and isentropic fluids are only considered. The first screening resulted in emerging four working fluids as potential candidates which are presented along with their thermodynamic, safety and environmental properties in Table 4.2. These working fluids are then comparatively assessed to obtain the most appropriate fluid for the current ORC system.

Several parameters are used as evaluation criteria to select the optimal working fluid for the hybrid ORC system. This includes the ORC efficiency, overall system efficiency, BWR, VFR, required ETC area and the total heat transfer capacity (UA_{tot}). The product UA_{tot} can approximately indicate the requited total area of the heat exchangers [65, 100]. The UA_{tot} can be determined in terms of evaporator and condenser heat transfer capacities as follows:

$$UA_{tot} = UA_e + UA_c \tag{4.1}$$

The heat transfer capacity of the evaporator, UA_e, and condenser, UA_c, can be obtained as the sum of their heat exchanger's different zones and for each zone it is calculated by rearranging Eq.3.22 as

$$UA = \frac{\dot{Q}}{LMTD} \tag{4.2}$$

Table 4.1 The most common working fluids used in low-temperature applications [81, 173]

Substance	Group	T_c [°C]	ODP	GWP [100 yr]
R125	HFC	66.02	0	3500
R218	PFC	71.95	0	8830
R143a	HFC	72.71	0	4470
R32	HFC	78.11	0	675
R115	CFC	79.95	0.44	7370
R1234yf	HFO	94.70	0	4
R22	HCFC	96.15	0.05	1810
R134a	HFC	101.06	0	1430
R227ea	HFC	101.65	0	3220
R12	CFC	111.97	1.0	10890
RC318	PFC	115.23	0	10250
R124	HCFC	122.28	0.02	609
R236fa	HFC	124.92	0	9810
R142b	HCFC	137.11	0.07	2310
R114	CFC	145.68	1.0	10040
R600 (n-butane)	HC	151.98	0	~20
R245fa	HFC	154.05	0	1030

Table 4.2 Thermodynamic and environmental properties of the selected fluids [81, 83, 202]

Substance	Thermodynamic properties				Safety properties ASHRAE 34 group	Environmental properties		Type
	M [kg/kmol]	T_{bp} [°C]	T_c [°C]	P_c [bar]		ODP	GWP	
R1234yf	114.04	-29.45	94.7	33.8	A2L	0	4	Isen
R134a	102.03	-26.07	101.06	40.6	A1	0	1430	Isen
R600	58.12	-0.55	151.98	37.9	A3	0	~20	Dry
R245fa	134.05	14.9	154.05	36.4	B1	0	1030	Dry

Since the wet fluids are not included in this work, there is no concern about wet droplets formation during the expansion process and the superheating process can consequently be avoided. On the other hand, superheating requires a large heat exchanger size due to the poor heat transfer coefficients accompanied with the vapour phase, resulting in a higher system cost [57]. Therefore, superheating of the working fluid is not considered in the current work.

When the working fluids are economically compared at different values of net output power, this approach does not lead to the accurate fluid selection. In this work, however, the comparative assessment of the four candidate working fluids is carried out at the same net output power of 10 kW using a set of operating parameters and specifications listed in Table 4.3. Saturated vapour was assumed at the expander inlet and the vapour quality at the expander exit is set to a minimum value of 0.95. The global solar irradiance value is set to 700 W/m^2.

Table 4.3 Operating parameters and specifications of the hybrid ORC system

Parameter	Data
Net output power, kWe	10
Heat source inlet temperature, ^{o}C	120
Heat source operating pressure, bar	3
Biomass boiler efficiency, %	85
Biomass fuel (wood pellets) heating value, MJ/kg	17
Cooling water inlet temperature, ^{o}C	18
Condensation temperature, ^{o}C	35
Evaporator pinch point temperature difference, K	8
Condenser pinch point temperature difference, K	5
Ambient temperature, ^{o}C	25
Maximum ORC operating temperature, ^{o}C	100
Maximum ORC operating pressure, bar	30
Expander isentropic efficiency, %	70
Pump isentropic efficiency, %	80
Electric generator efficiency, %	96
Pump motor efficiency, %	96

Figures 4.1 to 4.5 present comparisons between the four preselected working fluids based on different criteria. Fig. 4.1 shows the variation of the ORC efficiency and overall system efficiency with the evaporation pressure for the candidate working fluids. It can be seen that for all working fluids, both the ORC efficiency and overall system efficiency significantly increase with the rise of the evaporation pressure. In addition, both R134a and R1234yf require higher operating pressures compared to R245fa and R600. The figure shows that fluids with higher critical temperatures provide higher efficiencies. R245fa provides the highest overall efficiency of 6.75% followed by R600. Also, the system with R134a achieves higher overall efficiency when compared to R1234yf.

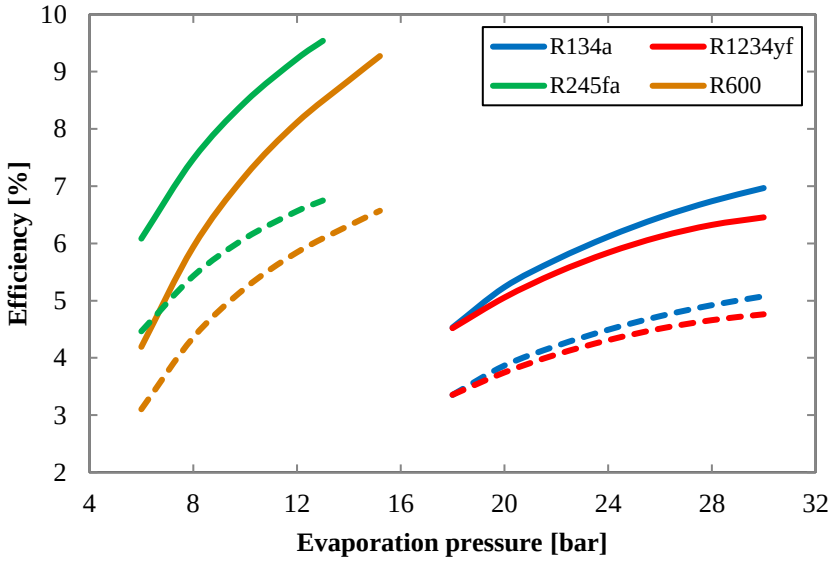

Figure 4.1 Variation of ORC efficiency (solid line) and overall system efficiency (dashed line) with evaporation pressure

The variation of the working fluid mass flow rate with the evaporation pressure for all the working fluids is shown in Fig. 4.2. The figure shows a decrease in the working fluid mass flow rate as the evaporation pressure increases. For the same output power, the increase in the evaporation pressure yields an enthalpy difference increase across the expander and hence a decrease in the mass flow rate. It can be seen that the ORC system with R1234yf and R134a requires much higher mass flow rate than that with R245fa and R600.

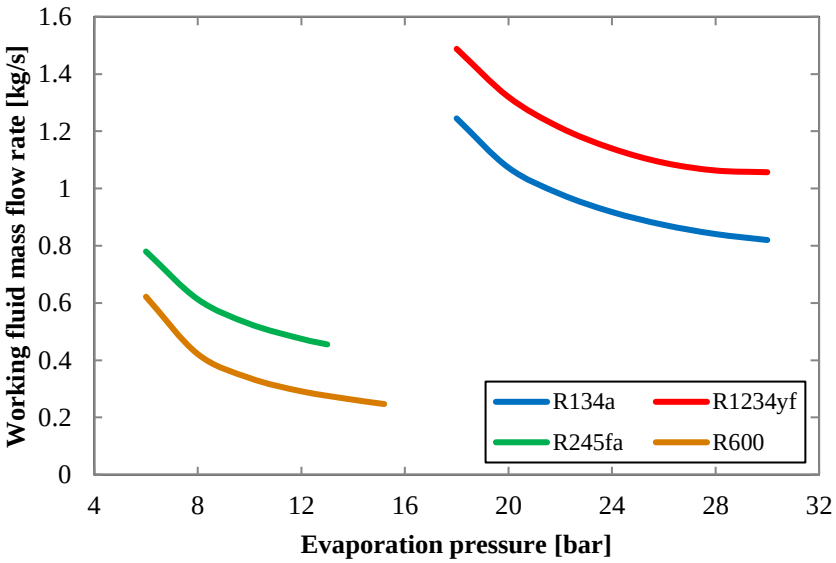

Figure 4.2 Variation of the working fluid mass flow rate with evaporation pressure

Fig. 4.3 shows the power consumed by the pump and the back work ratio, *BWR*, versus the evaporation pressure. As it can be seen, the use of R1234yf leads to comparatively high pumping power and, consequently, high *BWR* values. The figure also indicates that the pump power for R1234yf might be as high as about 22% of the expander power, resulting in lower system efficiency. The high pump power can be attributed to the high working fluid mass flow rate and also to the big pressure difference between the evaporation and condensation processes of the cycle. On the other hand, R245fa requires the lowest pump power and *BWR* value.

The solar collector area and the size of the heat exchangers play a vital role in the economics of the hybrid ORC system. Fig. 4.4 shows results on determination of the total ETC area and the total heat transfer capacity, UA_{tot}, of the heat exchangers, required for achieving the 10 kW net power output. It is obvious that both the ETC area and UA_{tot} decrease sharply with the increase of the evaporation pressure for all working fluids. The system requires smallest collector area when R245fa and R600 are used and these values are 211.7 and 217.4 m^2, respectively. Smaller UA_{tot} values indicate smaller heat exchangers area that required for satisfying the heat exchange process, leading to the lower equipment

cost. R245fa and R600 are promising fluids among the cost-effective substances due to the smaller solar collector areas required and UA_{tot} values.

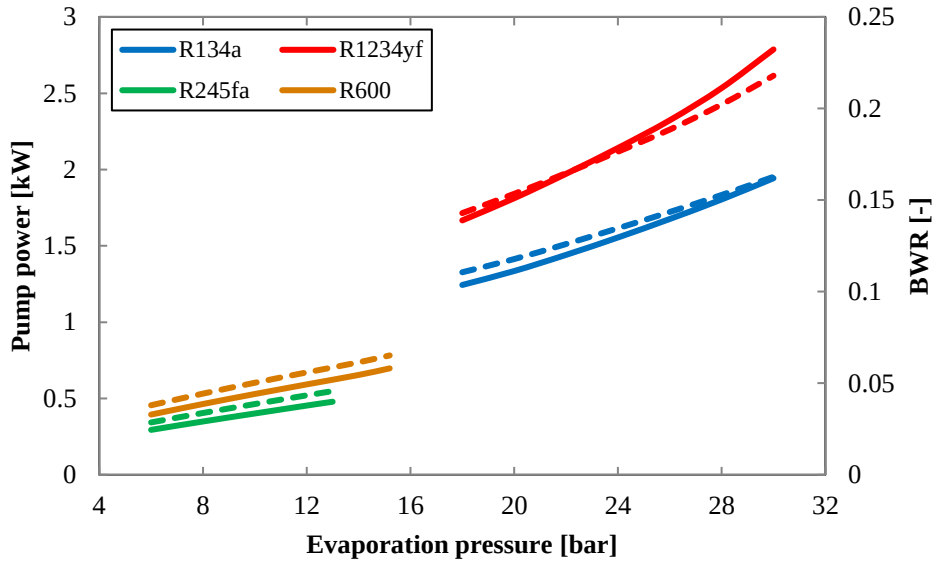

Figure 4.3 Variation of the pump power (solid line) and BWR (dashed line) with evaporation pressure

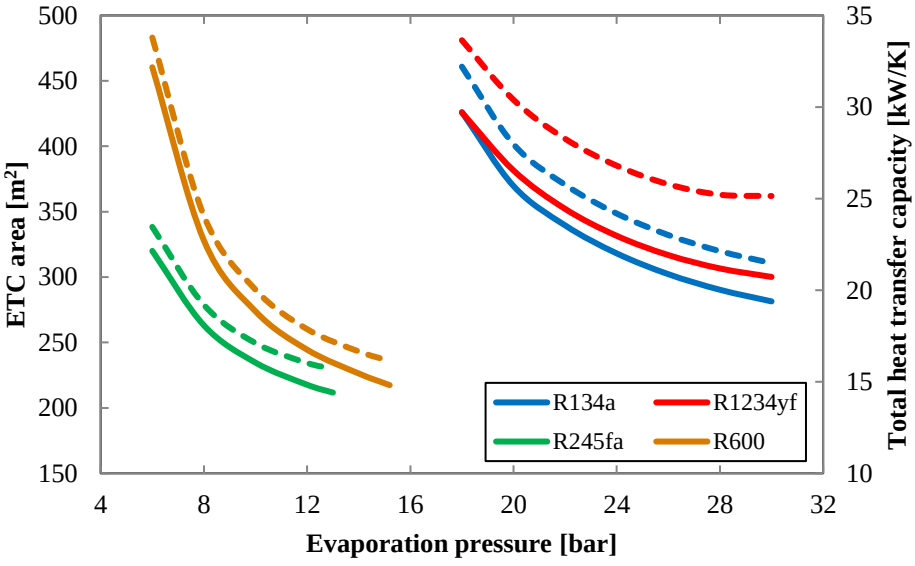

Figure 4.4 Variation of the ETC area (solid line) and UA_{tot} (dashed line) with evaporation pressure

The variation of the volume flow ratio, *VFR*, with the evaporation pressure for the investigated working fluids is illustrated in Fig. 4.5. Lower *VFR* values ensure a smaller expander size and, simultaneously, higher isentropic expander efficiency. As mentioned in Chapter 3, the *VFR* value should be less than 50 in order to achieve turbine isentropic efficiency higher than 80%. As it can be seen in Fig. 4.5, the *VFR* always increases as the evaporation pressure increases. In addition, the *VFR* value for all the working fluids does not exceed 7, thus expander efficiency higher than 80% can be achieved. However, at the maximum system efficiency of each working fluid, R134a has the smallest *VFR* with a value of 4.26 which leads to the smaller expander size and higher isentropic efficiency.

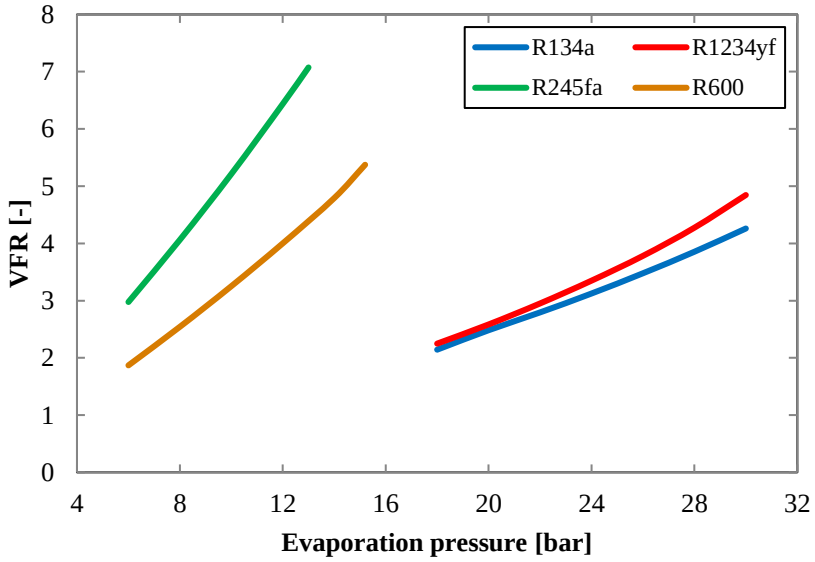

Figure 4.5 Variation of VFR with evaporation pressure

Based on the above discussion, it is clear that R245fa provides the best overall thermodynamic performance while R1234yf produces poor performance. From economic point of view, R245fa is the most cost-effective fluid since it ensures the smallest solar collector area and UA_{tot} value. However, R134a provides the lowest VFR, resulting in the smallest size and most efficient expander. Considering the safety and environmental issues, the use of R600 requires extra engineering precautions due to its high flammability. Therefore, R245fa and R134a are chosen for further investigations.

4.3 The ETC selection

The overall solar system performance is affected by the solar collector performance. The efficiency of the solar collector is a function of the solar irradiance, mean operating temperature and ambient temperature. In addition, the collector area is determined by its efficiency and the input heat required for the ORC, and it can be changed as the working condition varies. In this section, three different ETCs from different manufacturers (listed in Table 3.1) are examined at a range of solar irradiance in order to investigate the impact of such a component on the overall system performance.

Fig. 4.6 shows the variation of the efficiency and the required area of the three different ETCs with the solar irradiance for R134a and R245fa. It can be noticed that the ETC efficiency is improved as the solar irradiance increases for all collectors which in turn leads to a significant reduction in the required ETC area. The figure also shows that VR12 has the highest collector efficiency and accordingly the minimum required ETC area for the two working fluids. For all collector types, the ETC efficiency with R134a is higher than that with R245fa. For instance, the ETC efficiency values using VR12 at 700 W/m^2 for R134a and R245fa are 72.7% and 70.7%, respectively. This is due to the lower collector inlet temperature for the system using R134a. Although a higher ETC efficiency is achieved with R134a, a larger ETC area is also required. The minimum ETC area required using R134a and R245fa are 260 m^2 and 199 m^2, respectively. This can be justified by the higher amount of input heat required when R134a is used for producing the same output power as a result of the lower overall system efficiency.

Fig. 4.7 shows the variation of the overall system efficiency with the solar irradiance for both fluids using the three ETCs. The overall efficiency increases with increasing the solar irradiance for all collectors. This is mainly because the improvement in the ETC efficiency with increasing of the solar irradiance. It can be clearly seen that the overall efficiency is significantly affected by the collector type. For both working fluids, the system achieves the highest overall efficiency when VR12 is used. The maximum obtained overall efficiency using R134a and R245fa are 5.5% and 7.2%, respectively.

It can be concluded from Figs. 4.6 and 4.7 that the ETC type plays an important role in both system performance and the total area required. Therefore, VR12 is selected as it ensures better system performance and minimum area requirement.

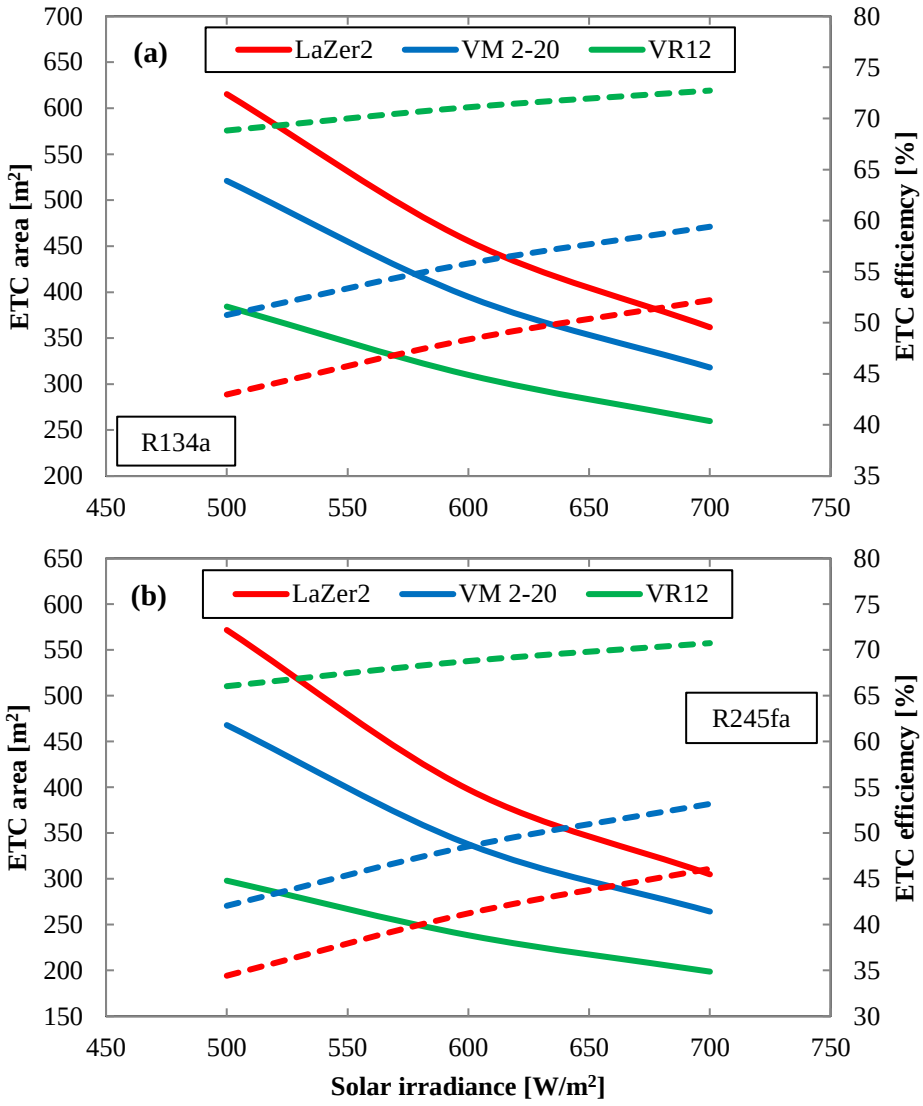

Figure 4.6 Variation of the ETC area (solid line) and its efficiency (dashed line) with solar irradiance for different collectors, (a) R134a and (b) R245fa

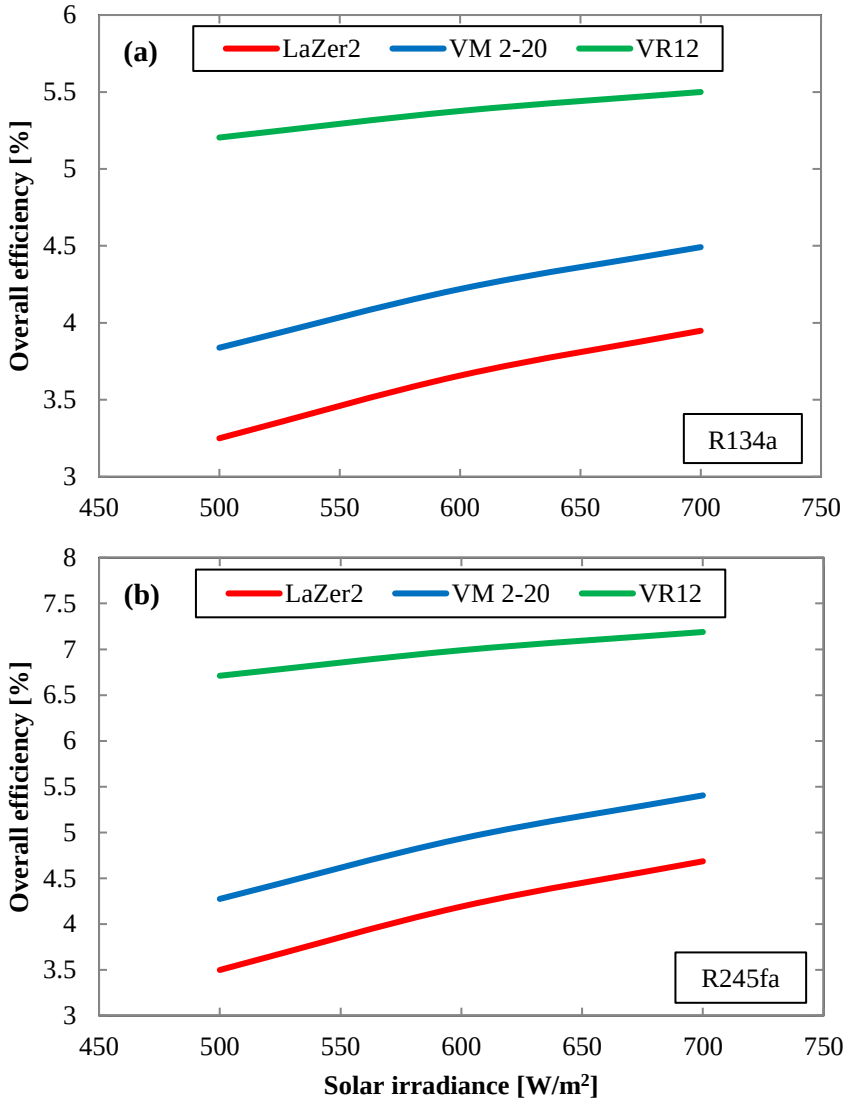

Figure 4.7 Variation of overall system efficiency with solar irradiance for different collectors, (a) R134a and (b) R245fa

4.4 The hybrid ORC system

In the hybrid operation mode, some of the heat input to the ORC is provided by solar energy and the rest is supplied by biomass energy. This is a typical system operation when the solar radiation is insufficient to generate the desired power output. In this scenario, the HTF is heated using the ETC array to a particular temperature depending on the available solar irradiance and the ETC area. The biomass boiler is then used to raise the HTF

temperature to the set outlet point (120 ^{o}C) by burning the corresponding amount of wood pellets. The HTF is circulated in the heating circuit to heat the ORC fluid within the evaporator.

In this section, the hybrid ORC system performance is investigated for different cases based on the energy share of solar and biomass sources including solar mode only and biomass mode only. The system is examined using the two selected working fluids at different values of solar irradiance to produce 10 kW net power output. It should be mentioned that the ORC operating parameters are kept unchanged and consequently the predicted ORC efficiency remained constant with values of 7.56% and 10.16% using R134a and R245fa, respectively.

Figs. 4.8 to 4.10 present the ETC efficiency, ETC area needed, the wood pellets consumption rate and the overall efficiency for different solar and biomass energy share modes at a solar irradiance of 500 W/m^2. Fig. 4.8 presents the ETC efficiency and its outlet temperature for the two working fluids at a value of solar irradiance of 500 W/m^2. As it can be seen, increasing the solar energy share leads to an increase in the ETC outlet temperature, reaching to 120 ^{o}C at 100% solar share. An opposite trend is noticed for the ETC efficiency with increasing the solar energy share. The decline in the ETC efficiency with the solar share is due to the increase in the ETC mean operating temperature, as a result of the gradual increase in its outlet temperature (see Eq. 3.13). The figure also indicates that the ETC efficiency is higher in case of using R134a than R245fa as a result of the lower ETC mean temperature.

The required ETC area and the biomass fuel consumption rate for different energy share scenarios at 500 W/m^2 are shown in Fig. 4.9. The figure demonstrates that with increasing the solar energy share, a larger ETC area is required and, simultaneously, a lower consumption rate of biomass fuel is needed. The hybrid ORC system requires a smaller ETC area and less fuel consumption rate using R245fa as the working fluid. To supply the whole ORC by solar energy, ETC area values of 384 and 298 m^2 are required using R134a and R245fa, respectively. On the other hand, burning of 32.94 kg/h of wood pellets can supply all the ORC heat needs using R134a and only 24.52 kg/h when R245fa is used.

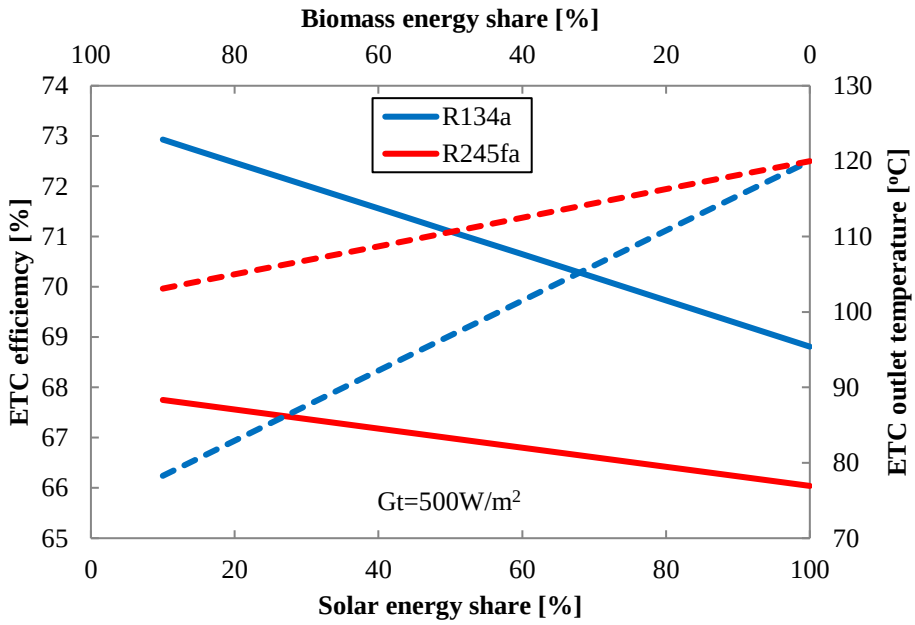

Figure 4.8 Variation of the ETC efficiency (solid line) and its outlet temperature (dashed line) with the solar and biomass energy share at G_t=500 W/m^2

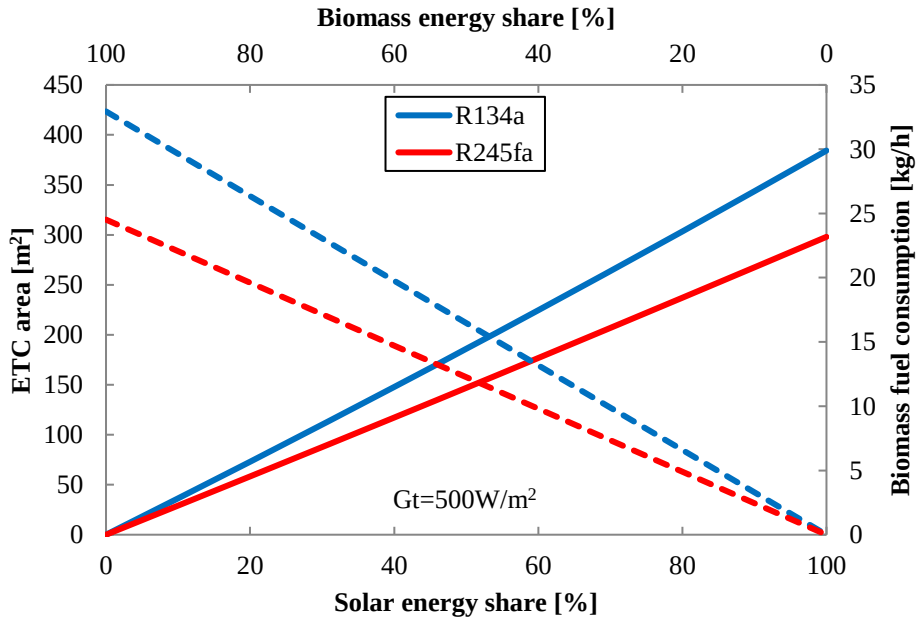

Figure 4.9 Variation of the ETC area (solid line) and biomass consumption (dashed line) with the solar and biomass energy share at G_t=500 W/m^2

Fig. 4.10 illustrates the variation of the overall system efficiency with the share of solar and biomass energy sources for both working fluids at 500 W/m^2. It can be seen that the overall system efficiency is inversely proportional to the solar energy share. In addition, the system achieves comparatively higher overall efficiency in both solar and biomass energy modes using R245fa. The overall efficiency decreases from 8.64% to 6.71% using R245fa and from 6.43% to 5.20% using R134a as the solar energy share increases from 0% to 100%. This can be attributed to the higher efficiency of the biomass boiler than that of the ETC.

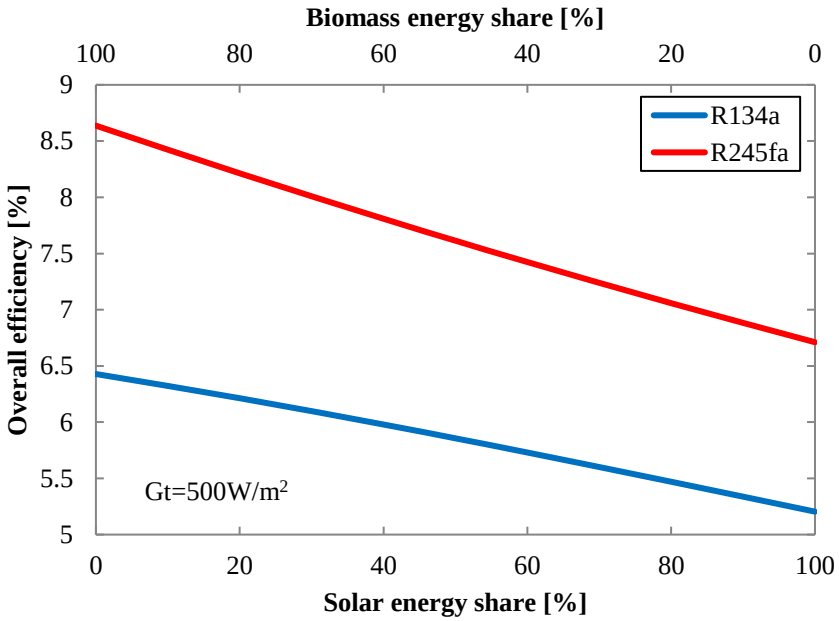

Figure 4.10 Variation of the overall efficiency with the solar and biomass energy share at G_t=500 W/m^2

Figs. 4.11 to 4.13 present the ETC efficiency, required ETC area, the wood pellets consumption rate needed and the overall system efficiency for different modes of solar and biomass energy share at solar irradiance value of 700 W/m^2. Fig. 4.11 shows the ETC efficiency and its outlet temperature for the two working fluids as a function of the solar and biomass energy share. The figure shows that the ETC efficiency and the outlet temperature at solar irradiance value of 700 W/m^2 have similar trends to those in case of 500 W/m^2. However, the ETC efficiency values are higher at solar irradiance value of 700 W/m^2 compared with those at 500 W/m^2. The solar energy share has more impact on the

ETC efficiency in case of R134a than that of R245fa. The ETC efficiency drops by 3.9% using R134a and only 1.7% using R245fa when the solar share increases from 10% to 100%. This is due to the steeper increase in the ETC outlet temperature with the solar share increase when R134a is used as a working fluid.

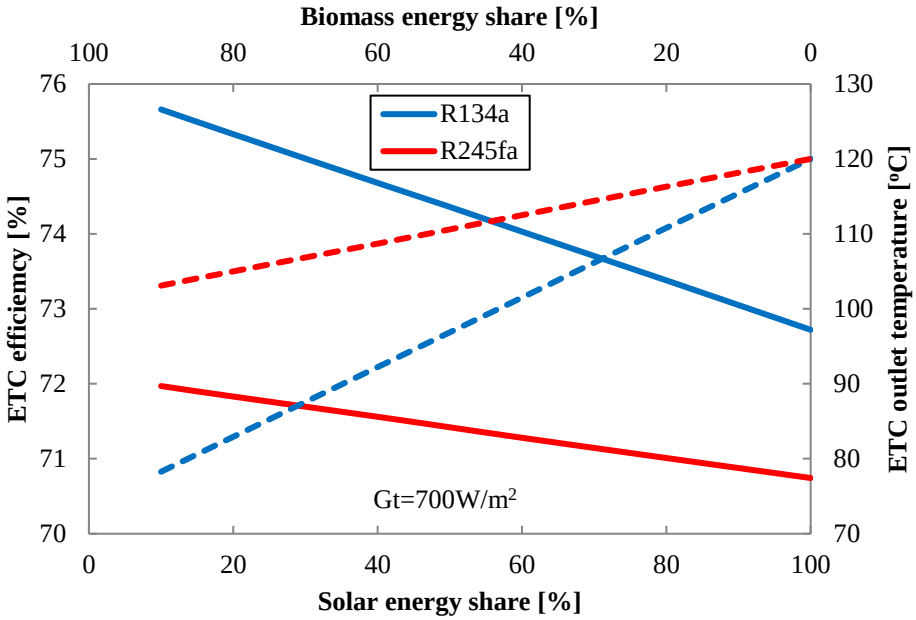

Figure 4.11 Variation of the ETC efficiency (solid line) and its outlet temperature (dashed line) with the solar and biomass energy share at G_t=700 W/m^2

Fig. 4.12 shows the variation of the required ETC area and the biomass fuel consumption rate with the solar and biomass energy share at solar irradiance value of 700 W/m^2. The figure shows that increasing the solar energy share increases the required ETC area and consequently decreases the wood pellets consumption rate. Compared with the case of 500 W/m^2, the system at 700 W/m^2 requires smaller ETC areas for all the range of solar energy share while the required wood pellets consumption rate is the same. As the energy share is based on the ORC heat input, the rate of the biomass fuel consumption does not change with the solar irradiance. For the 50% solar energy share scenario, increasing the solar radiation from 500 W/m^2 to 700 W/m^2 results in a reduction in the required ETC area by an average of 33% for both working fluids.

The variation of the overall system efficiency with the share of solar and biomass energy for both working fluids at solar irradiance value of 700 W/m^2 is shown in Fig. 4.13. It is shown that the overall efficiency decreases as the solar energy share increases. As the solar share increases from 0% to 100%, the overall efficiency drops from 8.64% to 7.19% using R245fa while it decreases from 6.43% to 5.50% using R134a. However, for both working fluids, the overall system efficiency is higher at a solar irradiance value of 700 W/m^2 as compared with that at 500 W/m^2.

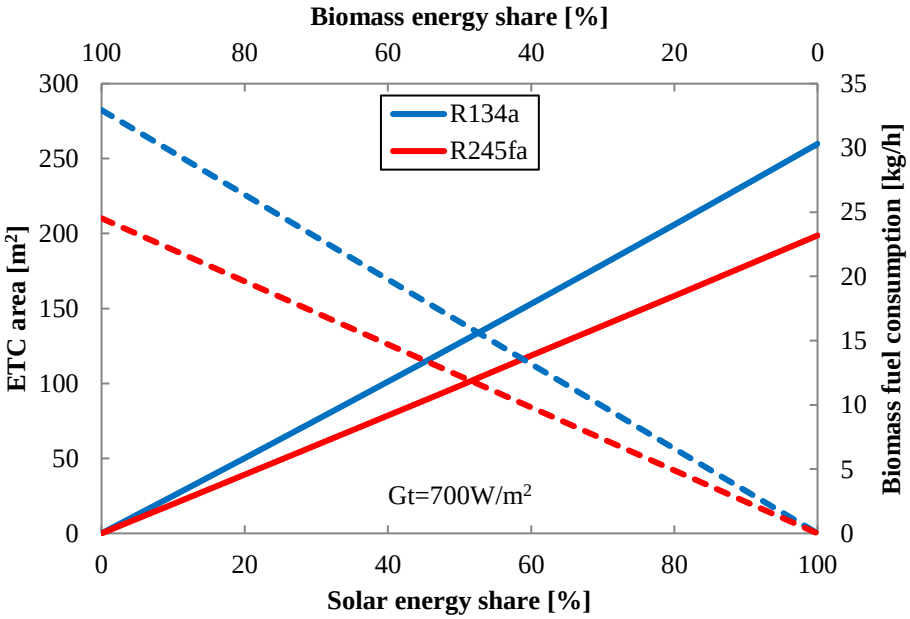

Figure 4.12 Variation of the ETC area (solid line) and biomass consumption (dashed line) with the solar and biomass energy share at G_t=700 W/m^2

The variation of the overall system efficiency with the share of solar and biomass energy for both working fluids at solar irradiance value of 700 W/m^2 is shown in Fig. 4.13. It can be seen that the overall efficiency decreases as the solar energy share increases. As the solar share increases from 0% to 100%, the overall efficiency drops from 8.64% to 7.19% using R245fa while it decreases from 6.43% to 5.50% using R134a. However, for both working fluids, the overall system efficiency is higher at a solar irradiance value of 700 W/m^2 as compared with that at 500 W/m^2.

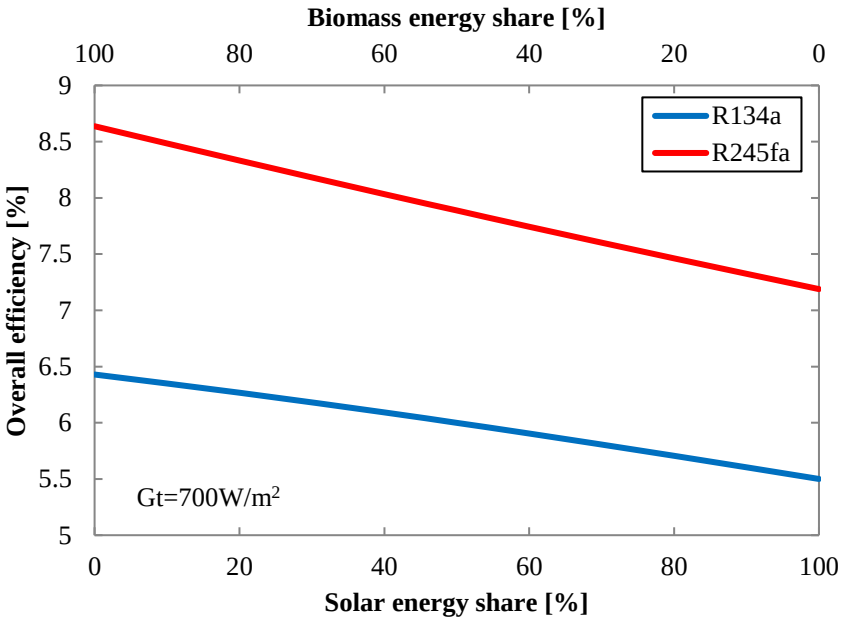

Figure 4.13 Variation of the overall efficiency with the solar and biomass energy share at G_t=700 W/m^2

4.5 Parametric analysis

The performance of the hybrid ORC system is influenced by several operating parameters. A comprehensive parametric analysis is therefore performed to investigate the effect of six different operating parameters on the system performance. These include the evaporation pressure, condensation temperature and pinch point temperature differences in the evaporator and condenser, in addition to the expander and pump isentropic efficiencies. The purpose of the parametric analysis is also to find out which of the parameters have more impact on the hybrid ORC system performance.

The effects of these parameters are discussed in the following sections based on investigations using the developed Thermolib simulation model. In each case, only the value of the one parameter is changed within the range given in Table 4.4 whereas the remaining parameters are kept constant and equal to the basic values listed in Table 4.4. A solar irradiance value of 700 W/m^2 is used in the simulations.

Table 4.4 The basic values and ranges of the investigated operating parameters

Parameter	Basic value	Investigated range
Evaporation pressure, bar	Max. value	≤ max [P_{sat} at 100 °C , 30]
Condensation temperature, °C	35	30-40
Evaporator pinch point temperature difference, K	9	6-12
Condenser pinch point temperature difference, K	6	4-8
Expander isentropic efficiency, %	75	70-80
Pump isentropic efficiency, %	80	70-80

4.5.1 The effect of evaporation pressure

Fig. 4.14 shows the effect of the evaporation pressure on both the ORC and overall system efficiencies for the two selected working fluids. As it can be seen, both the ORC and overall efficiencies improve significantly as the evaporation pressure increases for the two fluids. The maximum efficiencies are obtained at the maximum evaporation pressure of each working fluid. For the same output power, increasing the evaporation pressure results in less heat input to the ORC and consequently both ORC and overall system efficiencies increase. Furthermore, the system with R245fa achieves higher values of ORC and overall efficiencies than with R134a. The maximum overall efficiency using R245fa is 7.19%, which is greater than that of R134a by about 30.7%. The maximum system operating pressure using R245fa is lower than that of R134a with values of 12.7 bar and 30 bar, respectively, ensuring less system complexity with the former fluid.

Fig. 4.15 illustrates the effect of the evaporation pressure on the working fluid, HTF and cooling water mass flow rates. The figure shows that the working fluid mass flow rate decreases as the evaporation pressure increases for both working fluids. At a fixed net power output, increasing the evaporation pressure leads to a higher enthalpy drop across the expander which in turn reduces the working fluid mass flow rate in the cycle (see Eq. 3.5). The HTF mass flow rate increases as the evaporation pressure increases using R245fa while it slightly changes with the evaporation pressure using R134a. The HTF mass flow rate is determined by the heat input to the ORC as well as the HTF temperature leaves the evaporator (see Eq. 3.5). The mass flow of the cooling water in the condenser significantly decreases for the two working fluids with increasing the evaporation pressure. This is

mainly due to the considerable drop in the heat rejected in the condenser with the rise of the evaporation pressure.

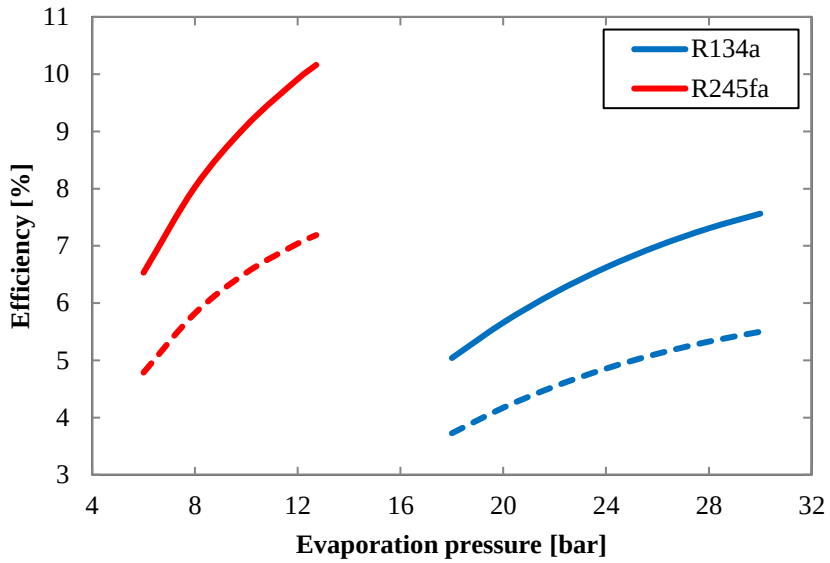

Figure 4.14 Effect of evaporation pressure on the ORC efficiency (solid line) and overall efficiency (dashed line)

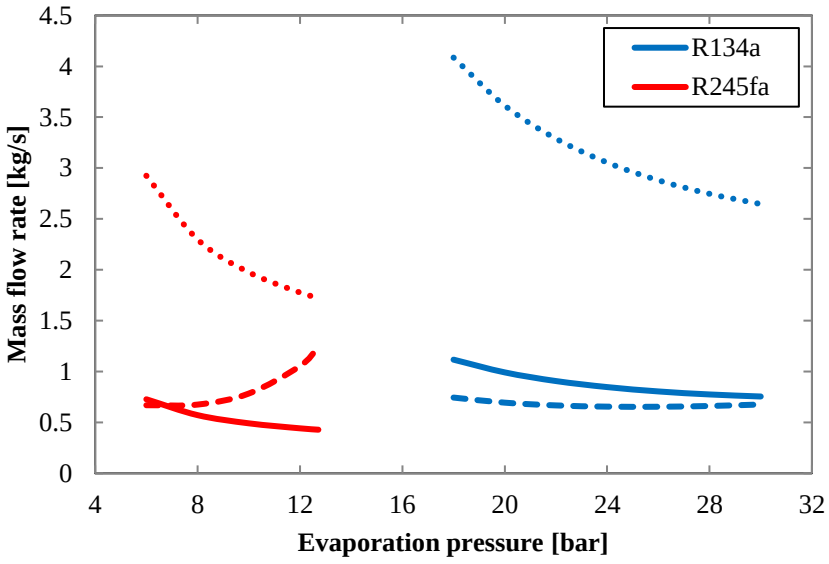

Figure 4.15 Effect of evaporation pressure on the working fluid (solid line), HTF (dashed line) and cooling water (dotted line) mass flow rates

The effect of the evaporation pressure on the ETC area and its efficiency is shown in Fig. 4.16. It can be seen that although the ETC efficiency declines as the evaporation pressure increases, the required ETC area decreases sharply. This is can be attributed to the considerable decrease in the required heat input to the ORC with increasing the evaporation pressure. The decrease in the ETC efficiency with the evaporation pressure is due to the increase in the ETC inlet temperature. Both R134a and R245fa require the smallest ETC area at the maximum evaporation pressure. For a 10 kW net power output, R245fa requires only 198.7 m^2 which is 23.5% less than that of R134a.

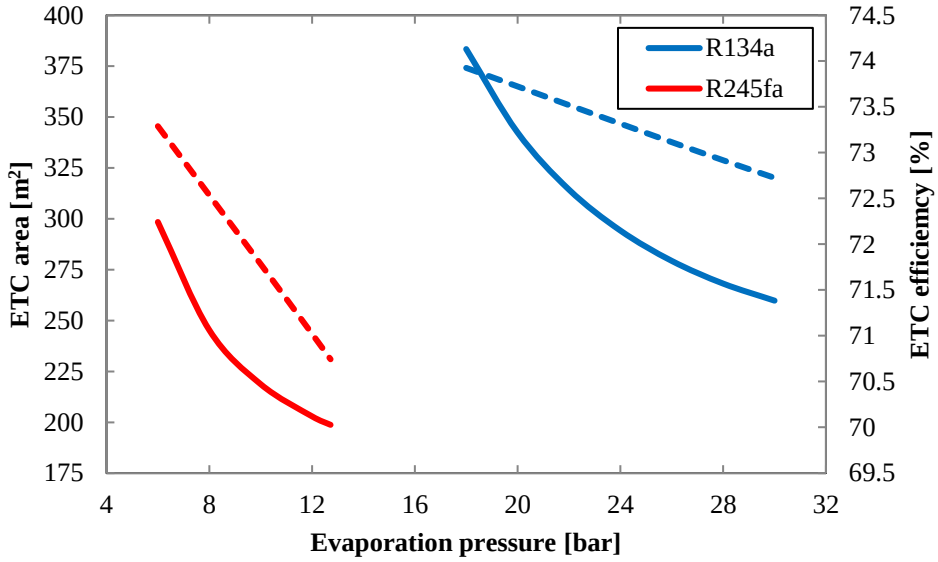

Figure 4.16 Effect of evaporation pressure on the ETC area (solid line) and ETC efficiency (dashed line)

Fig. 4.17 shows the influence of the evaporation pressure on both the evaporator and condenser areas for the two selected working fluids. As demonstrated in the figure, the increase in the evaporation pressure results in decreasing both the evaporator and condenser areas for the two working fluids. For both working fluids, the required area of the condenser is larger than that of the evaporator. Moreover, the hybrid ORC system requires smaller evaporator and condenser areas when R245fa is used as the working fluid, resulting in a reduction in the total system cost. This is basically due to the smaller amounts of heat input and heat rejected in the evaporator and condenser, respectively, using R245fa. At the maximum evaporation pressure of each fluid, R245fa requires

evaporator and condenser areas of 2.93 and 4.23 m^2, respectively, whereas these values are 4.36 and 5.62 m^2 for R134a.

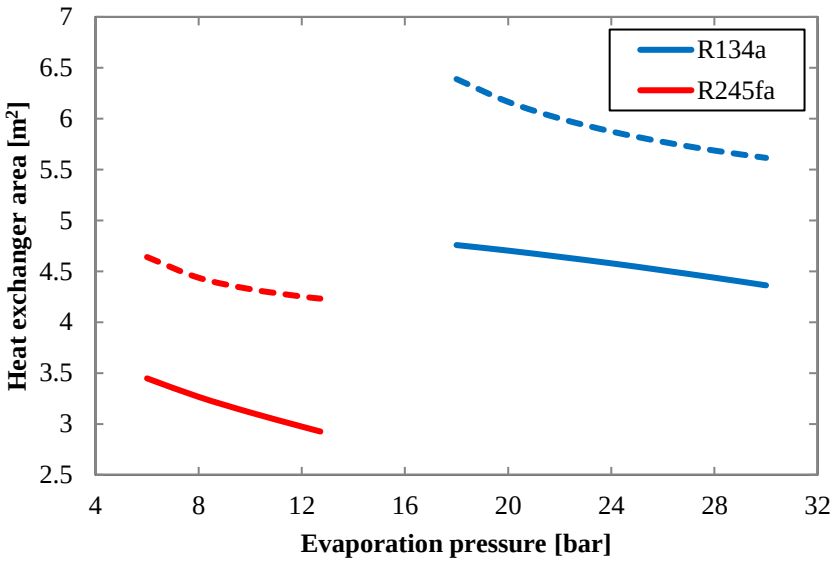

Figure 4.17 Effect of evaporation pressure on the evaporator area (solid line) and condenser area (dashed line)

4.5.2 The effect of condensation temperature

The effect of the condensation temperature on the ORC and overall system efficiencies is presented in Fig. 4.18. It is shown in the figure that the condensation temperature has a great influence on the ORC and overall efficiencies. The figure demonstrates that the ORC and overall efficiencies decrease with increasing the condensation temperature for the two working fluids. It can be noticed that the maximum efficiencies can be achieved at the minimum condensation temperature. When the condensation temperature decreases from 40 ^oC to 30 ^oC, the overall system efficiency using R134a and R245fa improves by 22.2% and 14.9%, respectively. For all the range of condensation temperatures, the use of R245fa ensures higher ORC and overall efficiencies than R134a. The maximum overall efficiency using R245fa and R134a are 7.69% and 6.05%, respectively.

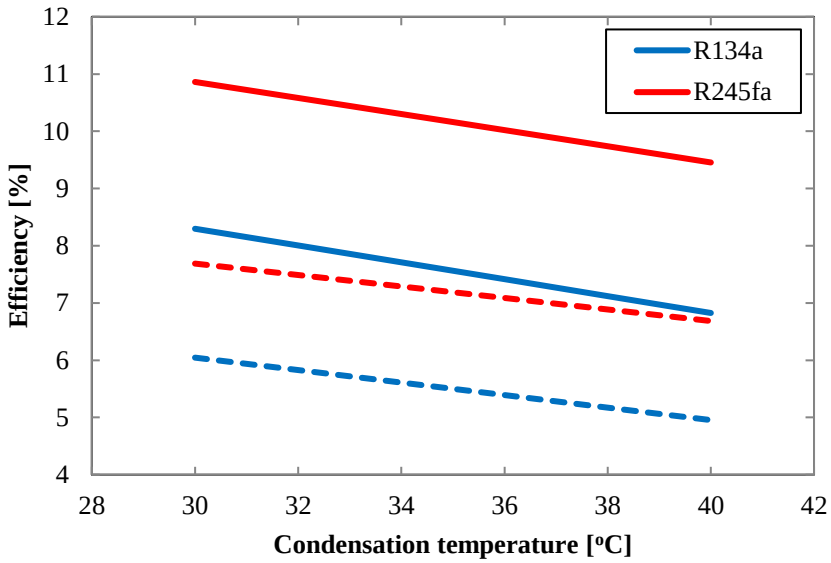

Figure 4.18 Effect of condensation temperature on the ORC efficiency (solid line) and overall efficiency (dashed line)

Fig. 4.19 shows the effect of the condensation temperature on the working fluid, HTF and cooling water mass flow rates. As the condensation temperature increases, the working fluid mass flow rate for maintaining the same net power output increases due to the reduction in the enthalpy difference in the expander (see Eq. 3.7). The HTF mass flow rate follows the same trend of the working fluid mass flow rate, increasing as the condensation temperature increases. However, an opposite trend for the cooling water mass flow rate with the condensation temperature can be observed. The cooling water mass flow rate significantly decreases with increasing the condensation temperature. At a constant pinch point temperature difference in the condenser, increasing the condensation temperature leads to a higher temperature difference between the cooling water inlet and outlet. This results in a decrease in the cooling water mass flow rate (see Eq. 3.9).

The effect of the condensation temperature on the required ETC area and its efficiency is illustrated in Fig. 4.20. As the condensation temperature increases, the required ETC area considerably increases whereas the ETC efficiency slightly decreases. The decrease in the ETC efficiency is due to the increment in the ETC inlet temperature as the condensation temperature increases. The substantial increase in the ETC area with increasing the condensation temperature can be attributed to the increase in the required

heat input to the ORC as well as the decrease in the ETC efficiency. The minimum required ETC area for both working fluids is obtained at the lowest condensation temperature. Decreasing the condensation temperature from 40 ºC to 30 ºC leads to reductions in the required ETC area of about 18% and 13% using R134a and R245fa, respectively. Also, the ORC system needs an ETC area of 213.7 m^2 using R245fa compared to 288.4 m^2 using R134a at a condensation temperature of 30 ºC.

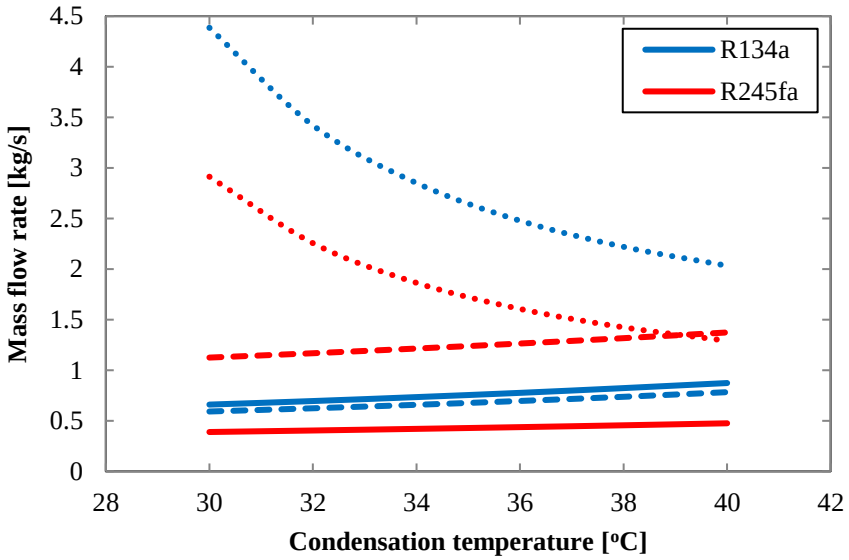

Figure 4.19 Effect of condensation temperature on the working fluid (solid line), HTF (dashed line) and cooling water (dotted line) mass flow rates

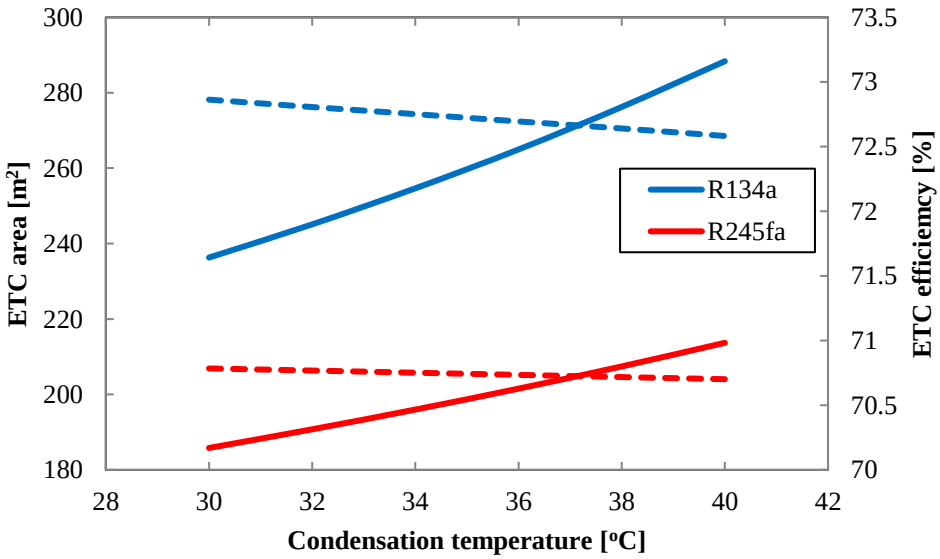

Figure 4.20 Effect of condensation temperature on the ETC area (solid line) and ETC efficiency (dashed line)

Fig. 4.21 shows the effect of the condensation temperature on the evaporator and condenser areas for the two selected working fluids. As it can be seen, the condensation temperature has a greater impact on the condenser area than on the evaporator area for the two working fluids. As the condensation temperature increases from 30 °C to 40 °C, the required condenser area increases by 14.2% and 17.1% using R134a and R245fa, respectively. However, the evaporator area increases by only 2.8% and 3.5% for R134a and R245fa, respectively. The more significant increase in the condenser area compared to that of the evaporator is due to the large decrease in the cooling mass flow rate which leads to a considerable decrease in the overall heat transfer coefficient of the condenser. The minimum required evaporator and condenser areas are found to be 4.3 and 5.2 m^2, respectively, using R134a. These values are 2.88 and 3.86 m^2, respectively, using R245fa as the working fluid.

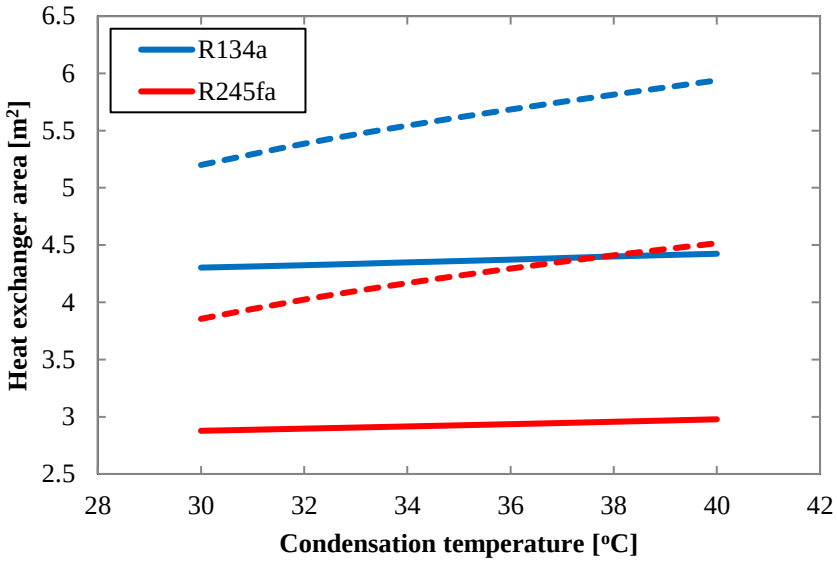

Figure 4.21 Effect of condensation temperature on the evaporator area (solid line) and condenser area (dashed line)

4.5.3 The effect of evaporator pinch point temperature difference

At constant ORC operating parameters, the evaporator pinch point temperature difference ΔTpp_e has no effect on the ORC efficiency; however, it affects the overall system efficiency. The effect of the evaporator pinch point temperature difference, ΔTpp_e, on the

overall system efficiency for the two working fluids is depicted in Fig. 4.22. The figure shows that the overall efficiency slightly decreases with increasing the pinch point temperature ΔTpp_e as a result of the ETC efficiency decrease. By increasing the pinch point temperature ΔTpp_e from 6 K to 12 K, the overall efficiency decreases from 5.53% to 5.47% for R134a and from 7.23% to 7.15% for R245fa. For all the range of the pinch point temperatures ΔTpp_e, the overall efficiency using R245fa is higher than that of R134a by an average of 30.7%.

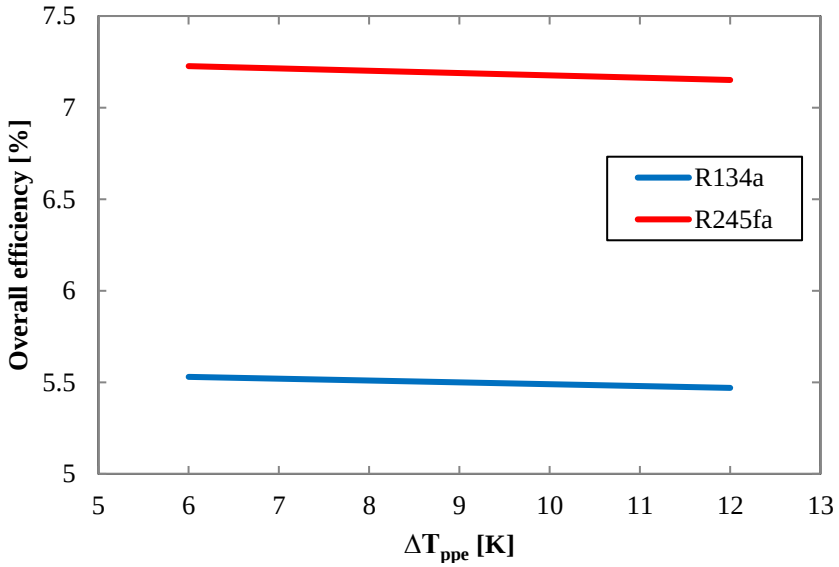

Figure 4.22 Effect of evaporator pinch point temperature on the overall efficiency

Fig. 4.23 presents the effect of the pinch point temperature difference in the evaporator ΔTpp_e on the HTF mass flow rate. As it can be seen, the HTF mass flow rate increases with the increase of the pinch point temperature ΔTpp_e for both working fluids. At a particular evaporation pressure, increasing the pinch point temperature ΔTpp_e leads to an increase in the evaporator outlet temperature and hence a decrease in the temperature difference between the evaporator inlet and outlet. This effect results in a rise in the HTF mass flow rate. The increasing rate in the HTF mass flow rate is higher when R245fa is used. Also, a higher amount of HTF mass flow rate needs to be circulated in the heating circuit using the same fluid.

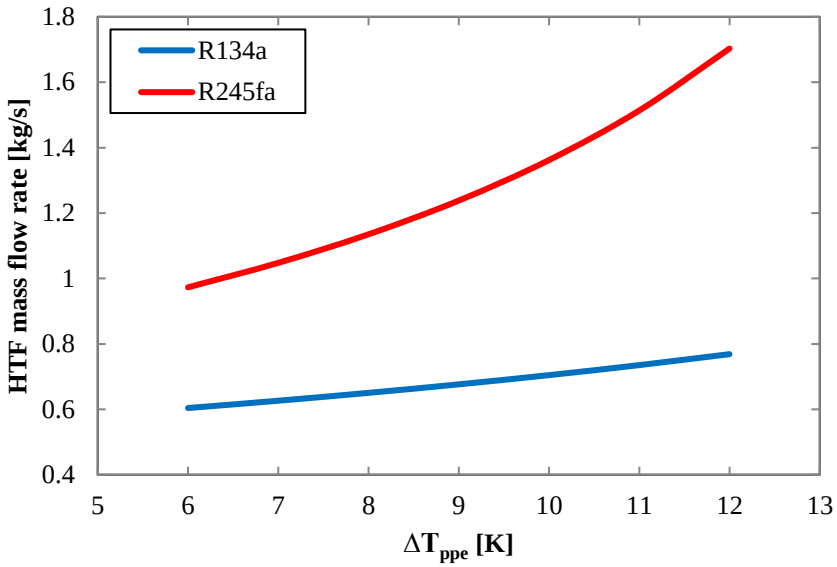

Figure 4.23 Effect of evaporator pinch point temperature on the HTF mass flow rate

Fig. 4.24 illustrates the variation of the required ETC area and its efficiency with the change in the evaporator pinch point temperature difference ΔTpp_e. It can be observed that as the pinch point temperature ΔTpp_e increases, the area of the ETC also slightly increases whereas the collector efficiency decreases. The decrease in the ETC efficiency is due to the increase in the ETC mean temperature as a result of increasing the ETC inlet temperature with increasing the pinch point temperature ΔTpp_e (see Eq. 3.13). Accordingly, a slightly larger ETC area is required for both working fluids due to the drop in its efficiency. As the pinch point temperature ΔTpp_e increases from 6 K to 12 K, the increase in the ETC area is only in the order of 1% for both working fluids.

The effect of the evaporator pinch point temperature difference ΔTpp_e on the evaporator area is shown in Fig. 4.25. The figure demonstrates that the evaporator area strongly affected by the pinch point temperature ΔTpp_e. As the pinch point temperature ΔTpp_e increases, the area of the evaporator largely decreases. It decreases from 5.58 to 3.57 m^2 for R134a and from 3.70 to 2.39 m^2 for R245fa as the pinch point temperature ΔTpp_e increases from 6 K to 12 K. This can be explained as follows: increasing the pinch point temperature ΔTpp_e results in an increase in the HTF mass flow rate which leads to a rise in the overall heat transfer coefficient in the evaporator. In addition, the logarithmic

mean temperature difference in the evaporator also increases with increasing the pinch point temperature ΔTpp_e. Increasing these two parameters result in the large decrease in the evaporator area.

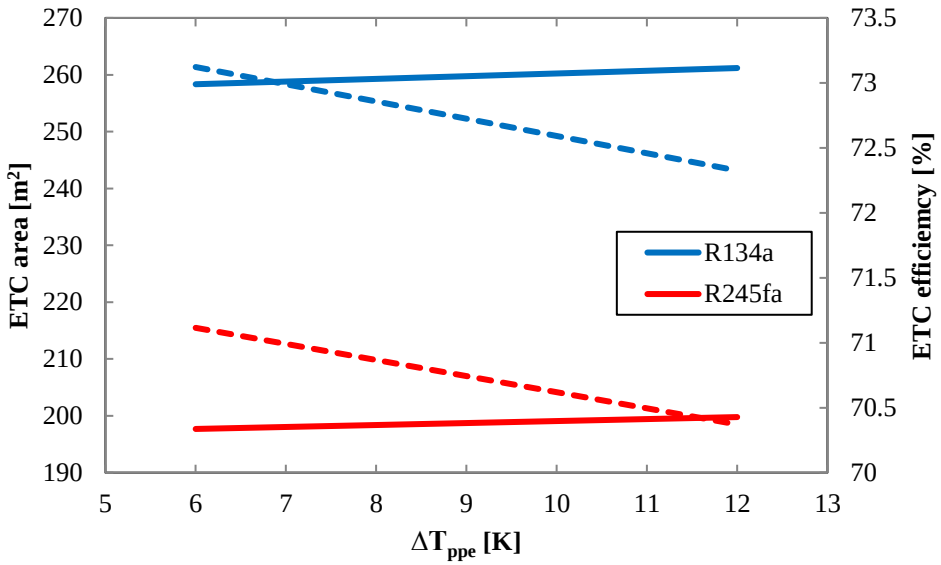

Figure 4.24 Effect of evaporator pinch point temperature on the ETC area (solid line) and ETC efficiency (dashed line)

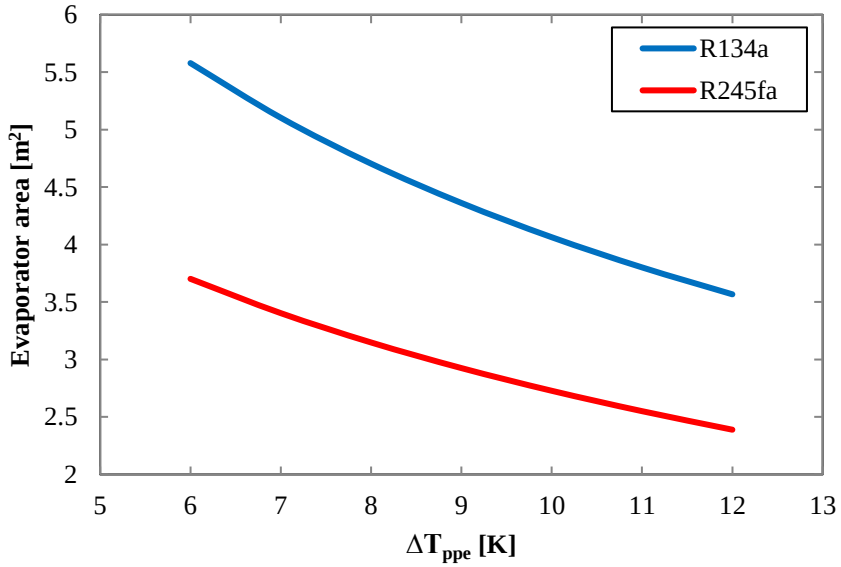

Figure 4.25 Effect of evaporator pinch point temperature on the evaporator area

4.5.4 The effect of condenser pinch point temperature difference

The pinch point temperature difference in the condenser, ΔTpp_c, determines the amount of cooling water mass flow rate which directly affects the condenser heat transfer area needed. The effect of the pinch point temperature ΔTpp_c on the cooling water mass flow rate is presented in Fig. 4.26. As shown in the figure, increasing the pinch point temperature ΔTpp_c significantly increases the cooling water mass flow rate. At a fixed condensation temperature, the increase in the pinch point temperature ΔTpp_c leads to a smaller temperature difference of the cooling water in the condenser which in turn increases its mass flow rate for the condensation process (see Eqs. 3.9 and 3.10). The use of R134a requires a much higher mass flow rate of the cooling water for completely converting the working fluid into a liquid sate. This is due to the much higher rate of heat rejection in the condenser in case of using R134a.

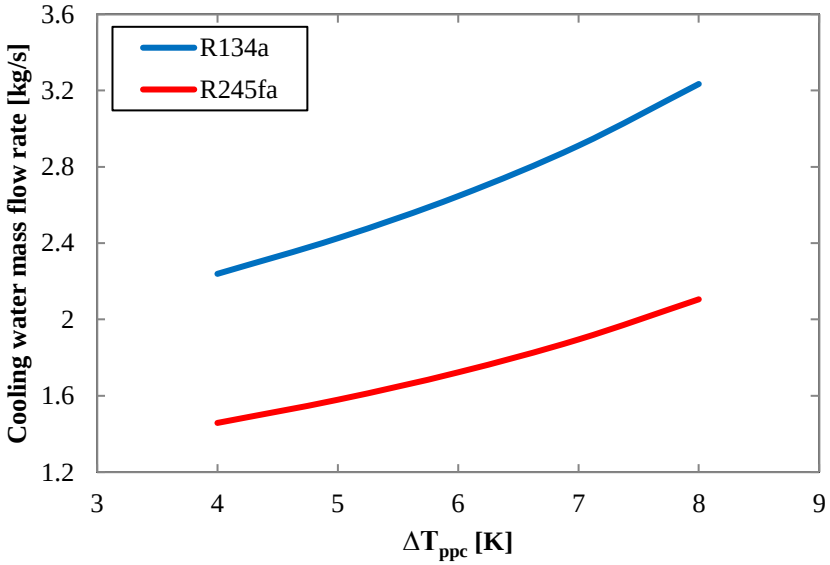

Figure 4.26 Effect of condenser pinch point temperature on the cooling water mass flow rate

Fig. 4.27 shows the impact of the condenser pinch point temperature difference, ΔTpp_c, on the area of the condenser for the two working fluids. The figure clearly shows that the condenser area significantly decreases with increasing the pinch point temperature ΔTpp_c. As it can be seen, increasing the pinch point temperature ΔTpp_c from 4 K to 8 K

reduces the condenser area by about 37% for both working fluids. The condenser area decreases from 7.16 to 4.53 m^2 for R134a and from 5.41 to 3.41 m^2 for R245fa. The decrease in the condenser area is due to the increase in the condenser overall heat transfer coefficient as a result of increasing the cooling water mass flow rate with increasing the pinch point temperature ΔTpp_c. The reduction in the condenser area can also be attributed to the increase occurred in the condenser logarithmic mean temperature difference.

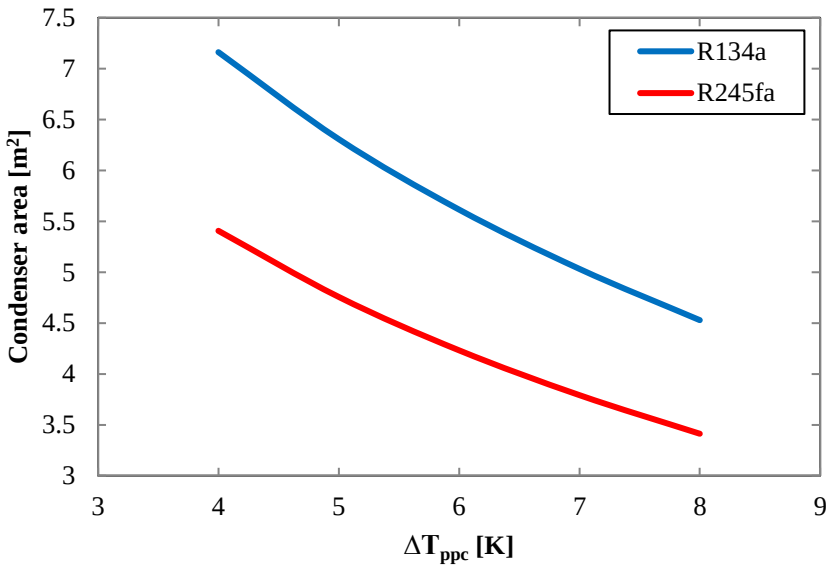

Figure 4.27 Effect of condenser pinch point temperature on the condenser area

4.5.5 The effect of expander isentropic efficiency

The expander isentropic efficiency has a direct impact on the expander power output which in turn affects the overall hybrid ORC performance. The effect of the expander isentropic efficiency on the ORC and overall efficiencies is illustrated in Fig. 4.28. This figure shows that both the ORC and overall efficiencies increases by increasing the expander isentropic efficiency for the two working fluids. Increasing the expander isentropic efficiency from 70% to 80% leads to improvements in the overall efficiency of 17% and 14.9% using R134a and R245fa, respectively. This is basically due to the enhancement in the ORC efficiency as a result of the higher expander performance.

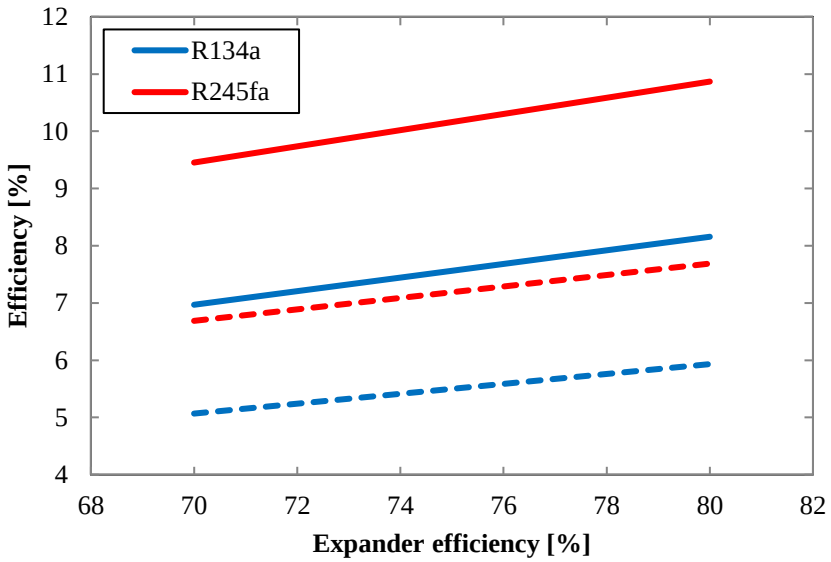

Figure 4.28 Effect of expander isentropic efficiency on the ORC efficiency (solid line) and overall efficiency (dashed line)

Fig. 4.29 shows the effect of the expander isentropic efficiency on the working fluid, HTF and cooling water mass flow rates. As it can be seen, the working fluid mass flow rate declines slightly as the expander isentropic efficiency increases. By increasing the expander isentropic efficiency, the enthalpy difference in the expander increases and consequently the working fluid mass flow rate decreases. The figure also demonstrates that both the HTF and cooling water mass flow rates decrease with increasing the expander isentropic efficiency. This is due to the decreases in the heat input and heat rejected in the evaporator and condenser, respectively, at a fixed net power output.

The influence of the expander isentropic efficiency on the required ETC area is illustrated in Fig. 4.30. The figure shows that the ETC area decreases as the expander isentropic efficiency increases. Increasing the expander isentropic efficiency from 70% to 80% leads to reductions in the required ETC area by 14.6% and 13% for R134a and R245fa, respectively. As the expander isentropic efficiency increases, the ORC efficiency also increases and the required heat input to the ORC to produce the same net power output decreases. This explains the reduction in the ETC area with increasing the expander isentropic efficiency.

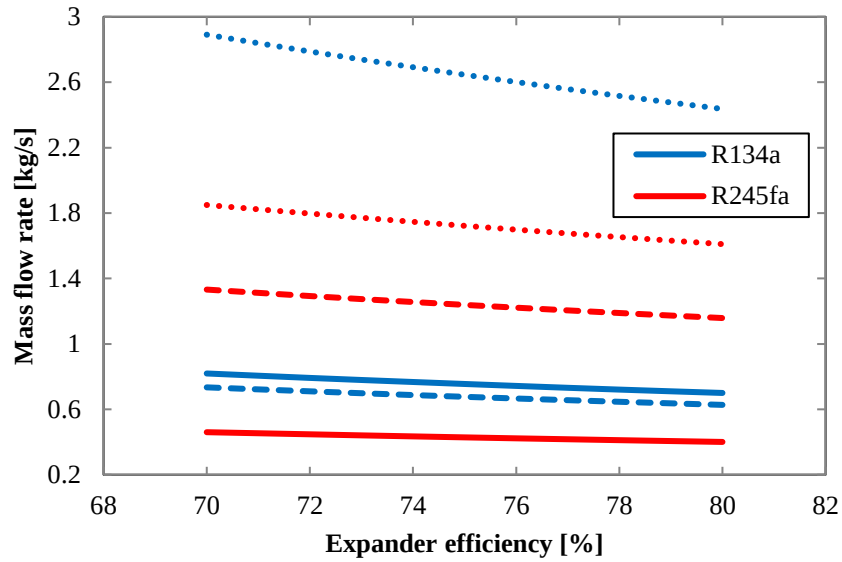

Figure 4.29 Effect of expander isentropic efficiency on the working fluid (solid line), HTF (dashed line) and cooling water (dotted line) mass flow rates

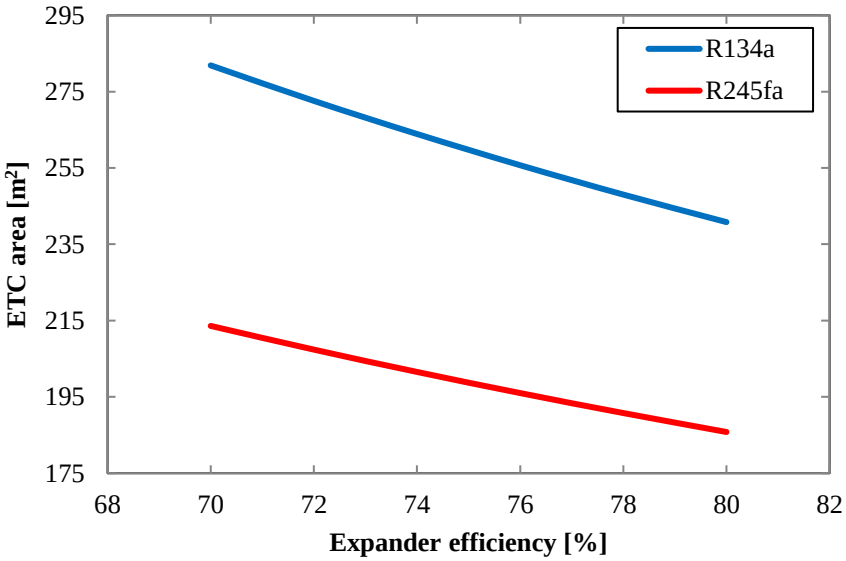

Figure 4.30 Effect of expander isentropic efficiency on the ETC area

Fig. 4.31 shows the effect of the expander isentropic efficiency on the evaporator and condenser areas for the two selected working fluids. As it can be seen, both the evaporator and condenser areas gradually decrease with increasing the expander isentropic efficiency.

The required evaporator area is reduced by 3.8% and 3.3% for R134a and R245fa, respectively, when increasing the expander isentropic efficiency from 70% to 80%. Furthermore, the condenser area decreases by 4.7% and 5.1% using R134a and R245fa, respectively, for the same range of the expander isentropic efficiency. Although the overall heat transfer coefficients in the evaporator and condenser decrease which lead to increasing the required areas, the heat transfer rates in these components also decrease. The rate of decreasing the latter is higher than that of the former, resulting in a decrease in the evaporator and condenser areas.

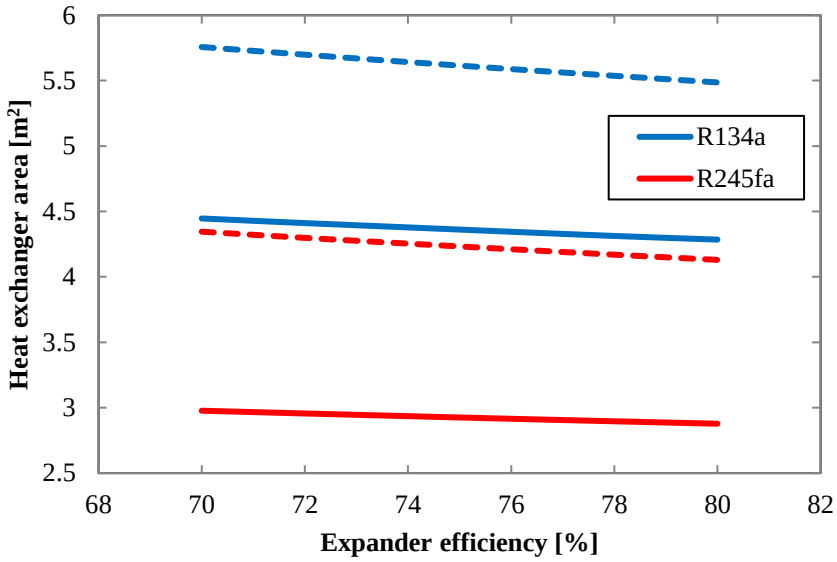

Figure 4.31 Effect of expander isentropic efficiency on the evaporator area (solid line) and condenser area (dashed line)

4.5.6 The effect of pump isentropic efficiency

The pump isentropic efficiency also affects the overall performance of hybrid ORC system; however, its effect is not as strong as that of the expander isentropic efficiency. The effect of the pump isentropic efficiency on the main system parameters are presented in Table 4.5. Duo to this slight influence, the results are presented only at the minimum and maximum values of the pump isentropic efficiency. As shown in the Table, the ORC and overall efficiency slightly increase as the pump isentropic efficiency increases from 70% to 80% for both working fluids. This is due to the reduction in the pump power. Also,

there are very small decreases in the working fluid, HTF and cooling water mass flow rates. The Table also shows that the ETC area decreases only by 2.36% and 0.57% using R134a and R245fa, respectively, as the pump isentropic efficiency increases from 70% to 80%. Moreover, the changes in the evaporator and condenser areas with the pump isentropic efficiency for both working fluids are insignificant and less than 1%.

Table 4.5 The effect of the pump isentropic efficiency on the system performance

Parameter	R134a		R245fa	
	$\eta_p = 70\%$	$\eta_p = 80\%$	$\eta_p = 70\%$	$\eta_p = 80\%$
ORC efficiency, %	7.39	7.56	10.10	10.16
Overall efficiency, %	5.37	5.50	7.15	7.19
Working fluid mass flow rate, kg/s	0.774	0.755	0.431	0.429
HTF mass flow rate, kg/s	0.694	0.676	1.25	1.24
Cooling water mass flow rate, kg/s	2.71	2.65	1.73	1.72
ETC area, m^2	266.02	259.75	199.86	198.73
Evaporator area, m^2	4.38	4.36	2.930	2.926
Condenser area, m^2	5.65	5.62	4.239	4.232

4.6 Summary

In this chapter, the overall thermodynamic performance results of the hybrid ORC system were presented. The selection procedure of the optimal working fluid for the proposed ORC system was firstly described. Based on thermo-economic, safety and environmental criteria, R245fa and R134a were selected for further investigations among different potential candidates. The hybrid ORC system was investigated under different solar and biomass energy supply share scenarios using different ETCs. Increasing the solar share reduces the overall system efficiency. In addition, a comprehensive parametric analysis was performed, aiming for assessing the influence of different operating parameters on the overall system performance. It can be concluded that the evaporation pressure and condensation temperature have the most profound impacts on the system performance as well as the equipment sizing whereas the pump isentropic efficiency has almost no effect.

Chapter 5 Economic Analysis of the Hybrid ORC System

This Chapter outlines the economic analysis of the proposed hybrid ORC system. The estimation procedure to obtain the total capital cost based on the individual costing correlation for each component in the system is described. All other direct and indirect costs as well as the operating and maintenance expenses are taken into account. The effect of different operating parameters on the economic indicators of the system is discussed in this Chapter. The simulation model using a MATLAB/Simulink environment is also presented.

5.1 Introduction

The successful completion of any thermal system design requires estimation of the major costs involved in the system using techniques from engineering economics. After calculation of all costs involved an important phase, with respect to the design of thermal systems, is then selection between different alternatives [203]. A very large initial investment for a given system would not be attractive for investors. Decisions at various stages of the design are also affected by economic considerations. The choice of materials and components is often determined by the costs involved [204].

Although the overall system performance is of key importance of any thermal power system, the economic considerations cannot be ignored. However, the task of reduction of system costs and maintaining high system performance is a great challenge. An economically-feasible ORC system design depends on the working fluid selection as well as the design and operating features of the system**.** Different working fluids or operating parameters could lead to different equipment sizing to ensure the desired energy transfer processes, resulting in changes in costs of the final system products [147, 205].

Therefore, the economic aspects should be closely coupled with the technical and performance considerations in the development of a thermal system in order to achieve the desired objectives.

The economic analysis is discussed in this chapter, based on a commonly used method for evaluating the economics of the proposed hybrid ORC system. The cost estimation is conducted after the flow rates and thermodynamic states have been determined and the sizes and materials have been specified for each component in the system. The total capital cost and the levelized energy cost are among the economic indicators used in the current economic analysis to evaluate the system economic feasibility. The total capital cost is determined based on the individual costing correlation of each component in the system, considering all the direct and indirect costs of the proposed equipment. The operating and maintenance (O&M) expenses are also evaluated as a fraction of the total capital cost.

In addition, the economic analysis is conducted for the proposed system using the previously selected working fluids meeting the same value of net power output in order to select among different alternatives. Also, a parametric analysis is performed, aiming for assessing the influence of variations in the operating parameters on the system economic performance. The economic feasibility computations of the proposed hybrid ORC system are carried out in the Simulink® environment. The developed Simulink economic model is integrated with the hybrid ORC Thermolib simulation model, described in Chapter 3, in which the equipment sizing and design parameters data is obtained.

5.2 Total Cost Estimation

The total capital cost estimation is crucial for evaluation of processing alternatives in most engineering endeavours, particularly in all design stages and economic analysis. In engineering practice, the estimation of costs receives much more attention than revenue estimation. The total capital cost of a thermal power system is a one-time expense for the design and construction [206].

For cost estimates to be reasonable and accurate enough to support economic scrutiny, numerous costs other than the purchased cost of equipment must be considered in the total capital cost evaluation of a power plant. A list of these cost items is summarized in Table 6.1 as described in Seider et al [207].

Table 5.1 Items of total capital cost estimation

Cost item
A. Direct costs
1. Purchased equipment cost
2. Materials required for installation
3. Labour to install equipment and materials
B. Indirect costs
1. Freight, insurance and taxes
2. Construction overhead
3. Contractor engineering expenses

Direct costs are referred to the purchased equipment costs at the manufacturer's site, the costs of materials for installation and the costs of labour to install all equipment. The costs of materials required for installation include piping, instrumentation and controls, and lighting and electrical equipment.

Indirect costs include all other costs such as the costs of freight to deliver the equipment to the plant site, with associated insurance and taxes. These are accompanied by construction overhead costs which include the fringe benefits for the workers (health insurance, vacation pay, sick leave, etc.), so-called burden (social security tax, unemployment insurance, etc.) and salaries of supervisory personnel. The contractor engineering expenses are also considered to be indirect costs. This covers the costs of engineering supervision and inspections, designers, drawings, including salaries and procurement expenses.

Auxiliary expenses such as the cost of land and cost of spares are not considered in the present economic analysis.

To estimate the total cost of the hybrid ORC system, the module costing technique, described by Turton et al. [208], is used. This technique is one of the common cost estimation approaches for thermal power system equipment and has been also used for cost evaluation of ORC systems [209-211].

5.2.1 Equipment Cost Estimation

The total cost of the proposed system is basically determined by the costs of the major system components, including the evaporator, condenser, expander, pump, solar collector, biomass boiler, electric generator, and pump motor. Therefore, it is essential for the cost of each individual component in the system to be available in order to estimate the total plant cost.

Given the purchased cost of equipment, the total installed cost of the equipment is obtained by adding the cost of installation. As mentioned in the previous section, the module costing approach is adopted in the present cost evaluation. In this approach, introduced by Guthrie (1969, 1974), the cost of installation is estimated using factored-cost methods based on the purchased cost of the equipment at base conditions. Deviations from the base conditions are handled using multiplying factors, depending on the specific equipment type, material of construction and operating pressure. These factors are provided for each piece of equipment to estimate the direct costs of materials and labour, as well as all indirect costs, involved in the installation procedure. When these costs are added to the purchased cost, the resultant total installed cost of the equipment is called *bare-module cost.* In the technique used in this study, all of these data are obtained from a survey of equipment manufacturers and quotes from vendors for a variety of common thermal power system equipment.

The bare module cost for each piece of equipment (*i*), which represents the sum of the direct and indirect costs listed in Table 5.1, is calculated as described by Turton et al. [208].

$$C_{BM,i} = C_{P,i}^{0} F_{BM,i} \tag{5.1}$$

where $C_{BM,i}$ is the bare module equipment cost; $C_{P,i}^{0}$ is the purchased equipment cost at base conditions: equipment made of the most common material, usually carbon steel, and operating at ambient pressure; $F_{BM,i}$ is the bare module factor.

In order to estimate bare module costs for equipment, purchased costs for the equipment at base case conditions must be available along with the corresponding bare module factor and other factors to account for different operating pressures and materials of construction. The basic purchased cost of a given component is correlated as a function of its design size parameter such as the heat exchanger area, expander power or pump power. The costs obtained using these correlations are estimated in US dollars.

For all heat exchangers, including the evaporator and condenser, the purchased equipment cost at the base condition (carbon steel and ambient pressure) is calculated in terms of the heat transfer surface area by the following equation

$$\log_{10} C_{P,hx}^{0} = K_{1,hx} + K_{2,hx}\log_{10}(A_{hx}) + K_{3,hx}[\log_{10}(A_{hx})]^{2} \tag{5.2}$$

where A_{hx} is the heat exchanger area in m^2. $K_{1,hx}$, $K_{2,hx}$ and $K_{3,hx}$ are constants for the heat exchanger type. These constants are given in Table 5.2 for the plate heat exchanger.

The bare module factor of the heat exchanger is given by

$$F_{BM,hx} = B_{1,hx} + B_{2,hx}F_{M,hx}F_{P,hx} \tag{5.3}$$

where $B_{1,hx}$ and $B_{2,hx}$ are constants depending on the heat exchanger type; $F_{M,hx}$ is a factor to account for material of construction (stainless steel) and $F_{P,hx}$ is the pressure factor which can be determined from the following relation

$$\log_{10} F_{P,hx} = C_{1,hx} + C_{2,hx}\log_{10}(P_{hx}) + C_{3,hx}[\log_{10}(P_{hx})]^{2} \tag{5.4}$$

where P_{hx} is the operating gauge pressure in the heat exchanger in bar gauge; $C_{1,hx}$, $C_{2,hx}$ and $C_{3,hx}$ are coefficients for the heat exchanger type.

The purchased cost of the expander at base conditions is given by the following equation

$$\log_{10} C_{P,t}^{0} = K_{1,t} + K_{2,t}\log_{10}(\dot{W}_{t,s}) + K_{3,t}\left[\log_{10}(\dot{W}_{t,s})\right]^{2} \tag{5.5}$$

where $\dot{W}_{t,s}$ is the mechanical output power in kW. $K_{1,t}$, $K_{2,t}$ and $K_{3,t}$ are constants for the expander type. The bare module factor used to calculate the bare module cost of the expander is given in Table 5.2.

The pump used in the proposed hybrid ORC system is a centrifugal type. The basic purchased cost of the pump is estimated based on the following equation

$$\log_{10} C_{P,p}^{0} = K_{1,p} + K_{2,p}\log_{10}\left(\dot{W}_{p,s}\right) + K_{3,p}\left[\log_{10}\left(\dot{W}_{p,s}\right)\right]^{2} \tag{5.6}$$

where $\dot{W}_{p,s}$ is the pump power in kW. $K_{1,t}$, $K_{2,t}$ and $K_{3,t}$ are constants for the pump type. The bare module factor of the pump is given as

$$F_{BM,p} = B_{1,p} + B_{2,p}F_{M,p}F_{P,p} \tag{5.7}$$

where $B_{1,p}$ and $B_{2,p}$ are constants for the pump type; $F_{M,p}$ is equipment material factor and $F_{P,p}$ is the pressure factor. The pressure factor for the pump can be obtained using the following equation

$$\log_{10} F_{P,p} = C_{1,p} + C_{2,p}\log_{10}\left(P_{p}\right) + C_{3,p}\left[\log_{10}\left(P_{p}\right)\right]^{2} \tag{5.8}$$

where P_p is the pump discharge pressure; $C_{1,p}$, $C_{2,p}$ and $C_{3,p}$ are pump-type constants.

The basic purchased cost of the pump motor depends on its power consumption. The cost of an *open, drip-proof* motor type is given by the following equation [207]

$$\begin{aligned}\ln C_{P,m}^{0} = {} & K_{1,m} + K_{2,m}\ln\left(\dot{W}_{p}\right) + K_{3,m}\left[\ln\left(\dot{W}_{p}\right)\right]^{2} + K_{4,m}\left[\ln\left(\dot{W}_{p}\right)\right]^{3} \\ & + K_{5,m}\left[\ln\left(\dot{W}_{p}\right)\right]^{4}\end{aligned} \tag{5.9}$$

where $\dot{W}_p$ is the required electrical power for the pump in hp. $K_{1,m}$, $K_{2,m}$, $K_{3,m}$, $K_{4,m}$ and $K_{5,m}$ are constants for the motor cost equation.

For the electric generator, the purchased equipment cost is determined using the following formula as presented in [129]

$$C_{P,g}^{0} = K_{1,g}\left(\dot{W}_{t}\right)^{k_{2,g}} \tag{5.10}$$

where $\dot{W}_t$ is the electrical output power of the generator in kW. $K_{1,g}$ and $K_{2,g}$ are constants for the generator cost estimation equation. The bare-module factors of the pump motor and electric generator are listed in Table 5.2 as given in [208] and [212], respectively.

The solar collector used in the proposed hybrid ORC system is an evacuated tube collector (ETC) type. Apart from the technology, the collector costs also depend on the size of the collector. Collector modules with large areas are cheaper, relative to their size, than small collectors [213]. The cost of the ETC is calculated using the unit price obtained from the literature. A survey on the ETC prices was conducted, in 2013, by Shatat et al. [214] based on data from various suppliers. It was reported that the unit cost of the ETC is estimated as \$150 per square metre. Nafey et al. [112] stated that the solar collector costs about \$150-200 /m^2.

In this study, a value of \$150/m^2 is adopted to evaluate the ETC purchased cost. The purchased equipment cost of the ETC is then calculated as

$$C_{P,ETC}^{0} = A_{col}.\bar{C}_{ETC} \tag{5.11}$$

where A_{col} is the collector aperture area and $\bar{C}_{ETC}$ is the collector unit price. In order for the cost items listed in Table 5.1 to be considered, the cost of the component is estimated as 4.3 times the purchased equipment cost as given by Bejan [203].

The cost of the biomass boiler is estimated based on a quotation received by Northumbria University from ENOGIA [215] in 2013. The biomass boiler with a capacity of 116 kW thermal output costs about \$81,500 including installation, shipping and accessories costs.

The cost rate of biomass fuel can be determined using the following equation [135]

$$\dot{C}_{bf} = \bar{C}_{bf}.\dot{m}_{bf}.LHV_{bf} \tag{5.12}$$

where $\bar{C}_{bf}$ is the biomass fuel unit cost which takes the value of 0.01 \$/kWh [135]. The fuel cost per kWh output is then defined as

$$C_{bf} = \dot{C}_{bf}/\dot{W}_{net} \tag{5.13}$$

Although the working fluid is also an item of the ORC system, the working fluid cost is not considered in the total cost estimation of the present economic analysis. This is based on the assumption of the previous studies, indicating that the working fluid cost is very small compared to the total system cost [209, 216, 217].

The constants required for cost estimation for all system equipment are listed in Table 5.2.

Table 5.2 Constants for cost estimation of system equipment

Constant	Value	Constant	Value	Constant	Value
Heat exchanger (Stainless steel)		$K_{3,t}$	-0.1776	$K_{2,m}$	0.1314
		$F_{BM,t}$	6.1	$K_{3,m}$	0.053255
$K_{1,hx}$	4.6656	**Pump** (Carbon steel)		$K_{4,m}$	0.028628
$K_{2,hx}$	-0.1557			$K_{5,m}$	0.0035549
$K_{3,hx}$	0.1547	$K_{1,p}$	3.3892	$F_{BM,m}$	1.5
$C_{1,hx}$	0.0	$K_{2,p}$	0.0536	**Electric generator**	
$C_{2,hx}$	0.0	$K_{3,p}$	0.1538	$K_{1,g}$	60
$C_{3,hx}$	0.0	$C_{1,p}$	-0.3935	$K_{2,g}$	0.95
$B_{1,hx}$	0.96	$C_{2,p}$	0.3957	$F_{BM,g}$	1.5
$B_{2,hx}$	1.21	$C_{3,p}$	-0.00226	**Solar collector**	
$F_{M,hx}$	2.45	$B_{1,p}$	1.89	$F_{BM,ETC}$	4.3
Expander (Stainless steel)		$B_{2,p}$	1.35		
		$F_{M,p}$	1.6		
$K_{1,t}$	2.6259	**Pump motor**			
$K_{2,t}$	1.4398	$K_{1,m}$	5.4866		

5.2.2 Cost Index

The cost data used for any equipment cost evaluation are often applicable only for a particular time, usually an average of a particular year. These costs, however, generally increase with time due to inflation. Therefore, all cost data used in the economic analysis must be brought to the same reference year. This can be achieved with the use of an appropriate cost index as indicated in the following general relation [206]

$$Cost\ at\ time\ t = Cost\ at\ time\ t_0 \left(\frac{Cost\ index|_t}{Cost\ index|_{t_0}} \right) \tag{5.14}$$

The cost index is an inflation indicator used to update the cost of equipment items, materials and labour. Examples of some common existing cost indices include Chemical Engineering Plant Cost Index (CEPCI), Marshal and Swift (M&S) Equipment Cost Index, Engineering News Record (ENR), Construction Cost Index and Nelson-Farrar Refinery Cost Index. For thermal design projects, M&S is recommended for single equipment items. However, CEPCI is recommended for whole plants or group of components [203].

In this study, the Chemical Engineering Plant Cost Index (CEPCI) is used to consider the effect of inflation. CEPCI takes into consideration the costs of labour and material to fabricate the equipment, installation, and its delivery. It is also applied to several categories of processing equipment, including heat exchangers, pumps, compressors and other machinery. CEPCI is published on a monthly basis in the Chemical Engineering Magazine with a value of 100 for the year 1958 [218].

It should be noted that the correlations for purchased equipment cost estimation, described in [203], for the heat exchanger, expander and pump were developed based on the CEPCI of 397 for the year of 2001. The pump motor purchased cost correlation is indexed to mid-2000 with CEPCI of 394, as given in [207]. The electric generator equation is based on 2010 with CEPCI equal to 550.8 [129]. For the ETC and biomass boiler, the corresponding CEPCI for the year 2013 is 567.3. A value of CEPCI equal to 556.8, corresponding to the year of 2015, is used in this study to update all the equipment costs to the same reference year.

The total capital cost is the sum of costs of all system components as given by the following equation

$$C_{tot} = \sum_{i=1}^{n} C_{BM,i} \cdot \left(\frac{CEPCI_{2015}}{CEPCI_{t(i)}} \right) \tag{5.15}$$

Here, $CEPCI_{t(i)}$ is the cost index corresponding to time at which the data-based correlation was developed of the system component (i).

5.3 Levelized Energy Cost

There are several criteria used as a measure of economic soundness of a given system to select the most attractive alternative. The levelized energy cost (LEC) is considered as a useful evaluation criterion for the economic performance of thermal power systems. It is an indicator for the electricity production cost. In contrast to the total capital cost, the levelized energy cost takes into consideration the system effective operation time, the capital recovery cost and the operating and maintenance cost [216].

The levelized energy cost can be estimated based on the following relation [219]

$$LEC = (CRF.C_{tot} + C_{OM})/(t_{op}.\dot{W}_{net}) \quad (5.16)$$

where CRF is the capital recovery factor, C_{OM} is the operating and maintenance cost and t_{op} is the annual operation time. The operating and maintenance cost is estimated to be as 1.5% of the total capital cost and the annual operation time is assumed to be 8000 hours [219].

The capital recovery factor can be expressed as [83, 220].

$$CRF = i(1+i)^{LT_{pl}}/[(1+i)^{LT_{pl}} - 1] \quad (5.17)$$

where the interest rate i is set as 5% and the plant life time LT_{pl} is set as 20 years [220].

5.4 Economic Results

The estimation of the system costs at different net power output could lead to inaccurate outcomes due to the concept of economy of scale. In this work, the equipment cost estimation as well as the system economic indicators are evaluated for the same system net power output of 10 kW during changing the operating conditions. The total capital cost and levelized energy cost are used as evaluation criteria for the hybrid ORC system. The results of using the two selected working fluids are then presented in such a way that comparison is made easy. In the economic analysis, the global solar irradiance value is set to 700 W/m^2. The developed Simulink model and its sub-models for

conducting all the system cost estimations are shown in Figs. 5.1 and 5.2, respectively. The flow chart of the calculation procedure in the economic modelling is shown in Fig. 5.3.

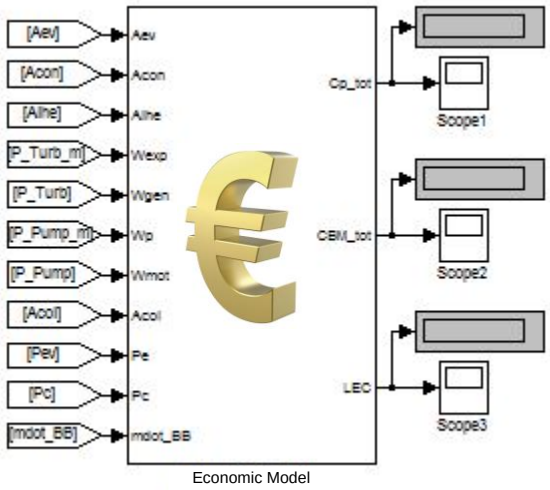

Figure 5.1 The overall economic Simulink model

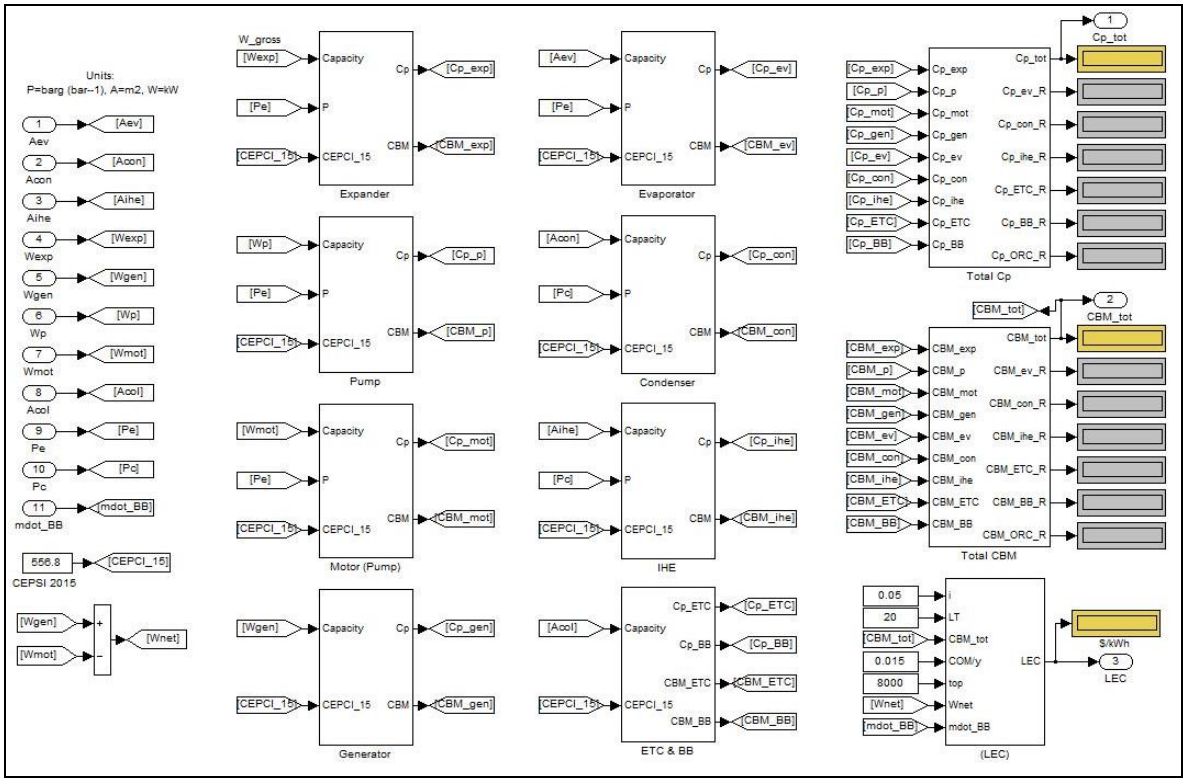

Figure 5.2 The economic Simulink sub-models of the system equipment

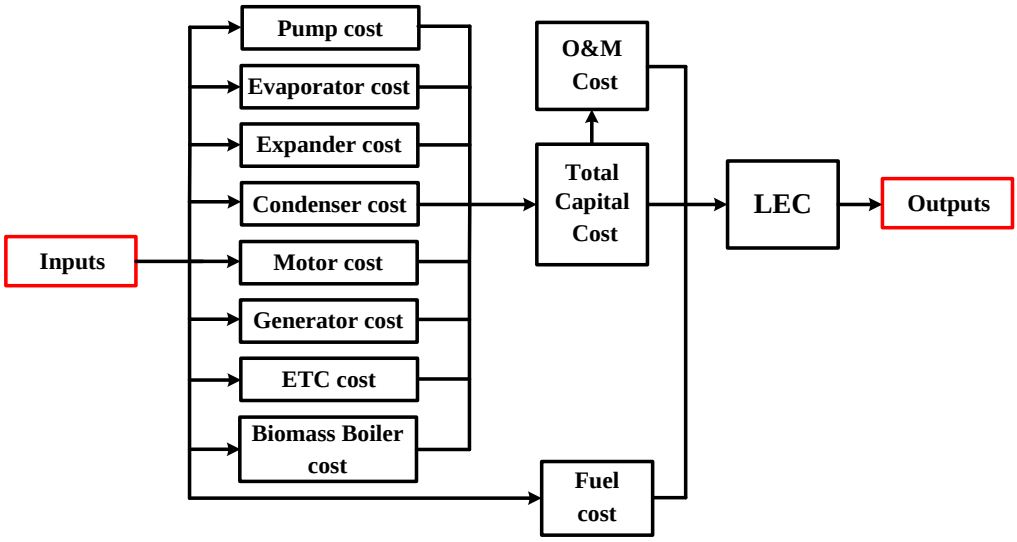

Figure 5.3 Flow chart of the economic model

5.4.1 The hybrid ORC system economic evaluation

In this section, the economic performance of the hybrid ORC system is investigated for a range of different scenarios based on the energy share of solar and biomass sources. It should be mentioned that the cost of the biomass boiler is included in the total capital cost estimation in all system operation modes including the 100% solar energy share. However, the ORC operating parameters are kept fixed.

Figs. 5.4 and 5.5 present the total capital cost and LEC for different solar and biomass energy share modes. Fig. 5.4 shows the variation of the total capital cost with the share of solar and biomass energy sources for two working fluids. It can be seen for both working fluids, increasing the solar energy share leads to a large increase in the total capital cost. As the solar share increases from 0% to 100%, the total capital cost increases by about 47% and 40% for R134a and R245fa, respectively. This is mainly due to the larger ETC area needed at higher values of solar energy share. The figure also indicates that the system total capital cost for R245fa is comparatively lower than that for R134a under the same operating conditions. The total capital cost with R134a is in average 14% higher than the cost with R245fa. The hybrid ORC system with R134a requires larger ETC and heat exchanger area as compared to that with R245fa.

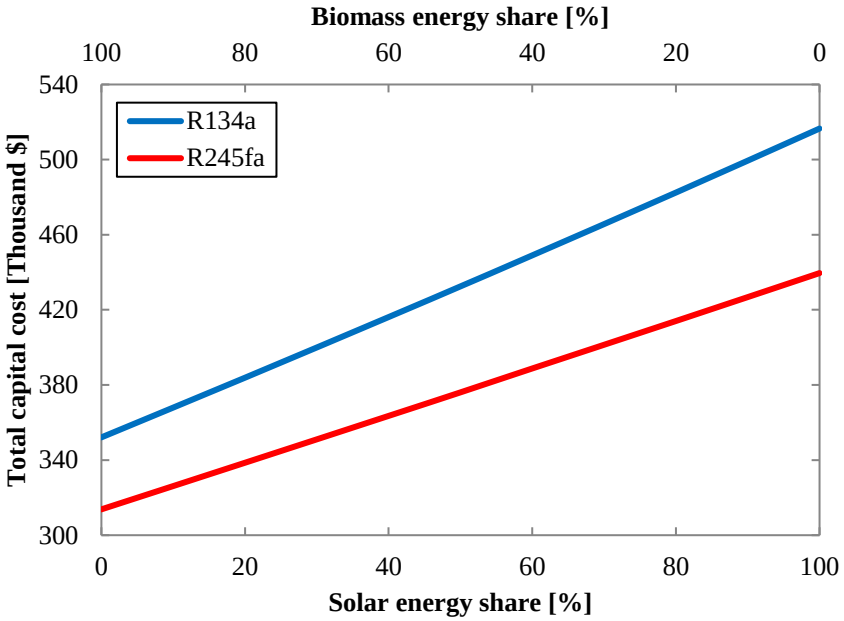

Figure 5.4 Variation of the total capital cost with the solar and biomass energy share

The LEC is an indicator for the electricity production cost and it is used to evaluate the economic performance of the hybrid ORC system. Fig. 5.5 shows the variation of the LEC with the share of solar and biomass energy sources for the two working fluids. The figure shows that the LEC values increase with the increase of the solar energy share for both working fluids. Increasing the solar energy share leads to an increase in the required ETC area but a decrease in the biomass fuel consumption. However, the increase rate of the ETC cost is higher than the decrease rate of the biomass fuel cost and this explains the increase in the LEC values. Obviously, the system with R245fa has lower LEC values compared to those with R134a. In the biomass energy mode, the LEC values are $0.575 /kWh and $0.489/kWh for R134a and R245fa, respectively. In the hybrid mode, these values are $0.615/kWh and $0.523/kWh for R134a and R245fa, respectively.

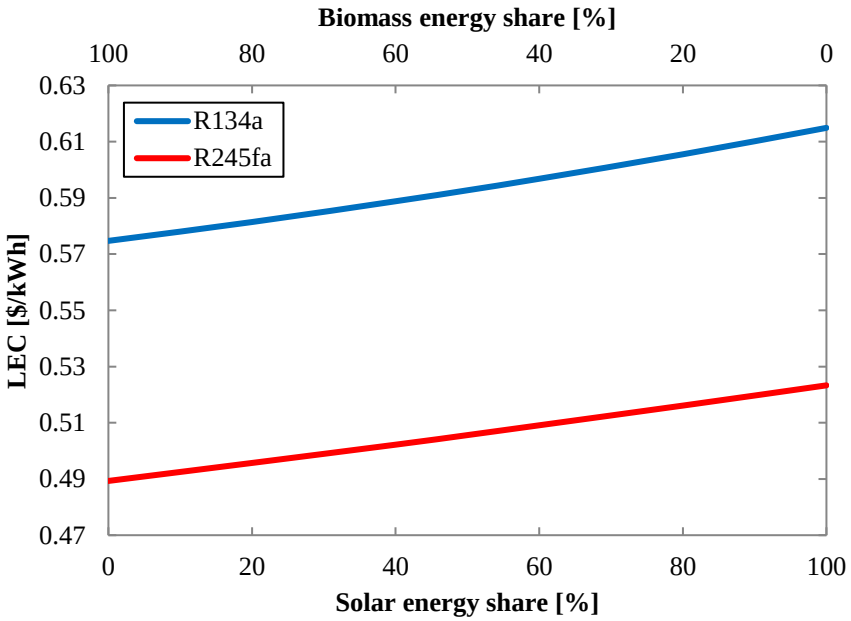

Figure 5.5 Variation of the LEC with the solar and biomass energy share

Fig. 5.6 illustrates the share of the different system components in the total capital cost in the hybrid operation mode for the two working fluids. It is obvious from the figure that the heat source (ETC and biomass boiler) represents a considerable share in the total capital cost with about 47.3% and 46.8% for R134a and R245fa, respectively. Also, the solar collector field has the largest share in the total capital cost for both fluids. It accounts for 31.8% and 28.6% for R134a and R245fa, respectively. With regard to the ORC components, the condenser represents the largest share with 18.5% and 18.9% for R134a and R245fa, respectively, followed by the evaporator. The pump accounts for only about 3% for both working fluids.

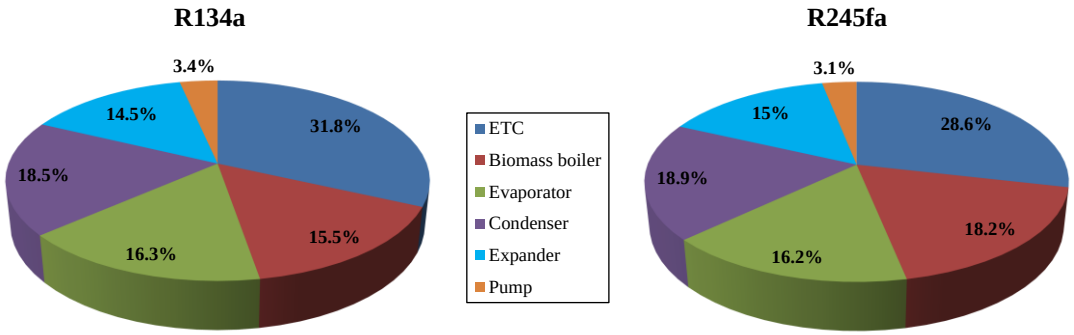

Figure 5.6 The share of system components in the total capital cost in the hybrid operation mode

5.4.2 Effects of system operating parameters

In this section, the economic performance of the hybrid ORC system is investigated for a range of different operating parameters. The effects of the evaporation pressure, condensation temperature, pinch point temperature difference in the evaporator and condenser, expander isentropic efficiency and pump isentropic efficiency are discussed. Only the value of one parameter varies whereas the remaining parameters are kept constant and equal to the basic values as listed in Table 4.4.

Fig. 5.7 shows the effect of the evaporation pressure on both the total capital cost and LEC for the both selected working fluids. As it can be seen in Fig. 5.7a, the total capital cost significantly decreases as the evaporation pressure increases for both fluids. The minimum total capital cost is obtained at the maximum evaporation pressure of each working fluid. For the same net output power, the hybrid ORC system requires a much smaller ETC area as well as smaller evaporator and condenser areas as the evaporation pressure increases and consequently the total capital cost decreases. A reduction in the total capital cost by approximately 14% is obtained for both working fluids when increasing the evaporation pressure from its minimum to the maximum operating value of each working fluid. Also, Fig. 5.7b shows that the LEC value sharply decreases with increasing the evaporation pressure. The minimum LEC values are also found corresponding to the minimum total capital cost value for both working fluids. At the maximum operating

pressures, the system with R245fa has a smaller LEC value of $0.523/kWh compared to $0.615/kWh for R134a.

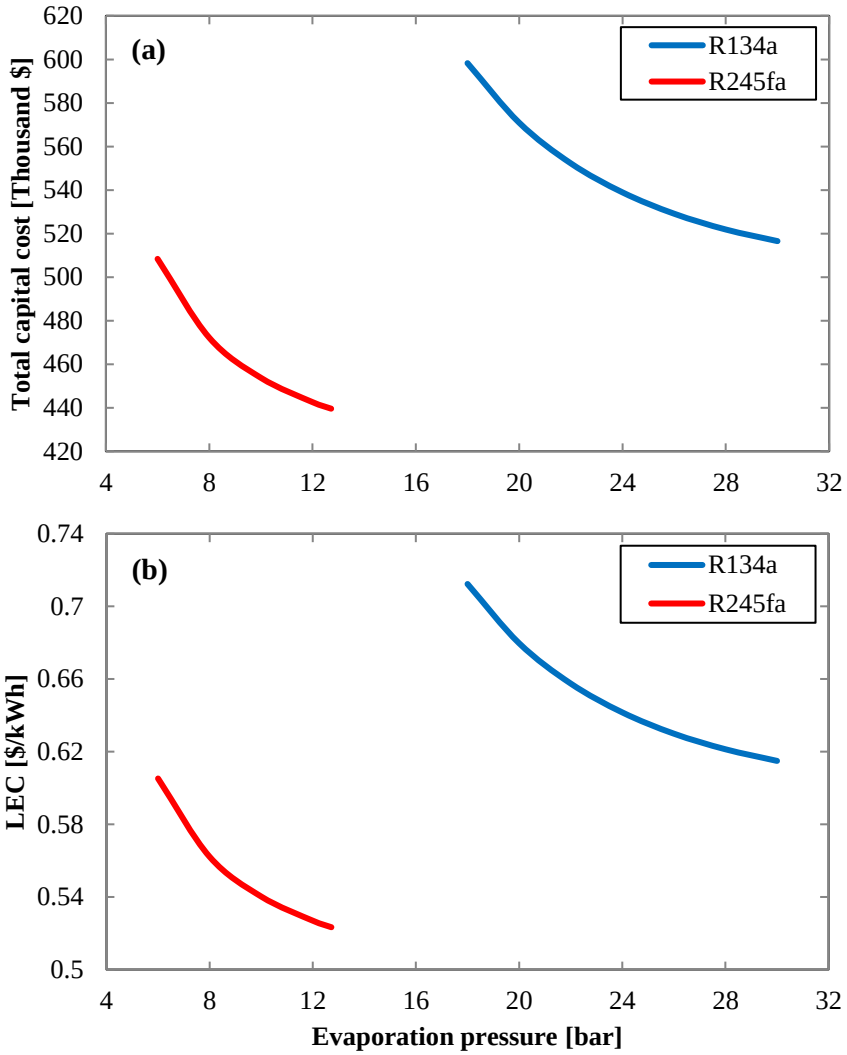

Figure 5.7 Effect of evaporation pressure on the total capital cost and LEC

The effect of the condensation temperature on the total capital cost and LEC is presented for both working fluids in Fig. 5.8. Fig. 5.8a demonstrates that the total capital cost increases with increasing the condensation temperature for the two working fluids. It can be noticed that the minimum total capital cost is found at the minimum condensation temperature. The total capital cost decreases by 8.1% and 5.5% for R134a and R245fa, respectively, as the condensation temperature decreases from 40 ^{o}C to 30 ^{o}C. This can be attributed to the reductions in the required ETC area as well as evaporator and condenser

areas with decreasing the condensation temperature. In addition, for the investigated range of condensation temperatures, the use of R245fa instead of R134a reduces the total capital cost by an average of 15%. Similarly, as shown in Fig. 5.8b, the LEC values increase as the condensation temperature increases. Minimum LEC values are obtained at a condensation temperature equal to 30 ^{o}C for both working fluids. These values are found to be as \$0.59/kWh and \$0.509/kWh for R134a and R245fa, respectively.

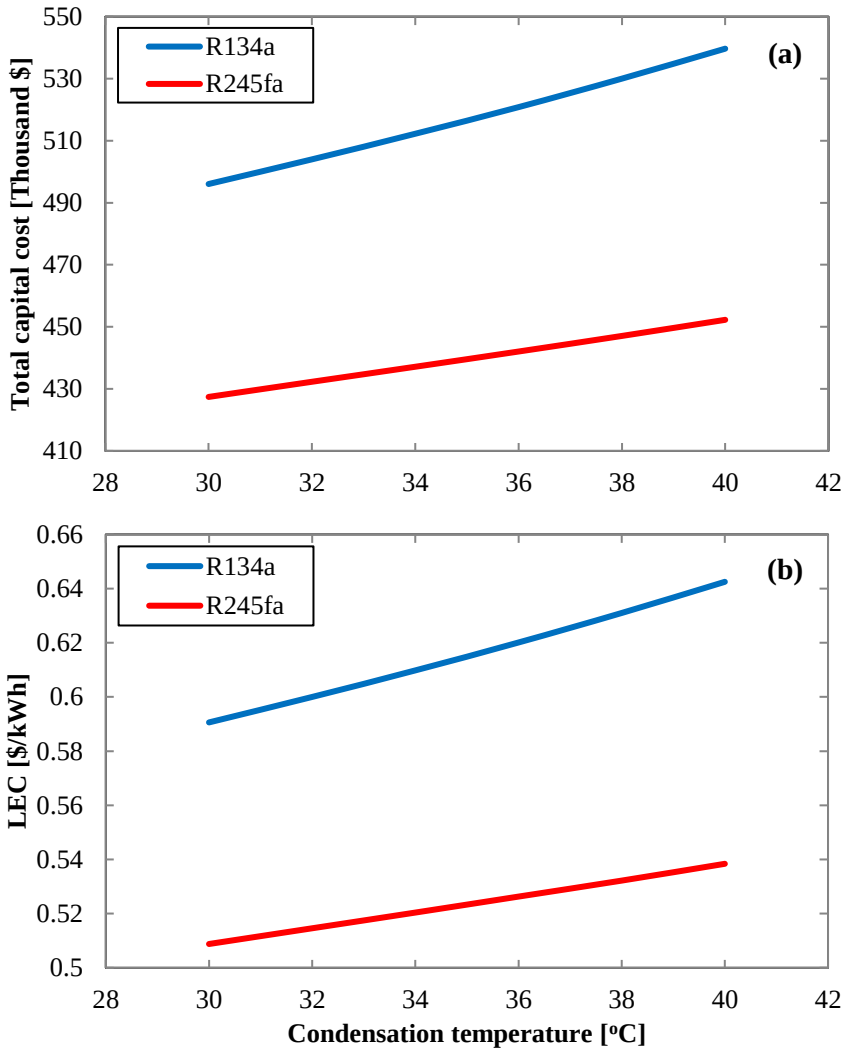

Figure 5.8 Effect of condensation temperature on the total capital cost and LEC

The effect of the evaporator pinch point temperature difference, ΔTpp_e, on the total capital cost and LEC for two working fluids is depicted in Fig. 5.9. As it is demonstrated in Fig. 5.9a, the total capital cost steadily decreases with increase of the pinch point temperature

ΔTpp_e. Although the ETC area slightly increases with increasing the pinch point temperature ΔTpp_e, the evaporator area significantly decreases which in turn leads to the decrease in the total capital cost. As the pinch point temperature ΔTpp_e increases from 6 K to 12 K, the total capital cost decreases by 3.1% and 2.4% for R134a and R245fa, respectively. Fig. 5.9b shows that the LEC values also decline with the raise of the pinch point temperature ΔTpp_e for both working fluids. The LEC values decrease from \$0.627/kWh to \$0.608/kWh for R134a and from \$0.531/kWh to \$0.518/ kWh for R245fa as the pinch point temperature ΔTpp_e increases from 6 K to 12 K.

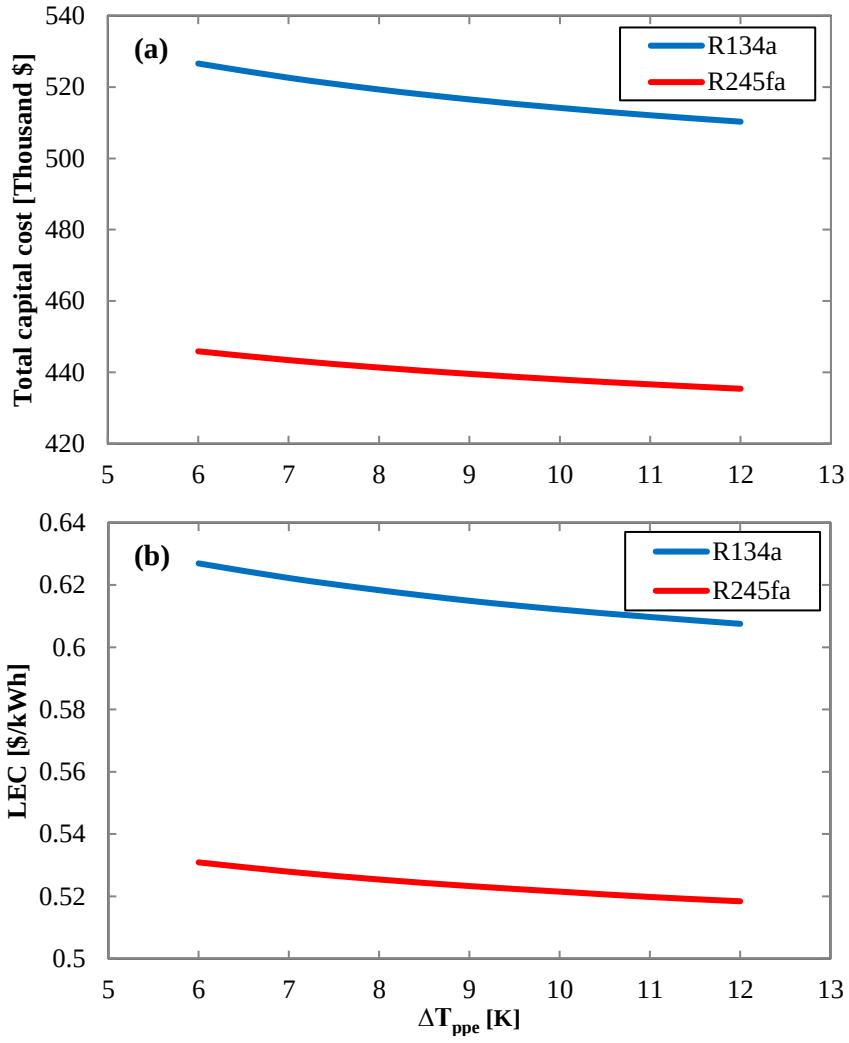

Figure 5.9 Effect of evaporator pinch point temperature on the total capital cost and LEC

Fig. 5.10 shows the effect of the pinch point temperature difference in the condenser, ΔTpp_c, on both the total capital cost and LEC for both selected working fluids. Fig. 5.10a shows that the total capital cost gradually decreases with increasing the pinch point temperature ΔTpp_c. This is due to the fact that a smaller condenser area is needed at higher values of the pinch point temperature ΔTpp_c. Increasing the pinch point temperature ΔTpp_c from 4 K to 8 K leads to a reduction in the total capital cost by about 4.5% for R134a and by 4% for R245fa. A similar trend can be noticed in Fig. 5.10b for the LEC with the condenser pinch point temperature ΔTpp_c. As the pinch point temperature ΔTpp_c increases from 6 K to 12 K, the LEC values decrease from \$0.632/ kWh to \$0.603/ kWh for R134a and from \$0.536/ kWh to \$0.515/ kWh for R245fa.

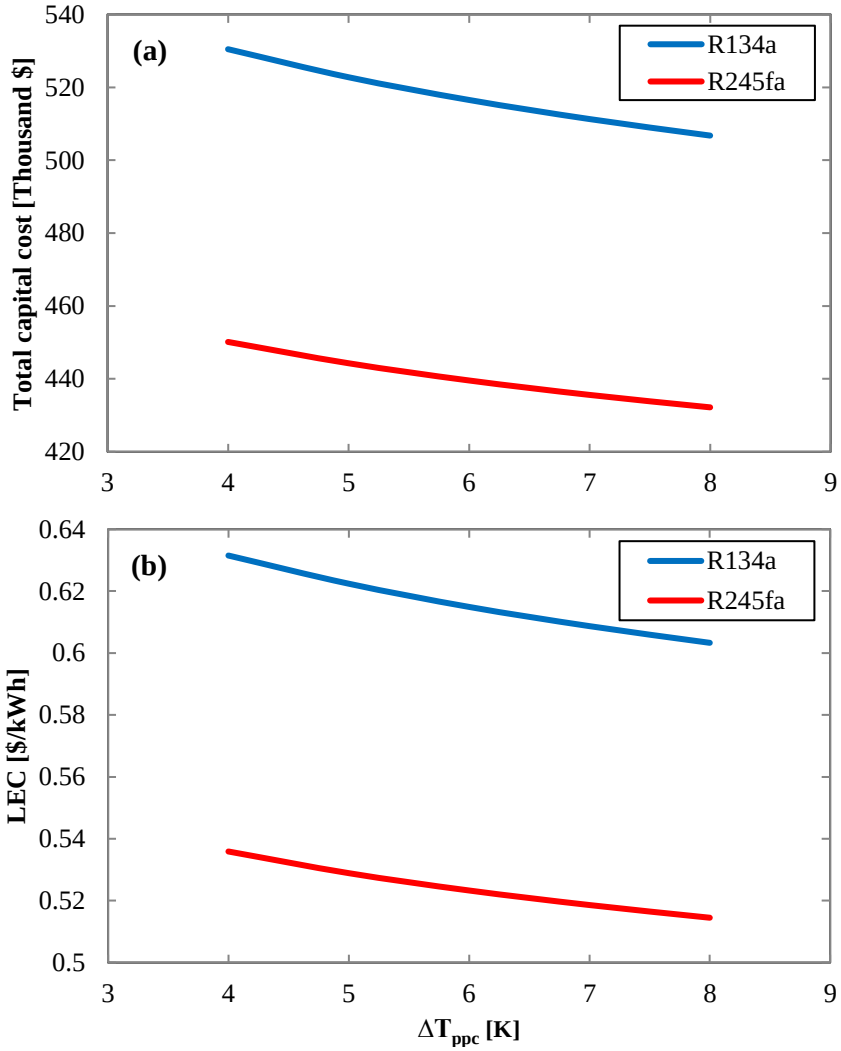

Figure 5.10 Effect of condenser pinch point temperature on the total capital cost and LEC

The influence of the expander isentropic efficiency on the total capital cost and LEC for both working fluids is illustrated in Fig. 5.11. As it can be seen from Fig. 5.11a, the total capital cost decreases as the expander isentropic efficiency increases. Generally, increasing the expander isentropic efficiency leads to an improvement in the overall system performance, resulting in less ETC area as well as less evaporator and condenser areas. This explains the reduction in the total capital cost. The total capital cost is reduced by 6% and 4.6% for R134a and R245fa, respectively, as the expander isentropic efficiency increases from 70% to 80%. Fig. 5.11b shows that the LEC values decrease from \$0.636/ kWh to \$0.597/ kWh for R134a and from \$0.537/ kWh to \$0.512/ kWh for R245fa.

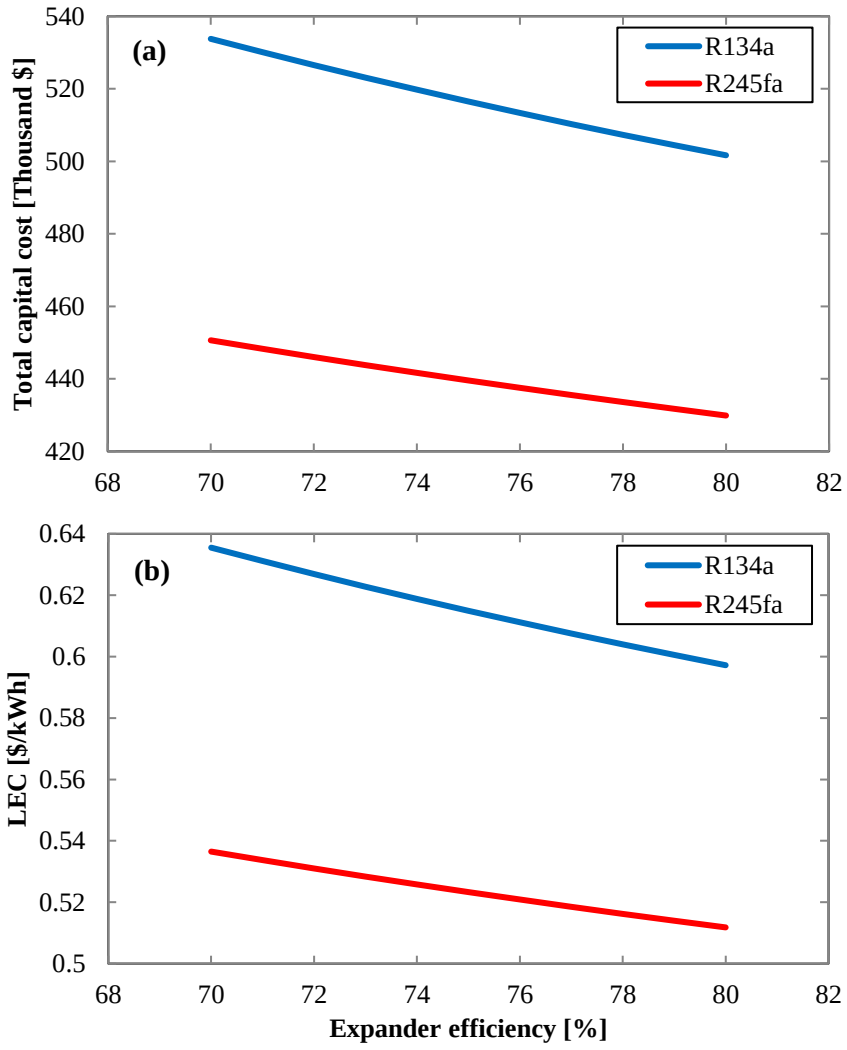

Figure 5.11 Effect of expander isentropic efficiency on the total capital cost and LEC

The effect of the pump isentropic efficiency on the total capital cost and LEC for both working fluids is presented in Table 5.3. As it can be seen, the total capital cost decreases by only 1.3% and 0.3% for R134a and R245fa, respectively, as the pump isentropic efficiency increases from 70% to 80%. Also, the LEC values drop from \$0.623/ kWh to \$0.615/ kWh for R134a and from \$0.525/ kWh to \$0.523/ kWh for R245fa.

Table 5.3 The effect of the pump isentropic efficiency on the economic performance

Parameter	R134a		R245fa	
	$\eta_p = 70\%$	$\eta_p = 80\%$	$\eta_p = 70\%$	$\eta_p = 80\%$
Total capital cost, \$	523,472	516,528	440,739	439,567
LEC, \$/kWh	0.6232	0.6149	0.5247	0.5233

5.5 Summary

Results of the economic analysis of the proposed hybrid ORC system are presented. The total capital cost was estimated based on the individual costing correlation for each component in the system, including all direct and indirect costs. A detailed parametric analysis of the proposed system was also conducted in this Chapter. It was found that the total capital cost of the hybrid ORC system is significantly affected by the selection of the working fluid used. Based on the thermo-economic performance conducted, R245fa was found to provide best results. The system operational parameters play a vital role in the system economics. Therefore, the best combination between the operating parameters should be established to obtain the optimal thermo-economic performance of the system. The optimization of the operating parameters will be the main objective in the following Chapter.

Chapter 6 Optimization of the Hybrid ORC System

From the parametric study conducted in the previous Chapters, the operating parameters were established that have more impact on the thermodynamic and economic performance of the hybrid ORC system. In order to determine the optimum set of operating parameters for a particular heat source, it is crucial to couple the overall ORC simulation model with an appropriate optimization technique. This chapter describes the optimization processes of the ORC system operating parameters based on the Genetic Algorithm approach. The results obtained from the optimization of the hybrid ORC system are also presented and discussed in this Chapter.

6.1 Optimization Approach

The optimization is an exploration technique to find the optimal solution for a given problem based on a specific criterion. The appropriate optimization approach needs to overcome several challenges. For instance, if there is more than one local optimum solution in the search domain, then there is a possibility for the optimization search to be trapped in a local optimum solution location rather than to converge to the global optimum. Moreover, if the search domain is quite large, then there is a possibility that the exact global solution cannot be found within a reasonable period of time. In addition, the problem nature and its degree of complexity play a vital role in the selection of the appropriate optimization technique that could be used to achieve the desired objectives [221]. If there is only one variable, the optimization is one-dimensional. Problems having more than one variable require multidimensional optimization. As the number of dimensions increases, optimization becomes increasingly difficult [222].

The optimization algorithms can be broadly classified into two main categories: conventional and evolutionary. The convergence of the conventional optimization

algorithms depends on the initial guess which might lead convergence onto a local optimal solution. The conventional optimization algorithms search for optimum solutions based on a point-by-point approach whereby the objective function guides the search towards optimum solutions. In addition, conventional methods are applicable only for certain types of problems with a limited number of design variables and less complexity. Moreover, these methods are sensitive to the design variables (continuous or discrete) and the objective function characteristic (smooth or non-smooth). Evolutionary Algorithms are one of the most widely used optimization methods nowadays in most aspects of the optimization problems. These methods are developed to overcome all of the preceding difficulties for which the conventional algorithms could not provide satisfactory results. In contrast to the conventional algorithms, evolutionary algorithms are less sensitive to the characteristics of the objective function and can handle larger number of design variables. The Genetic Algorithm (GA) optimization approach is the most common method of the evolutionary algorithms which shows excellent performance with most of the engineering problems. In addition, this approach is widely tested and validated in literature for a wide range of thermodynamic applications [221].

6.2 Genetic Algorithm

Genetic algorithm (GA) is an optimization and search technique to find the optimum solution of an optimization problem based on the principle of genetics and natural selection. The GA optimization method was firstly developed by John Holland during the 1960s and 1970s and it was described in his book published in 1975. The GA technique was then popularized by David Goldberg (1989) to be applicable for different disciplines including engineering applications. Basically, the GA method imitates the biological creation processes which occur naturally and it repeatedly enhances the characteristics from one generation to another aiming to achieve the optimum characteristics. The GA optimization process starts by generating the initial population which is formed by a random set of individuals called chromosomes. Each individual chromosome, which consists of an array of variables to be optimized, represents a possible solution to the

optimization problem. Only the fittest chromosomes would be able to be passed on to the next generation while the rest are discarded.

In the GA approach, the fitness acts as the criteria upon which the optimization process is based; and its value represents the solution encoded in the individual's chromosome. In order to measure the fitness value of each chromosome, an objective function needs to be defined and integrated into the optimization process. This objective function could be efficiency, power output, cost, etc. The set of chromosomes are then ranked based on their fitness values starting with the fittest one. Then, the fittest chromosomes are selected to be parents to reproduce newly generated chromosomes called offspring. The reproduction of offspring is performed by recombination of the crossover and mutation processes. The entire GA processes are repeated for several generations until the optimization criteria is satisfied [222].

The GA has several advantages over the conventional optimization methods which can be summarised in the following points:

- The GA can deal with both continuous and discrete variables.
- It is simple since derivative information is not required in the GA procedure.
- The GA is able to handle a large number of variables.
- It is suitable for simultaneous search and parallel calculations which significantly reduce the overall computational time.
- The GA can work with different data types of objective functions including numerical data, experimental data and analytical functions.

The optimization using GA method has two main techniques: binary and real-value (continuous). The binary GA technique is based on encoding and decoding the variable values. The variables are firstly converted into bit numbers made up of ones and zeros in the encoding process and then reversed to the original values in the decoding process. Both relatively large memory space and long computational time are required for the encoding and decoding processes, especially when a large number of variables are used in the optimization problem. In the real-value GA technique, the variables are denoted by single floating point numbers and the encoding and decoding processes are however eliminated [222].

In this work, the real-value GA is employed in order to reduce the computational time and avoid the PC memory limitations. The description of each calculation process of the GA method is presented in more details in the next sections.

6.3 Optimization of the hybrid ORC system using GA approach

An optimization procedure based on the real value GA approach is applied to the hybrid ORC system to determine the optimum operating parameters for the system using R245fa as the working fluid. The optimization of the system is conducted in which the net output power is maintained at 10 kW. The objective function, design variables and constraints, and overall optimization procedure are described in this section.

6.3.1 Definition of the objective function and design variables

In optimisation problems that include components' sizing, an appropriate objective function is required in which the system performance is maximized, whereas system complexity is minimized. System performance can be evaluated by the cycle efficiency or the net power output, while complexity is closely linked to the costs. Therefore, the objective function must quantify the trade-off between these aspects in order to obtain the optimal thermo-economic performance of the system. However, in such problems, a given parameter may influence the system performance and its cost differently in terms of the way and order of magnitude. In addition, the set of operating parameters that ensure the best thermodynamic performance could lead to a substantially expensive system as a result of larger equipment sizes required to perform the desired energy transfer processes. This of course adds a further complexity to the optimization problem.

The levelized energy cost (LEC), which needs to be minimized, is considered as the objective function for the optimization problem in this study. It is an indicator for the electricity production cost which can be basically minimized by reducing the total system cost and/or increasing the net output power.

Four operating parameters are selected in this study to be design variables of the optimization problem. These include the evaporation pressure (P_e), condensation temperature (T_c), pinch point temperature difference in the evaporator (ΔT_{ppe}) and pinch point temperature difference in the condenser (ΔT_{ppc}). The upper and lower boundaries of each variable are given in Table 6.1. The rest of the operating parameters are however kept unchanged. During the optimization, a number of constraints are considered for the working fluid conditions at the expander inlet and outlet. The maximum temperature at the expander inlet is 100 ^{o}C with a degree of superheating of zero whereas the vapour quality at the expander outlet must be greater than or equal to 0.95 to avoid erosion of the expander blades.

Table 6.1 Upper and lower limits of design variables for GA optimization

Parameter	Lower bound	Upper bound
Evaporation pressure, P_e	8 bar	P_{sat} at 100 ^{o}C
Condensation temperature, T_c	30 ^{o}C	40 ^{o}C
Evaporator pinch point temperature, ΔT_{ppe}	6 K	12 K
Condenser pinch point temperature, ΔT_{ppc}	4 K	8 K

The real-value GA optimization begins by defining a chromosome as an array of random values of the variables to be optimized. Thus, the chromosome can be written as an array with four elements as

$$Chromosome = \left(P_e, T_c, \Delta T_{ppe}, \Delta T_{ppc}\right) \tag{6.1}$$

Each chromosome, as a possible solution, is evaluated by its corresponding LEC value obtained from the overall Thermolib model of the hybrid ORC system. This can be formulated as

$$LEC = f(Chromosome) = f\left(P_e, T_c, \Delta T_{ppe}, \Delta T_{ppe}\right) \tag{6.2}$$

6.3.2 Initial population

To start the GA optimization procedure, an initial population is defined with N_{pop} chromosomes. If each chromosome consists of N_{var} variables, a matrix of $N_{pop} \times N_{var}$ random values is generated as

$$Population = rand(N_{pop}, N_{var}) \tag{6.3}$$

The size of the population strongly influences the overall computational time of the optimization problem, therefore N_{pop} should be carefully defined. The recommended number of chromosomes N_{pop} is between 30 and 100 per generation when using the GA optimization [223].

6.3.3 Evaluation

The developed Thermolib model of the hybrid ORC system is used to calculate the LEC for each chromosome. The corresponding LEC for each chromosome represents the value of the chromosome. To evaluate each chromosome, the fitness function is used which can be calculated for minimization problems using the following formula [224]

$$Fitness = \frac{1}{1 + value - value_{min}} \tag{6.4}$$

where $value$ is the value of each chromosome and $value_{min}$ is the minimum obtained value of all chromosomes.

6.3.4 Selection process

In the selection process, the chromosomes are firstly ranked based on their fitness values in a descending order. Only chromosomes with the highest fitness values will survive to be used to reproduce offspring for the next generation. The number of survival chromosomes N_{keep} depends on the selection rate X_{rate} as

$$N_{keep} = X_{rate} \times N_{pop} \tag{6.5}$$

The recommended value of the selection rate is 50%. In this case, only the fittest fifty percent of the generation are used for the next generation reproduction whereas the rest is discarded. Then, the chromosomes are randomly selected in pairs using the weighted random pairing selection method based on the rank weighting technique, described in [222], to be parents in the reproduction operation.

6.3.5 Mating process

In the mating process, the offspring is produced by a combination between the two parental chromosomes selected in the pairing process. Although, there are different approaches to combine the parental chromosomes in the real-value GA, the single point crossover is the simplest method for the mating process. In this method, one point in each parental chromosome is marked as a crossover point. Then, the variables allocated in these points are swapped between the two parental chromosomes [225].

6.3.6 Mutation process

In real optimization problems, there are often several local optimum points in the overall search domain in addition to the global optimum which represents the real target of the optimization problem. In order to avoid the optimization search of being converged to a local optimum, which may occur if the chromosomes become very similar, a mutation process is applied in which the search is redirected to explore a different area of the search domain. This is performed by introducing random changes into the values of certain variables in a number of chromosomes depending on the mutation rate. Thus, another region of the variable space is investigated. Mutation is neither applied on the best ranked chromosome nor on the final generation. In this study, a mutation rate of 20% is used which represents the fraction of the variables in the chromosomes to be altered. Although this value seems to be quite high which leads to slowing down the convergence process, it ensures that the global solution is obtained [222].

6.3.7 Convergence criteria

The GA optimization procedure described above is an iterative-based technique in which all the processes are continuously repeated until the optimum solution is reached. During the computation process, two stopping criteria need to be examined before the algorithm is terminated. The first criterion is met if the set maximum number of generations is exceeded. The recommended maximum number of generations is 80 in order to ensure that the algorithm reaches the optimum solution [225]. The second criterion is satisfied if the value of the objective function (LEC) remains without any significant change for at least twenty generations. In this scenario, the calculations are terminated before the maximum number of generations is reached.

6.4 MATLAB Implementation

A basic MATLAB code for the real-value GA optimization was presented by Haupt [222]. This code was further developed by Kraitong [225] for optimization of design parameters of Stirling engines. Later, it was adapted by Belgasim [226] for optimizing a dynamic solar desalination unit. These codes are used in the current work, after being modified in a MATLAB environment, for optimizing the hybrid ORC system. The modified GA code is coupled with the hybrid ORC system's overall simulation model described in Chapters 3 and 5 to find the optimum operating parameters of the system. The flowchart of the real-value GA optimization for determining the optimum operating parameters of the hybrid ORC system is shown in Fig. 6.1.

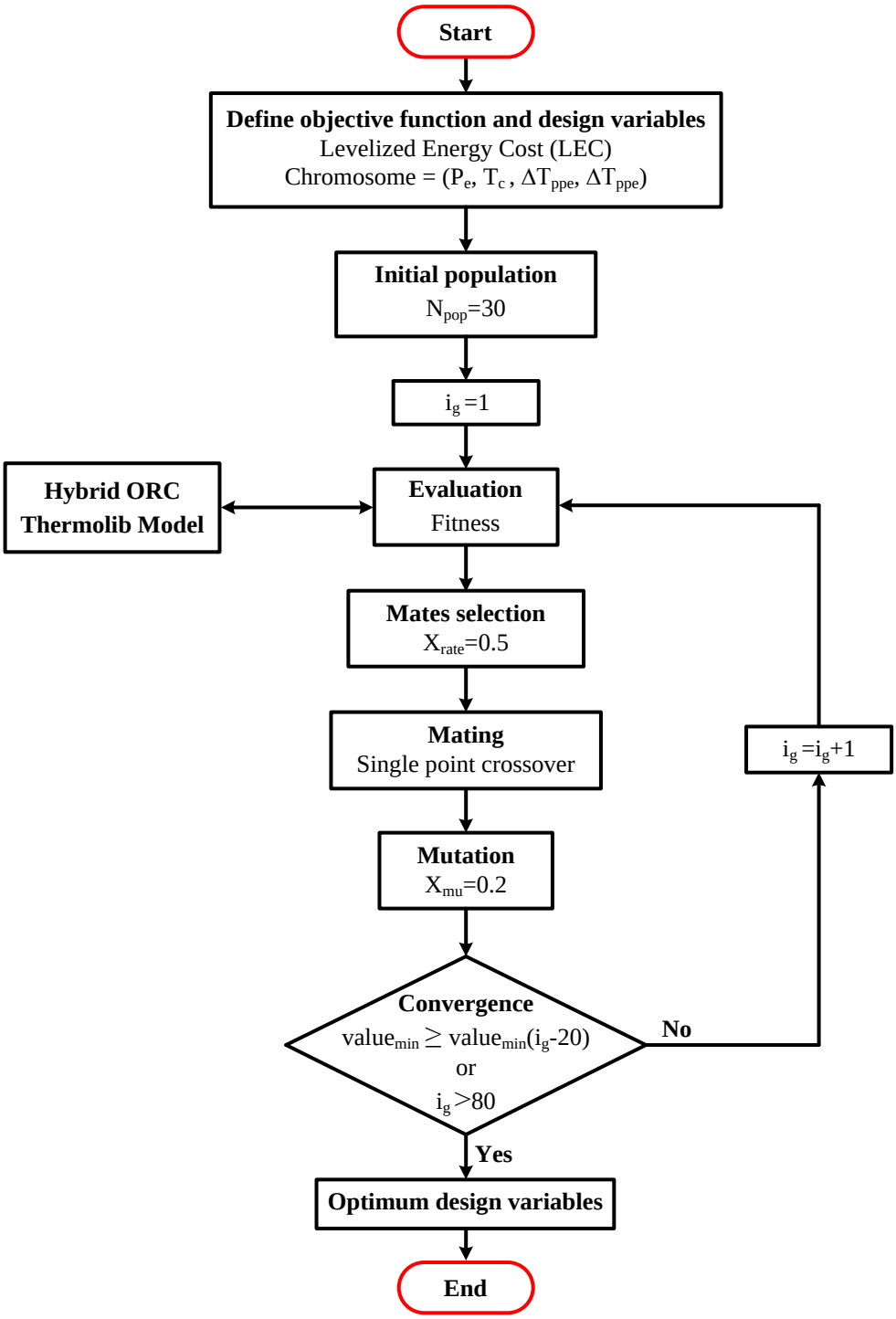

Figure 6.1 Real-value GA procedure flowchart

6.5 Optimization results

The results obtained from the optimisation of the operating parameters of the hybrid ORC system using the GA MATLAB code, coupled with the developed overall simulation model of the system, are presented in this section. The real-value GA optimization approach was applied to obtain the optimal set of operating parameters based on a thermo-economic criterion in which the LEC was defined as the objective function. The value of the LEC with the basic operating parameters, listed in Table 4.4, is $/0.5233/kWh, which will be used as a reference value. The objective of the optimization is therefore to minimize the LEC for the Hybrid ORC system. The upper and lower limits of each operating parameter are listed in Table 6.1. During the optimization, the maximum expander inlet temperature was set to 100 ^{o}C, the degree of superheating was set to zero and the minimum vapour quality at the expander outlet was set to 0.95 to avoid expander blades erosion. The GA optimisation parameters were selected as discussed previously in this Chapter with a population size of 30, a selection rate of 50% and a mutation rate of 20%. The maximum number of generations was set as 80.

The change in the minimum LEC as a function of the generations during the entire GA optimisation process is presented in Fig. 6.2. It can be seen from this figure that the minimum LEC rapidly decreases and then its decrease slows down until the final set of optimum operating parameters are found. The optimum operating parameters are found at the 64th generation of the calculations with a minimum LEC of $0.4686 /kWh. The LEC for the obtained set of optimum parameters is decreased by around 10.5% compared to the reference value obtained at the basic operating parameters. The final optimum operating parameters obtained from the GA optimisation process are presented in Table 6.2. Also, the thermo-economic performance parameters of the hybrid ORC system at the optimal conditions are presented in Table 6.3.

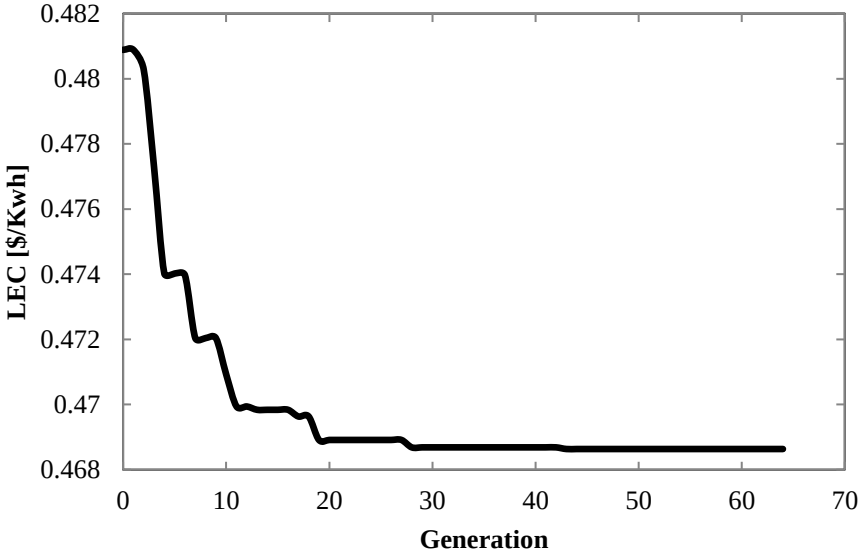

Figure 6.2 The LEC variation with the number of generation

Table 6.2 The set of optimum operating parameters obtained from the GA optimization

Parameter	Optimal operating parameter
Evaporation pressure, P_e	12.71 bar
Condensation temperature, T_c	30.03 °C
Evaporator pinch point temperature, ΔT_{ppe}	11.94 K
Condenser pinch point temperature, ΔT_{ppc}	7.96 K

Table 6.3 Thermo-economic performance of the hybrid ORC system at optimal conditions

Parameter	Value
Net power output, kWe	10
Expander power output, kWe	10.407
Pump consumed power, kWe	0.407
ORC efficiency, %	10.86
Overall system efficiency, %	7.65
Working fluid mass flow rate, kg/s	0.3895
Total ETC area, m^2	186.8
Evaporator area, m^2	2.35
Condenser area, m^2	2.95
Total capital cost, $	393,630
LEC, $/kWh	0.4686

6.6 Summary

In this Chapter, the optimisation procedure was realised based on the real-value GA approach to obtain the optimum operating parameters of the hybrid ORC system using R245fa as the working fluid. A thermo-economic criterion was selected as an objective function for the optimization study in order to obtain a cost-effective system and high thermodynamic performance. The set of optimum operating parameters was determined which provides about a 10.5% decrease in the LEC value.

Chapter 7 Dynamic Modelling Results

The rational set of operating parameters based on the optimum system thermo-economic performance was obtained in the previous Chapter. Chapter 7 presents the overall thermodynamic performance results for the optimized hybrid ORC system over a day-long period of operation for different annual seasons in the city of Newcastle upon Tyne. The dynamic results for two different days representing summer and winter seasons are analysed and discussed.

7.1 Results and analysis

In any particular location, solar energy utilization is subjected to the change with the season and time of the day. As a consequence, the amount of heat energy required from the biomass energy source varies with the solar irradiance variation.

In order to investigate the dynamic behaviour of the hybrid ORC system over a day-long period, a quasi-steady model was developed. The dynamic simulation provides a useful tool to understand the variation of the hybrid ORC system performance as well as the energy management processes during the whole-day operation. In this model, the thermal inertia of solar collectors is neglected and the time step in numerical modelling procedure is set to 5 sec. Two different weather conditions in Newcastle upon Tyne, representing typical summer and winter days were selected to examine the system dynamic performance. Fig. 7.1 shows the hourly global solar irradiance on a horizontal surface for 13th of June and 21st of February, estimated using the clear sky model described in Chapter 3.

For each season, the hybrid ORC system is designed capable to generate 10 kW net power output using only the solar source at the midday conditions when the solar irradiance is at its maximum value. In this way, the biomass boiler operates in a full-mode operation at night time and only in a part mode during the day. The ORC operating

parameters are kept constant and R245fa is used as the working fluid. The HTF mass flow rate circulating in the heating loop is fixed during the day-long operation for each season with a set-point temperature of 120 ºC in order to ensure a stable net power output. If the outlet temperature of the ETC drops below the reference set-point temperature due to insufficient solar radiation or at night, the biomass boiler is used to raise the HTF temperature to the set-point (120 ºC) by burning the required amount of wood pellets.

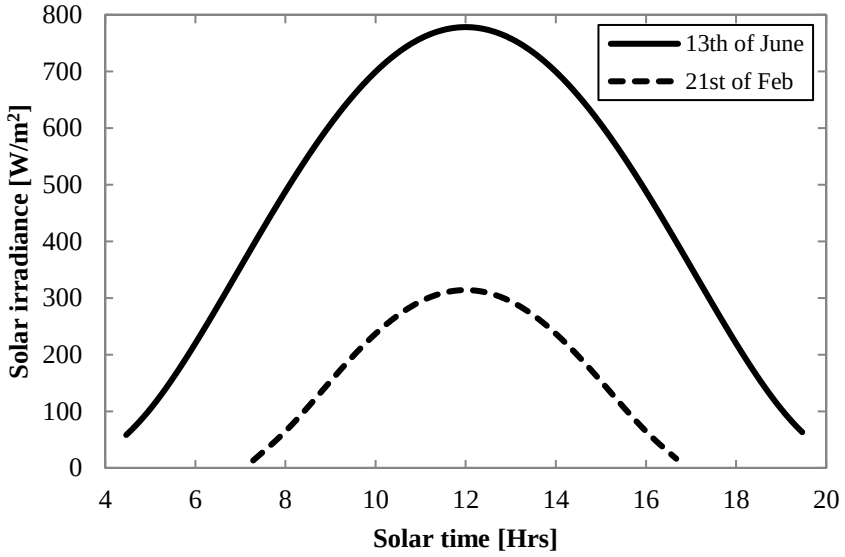

Figure 7.1 Solar irradiance for typical summer and winter days in Newcastle upon Tyne

7.1.1 Summer season simulation

The model was used to simulate the hybrid ORC system performance for a typical summer day in Newcastle upon Tyne. The ORC operating parameters were chosen to be equal to the same values obtained from the optimization process conducted in the previous Chapter that minimize the LEC. The condensation, ambient and cooling water temperatures are equal to 30 ºC, 20 ºC and 18 ºC, respectively in the simulation. In order to generate a net power output of 10 kW using only solar energy at noon, the ETC area of 166.8 m^2 is needed. This value is kept constant during the whole-day simulation.

Fig. 7.2 shows the variations of different temperatures in the hybrid system over a course of the summer day. It can be seen that the HTF set-point temperature (T_5) is

maintained constant at 120 ºC during the whole day using the hybrid energy source. Also, the figure shows that the maximum ORC temperature (T_3) leaving the evaporator is unchanged during the day with a value of 100 ºC. This is due to the constant available HTF temperature and mass flow rate in the heating circuit. At fixed ORC operating conditions, the ETC inlet temperature which is equal to that at the evaporator outlet is also constant with a value of 106.7 ºC . As it can be seen in Figs. 7.1 and 7.2, the solar irradiance has an impact on the ETC outlet temperature when its value reaches about 100 W/m^2 at 5:00. At this point, the ETC outlet temperature starts to increase, reaching its maximum value of 120 ºC at noon. It drops again with decreasing the solar irradiance until the difference between the outlet and inlet temperatures becomes zero at about 19:00.

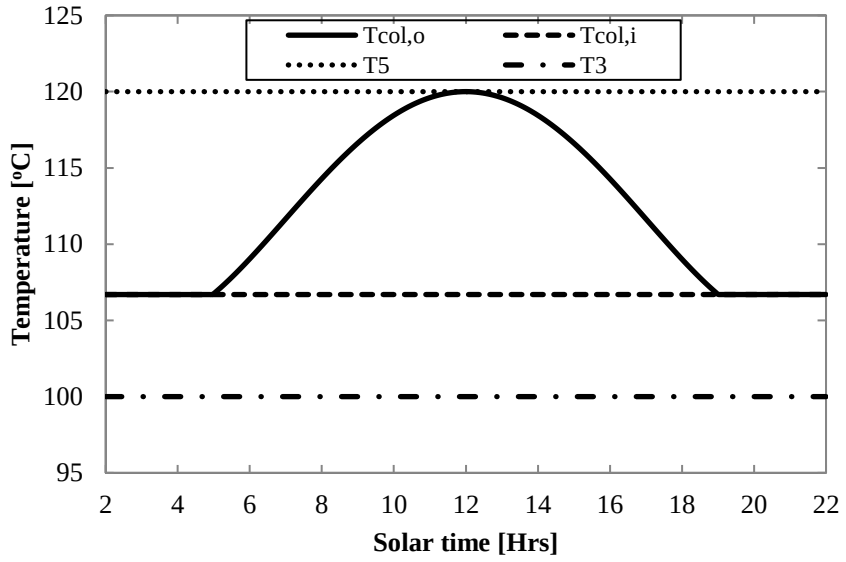

Figure 7.2 Variation of the system temperatures during a typical summer day

Fig. 7.3 depicts the variations of the thermal power input and net electric power output by each heat source in the hybrid ORC system with the time during the summer day. It can be seen that the biomass boiler supplies about 92 kW_{th} to the ORC during the night time and until 5:00, fulfilling all the ORC thermal power requirements. During this period, the net power output of 10 kW is generated by only a biomass energy source. At 5:00, the ETC gradually begins providing thermal power to the ORC and consequently the thermal power from the biomass boiler decreases. The thermal power from the ETC

continuously increases as the solar irradiance increases until midday. At this point, the ORC is supplied with heat by only a solar energy source to generate the total net power output of 10 kW. Beyond the solar noon, the thermal power from the ETC decreases while that from the biomass boiler increases until 19:00. Then, the system is driven by only the biomass boiler.

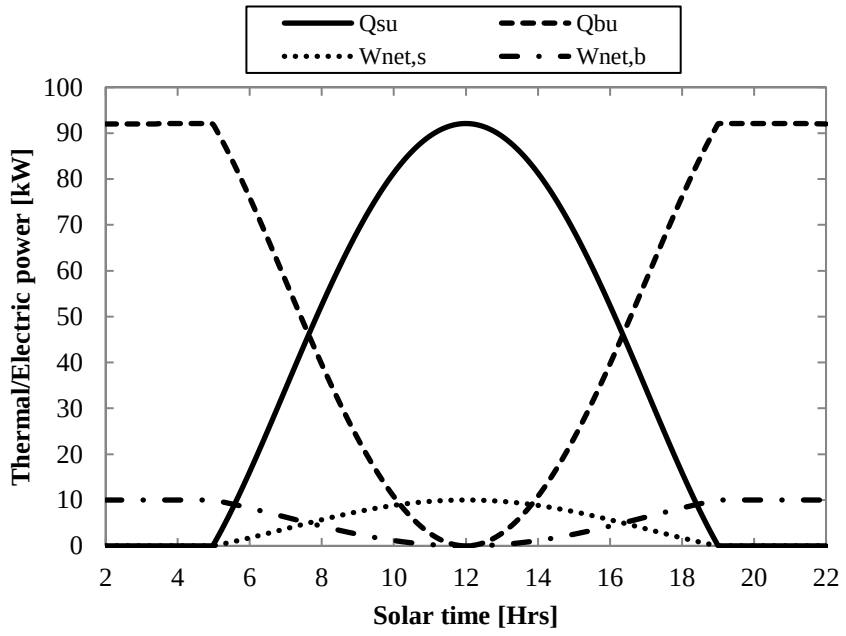

Figure 7.3 Variation of the thermal and electric power for each energy source during a typical summer day

The variations of the ETC efficiency and the biomass fuel consumption during the summer day are illustrated in Fig. 7.4. Practically, the ETC efficiency varies during the day due to the variation in the solar irradiance and its operating temperature. As it can be seen, the ETC efficiency increases sharply with increasing the solar irradiance, starting from 0% at around 5:00. Then its raise slows down until the maximum value of 70.9% is reached at the midday. Afterwards, it reduces as the solar irradiance decreases to 0% at about 19:00. On the other hand, the biomass fuel consumption is reversely proportional to the solar energy availability. During the night time, the biomass fuel consumption is at the highest rate of 22.94 kg/h where the hybrid ORC system is only powered by the biomass boiler. During the day, the consumption rate starts to decrease as the share of the solar source

increases, reaching to zero consumption rate at the mid of the day due to the instantaneous autonomous solar operation.

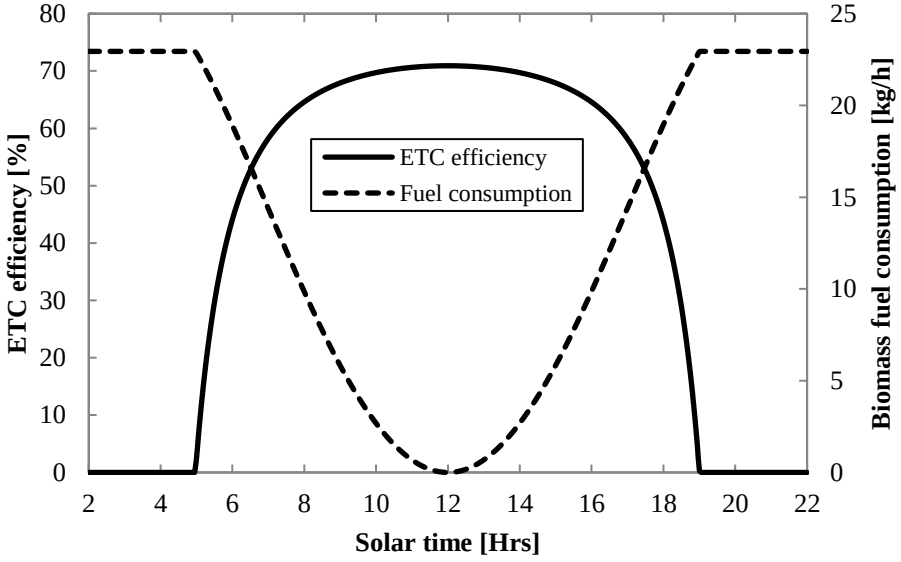

Figure 7.4 Variation of the ETC efficiency and biomass fuel consumption during a typical summer day

Fig. 7.5 presents the variations of the overall system efficiency and ORC efficiency with the time of the day. As demonstrated in the figure, the ORC efficiency does not change during the day and it has a constant value of 10.86% due to the fixed ORC operating parameters. On the other hand, the overall system efficiency varies depending on the type of the energy source supply. The figure shows that the maximum overall efficiency is achieved during the stand-alone biomass operation with a value of about 9.2%. This is basically due to the higher biomass boiler combustion efficiency compared to the ETC efficiency. Then, the overall efficiency decreases rapidly during the period between the sunrise and 5:00. The rapid decrease in this period is due to the fact that there is an increase in the overall heat input to the system without any additional gain in the power output. After 5:00, the overall efficiency slowly decreases from 8% to about 7.7% at the solar noon. Although the ETC efficiency increases during this period, the reduction rate in overall efficiency due the decrease in the biomass energy share is higher than the gain resulted from the ETC efficiency improvement.

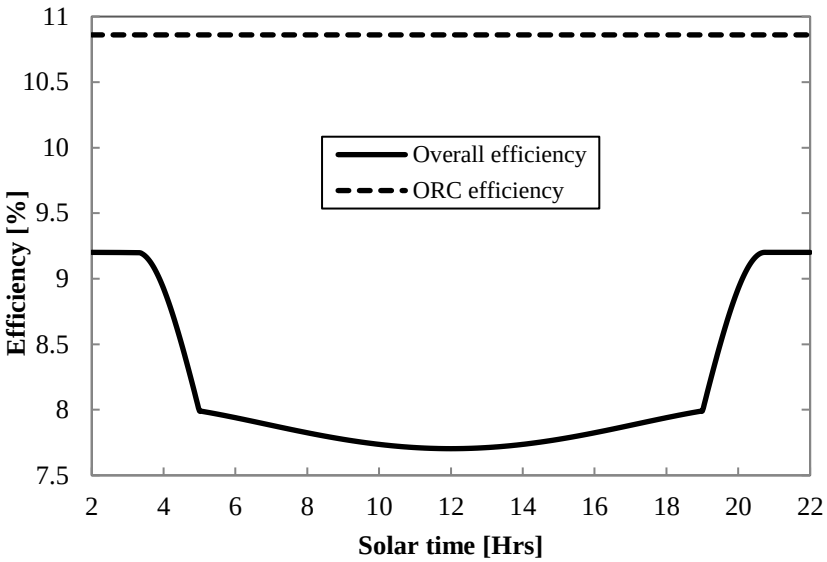

Figure 7.5 Variation of the ORC efficiency and overall system efficiency during a typical summer day

7.1.2 Winter season simulation

In this section, the performance of the hybrid ORC system is predicted for a typical winter day in Newcastle upon Tyne. To benefit from the low ambient and cooling water temperatures in winter season, the condensation temperature was set to 20 ^{o}C in order to improve the overall system performance. An ambient temperature of 12 ^{o}C and a cooling water temperature of 10 ^{o}C were used in the calculations. The required ETC area for the hybrid ORC system to be able to generate a 10 kW net power output at the solar noon using only a solar heat source is 509 m^2.

Fig. 7.6 shows the variations of different temperatures in the hybrid system with the time during a winter day. A similar trend to the summer day of system temperatures can be observed. During the entire day, the set-point HTF temperature is 120 ^{o}C while the maximum ORC temperature at the evaporator outlet is 100 ^{o}C. The temperature of the HTF at the ETC inlet after being cooled down in the evaporator is 107.3 ^{o}C. For the winter conditions, the effect of the solar irradiance on the ETC outlet temperature becomes obvious during the period from about 8:30 to 15:30. During this period, the ETC outlet temperature increases steadily with the solar irradiance until it reaches the set-point

temperature of 120 ºC at 12:00 noon then it decreases again as a result of decreasing the solar irradiance.

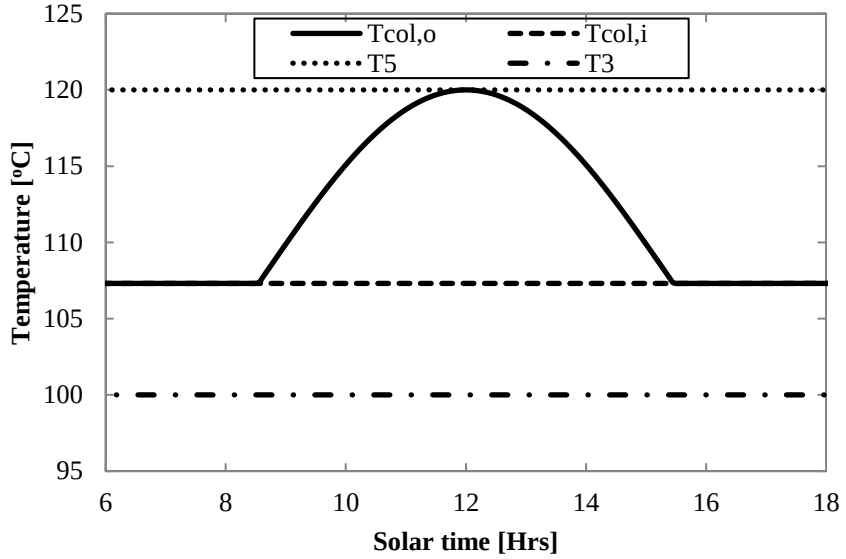

Figure 7.6 Variation of the system temperatures during a typical winter day

The variations of the thermal power input to the ORC and net electric power output in terms of each heat source with time for the winter conditions are presented in Fig. 7.7. The figure shows that the hybrid ORC system requires a total thermal power of 81.6 kW_{th} to generate the 10 kW net power output. This value is lower than that for the summer day due to the higher ORC efficiency in the winter as a result of the lower condensation temperature. As it can be seen, the biomass boiler provides the ORC with the whole thermal power needed during night time. At 8:30, the thermal power from the biomass boiler starts to decrease due to the increase in thermal power provided by the ETC. The thermal power from the ETC increases with increasing the solar irradiance until the mid of the day where the system is autonomously driven by solar energy. After solar noon, the thermal solar power input to the ORC declines while that from the biomass boiler increases until 15:30. The ORC system is then supplied with heat by only the biomass source.

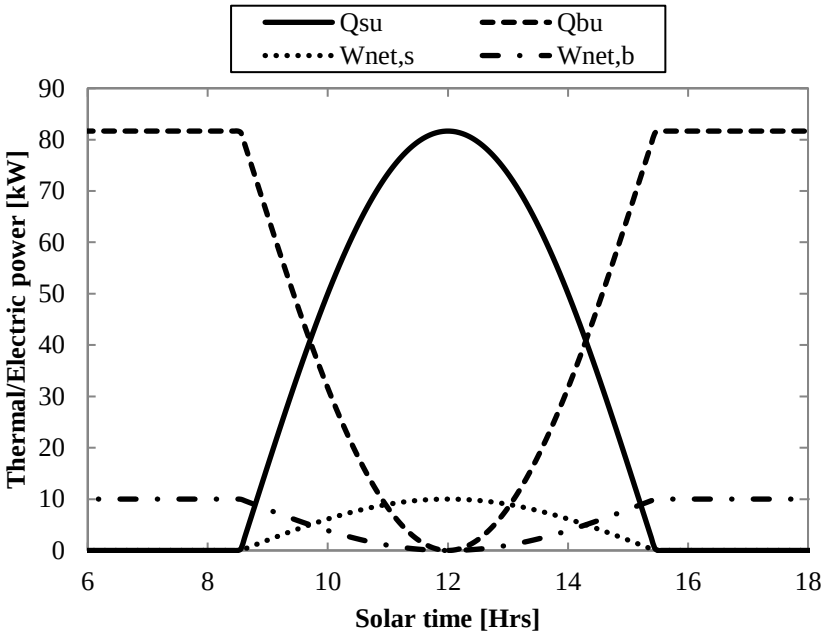

Figure 7.7 Variation of the thermal and electric power for each energy source during a typical winter day

Fig. 7.8 illustrates the variations of the ETC efficiency and the biomass fuel consumption during the time of the winter day. The figure shows that the ETC efficiency quickly increases with increasing the solar irradiance at the beginning then its increase gradually slows down until the maximum value is reached at the solar noon time. The maximum achieved ETC efficiency in the winter condition is about 51.1% which is much lower than that in the summer day due to the lower solar irradiance. This justifies the large ETC area required compared with summer conditions. The ETC efficiency then decreases again to reach 0% at 15:30. Also, the figure demonstrates that the biomass fuel consumption follows the same trend of the heat supplied by the boiler. At night time, the biomass fuel consumption rate is 20.3 kg/h which is lower than that of summer conditions. Between 8:30 and 15:30, it decreases to reach zero at the mid of the day then it increases again towards it maximum consumption at 15:30.

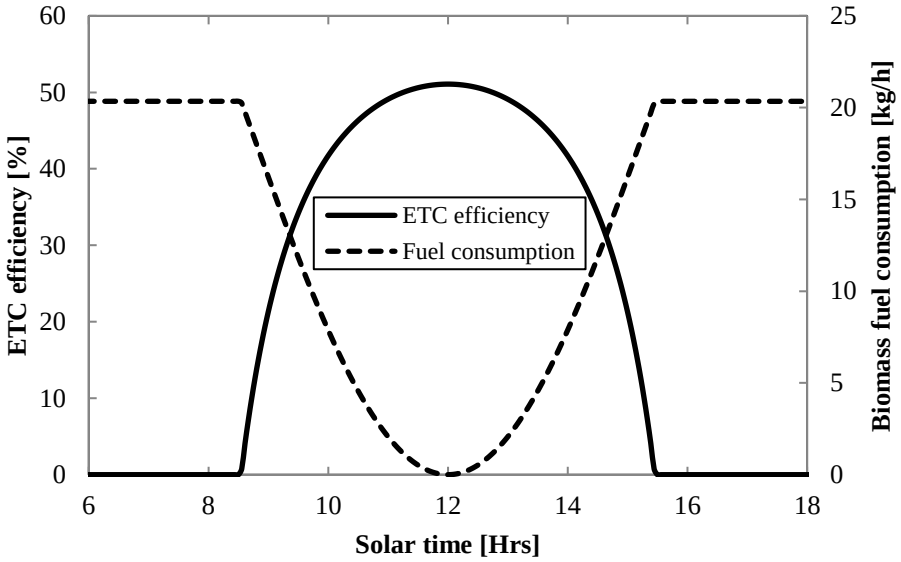

Figure 7.8 Variation of the ETC efficiency and biomass fuel consumption during a typical winter day

Fig. 7.9 shows the variation of the overall system efficiency and ORC efficiency with the time for the winter day. At constant ORC operating parameters, the ORC efficiency is constant with a value of 12.25% which is higher than that of summer conditions. This is attributed to the lower condensation temperature used in the winter season. The figure also shows that the trend of the overall system efficiency is similar to that in the summer conditions. The maximum overall efficiency of 10.4% is achieved when the system operates using only a biomass energy source. This value is higher than that of the summer conditions due to the higher ORC efficiency. After sunrise, the overall efficiency falls sharply to reach 6.6% at 8:30. This is due to the additional heat input to the system from the solar source for the same net power produced. Beyond 8:30, the overall efficiency slightly decreases to reach 6.3% at the noon time. It can be noticed that during the day the overall efficiency is much lower than that in the summer conditions. Although the ORC efficiency in the winter conditions is higher, the ETC efficiency is much lower which leads in a decrease in the overall efficiency.

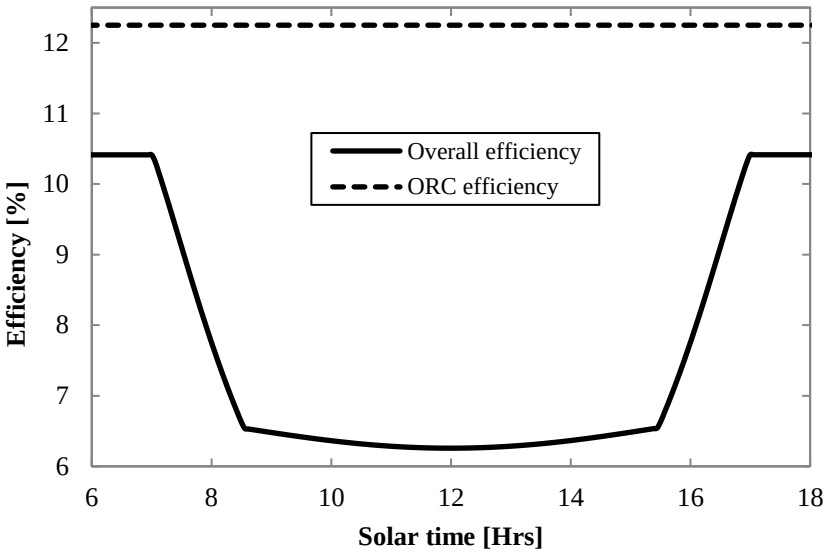

Figure 7.9 Variation of the ORC efficiency and overall system efficiency during a typical winter day

7.2 Summary

In this Chapter, the overall thermodynamic performance results of the hybrid ORC system over a day-long period were presented and analysed, considering the solar intensity variations. A quasi-steady model has been developed to simulate and predict the system dynamic behaviour over the day-long period for different annual seasons in Newcastle upon Tyne. Two different weather conditions, representing typical summer and winter days, were selected to examine the system performance. It can be concluded that the overall system efficiency is higher when the system is driven by the biomass energy source for both seasons. For winter conditions, the overall efficiency drops significantly with increasing the solar share during the day due to the low solar irradiance.

Chapter 8 Conclusions and Recommendations for Future Work

The novelty and contribution to the knowledge of this research study is highlighted in this Chapter. The major findings of this study are highlighted and recommendations on further improvements which should be introduced to theoretical model of the hybrid ORC system are presented.

8.1 Conclusions

The use of renewable energy sources in power generation is a promising way to alleviate the continuous increase in energy demand and mitigate the negative environmental impacts caused by fossil fuels. The ORC is considered as one of the most promising technologies in the field of small and medium scale CHP systems due to its ability to efficiently recover low-grade heat sources such as solar, biomass, geothermal and waste heat from industrial processes.

The novelty and contribution of this work is the development of a comprehensive computational tool for detailed modelling of the hybrid ORC plant for designing and controlling purposes. The developed model can be used for selection of the most appropriate working fluid, thermo-economic optimisation of design and working parameters of the plant and also takes into account the dynamic variation of the performance of the plant during the day at different climatic seasons. Results of dynamic modelling then can be used to develop controlling strategy of the plant. The developed tool can be used to model the operation of the hybrid plant and optimise its parameters at any geographical location. The tool is being used for designing the ORC plant in the framework of Horizon 2020 project, led by Northumbria University.

The model can be used for simulations of ORC systems consisting of two circuits, namely organic fluid circuit and solar heating circuit in which thermal energy is provided by an array of ETCs with heat pipes. A biomass boiler is also integrated to compensate for solar energy intermittence.

In this work the developed tool was demonstrated for modelling and techno-economic optimisation of a 10 kW-scale hybrid ORC system within a wide range of operating parameters under the UK climatic conditions. For demonstrational purposes, Newcastle upon Tyne was chosen as a geographical location.

The following conclusions can be drawn from the current research:

- Analysis of the existing literature demonstrates that even solar large-scale ORCs are at early stages and not fully commercialized, whilst the small-scale solar ORC technology is still being at the development phase. Also, the integration of two renewable energy sources to drive an ORC system has not been well investigated. These findings highlighted the importance of developing an accurate comprehensive simulation model with a capability to predict the thermodynamic performance, equipment sizing and economic feasibility of the low-temperature hybrid ORC system for a wide range of working fluids and operating conditions.
- A mathematical model of the hybrid ORC system was developed based on the mass and energy conservation equations. The set of equations were solved numerically using Thermolib toolbox which works in a MATLAB/Simulink® environment. The results obtained from the developed model were validated against theoretical and experimental data available in the open literature. The comparisons demonstrated that the developed simulation model of the ORC plant accurately predicts its performance with a maximum deviation of less than 7%.
- The validated model was then further evolved in order to improve the overall system performance by including the selection procedure for the optimal working fluid in the hybrid system. Thermodynamic investigations of the hybrid ORC system under different solar and biomass energy share scenarios showed that increasing the solar energy share decreases the overall system efficiency. A detailed parametric analysis was

also conducted to examine the effect of different operating parameters on the system performance. It was found that the evaporation pressure and condensation temperature have the most profound impacts on the system performance and the equipment sizing whereas the pump isentropic efficiency has almost no effect.

- An economic analysis of the hybrid ORC system was incorporated into the mathematical model and it was performed using the equipment costing technique. The total capital cost is estimated based on the individual costing correlation of each component in the system, considering all direct and indirect costs. The economic simulation model was developed using Simulink. It was found that the total capital cost of the hybrid ORC system is significantly affected by the working fluid used. Based on thermo-economic, safety and environmental criteria, R245fa was selected among different potential candidates. Furthermore, the economic results showed that the system operational parameters play a crucial role in the system costs.
- An optimization procedure based on the GA approach to obtain the optimum set of operating parameters of the hybrid ORC system was integrated into the mathematical modelling tool of the hybrid ORC plant. The LEC is selected as an objective function for the optimization problem in order to obtain a cost-effective system with high thermodynamic performance. The set of optimum operating parameters was determined for the 10-kW plant, used for demonstration of the computational tool. This optimal set of parameters reduces the LEC value by about 10.5%.
- The last stage of this research was focused on developing a segment of the tool, capable to predict dynamically the overall thermodynamic performance of the hybrid ORC system over a day-long period. A quasi-steady model is developed to simulate and predict the system dynamic behaviour over the day-long operation for different annual seasons. Calculations were performed for conditions in Newcastle upon Tyne, as an example. Two different weather conditions representing typical summer and winter days were chosen to examine the system performance. It was concluded that the overall system efficiency is higher when the system is driven by the biomass energy source for both seasons. For winter conditions, the overall efficiency significantly decreases with increasing the solar share during the day due to the low solar irradiance. The obtained results then can be used to develop controlling strategy of the operation of the plant.

The findings of this research were partially presented in the following conference papers:

- K. Hossin, K. Mahkamov and B. Belgasim, 'Dynamic modelling of a small-scale standalone solar organic Rankine cycle system', 4th International Conference on Nuclear and Renewable Energy Resources, Antalya, Turkey, October 2014.
- K. Hossin and K. Mahkamov, 'Thermodynamic analysis of an organic Rankine cycle plant operating with the low-temperature solar heat source', Northumbria Research Conference, Newcastle upon Tyne, UK, May 2015.
- K. Hossin and K. Mahkamov, 'Performance evaluation for a 10 kW solar organic Rankine cycle power system to operate in the UK climate conditions', The European Conference on Sustainability, Energy & the Environment, Brighton, UK, July 2015.
- K. Hossin, K. Mahkamov and G. Hashem, 'Comparative assessment of working fluids for a low-temperature solar organic Rankine cycle power system', Conference on Advances in Mechanical Engineering, Istanbul, Turkey, May 2016.

8.2 Recommendation for future work

The theoretical model developed in this study can be effectively used for designing and optimisation of the hybrid ORC system as well as for the prediction of its dynamic performance. However, a number of improvements can be introduced in future work as follows:

- In this work, the thermodynamic analysis conducted was based on the first law of thermodynamics. The mathematical model could be further developed to include the exergy analysis, which enables improving the design of individual system components.
- Although several working fluids were evaluated in this study, the potential of using more fluids needs to be investigated which could enhance the overall system performance. Therefore the tool library of the working fluids with their properties can be significantly extended and continuously updated.

- Only evacuated tube solar collectors were considered in this research. Different types of solar collectors with various levels of operating temperatures such as flat plate, parabolic trough collectors etc., could be included in the developed modelling tool.
- Different architectures of the ORC systems such as the recuperated and regenerative ORCs also need to be included into the developed modelling program.
- The system performance can be significantly improved and its specific cost can be comparatively reduced if the system is used in power and heat cogeneration applications. The waste heat from the biomass boiler and the heat rejected in the condenser can be recovered to produce hot water for domestic use or space heating. The modelling tool should be further developed to include cogeneration mode of the plant's operation.
- An environmental study should be performed to assess the reduction in greenhouse gas emissions as a result of using such a system.

References

[1] *Energy Information Adminstration (EIA), Total World Energy Consumotion, 2015*. Available: http://www.eia.gov/

[2] *BP, Statistical Review of World Energy 2016*. Available: http://www.bp.com/statisticalreview

[3] T. Yamamoto, T. Furuhata, N. Arai, and K. Mori, "Design and testing of the Organic Rankine Cycle," *Energy*, vol. 26, pp. 239-251, 2001.

[4] J. Bao and L. Zhao, "A review of working fluid and expander selections for organic Rankine cycle," *Renewable and Sustainable Energy Reviews*, vol. 24, pp. 325-342, 2013.

[5] S. Ozlu and I. Dincer, "Development and analysis of a solar and wind energy based multigeneration system," *Solar Energy*, vol. 122, pp. 1279-1295, 2015.

[6] F. Kreith and J. F. Kreider, *Principles of Solar Engineering*. New York: McGraw-Hill, 1978.

[7] J. Seitz and K. Hite, *Global Issue: An Introduction*, 4th ed. UK: Wiley-Blackwell, 2012.

[8] H. Z. Hassan, A. A. Mohamad, and R. Bennacer, "Simulation of an adsorption solar cooling system," *Energy*, vol. 36, pp. 530-537, 2011.

[9] P. Gang, L. Jing, and J. Jie, "Design and analysis of a novel low-temperature solar thermal electric system with two-stage collectors and heat storage units," *Renewable Energy*, vol. 36, pp. 2324-2333, 2011.

[10] A. Schuster, S. Karellas, E. Kakaras, and H. Spliethoff, "Energetic and economic investigation of Organic Rankine Cycle applications," *Applied Thermal Engineering*, vol. 29, pp. 1809-1817, 2009.

[11] T. C. Hung, T. Y. Shai, and S. K. Wang, "A review of organic rankine cycles (ORCs) for the recovery of low-grade waste heat," *Energy*, vol. 22, pp. 661-667, 7// 1997.

[12] S. Quoilin, M. Orosz, H. Hemond, and V. Lemort, "Performance and design optimization of a low-cost solar organic Rankine cycle for remote power generation," *Solar Energy*, vol. 85, pp. 955-966, 2011.

[13] D. Wei, X. Lu, Z. Lu, and J. Gu, "Performance analysis and optimization of organic Rankine cycle (ORC) for waste heat recovery," *Energy Conversion and Management*, vol. 48, pp. 1113-1119, 2007.

[14] S. Lecompte, S. Lemmens, H. Huisseune, M. van den Broek, and M. De Paepe, "Multi-Objective Thermo-Economic Optimization Strategy for ORCs Applied to Subcritical and Transcritical Cycles for Waste Heat Recovery," *Energies*, vol. 8, pp. 2714-2741, 2015.

[15] Y. Feng, Y. Zhang, B. Li, J. Yang, and Y. Shi, "Sensitivity analysis and thermoeconomic comparison of ORCs (organic Rankine cycles) for low temperature waste heat recovery," *Energy*, vol. 82, pp. 664-677, 2015.

[16] M. Imran, B.-S. Park, H.-J. Kim, D.-H. Lee, and M. Usman, "Economic assessment of greenhouse gas reduction through low-grade waste heat recovery using organic Rankine cycle (ORC)," *Journal of Mechanical Science and Technology*, vol. 29, pp. 835-843, 2015.

[17] *International Energy Agency (IEA), Key World Energy Statistics, 2015*. Available: www.iea.org

[18] R. C. Saxena, D. K. Adhikari, and H. B. Goyal, "Biomass-based energy fuel through biochemical routes: A review," *Renewable and Sustainable Energy Reviews*, vol. 13, pp. 167-178, 2009.

[19] M. Badami and M. Mura, "Preliminary design and controlling strategies of a small-scale wood waste Rankine Cycle (RC) with a reciprocating steam engine (SE)," *Energy*, vol. 34, pp. 1315-1324, 2009.

[20] H. Liu, Y. Shao, and J. Li, "A biomass-fired micro-scale CHP system with organic Rankine cycle (ORC) – Thermodynamic modelling studies," *Biomass and Bioenergy,* vol. 35, pp. 3985-3994, 2011.

[21] A. M. Delgado-Torres and L. García-Rodríguez, "Analysis and optimization of the low-temperature solar organic Rankine cycle (ORC)," *Energy Conversion and Management,* vol. 51, pp. 2846-2856, 2010.

[22] M. J. Proctor, W. Yu, R. D. Kirkpatrick, and B. R. Young, "Dynamic modelling and validation of a commercial scale geothermal organic rankine cycle power plant," *Geothermics,* vol. 61, pp. 63-74, 2016.

[23] U. Drescher and D. Brüggemann, "Fluid selection for the Organic Rankine Cycle (ORC) in biomass power and heat plants," *Applied Thermal Engineering,* vol. 27, pp. 223-228, 2007.

[24] V. Maizza and A. Maizza, "Unconventional working fluids in organic Rankine-cycles for waste energy recovery systems," *Applied Thermal Engineering,* vol. 21, pp. 381-390, 2001.

[25] E. H. Wang, H. G. Zhang, Y. Zhao, B. Y. Fan, Y. T. Wu, and Q. H. Mu, "Performance analysis of a novel system combining a dual loop organic Rankine cycle (ORC) with a gasoline engine," *Energy,* vol. 43, pp. 385-395, 2012.

[26] C. O. Katsanos, D. T. Hountalas, and E. G. Pariotis, "Thermodynamic analysis of a Rankine cycle applied on a diesel truck engine using steam and organic medium," *Energy Conversion and Management,* vol. 60, pp. 68-76, 2012.

[27] V. Dolz, R. Novella, A. García, and J. Sánchez, "HD Diesel engine equipped with a bottoming Rankine cycle as a waste heat recovery system. Part 1: Study and analysis of the waste heat energy," *Applied Thermal Engineering,* vol. 36, pp. 269-278, 2012.

[28] M. Yari and S. M. S. Mahmoudi, "Utilization of waste heat from GT-MHR for power generation in organic Rankine cycles," *Applied Thermal Engineering,* vol. 30, pp. 366-375, 2010.

[29] V. Zare, M. Yari, and S. M. S. Mahmoudi, "Proposal and analysis of a new combined cogeneration system based on the GT-MHR cycle," *Desalination,* vol. 286, pp. 417-428, 2012.

[30] P. J. Mago, A. Hueffed, and L. M. Chamra, "Analysis and optimization of the use of CHP–ORC systems for small commercial buildings," *Energy and Buildings,* vol. 42, pp. 1491-1498, 2010.

[31] F. Fang, L. Wei, J. Liu, J. Zhang, and G. Hou, "Complementary configuration and operation of a CCHP-ORC system," *Energy,* vol. 46, pp. 211-220, 2012.

[32] B. Peñate and L. García-Rodríguez, "Seawater reverse osmosis desalination driven by a solar Organic Rankine Cycle: Design and technology assessment for medium capacity range," *Desalination,* vol. 284, pp. 86-91, 2012.

[33] P. Colonna, E. Casati, C. Trapp, T. Mathijssen, J. Larjola, T. Turunen-Saaresti, *et al.*, "Organic Rankine Cycle Power Systems: From the Concept to Current Technology, Applications, and an Outlook to the Future," *Journal of Engineering for Gas Turbines and Power,* vol. 137, p. 100801, 2015.

[34] G. Angelino, M. Gaia, and E. Macchi, "A review of Italian activity in the field of organic Rankine cycles," presented at the International VDI-Seminar, Zurich, Switzerland, 1984.

[35] *Turboden - Organic Rankine cycle turbogenerators for clean energy production*. Available: www.turboden.eu

[36] A. Giuffrida, "Modelling the performance of a scroll expander for small organic Rankine cycles when changing the working fluid," *Applied Thermal Engineering,* vol. 70, pp. 1040-1049, 2014.

[37] M. Chys, M. van den Broek, B. Vanslambrouck, and M. De Paepe, "Potential of zeotropic mixtures as working fluids in organic Rankine cycles," *Energy,* vol. 44, pp. 623-632, 2012.

[38] M. J. Moran, H. N. Shapiro, D. D. Boettner, and M. B. Bailey, *Fundamentals of Engineering Thermodynamics*, 7th ed. USA: John Wiley & Sons, Inc., 2011.

[39] P. Bombarda, C. Invernizzi, and M. Gaia, "Performance Analysis of OTEC Plants With Multilevel Organic Rankine Cycle and Solar Hybridization," *ASME J. Eng. Gas Turbines Power*, vol. 135, pp. 042302-1 042302-8, 2013.

[40] S. Quoilin, M. V. D. Broek, S. Declaye, P. Dewallef, and V. Lemort, "Techno-economic survey of Organic Rankine Cycle (ORC) systems," *Renewable and Sustainable Energy Reviews*, vol. 22, pp. 168-186, 2013.

[41] B. F. Tchanche, G. Lambrinos, A. Frangoudakis, and G. Papadakis, "Low-grade heat conversion into power using organic Rankine cycles – A review of various applications," *Renewable and Sustainable Energy Reviews*, vol. 15, pp. 3963-3979, 10// 2011.

[42] I. Vankeirsbilck, B. Vanslambrouck, S. Gusev, and M. De-Paepe, "Organic Rankine cycle as efficient alternative to steam cycle for small scale power generation," presented at the 8th International Conference on Heat Transfer, Fluid Mechanics and Thermodynamics, Mauritius, 2011.

[43] BCS Incorporated, "Waste Heat Recovery: Technology and Opportunities in U.S. Industry," U.S. Department of Energy, 2008.

[44] *United Nations Environment Program (UNEP), Montreal Protocol on Substances that Deplete the Ozone Layer, Final Act, United Nations, New York, 1997*.

[45] G. D. Hayman and R. G. Derwent, "Atmospheric Chemical Reactivity and Ozone-Forming Potentials of Potential CFC Replacements," *Environ. Sci. Technol.*, vol. 31, pp. 327-336, 1997.

[46] W.-T. Tsai, "A review of environmental hazards and adsorption recovery of cleaning solvent hydrochlorofluorocarbons (HCFCs)," *Journal of Loss Prevention in the Process Industries*, vol. 15, pp. 147-157, 2002.

[47] W. W. Husband and A. Beyene, "Low-grade heat-driven Rankine cycle, a feasibility study," *International Journal of Energy Research*, vol. 32, pp. 1373-1382, 2008.

[48] W.-T. Tsai, H.-P. Chen, and W.-Y. Hsien, "A review of uses, environmental hazards and recovery/recycle technologies of perfluorocarbons (PFCs) emissions from the semiconductor manufacturing processes," *Journal of Loss Prevention in the Process Industries*, vol. 15, pp. 65-75, 2002.

[49] *Kyoto Protocol, Report of the Conference of the Parties, United Nations Framework Convention on climate change (UNFCCC), 1997*.

[50] T. J. Wallington and O. J. Nielsen, "Atmospheric Chemistry and Environmental Impact of Hydrofluorocarbons (HFCs) and Hydrofluoroethers (HFEs)," in *Organofluorines*. vol. 3, A. H. Neilson ed Germany: Springer Berlin Heidelberg, 2002, pp. 85-102.

[51] J. M. Calm and G. C. Hourahan, "Refrigerant Data Update," *Heating/Piping/Air Conditioning Engineering*, vol. 79, pp. 50-64, 2007.

[52] W. T. Tsai, "Environmental risk assessment of hydrofluoroethers (HFEs)," *J Hazard Mater*, vol. 119, pp. 69-78, Mar 17 2005.

[53] B. Saleh and M. Wendland, "Screening of pure fluids as alternative refrigerants," *International Journal of Refrigeration*, vol. 29, pp. 260-269, 2006.

[54] *DuPont, Suva refrigerants, General replacement guide: CFC to an HCFC; CFC or HCFC to an HFC*. Available: http://www.hvacwebtech.com/downloads/1_h71061-3.pdf

[55] T.-C. Hung, "Waste heat recovery of organic Rankine cycle using dry fluids," *Energy Conversion and Management*, vol. 42, pp. 539-553, 2001.

[56] K. Rahbar, S. Mahmoud, R. K. Al-Dadah, and N. Moazami, "Parametric analysis and optimization of a small-scale radial turbine for Organic Rankine Cycle," *Energy*, vol. 83, pp. 696-711, 2015.

[57] H. Yu, X. Feng, and Y. Wang, "A new pinch based method for simultaneous selection of working fluid and operating conditions in an ORC (Organic Rankine Cycle) recovering waste heat," *Energy*, 2015.

[58] S. Quoilin, "Sustainable Energy Conversion Through the Use of Organic Rankine Cycles for Waste Heat Recovery and Solar Applications," PhD Thesis, University of Liège, 2011.

[59] B.-T. Liu, K.-H. Chien, and C.-C. Wang, "Effect of working fluids on organic Rankine cycle for waste heat recovery," *Energy,* vol. 29, pp. 1207-1217, 2004.

[60] T. Wang, Y. Zhang, Z. Peng, and G. Shu, "A review of researches on thermal exhaust heat recovery with Rankine cycle," *Renewable and Sustainable Energy Reviews,* vol. 15, pp. 2862-2871, 2011.

[61] I. H. Aljundi, "Effect of dry hydrocarbons and critical point temperature on the efficiencies of organic Rankine cycle," *Renewable Energy,* vol. 36, pp. 1196-1202, 2011.

[62] T. C. Hung, S. K. Wang, C. H. Kuo, B. S. Pei, and K. F. Tsai, "A study of organic working fluids on system efficiency of an ORC using low-grade energy sources," *Energy,* vol. 35, pp. 1403-1411, 2010.

[63] O. Badr, S. D. Probert, and P. W. O'Callaghan, "Selecting a working fluid for a Rankine-cycle engine," *Applied Energy,* vol. 21, pp. 1-42, 1985.

[64] R. Rayegan and Y. X. Tao, "A procedure to select working fluids for Solar Organic Rankine Cycles (ORCs)," *Renewable Energy,* vol. 36, pp. 659-670, 2011.

[65] K. Braimakis, M. Preißinger, D. Brüggemann, S. Karellas, and K. Panopoulos, "Low grade waste heat recovery with subcritical and supercritical Organic Rankine Cycle based on natural refrigerants and their binary mixtures," *Energy,* vol. 88, pp. 80-92, 2015.

[66] H. Chen, D. Y. Goswami, and E. K. Stefanakos, "A review of thermodynamic cycles and working fluids for the conversion of low-grade heat," *Renewable and Sustainable Energy Reviews,* vol. 14, pp. 3059-3067, 2010.

[67] G. Qiu, "Selection of working fluids for micro-CHP systems with ORC," *Renewable Energy,* vol. 48, pp. 565-570, 2012.

[68] M. Z. Stijepovic, P. Linke, A. I. Papadopoulos, and A. S. Grujic, "On the role of working fluid properties in Organic Rankine Cycle performance," *Applied Thermal Engineering,* vol. 36, pp. 406-413, 2012.

[69] J. Wang, J. Zhang, and Z. Chen, "Molecular Entropy, Thermal Efficiency, and Designing of Working Fluids for Organic Rankine Cycles," *International Journal of Thermophysics,* vol. 33, pp. 970-985, 2012.

[70] D. Mikielewicz and J. Mikielewicz, "A thermodynamic criterion for selection of working fluid for subcritical and supercritical domestic micro CHP," *Applied Thermal Engineering,* vol. 30, pp. 2357-2362, 2010.

[71] C.-R. Kuo, S.-W. Hsu, K.-H. Chang, and C.-C. Wang, "Analysis of a 50kW organic Rankine cycle system," *Energy,* vol. 36, pp. 5877-5885, 2011.

[72] T. Deethayat, A. Asanakham, and T. Kiatsiriroat, "Performance analysis of low temperature organic Rankine cycle with zeotropic refrigerant by Figure of Merit (FOM)," *Energy,* vol. 96, pp. 96-102, 2016.

[73] B. Saleh, G. Koglbauer, M. Wendland, and J. Fischer, "Working fluids for low-temperature organic Rankine cycles," *Energy,* vol. 32, pp. 1210-1221, 2007.

[74] P. J. Mago, L. M. Chamra, and C. Somayaji, "Performance analysis of different working fluids for use in organic Rankine cycles," *Proceedings of the Institution of Mechanical Engineers, Part A: Journal of Power and Energy,* vol. 221, pp. 255-263, 2007.

[75] C. Somayaji, P. Mago, and L. Chamra, "Second Law Analysis and Optimization of Organic Rankine Cycle," presented at the ASME 2006 Power Conference, Atlanta, USA, 2006.

[76] A. I. Papadopoulos, M. Stijepovic, and P. Linke, "On the systematic design and selection of optimal working fluids for Organic Rankine Cycles," *Applied Thermal Engineering,* vol. 30, pp. 760-769, 2010.

[77] E. H. Wang, H. G. Zhang, B. Y. Fan, M. G. Ouyang, Y. Zhao, and Q. H. Mu, "Study of working fluid selection of organic Rankine cycle (ORC) for engine waste heat recovery," *Energy,* vol. 36, pp. 3406-3418, 2011.

[78] B. F. Tchanche, G. Papadakis, G. Lambrinos, and A. Frangoudakis, "Fluid selection for a low-temperature solar organic Rankine cycle," *Applied Thermal Engineering,* vol. 29, pp. 2468-2476, 2009.

[79] J. Xu and C. Yu, "Critical temperature criterion for selection of working fluids for subcritical pressure Organic Rankine cycles," *Energy,* vol. 74, pp. 719-733, 2014.

[80] S. Quoilin, S. Declaye, B. F. Tchanche, and V. Lemort, "Thermo-economic optimization of waste heat recovery Organic Rankine Cycles," *Applied Thermal Engineering,* vol. 31, pp. 2885-2893, 2011.

[81] T. Guo, H. X. Wang, and S. J. Zhang, "Fluids and parameters optimization for a novel cogeneration system driven by low-temperature geothermal sources," *Energy,* vol. 36, pp. 2639-2649, 2011.

[82] F. Heberle and D. Brüggemann, "Thermo-Economic Analysis of Zeotropic Mixtures and Pure Working Fluids in Organic Rankine Cycles for Waste Heat Recovery," *Energies,* vol. 9, p. 226, 2016.

[83] Z. Shengjun, W. Huaixin, and G. Tao, "Performance comparison and parametric optimization of subcritical Organic Rankine Cycle (ORC) and transcritical power cycle system for low-temperature geothermal power generation," *Applied Energy,* vol. 88, pp. 2740-2754, 2011.

[84] C. Liu, C. He, H. Gao, H. Xie, Y. Li, S. Wu, *et al.*, "The environmental impact of organic Rankine cycle for waste heat recovery through life-cycle assessment," *Energy,* vol. 56, pp. 144-154, 2013.

[85] H. Wang, J. Xu, X. Yang, Z. Miao, and C. Yu, "Organic Rankine cycle saves energy and reduces gas emissions for cement production," *Energy,* vol. 86, pp. 59-73, 2015.

[86] C. Walsh and P. Thornley, "The environmental impact and economic feasibility of introducing an Organic Rankine Cycle to recover low grade heat during the production of metallurgical coke," *Journal of Cleaner Production,* vol. 34, pp. 29-37, 2012.

[87] V. L. Le, M. Feidt, A. Kheiri, and S. Pelloux-Prayer, "Performance optimization of low-temperature power generation by supercritical ORCs (organic Rankine cycles) using low GWP (global warming potential) working fluids," *Energy,* vol. 67, pp. 513-526, 2014.

[88] W. Liu, D. Meinel, C. Wieland, and H. Spliethoff, "Investigation of hydrofluoroolefins as potential working fluids in organic Rankine cycle for geothermal power generation," *Energy,* vol. 67, pp. 106-116, 2014.

[89] M. O. McLinden, A. F. Kazakov, J. Steven Brown, and P. A. Domanski, "A thermodynamic analysis of refrigerants: Possibilities and tradeoffs for Low-GWP refrigerants," *International Journal of Refrigeration,* vol. 38, pp. 80-92, 2014.

[90] F. Molés, J. Navarro-Esbrí, B. Peris, A. Mota-Babiloni, Á. Barragán-Cervera, and K. Kontomaris, "Low GWP alternatives to HFC-245fa in Organic Rankine Cycles for low temperature heat recovery: HCFO-1233zd-E and HFO-1336mzz-Z," *Applied Thermal Engineering,* vol. 71, pp. 204-212, 2014.

[91] F. Molés, J. Navarro-Esbrí, B. Peris, A. Mota-Babiloni, and K. Kontomaris, "Thermodynamic analysis of a combined organic Rankine cycle and vapor compression cycle system activated with low temperature heat sources using low GWP fluids," *Applied Thermal Engineering,* vol. 87, pp. 444-453, 2015.

[92] S. Quoilin and V. Lemort, "Technological and Economical Survey of Organic Rankine Cycle Systems," presented at the Fifth European Conference on Economics and Management of Energy in Industry, Vilamoura, Portugal, 2009.

[93] G. Angelino and P. Colonna Di Paliano, "Multicomponent Working Fluids For Organic Rankine Cycles (ORCs)," *Energy,* vol. 23, pp. 449-463, 1998.

[94] F. Heberle, M. Preißinger, and D. Brüggemann, "Zeotropic mixtures as working fluids in Organic Rankine Cycles for low-enthalpy geothermal resources," *Renewable Energy,* vol. 37, pp. 364-370, 2012.

[95] H. Chen, D. Y. Goswami, M. M. Rahman, and E. K. Stefanakos, "A supercritical Rankine cycle using zeotropic mixture working fluids for the conversion of low-grade heat into power," *Energy,* vol. 36, pp. 549-555, 2011.

[96] J. L. Wang, L. Zhao, and X. D. Wang, "A comparative study of pure and zeotropic mixtures in low-temperature solar Rankine cycle," *Applied Energy,* vol. 87, pp. 3366-3373, 2010.

[97] W. Li, X. Feng, L. J. Yu, and J. Xu, "Effects of evaporating temperature and internal heat exchanger on organic Rankine cycle," *Applied Thermal Engineering,* vol. 31, pp. 4014-4023, 2011.

[98] X. D. Wang and L. Zhao, "Analysis of zeotropic mixtures used in low-temperature solar Rankine cycles for power generation," *Solar Energy,* vol. 83, pp. 605-613, 2009.

[99] Y. Wu, Y. Zhu, and L. Yu, "Thermal and economic performance analysis of zeotropic mixtures for Organic Rankine Cycles," *Applied Thermal Engineering,* vol. 96, pp. 57-63, 2016.

[100] F. Heberle and D. Brüggemann, "Thermo-Economic Evaluation of Organic Rankine Cycles for Geothermal Power Generation Using Zeotropic Mixtures," *Energies,* vol. 8, pp. 2097-2124, 2015.

[101] C. Kalra, G. Becquin, J. Jackson, A. L. Laursen, H. Chen, K. Myers, *et al.*, "High-potential working fluids and cycle concepts for next generation binary organic Rankine cycle for enhanced geothermal systems," presented at the 37th Workshop on Geothermal Reservoir Engineering, Stanford University, Stanford, California, 2012.

[102] F. Vélez, J. J. Segovia, M. C. Martín, G. Antolín, F. Chejne, and A. Quijano, "A technical, economical and market review of organic Rankine cycles for the conversion of low-grade heat for power generation," *Renewable and Sustainable Energy Reviews,* vol. 16, pp. 4175-4189, 2012.

[103] B. F. Tchanche, M. Pétrissans, and G. Papadakis, "Heat resources and organic Rankine cycle machines," *Renewable and Sustainable Energy Reviews,* vol. 39, pp. 1185-1199, 11// 2014.

[104] S. A. Kalogirou, "Solar thermal collectors and applications," *Progress in Energy and Combustion Science,* vol. 30, pp. 231-295, 2004.

[105] S. Kalogirou, "The potential of solar industrial process heat applications," *Applied Energy,* vol. 76, pp. 337-361, 2003.

[106] H. Zhai, Q. An, L. Shi, V. Lemort, and S. Quoilin, "Categorization and analysis of heat sources for organic Rankine cycle systems," *Renewable and Sustainable Energy Reviews,* vol. 64, pp. 790-805, 2016.

[107] Y. Goswami, *Principles of Solar Engineering,* 3rd ed. U.S.: Taylor & Francis Group, LLC, 2015.

[108] F. A. Al-Sulaiman, I. Dincer, and F. Hamdullahpur, "Exergy modeling of a new solar driven trigeneration system," *Solar Energy,* vol. 85, pp. 2228-2243, 2011.

[109] S. Canada, G. Cohen, R. Cable, D. Brosseau, and H. Price, "Parabolic Trough Organic Rankine Cycle Power Plant," presented at the DOE Solar Energy Technologies Program Review Meeting, Denver, USA, 2004.

[110] E. Georges, S. Declaye, O. Dumont, S. Quoilin, and V. Lemort, "Design of a small-scale organic Rankine cycle engine used in a solar power plant," *Int. J. Low-Carbon Technol.,* pp. 1-8, 2013.

[111] A. S. Nafey, M. A. Sharaf, and L. García-Rodríguez, "A new visual library for design and simulation of solar desalination systems (SDS)," *Desalination,* vol. 259, pp. 197-207, 2010.

[112] A. S. Nafey and M. A. Sharaf, "Combined solar organic Rankine cycle with reverse osmosis desalination process: Energy, exergy, and cost evaluations," *Renewable Energy,* vol. 35, pp. 2571-2580, 2010.

[113] J. Wang, Z. Yan, P. Zhao, and Y. Dai, "Off-design performance analysis of a solar-powered organic Rankine cycle," *Energy Conversion and Management,* vol. 80, pp. 150-157, 2014.

[114] C. Li, G. Kosmadakis, D. Manolakos, E. Stefanakos, G. Papadakis, and D. Y. Goswami, "Performance investigation of concentrating solar collectors coupled with a transcritical organic Rankine cycle for power and seawater desalination co-generation," *Desalination,* vol. 318, pp. 107-117, 2013.

[115] X. D. Wang, L. Zhao, J. L. Wang, W. Z. Zhang, X. Z. Zhao, and W. Wu, "Performance evaluation of a low-temperature solar Rankine cycle system utilizing R245fa," *Solar Energy,* vol. 84, pp. 353-364, 2010.

[116] T. Saitoh, N. Yamada, and S.-I. Wakashima, "Solar Rankine Cycle System Using Scroll Expander," *Journal of Environment and Engineering,* vol. 2, pp. 708-719
2007.

[117] B. Twomey, P. A. Jacobs, and H. Gurgenci, "Dynamic performance estimation of small-scale solar cogeneration with an organic Rankine cycle using a scroll expander," *Applied Thermal Engineering,* vol. 51, pp. 1307-1316, 2013.

[118] M. Marion, I. Voicu, and A.-L. Tiffonnet, "Wind effect on the performance of a solar organic Rankine cycle," *Renewable Energy,* vol. 68, pp. 651-661, 2014.

[119] G. Pei, J. Li, Y. Li, D. Wang, and J. Ji, "Construction and dynamic test of a small-scale organic rankine cycle," *Energy,* vol. 36, pp. 3215-3223, 2011.

[120] G. Kosmadakis, D. Manolakos, S. Kyritsis, and G. Papadakis, "Design of a two stage Organic Rankine Cycle system for reverse osmosis desalination supplied from a steady thermal source," *Desalination,* vol. 250, pp. 323-328, 2010.

[121] G. Kosmadakis, D. Manolakos, S. Kyritsis, and G. Papadakis, "Comparative thermodynamic study of refrigerants to select the best for use in the high-temperature stage of a two-stage organic Rankine cycle for RO desalination," *Desalination,* vol. 243, pp. 74-94, 2009.

[122] G. Kosmadakis, D. Manolakos, S. Kyritsis, and G. Papadakis, "Economic assessment of a two-stage solar organic Rankine cycle for reverse osmosis desalination," *Renewable Energy,* vol. 34, pp. 1579-1586, 2009.

[123] G. Kosmadakis, D. Manolakos, and G. Papadakis, "Parametric theoretical study of a two-stage solar organic Rankine cycle for RO desalination," *Renewable Energy,* vol. 35, pp. 989-996, 2010.

[124] J. J. Bao, L. Zhao, and W. Z. Zhang, "A novel auto-cascade low-temperature solar Rankine cycle system for power generation," *Solar Energy,* vol. 85, pp. 2710-2719, 2011.

[125] G. Pei, J. Li, and J. Ji, "Analysis of low temperature solar thermal electric generation using regenerative Organic Rankine Cycle," *Applied Thermal Engineering,* vol. 30, pp. 998-1004, 2010.

[126] M. Duku, S. Gu, and E. Hagan, "A comprehensive review of biomass resources and biofuels potential in Ghana," *Renewable and Sustainable Energy Reviews,* vol. 15, pp. 404-415, 2011.

[127] P. A. Filho and O. Badr, "Biomass resources for energy in North-Eastern Brazil," *Applied Energy,* vol. 77, pp. 51-67, 2004.

[128] J. Ruyck, F. Delattin, and S. Bram, "Co-utilization of biomass and natural gas in combined cycles through primary steam reforming of the natural gas," *Energy,* vol. 32, pp. 371-377, 2007.

[129] Z. T. Lian, K. J. Chua, and S. K. Chou, "A thermoeconomic analysis of biomass energy for trigeneration," *Applied Energy,* vol. 87, pp. 84-95, 2010.

[130] I. Obernberger, P. Thonhofer, and E. Reisenhofer, "Description and evaluation of the new 1,000 kWel Organic Rankine Cycle process integrated in the biomass CHP plant in Lienz, Austria," *Euroheat & Power,* vol. 10, pp. 1-17, 2002.

[131] F. A. Al-Sulaiman, I. Dincer, and F. Hamdullahpur, "Energy and exergy analyses of a biomass trigeneration system using an organic Rankine cycle," *Energy,* vol. 45, pp. 975-985, 2012.

[132] F. A. Al-Sulaiman, F. Hamdullahpur, and I. Dincer, "Greenhouse gas emission and exergy assessments of an integrated organic Rankine cycle with a biomass combustor for combined cooling, heating and power production," *Applied Thermal Engineering,* vol. 31, pp. 439-446, 2011.

[133] Y. Huang, Y. D. Wang, S. Rezvani, D. R. McIlveen-Wright, M. Anderson, J. Mondol, *et al.*, "A techno-economic assessment of biomass fuelled trigeneration system integrated with organic Rankine cycle," *Applied Thermal Engineering,* vol. 53, pp. 325-331, 2013.

[134] P. Ahmadi, I. Dincer, and M. A. Rosen, "Development and assessment of an integrated biomass-based multi-generation energy system," *Energy,* vol. 56, pp. 155-166, 2013.

[135] P. Ahmadi, I. Dincer, and M. A. Rosen, "Thermoeconomic multi-objective optimization of a novel biomass-based integrated energy system," *Energy,* vol. 68, pp. 958-970, 2014.

[136] D. Maraver, S. Quoilin, and J. Royo, "Optimization of Biomass-Fuelled Combined Cooling, Heating and Power (CCHP) Systems Integrated with Subcritical or Transcritical Organic Rankine Cycles (ORCs)," *Entropy,* vol. 16, pp. 2433-2453, 2014.

[137] R. DiPippo, *Geothermal Power Plants: Principles, Applications, Case Studies and Environmental Impact*, 2nd ed.: Elsevier Ltd., 2008.

[138] E. Barbier, "Geothermal energy technology and current status: an overview," *Renewable and Sustainable Energy Reviews,* vol. 6, pp. 3-65, 2002.

[139] E. Barbier, "Nature and technology of geothermal energy: A review," *Renewable and Sustainable Energy Reviews,* vol. 1, pp. 1-69, 1997.

[140] S. Köhler, "Analysis of the Combined Heat and Power Plant Neustadt-Glewe " in *Proceedings World Geothermal Congress 2005* Turkey, 2005.

[141] H. D. Madhawa Hettiarachchi, M. Golubovic, W. M. Worek, and Y. Ikegami, "Optimum design criteria for an Organic Rankine cycle using low-temperature geothermal heat sources," *Energy,* vol. 32, pp. 1698-1706, 9// 2007.

[142] F. Heberle and D. Brüggemann, "Exergy based fluid selection for a geothermal Organic Rankine Cycle for combined heat and power generation," *Applied Thermal Engineering,* vol. 30, pp. 1326-1332, 2010.

[143] R. S. El-Emam and I. Dincer, "Exergy and exergoeconomic analyses and optimization of geothermal organic Rankine cycle," *Applied Thermal Engineering,* vol. 59, pp. 435-444, 9/25/ 2013.

[144] M. Astolfi, M. C. Romano, P. Bombarda, and E. Macchi, "Binary ORC (organic Rankine cycles) power plants for the exploitation of medium–low temperature geothermal sources – Part A: Thermodynamic optimization," *Energy,* vol. 66, pp. 423-434, 2014.

[145] M. Astolfi, M. C. Romano, P. Bombarda, and E. Macchi, "Binary ORC (Organic Rankine Cycles) power plants for the exploitation of medium–low temperature geothermal sources – Part B: Techno-economic optimization," *Energy,* vol. 66, pp. 435-446, 2014.

[146] T. Guo, H. X. Wang, and S. J. Zhang, "Selection of working fluids for a novel low-temperature geothermally-powered ORC based cogeneration system," *Energy Conversion and Management,* vol. 52, pp. 2384-2391, 2011.

[147] M.-H. Yang and R.-H. Yeh, "Economic performances optimization of an organic Rankine cycle system with lower global warming potential working fluids in geothermal application," *Renewable Energy,* vol. 85, pp. 1201-1213, 2016.

[148] J. Bonilla, J. Blanco, L. Lbpez, and J. Sala, "Technological recovery potential of waste heat in the industry of the Basque Country," *Applied Thermal Engineering,* vol. 17, pp. 283-288, 1997.

[149] S. Latour, J. Menningmann, and B. Blaney, *Waste Heat Recovery Potential in Selected Industries* U.S.: Environmental Protection Agency (EPA), 1982.

[150] J. Armstead and S. Miers, "Review of Waste Heat Recovery Mechanisms for Internal Combustion Engines," *ASME J. Thermal Sci. Eng. Appl.,* vol. 6, pp. 014001-9, 2013.

[151] N. Galanis, E. Cayer, P. Roy, E. S. Denis, and M. Désilets, "Electricity Generation from Low Temperature Sources," *Journal of Applied Fluid Mechanics,* vol. 2, pp. 55-67, 2009.

[152] R. Bohl, "Waste heat recovery from existing simple cycle gas turbine plants: a case study," presented at the 18th Symposium on Industrial Application of Gas Turbines (IAGT), Canada, 2009.

[153] B. Tchanche, "Low-grade heat conversion into power using small scale organic Rankine cycles," PhD Thesis, Agricultural University of Athens, 2010.

[154] O. Bailey and E. Worrell, "Clean Energy Technologies: A Preliminary Inventory of the Potential for Electricity Generation," Lawrence Berkeley National Laboratory, 2005.

[155] G. Yu, G. Shu, H. Tian, H. Wei, and L. Liu, "Simulation and thermodynamic analysis of a bottoming Organic Rankine Cycle (ORC) of diesel engine (DE)," *Energy,* vol. 51, pp. 281-290, 2013.

[156] J. P. Roy, M. K. Mishra, and A. Misra, "Parametric optimization and performance analysis of a waste heat recovery system using Organic Rankine Cycle," *Energy,* vol. 35, pp. 5049-5062, 2010.

[157] K. K. Srinivasan, P. J. Mago, and S. R. Krishnan, "Analysis of exhaust waste heat recovery from a dual fuel low temperature combustion engine using an Organic Rankine Cycle," *Energy,* vol. 35, pp. 2387-2399, 2010.

[158] N. Zhou, X. Wang, Z. Chen, and Z. Wang, "Experimental study on Organic Rankine Cycle for waste heat recovery from low-temperature flue gas," *Energy,* vol. 55, pp. 216-225, 2013.

[159] U. Muhammad, M. Imran, D. H. Lee, and B. S. Park, "Design and experimental investigation of a 1kW organic Rankine cycle system using R245fa as working fluid for low-grade waste heat recovery from steam," *Energy Conversion and Management,* vol. 103, pp. 1089-1100, 2015.

[160] A. Desideri, S. Gusev, M. van den Broek, V. Lemort, and S. Quoilin, "Experimental comparison of organic fluids for low temperature ORC (organic Rankine cycle) systems for waste heat recovery applications," *Energy,* vol. 97, pp. 460-469, 2016.

[161] F. D. Doty and S. Shevgoor, "A Dual-Source Organic Rankine Cycle (DORC) for Improved Efficiency in Conversion of Dual Low- and Mid-Grade Heat Sources," presented at the ASME 2009 3rd International Conference on Energy Sustainability, California, USA, 2009.

[162] W. Yagoub, P. Doherty, and S. B. Riffat, "Solar energy-gas driven micro-CHP system for an office building," *Applied Thermal Engineering,* vol. 26, pp. 1604-1610, 2006.

[163] M. Kane, D. Larrain, D. Favrat, and Y. Allani, "Small hybrid solar power system," *Energy,* vol. 28, pp. 1427-1443, 2003.

[164] D. Tempesti, G. Manfrida, and D. Fiaschi, "Thermodynamic analysis of two micro CHP systems operating with geothermal and solar energy," *Applied Energy,* vol. 97, pp. 609-617, 2012.

[165] D. Tempesti and D. Fiaschi, "Thermo-economic assessment of a micro CHP system fuelled by geothermal and solar energy," *Energy,* vol. 58, pp. 45-51, 2013.

[166] M. Astolfi, L. Xodo, M. C. Romano, and E. Macchi, "Technical and economical analysis of a solar–geothermal hybrid plant based on an Organic Rankine Cycle," *Geothermics,* vol. 40, pp. 58-68, 2011.

[167] F. Calise, D. Capuano, and L. Vanoli, "Dynamic Simulation and Exergo-Economic Optimization of a Hybrid Solar–Geothermal Cogeneration Plant," *Energies,* vol. 8, pp. 2606-2646, 2015.

[168] S. Lecompte, H. Huisseune, M. van den Broek, B. Vanslambrouck, and M. De Paepe, "Review of organic Rankine cycle (ORC) architectures for waste heat recovery," *Renewable and Sustainable Energy Reviews,* vol. 47, pp. 448-461, 2015.

[169] G. Li, "Organic Rankine cycle performance evaluation and thermoeconomic assessment with various applications part I: Energy and exergy performance evaluation," *Renewable and Sustainable Energy Reviews,* vol. 53, pp. 477-499, 2016.

[170] S. Lecompte, B. Ameel, D. Ziviani, M. van den Broek, and M. De Paepe, "Exergy analysis of zeotropic mixtures as working fluids in Organic Rankine Cycles," *Energy Conversion and Management,* vol. 85, pp. 727-739, 9// 2014.

[171] Y. Dai, J. Wang, and L. Gao, "Parametric optimization and comparative study of organic Rankine cycle (ORC) for low grade waste heat recovery," *Energy Conversion and Management,* vol. 50, pp. 576-582, 2009.

[172] M. Imran, M. Usman, B.-S. Park, and Y. Yang, "Comparative assessment of Organic Rankine Cycle integration for low temperature geothermal heat source applications," *Energy,* vol. 102, pp. 473-490, 2016.

[173] T. Guo, H. Wang, and S. Zhang, "Comparative analysis of natural and conventional working fluids for use in transcritical Rankine cycle using low-temperature geothermal source," *International Journal of Energy Research,* vol. 35, pp. 530-544, 2011.

[174] P. J. Mago, L. M. Chamra, K. Srinivasan, and C. Somayaji, "An examination of regenerative organic Rankine cycles using dry fluids," *Applied Thermal Engineering,* vol. 28, pp. 998-1007, 2008.

[175] D. Meinel, C. Wieland, and H. Spliethoff, "Effect and comparison of different working fluids on a two-stage organic rankine cycle (ORC) concept," *Applied Thermal Engineering,* vol. 63, pp. 246-253, 2014.

[176] M. Yari and S. M. S. Mahmoudi, "A thermodynamic study of waste heat recovery from GT-MHR using organic Rankine cycles," *Heat and Mass Transfer,* vol. 47, pp. 181-196, 2010.

[177] B. F. Tchanche, G. Lambrinos, A. Frangoudakis, and G. Papadakis, "Exergy analysis of micro-organic Rankine power cycles for a small scale solar driven reverse osmosis desalination system," *Applied Energy,* vol. 87, pp. 1295-1306, 2010.

[178] N. B. Desai and S. Bandyopadhyay, "Process integration of organic Rankine cycle," *Energy,* vol. 34, pp. 1674-1686, 2009.

[179] H. Price and V. Hassani, "Modular Trough Power Plant Cycle and Systems Analysis," National Renewable Energy Laboratory (NREL), 2002.

[180] P. Petr and G. Raabe, "Evaluation of R-1234ze(Z) as drop-in replacement for R-245fa in Organic Rankine Cycles – From thermophysical properties to cycle performance," *Energy,* vol. 93, pp. 266-274, 2015.

[181] K. Mahkamov, E. Orda, B. Belgasim, and I. Makhkamova, "A novel small dynamic solar thermal desalination plant with a fluid piston converter," *Applied Energy,* vol. 156, pp. 715-726, 2015.

[182] X. B. Bu, H. S. Li, and L. B. Wang, "Performance analysis and working fluids selection of solar powered organic Rankine-vapor compression ice maker," *Solar Energy,* vol. 95, pp. 271-278, 2013.

[183] E. Macchi and A. Perdichizzi, "Efficiency Prediction for Axial-Flow Turbines Operating with Nonconventional Fluids," *Journal of Engineering for Power,* vol. 103, pp. 718-724, 1981.

[184] S. Kakaç, H. Liu, and A. Pramuanjaroenkij, *Heat Exchangers: Selection, Rating, and Thermal Design*, 3rd ed. USA: CRC Press, Taylor & Francis Group, LLC, 2012.

[185] F. P. Incropera, D. P. Dewitt, T. L. Bergman, and A. S. Lavine, *Principles of Heat and Mass Transfer*, Seventh ed. Singapore: John Wiley & Sons, 2013.

[186] Y. S. Kim, "An experimental study on evaporation heat transfer characteristics and pressure drop in plate heat exchanger," MSc Thesis, Yonsei University, 1999.

[187] J. R. García-Cascales, F. Vera-García, J. M. Corberán-Salvador, and J. Gonzálvez-Maciá, "Assessment of boiling and condensation heat transfer correlations in the modelling of

plate heat exchangers," *International Journal of Refrigeration*, vol. 30, pp. 1029-1041, 2007.
[188] Y. Y. Hsieh and T. F. Lin, "Saturated flow boiling heat transfer and pressure drop of refrigerant R-410A in a vertical plate heat exchanger," *International Journal of Heat and Mass Transfer*, vol. 45, pp. 1033-1044, 2002.
[189] D.-H. Han, K.-J. Lee, and Y.-H. Kim, "Experiments on the characteristics of evaporation of R410A in brazed plate heat exchangers with different geometric configurations," *Applied Thermal Engineering*, vol. 23, pp. 1209-1225, 7// 2003.
[190] D.-H. Han, K.-J. Lee, and Y.-H. Kim, "The Characteristics of Condensation in Brazed Plate Heat Exchangers with Different Chevron Angles," *Journal of the Korean Physical Society*, vol. 43, pp. 66-73, 2003.
[191] J. A. Duffie and W. A. Beckman, *Solar Engineering of Thermal Processes*, Fourth ed. New Jersey: John Wiley & Sons, 2013.
[192] G. Lorenzini, C. Biserni, and G. Flacco, *Solar Thermal and Biomass Energy*. UK: WIT Press, 2010.
[193] *Thermolib*. Available: http://www.eutech-scientific.de/products-services/thermolib.html
[194] *EUtech Scientific Engineering GmbH*. Available: http://www.eutech-scientific.de/
[195] B.-R. Fu, S.-W. Hsu, Y.-R. Lee, J.-C. Hsieh, C.-M. Chang, and C.-H. Liu, "Performance of a 250 kW Organic Rankine Cycle System for Off-Design Heat Source Conditions," *energies*, vol. 7, pp. 3684-3694, 2014.
[196] B.-R. Fu, S.-W. Hsu, Y.-R. Lee, J.-C. Hsieh, C.-M. Chang, and C.-H. Liu, "Effect of off-design heat source temperature on heat transfer characteristics and system performance of a 250-kW organic Rankine cycle system," *Applied Thermal Engineering*, vol. 70, pp. 7-12, 2014.
[197] L. Chena Power, "400kW Geothermal Power Plant at Chena Hot Springs, Alaska," Final Report Prepared for Alaska Energy Authority, 2007.
[198] G. Holdmann, "The Chena Hot Springs 400kW Geothermal Power Plant: Experience Gained During the First Year of Operation," *GRC Transactions*, vol. 31, pp. 515-519, 2007.
[199] M. Aneke, B. Agnew, and C. Underwood, "Performance analysis of the Chena binary geothermal power plant," *Applied Thermal Engineering*, vol. 31, pp. 1825-1832, 2011.
[200] C. Craggs, E. M. Conway, and N. M. Pearsall, "Stochastic modelling of solar irradiance on horizontal and vertical planes at a northerly location," *Renewable Energy*, vol. 18, pp. 445-463, 1999.
[201] C. Craggs, E. M. Conway, and N. M. Pearsall, "Statistical investigation of the optimal averaging time for solar irradiance on horizontal and vertical surfaces in the UK," *Solar Energy*, vol. 68, pp. 179-187, 2// 2000.
[202] N. Yamada, M. N. A. Mohamad, and T. T. Kien, "Study on thermal efficiency of low- to medium-temperature organic Rankine cycles using HFO−1234yf," *Renewable Energy*, vol. 41, pp. 368-375, 5// 2012.
[203] A. Bejan, G. Tsatsaronis, and M. Moran, *Thermal Design and Optimization*, 1st ed. U.S.: John Wiley & Sons, Inc., 1996.
[204] Y. Jaluria, *Design and Optimization of Thermal Systems*, 2nd ed. U.S.: Taylor & Francis Group, LLC, 2008.
[205] M. Li and B. Zhao, "Analytical thermal efficiency of medium-low temperature organic Rankine cycles derived from entropy-generation analysis," *Energy*, vol. 106, pp. 121-130, 2016.
[206] L. Blank and A. Tarquin, *Basics of Engineering Economy*, 1st ed. New York: McGraw-Hill, 2008.
[207] W. D. Seider, J. D. Seader, and D. R. Lewin, *Product and Process Design Principles: Synthesis, Analysis, and Evaluation*, 2nd ed. U.S.: John Wiley and Sons, Inc., 2003.

[208] R. Turton, R. C. Bailie, W. B. Whiting, J. A. Shaeiwitz, and D. Bhattacharyya, *Analysis, Synthesis, and Design of Chemical Processes*, Fourth ed. USA: Pearson Education Inc., 2012.

[209] M. Li, J. Wang, S. Li, X. Wang, W. He, and Y. Dai, "Thermo-economic analysis and comparison of a CO2 transcritical power cycle and an organic Rankine cycle," *Geothermics*, vol. 50, pp. 101-111, 4// 2014.

[210] D. Budisulistyo and S. Krumdieck, "Thermodynamic and economic analysis for the pre-feasibility study of a binary geothermal power plant," *Energy Conversion and Management*, vol. 103, pp. 639-649, 2015.

[211] Y. Feng, T. Hung, Y. Zhang, B. Li, J. Yang, and Y. Shi, "Performance comparison of low-grade ORCs (organic Rankine cycles) using R245fa, pentane and their mixtures based on the thermoeconomic multi-objective optimization and decision makings," *Energy*, vol. 93, pp. 2018-2029, 2015.

[212] V. L. Le, A. Kheiri, M. Feidt, and S. Pelloux-Prayer, "Thermodynamic and economic optimizations of a waste heat to power plant driven by a subcritical ORC (Organic Rankine Cycle) using pure or zeotropic working fluid," *Energy*, vol. 78, pp. 622-638, 2014.

[213] M. Kaltschmitt, W. Streicher, and A. Wiese, *Renewable Energy: Technology, Economics and Environment*, 1st ed.: Springer Science & Business Media, 2007.

[214] M. Shatat, M. Worall, and S. Riffat, "Economic study for an affordable small scale solar water desalination system in remote and semi-arid region," *Renewable and Sustainable Energy Reviews*, vol. 25, pp. 543-551, 2013.

[215] *ENOGIA - The small turbine ORC company* Available: http://www.enogia.com

[216] Y.-R. Li, M.-T. Du, C.-M. Wu, S.-Y. Wu, C. Liu, and J.-L. Xu, "Economical evaluation and optimization of subcritical organic Rankine cycle based on temperature matching analysis," *Energy*, vol. 68, pp. 238-247, 2014.

[217] E. Cayer, N. Galanis, and H. Nesreddine, "Parametric study and optimization of a transcritical power cycle using a low temperature source," *Applied Energy*, vol. 87, pp. 1349-1357, 2010.

[218] *Chemical Engineering Magazine*. Available: www.chemengonline.com/pci

[219] Y. Feng, T. Hung, K. Greg, Y. Zhang, B. Li, and J. Yang, "Thermoeconomic comparison between pure and mixture working fluids of organic Rankine cycles (ORCs) for low temperature waste heat recovery," *Energy Conversion and Management*, vol. 106, pp. 859-872, 2015.

[220] Y.-R. Li, M.-T. Du, C.-M. Wu, S.-Y. Wu, and C. Liu, "Potential of organic Rankine cycle using zeotropic mixtures as working fluids for waste heat recovery," *Energy*, vol. 77, pp. 509-519, 2014.

[221] A. F. Alajmi, "Efficient optimisation of building design using a genetic algorithm," PhD Thesis, Loughborough University, 2006.

[222] R. L. Haupt and S. E. Haupt, *Practical Genetic Algorithms*, 2nd ed. USA: John Wiley & Sons, Inc., 2004.

[223] A. M. S. Zalzala and P. J. Fleming, *Genetic Algorithms in Engineering Systems*. UK: Institution of Electrical Engineers, 1997.

[224] E. G. Shopova and N. G. Vaklieva-Bancheva, "BASIC—A genetic algorithm for engineering problems solution," *Computers & Chemical Engineering*, vol. 30, pp. 1293-1309, 2006.

[225] K. Kraitong, "Mathematical Modelling and Optimisation of Stirling Engines for Power Production," PhD Thesis, University of Northumbria, 2012.

[226] B. Belgasim, "Theoretical and Experimental Investigation of the Dynamic Solar Water Desalination Unit," PhD Thesis, Northumbria University, 2013.

Appendix A

MATLAB code for the optimisation of the hybrid solar/biomass ORC system

GA

```
%************************************************************************
%GA.m
%************************************************************************

global Pev
global DTPPe
global DTPPc
global Tc
global Mv

GA_optimisation_LPST
```

GA_optimisation_LPST

```
%*********************************************************************
%GA_optimisation_LPST.m
%*********************************************************************

function []=GA_optimisation_LPST


tic
%   Continuous Genetic Algorithm
%   Single objective function
%   Edited by K. Hossin 2015 and modified from K. Kraitong 2012 and B.
%   Belgasim 2013 (originally developed by Haupt & Haupt 2003)
%_____________________________________________________________________
%                       I Setup the GA
inputdata_GA_LPST
ff='objective_function_LPST';    % objective function
% variable limits*****************************************************
varhi=zeros(popsize,npar);
varlo=zeros(popsize,npar);
for i = 1:1:popsize
    varhi(i,:)=var_hi;
    varlo(i,:)=var_lo;
end
%_____________________________________________________________________
%                       II Stopping criteria
maxvalue=9999999;       % minimum cost
%_____________________________________________________________________
%                       III GA parameters
Nt=npar;                % continuous parameter GA Nt=#variables
%*********************************************************************
% objective function
%*********************************************************************
keep=floor(selection*popsize);      % #population members that survive
nmut=ceil((popsize-1)*Nt*mutrate);  % total number of mutations
M=ceil((popsize-keep)/2);           % number of matings
%_____________________________________________________________________
%               Create the initial population
```

```
iga=0;              % generation counter initialized
par=(varhi-varlo).*rand(popsize,npar)+varlo;  % random
result=feval(ff,par);       % calculates population value using f
value1=result(:,1);         % reult 1 from the objective function
%value2=result(:,2);         % reult 2 from the objective function
%***************************************************************
%***************************************************************
% single objective function
max_value1 = max(value1);
value = 1./(1+max_value1-value1); % evaluate fitness value for the
maximum problem
%***************************************************************
%***************************************************************
[value,inx]=sort(value,'descend');  % max value in element 1
par=par(inx,:);                     % sort continuous
value1= value1(inx,:);
%value2= value2(inx,:);
Dpar1(1)=par(1,1);
Dpar2(1)=par(1,2);
Dpar3(1)=par(1,3);
Dpar4(1)=par(1,4);
%Dpar5(1)=par(1,5);
%Dpar6(1)=par(1,6);
Dvalue1(1)=value1(1);
%Dvalue2(1)=value2(1);
maxvalue(1)=max(value1);            % maxvalue contains max of population
meanvalue(1)=mean(value1);          % meanvalue contains mean of
population
disp(['#generations=' num2str(iga) ' best value=' num2str(value(1)) '
mean value=' num2str(mean(value))])
disp([                              ' levelized energy cost='
num2str(value1(1))])
%disp([                             ' thermal efficiency='
num2str(value2(1))])
%_____________________________________________________________
%_____________________________________________________________
%               Iterate through generations
while iga<maxit
   iga=iga+1;               % increments generation counter
```

```
%_____________________________________________________________________
%                        Pair and mate
M=ceil((popsize-keep)/2);       % number of matings
prob=flipud([1:keep]'/sum([1:keep]));   % weights chromosomes
odds=[0 cumsum(prob(1:keep))']; % probability distribution function
pick1=rand(1,M);                        % mate #1
pick2=rand(1,M);                        % mate #2
% ma and pa contain the indicies of the chromosomes that will mate
ic=1;
while ic<=M
  for id=2:keep+1
    if pick1(ic)<=odds(id) && pick1(ic)>odds(id-1)
      ma(ic)=id-1;
    end
    if pick2(ic)<=odds(id) && pick2(ic)>odds(id-1)
      pa(ic)=id-1;
    end
  end
  ic=ic+1;
end
%_____________________________________________________________________
%           Performs mating using single point crossover
ix=1:2:keep;                          % index of mate #1
xp=ceil(rand(1,M)*Nt);                % crossover point
r=rand(1,M);                          % mixing parameter
for ic=1:M
    xy=par(ma(ic),xp(ic))-par(pa(ic),xp(ic));  % ma and pa mate
    par(keep+ix(ic),:)=par(ma(ic),:);          % 1st offspring
    par(keep+ix(ic)+1,:)=par(pa(ic),:);        % 2nd offspring
    par(keep+ix(ic),xp(ic))=par(ma(ic),xp(ic))-r(ic).*xy; % 1st
    par(keep+ix(ic)+1,xp(ic))=par(pa(ic),xp(ic))+r(ic).*xy; % 2nd
        if xp(ic)<npar % crossover when last variable not selected
            par(keep+ix(ic),:)=[par(keep+ix(ic),1:xp(ic))
par(keep+ix(ic)+1,xp(ic)+1:npar)];
            par(keep+ix(ic)+1,:)=[par(keep+ix(ic)+1,1:xp(ic))
par(keep+ix(ic),xp(ic)+1:npar)];
        end
end
%_____________________________________________________________________
```

```
%                        Mutate the population
mrow=sort(ceil(rand(1,nmut)*(popsize-1))+1);
mcol=ceil(rand(1,nmut)*Nt);
for ii=1:nmut
    par(mrow(ii),mcol(ii))=(varhi(mrow(ii),mcol(ii))-
varlo(mrow(ii),mcol(ii)))*rand+varlo(mrow(ii),mcol(ii));  % mutation
end % ii
%_____________________________________________________________
%   The new offspring and mutated chromosomes are evaluated
result=feval(ff,par);       % calculates population value using f
value1=result(:,1);         % reult from the objective function 1
%value2=result(:,2);         % reult from the objective function 2
%*************************************************************
% single objective function
%value=value1;
maxvalue1 = max(value1);
if maxvalue1>max_value1
    max_value1=maxvalue1;
end
value = 1./(1+max_value1-value1);   % evaluates fitness value for the
maximum problem
[value,inx]=sort(value,'descend') ; % max value in element 1
par=par(inx,:)  ;                   % sort continuous
value1= value1(inx,:);
%value2= value2(inx,:);
%_____________________________________________________________
%           Do statistics for a single nonaveraging run
Dpar1(iga+1)=par(1,1);
Dpar2(iga+1)=par(1,2);
Dpar3(iga+1)=par(1,3);
Dpar4(iga+1)=par(1,4);
%Dpar5(iga+1)=par(1,5);
%Dpar6(iga+1)=par(1,6);
Dvalue1(iga+1)=value1(1);
%Dvalue2(iga+1)=value2(1);
maxvalue(iga+1)=max(value1);
meanvalue(iga+1)=mean(value1);
```

```
disp(['#generations=' num2str(iga) ' best value=' num2str(value(1)) '
mean value=' num2str(mean(value))])
disp([                              ' levelized energy cost='
num2str(value1(1))])
disp(['%%%%%%%%%%%%%%%%%%%%%%%%%%%%%%%%%%%%%%%%%%%%%%%%%%%%%%%%%%%%%%%%%%%%%%%%%%%%%%%%
%'])
disp(['%%%%%%%%%%%%%%%%%%%%%%%%%%%%%%%%%%%%%%%%%%%%%%%%%%%%%%%%%%%%%%%%%%%%%%%%%%%%%%%%
%'])
disp(['%%%%%%%%%%%%%%%%%%%%%%%%%%%%%%%%%%%%%%%%%%%%%%%%%%%%%%%%%%%%%%%%%%%%%%%%%%%%%%%%
%'])
%_____________________________________________________________________
%                        Stopping criteria
    if iga>20 && iga<=maxit
        if maxvalue<=maxvalue(iga-20)
        break
        end
    elseif iga>maxit
        break
    end
end
%_____________________________________________________________________
%                       Displays the output
day=clock;
disp(datestr(datenum(day(1),day(2),day(3),day(4),day(5),day(6)),0))
%disp(['optimized function is 'ff ])
disp('continuous genetic algorithm')
format short g
disp(['popsize = ' num2str(popsize) ' mutrate = ' num2str(mutrate) ' #
par = ' num2str(npar)])
disp(['#generations=' num2str(iga)])
fprintf('Minimum levelized energy cost= %12.9f $/kWh\n',maxvalue(iga));
disp([' at best solution'])
fprintf('Evap pressure= %12.9f m3         DTPPe = %12.9f m
\n',par(1,1),par(1,2));
fprintf('DTPPc= %12.9f m                  Cond temperature = %12.9f Pa
\n',par(1,3),par(1,4));

%disp([num2str(par(1,:))])
```

```
%save data
iters=0:length(maxvalue)-1;
save LEC-G.xls iters Dvalue1 -ascii;
save Pev-G.xls iters Dpar1 -ascii;

figure(1)
plot(iters,maxvalue);
xlabel('generation');ylabel('value');
title('value vs generation ')

figure(2)
plot(iters,Dvalue1,'k');
xlabel('generation');ylabel('levelized energy cost($/kWh)');
title('levelized energy cost vs generation ')

figure(3)
plot(iters,Dpar1,'k');
xlabel('generation');ylabel('Evap pressure(Pa)');
title('Evap pressure vs generation ')

figure(4)
plot(iters,Dpar2,'k');
xlabel('generation');ylabel('DTPPe(K)');
title('DTPPe vs generation ')

figure(5)
plot(iters,Dpar3,'k');
xlabel('generation');ylabel('DTPPc(K)');
title('DTPPc vs generation ')

figure(6)
plot(iters,Dpar4,'k');
xlabel('generation');ylabel('Cond temperature(C)');
title('Cond temperature is function of generation ')

toc
end
```

Inputdata_GA_LPST

```
%*********************************************
%inputdata_GA_LPST.m
%*********************************************
global popsize
%*********************************************
%GA parameters
%popsize=input('population size =');
popsize=30;              % set population size
mutrate=0.2;             % set mutation rate
selection=0.5;           % fraction of population kept
maxit=80;                % max number of generations
%*************************************************************************
%*************************************************************************
%Define Hybrid ORC decision variables and define upper and lower bounds
%*************************************************************************
%M_Pev=input('Evap pressure is optimal HORC parameter : enter 1 if not
enter 0');
M_Pev=1;
%M_DTPPe=input('DTPPe is optimal HORC parameter : enter 1 if not enter
0');
M_DTPPe=1;
%M_DTPPc=input('DTPPc is optimal HORC parameter : enter 1 if not enter
0');
M_DTPPc=1;
%M_Tc=input('Cond temperature is optimal HORC parameter : enter 1 if not
enter 0');
M_Tc=1;

M=[M_Pev M_DTPPe M_DTPPc M_Tc];

npar=sum(M);
%disp ('define value of HORC parameter and also upper and lower bounds of
optimal HORC parameters')
var_hi=zeros(1,npar);
var_lo=zeros(1,npar);
sign=zeros(1,npar);
```

```
if M_Pev==0
    %Pev=input('evap pressure[Pa]');
    %Pev = 1200000;
elseif M_Pev==1
    var_hi(1,1)=1272000;        % upper bound
    sign(1,npar)=1;
    var_lo(1,1)=800000;         % lower bound
end
if M_DTPPe==0
    DTPPe=input('DTPPe [K]');
    %DTPPe = 0.025;
elseif M_DTPPe==1
    %var_hi(1,sum(sign)+1)=input('DTPPe-upper bound[m]');
    var_hi(1,sum(sign)+1)=12;        % upper bound
    %var_lo(1,sum(sign)+1)=input('DTPPe-lower bound[m]');
    var_lo(1,sum(sign)+1)=6;         % lower bound
    sign(1,sum(sign)+1)=1;
end
if M_DTPPc==0
    DTPPc=input('DTPPc[m]');
    %DTPPc = 0.025;
elseif M_DTPPc==1
    %var_hi(1,sum(sign)+1)=input('DTPPc-upper bound[m]');
    var_hi(1,sum(sign)+1)=8;        % upper bound
    %var_lo(1,sum(sign)+1)=input('DTPPc-lower bound[m]');
    var_lo(1,sum(sign)+1)=4;        % lower bound
    sign(1,sum(sign)+1)=1;
end
if M_Tc==0
    Tc=input('cond temperature[C]');
    %Tc = 0.025;
elseif M_Tc==1
    %var_hi(1,sum(sign)+1)=input('cond temperature-upper bound[Pa]');
    var_hi(1,sum(sign)+1)=40;        % upper bound
    %var_lo(1,sum(sign)+1)=input('cond temperature-lower bound[Pa]');
    var_lo(1,sum(sign)+1)=30;        % lower bound
    sign(1,sum(sign)+1)=1;
end
```

Objective_function_LPST

```
%************************************************************************
%objective_function_LPST.m
%************************************************************************

function ff=objective_function_LPST(x)

global popsize

for i=1:1:popsize
    %inputdata_GA
    Pev=x(i,1);
    DTPPe=x(i,2);
    DTPPc=x(i,3);
    Tc=x(i,4);
    [m]=LPST_modelling(Pev,DTPPe,DTPPc,Tc);
    fprintf('m= %9.5f  \n\n',m);
    Dm(i)=m;
end
ff = [Dm];
ff=ff';
end
```

LPST_modelling

```
%************************************************************************
%LPST_modelling.m
%************************************************************************

function [m]=LPST_modelling(Pev,DTPPe,DTPPc,Tc)

simparameter(Pev,DTPPe,DTPPc,Tc)
simout= sim('R245fa_Final_Opt');
m=max(-Mv.signals.values);

end
```

Simparameter

```
%************************************************************************
%simparameter.m
%************************************************************************

function vv=simparameter(Pev,DTPPe,DTPPc,Tc)


global Pev
global DTPPe
global DTPPc
global Tc


end
```